

Advanced Methods for Mapping the Radiofrequency Magnetic Fields in MRI

Francesco Padormo

A dissertation submitted for the degree of
Doctor of Philosophy

September 2012

Robert Steiner MRI Unit
Imaging Sciences Department
MRC Clinical Sciences Centre
Imperial College London

Abstract

As MRI systems have increased in static magnetic field strength, the radiofrequency (RF) fields that are used for magnetisation excitation and signal reception have become significantly less uniform. This can lead to image artifacts and errors when performing quantitative MRI. A further complication arises if the RF fields vary substantially in time. In the first part of this investigation temporal variations caused by respiration were explored on a 3T scanner. It was found that fractional changes in transmit field amplitude between inhalation and expiration ranged from 1% to 14% in the region of the liver in a small group of normal subjects. This observation motivated the development of a pulse sequence and reconstruction method to allow dynamic observation of the transmit field throughout the respiratory cycle. However, the proposed method was unsuccessful due to the inherently time-consuming nature of transmit field mapping sequences.

This prompted the development of a novel data reconstruction method to allow the acceleration of transmit field mapping sequences. The proposed technique posed the RF field reconstruction as a nonlinear least-squares optimisation problem, exploiting the fact that the fields vary smoothly. It was shown that this approach was superior to standard reconstruction approaches.

The final component of this thesis presents a unified approach to RF field calibration. The proposed method uses all measured data to estimate both transmit and receive sensitivities, whilst simultaneously insisting that they are smooth functions of space. The resulting maps are robust to both noise and imperfections in regions of low signal.

This work is dedicated to my grandparents, both present and departed.

Acknowledgements

This PhD would not have been possible without the help and support of many people. First and foremost, I would like to thank Professor Joseph Hajnal. Jo has been my supervisor and mentor for four years, and has been a limitless source of ideas, advice and constructive criticism throughout. Jo has guided me through many difficult times, and has always been generous with his time and finances. Good PhD supervisors are incredibly rare, and I realise how lucky I was to have a chance to work with Jo.

I am also indebted to Dr David Larkman, who I had the pleasure of being supervised by during the first year of my PhD. Not only did David inspire me to work in MRI, he also devoted significant time and energy to teaching me how to do proper science.

I would also like to thank everyone at the Images Sciences Department at Hammersmith Hospital, and those who have recently moved to St Thomas' Hospital. The ISD was a brilliant place to work, thanks to the great community which inhabited the Robert Steiner Unit. I am especially grateful to Dr Rob Eckersley and Dr Marzena Wylezinska-Arridge for keeping me on the straight and narrow, and also many of my colleagues: Shaihan, Tom, Gianlorenzo, Marta, Rita, Anthony, Anna, Sairam, Alle-Meije, and Irvin. Your advice, expertise, and most importantly your company, was invaluable to me. I would also like to thank Michelle Hetherington, Kate Baird and Anne Soutar for friendly and prompt administrative support.

As my officemates throughout my PhD, Angela and Kathryn deserve a huge amount of thanks. They kept me company; they kept me sane; and kept on making me laugh.

Finally, I would like to thank those closest to me. Vero, Maria and Sam, Ma and Pa – thank you for all your love and support over the years - none of this would have been possible without you.

Declaration of Originality

I declare that all of the work presented in this thesis was performed by myself, except where clearly stated in the text.

Francesco Padormo

Table of Contents

Abstract.....	2
Acknowledgements	4
Declaration of Originality.....	5
List of Figures and Tables	9
Abbreviations.....	13
Chapter 1 Overview	16
1.1 Motivation.....	16
1.2 Thesis Outline.....	17
1.3 References.....	18
Chapter 2 Magnetic Resonance Imaging	20
2.1 Nuclear Magnetic Resonance	20
2.1.1 Spin and Magnetic Moments	20
2.1.2 The Behaviour of Nuclei	23
2.1.3 The Bloch Equation	26
2.1.4 Signal Measurement	28
2.2 Magnetic Resonance Imaging	29
2.2.1 Spatial Encoding	29
2.2.2 Pulse sequences	35
2.2.3 Noise	40
2.3 References.....	41
Chapter 3 Radiofrequency Fields in MRI.....	43
3.1 Electromagnetic fields	43
3.2 Radiofrequency Fields in MRI	46
3.2.1 The Electromagnetic Spectrum.....	46
3.2.2 The B_1 Field.....	47
3.2.3 Quadrature.....	48
3.2.4 Phase.....	49
3.2.5 RF Coils	50
3.2.6 The Spatial Distribution of B_1 Field.....	55
3.3 Utilisation of RF Fields in MRI.....	58
3.3.1 Receive Field	58

3.3.2	Transmit Fields	61
3.4	Determination of RF Fields.....	67
3.4.1	Analytical Solutions to Maxwell's Equations	67
3.4.2	RF Simulations	68
3.4.3	Measurement of fields using MRI.....	69
3.5	References.....	79
Chapter 4	Observation and Measurement of Dynamic Changes in the Transmit Field	84
4.1	Motivation.....	84
4.1.1	Effect of RF Inhomogeneity on RF pulses.....	84
4.1.2	Effects of Transmit Inhomogeneity - Imaging	85
4.1.3	Effects of Transmit Inhomogeneity – Quantitative MRI.....	85
4.1.4	Motion and RF Inhomogeneity.....	86
4.2	Study 1: Measurement and Correction of Transmit Field Inhomogeneity in the Liver due to Respiratory Motion.....	88
4.2.1	Introduction	88
4.2.2	Methods.....	90
4.2.3	Results.....	97
4.2.4	Discussion	107
4.3	Study 2: Respiratory-Resolved Transmit Field Measurements.....	110
4.3.1	Introduction	110
4.3.2	Methods.....	113
4.3.3	Results.....	117
4.3.4	Discussion	126
4.4	References.....	128
Chapter 5	Accelerated Transmit Field Measurement using a Model-Based Reconstruction	133
5.1	Introduction	133
5.2	Theory.....	141
5.2.1	Strategy	142
5.3	Experimental Methods and Results	155
5.3.1	Structure	155
5.3.2	Study 1	156

5.3.3	Study 2	171
5.3.4	Study 3	179
5.4	Discussion	191
5.5	References.....	192
Chapter 6	PRIMO - Precise Radiofrequency Inference from Multiple Observations	196
6.1	Introduction	196
6.1.1	Current Paradigm of RF System Calibration	197
6.1.2	Data Redundancy	198
6.1.3	Proposed Strategy.....	199
6.2	Theory.....	200
6.2.1	Receive Mapping directly from k-space	201
6.2.2	Application to Full RF Calibration.....	207
6.3	Methods.....	211
6.3.1	Implementation Details.....	212
6.3.2	Simulations	214
6.4	Results	217
6.4.1	Simulation 1.....	217
6.4.2	Simulation 2.....	223
6.4.3	In-Vivo Experiments.....	224
6.5	Discussion	231
6.6	References.....	235
Chapter 7	Conclusions.....	238
7.1	Summary of Achievements	239
7.2	Future Work.....	240
7.3	References.....	241

List of Figures and Tables

Figure 2.1 – A charged rotating body and its dipolar magnetic field.....	22
Figure 2.2 – The representation of image data in k-space.....	32
Figure 2.3 – k-space and sampling.....	33
Figure 2.4 – Signal and sampling functions in both the image domain and k-space	35
Figure 2.5 – Pulse sequence diagram for a spoiled gradient echo pulse sequence	36
Figure 2.6 – FE and PE in k-space.....	38
Figure 2.7 – SPGR signal as a function of flip angle for several tissue types and sequence timings.....	40
Figure 3.1 – Demonstration of linear versus quadrature excitation.....	49
Figure 3.2 – Schematic of basic loop coil and its equivalent circuit.	52
Figure 3.3 – A birdcage coil	53
Figure 3.4 – The NMR phased array	54
Figure 3.5 – Principle of minimising coil coupling via overlapping.	55
Figure 3.6 – The SENSE mechanism.....	60
Figure 3.7 – The effect of inversion and refocusing pulses on magnetisation.....	63
Figure 3.8 – AFI pulse sequence.....	73
Figure 3.9 – The simulated dynamic range of the AFI sequence	77
Figure 4.1 – Gradient lobes and RF pulse shape of slice-selective AFI sequence.	92
Figure 4.2 – Measured inhale and exhale images from dataset 2.....	93
Figure 4.3 – ROI Selection.....	94
Figure 4.4 – Graphs showing inhale and exhale ROI flip angle averages of each breathhold of each dataset	98
Figure 4.5 – Average inhale and exhale flip angle maps of all datasets	99
Figure 4.6 – $\bar{\theta}_{n,i}(x)$, $\bar{\theta}_{n,e}(x)$, and $\Delta\bar{\theta}_n(x)$, ($^{\circ}$) inside each dataset's ROI.....	100
Figure 4.7 – Histograms of $\Delta\bar{\theta}_n(x)$ inside the respective ROIs.....	101
Figure 4.8 –Magnitude and phase transmit maps of inhale and exhale states	104
Figure 4.9 – Power of RF shim optimisation solutions for inhale and exhale.....	105
Figure 4.10 – Shimmed and unshimmed inhale and exhale transmit maps, and their spatial difference	106
Figure 4.11 – Relative transmitter drives.....	107

Figure 4.12 – Possible transmit field transitions between inhale and exhale respiratory states	111
Figure 4.13 – Schematic of acquisition scheme.....	114
Figure 4.14 – Timing of respiratory audio track.....	115
Figure 4.15 – Example respiratory bellows output and the corresponding PE acquisition markers.....	116
Figure 4.16 – Example respiratory bellows output from six volunteers.	118
Figure 4.17 – Number of PEs in each respiratory bin for each volunteer and N_b	120
Figure 4.18 – Results from volunteer 1	122
Figure 4.19 – Results from volunteer 3	123
Figure 4.20 – Results from volunteer 5	124
Figure 4.21 – Results from volunteer 6	125
Figure 5.1 – Demonstration of Trust-Region optimisation method.....	146
Figure 5.2 – Demonstration of the creation of d^{FDx}	150
Figure 5.3 – Body model, and example FDTD transmit and receive fields.....	158
Figure 5.4 – Body model in slice of interest, and T_1 and T_2 values assigned to the anatomy	159
Figure 5.5 – Individual transmit and receive fields, and the net quadrature fields	160
Figure 5.6 – Simulated data in image domain and k-space	161
Figure 5.7 – Sampling patterns for each trajectory class at many undersampling rates.	164
Figure 5.8 – Four versions of each sampling pattern	164
Figure 5.9 – Field map error vs regularisation parameter for all undersampling rates and trajectory types.....	167
Figure 5.10 – Reconstruction errors versus undersampling rate for all trajectory classes	168
Figure 5.11 – Example field maps at $U_s = 0.5$ and $U_s = 0.1$ for each trajectory type	169
Figure 5.12 – Results of truncation process	172
Figure 5.13 – Sampling patterns at each U_s and CR level.....	174
Figure 5.14 – Error versus regularisation parameter 1	175
Figure 5.15 – Error versus regularisation parameter 2	176
Figure 5.16 – Error of best reconstruction for each U_s and CR, and error versus U_s for each CR.....	177
Figure 5.17 – Optimal reconstructions at all CR and U_s	178

Figure 5.18 – High resolution k-space and resolution masks	181
Figure 5.19 – Example sampling strategy for $N_s = 240$	182
Figure 5.20 – Error of using a zero-filled reconstruction for coil 1.....	183
Figure 5.21 – Reconstruction error versus N_s for transmit configuration 1	185
Figure 5.22 – Reconstruction error versus N_s for transmit configuration 5	186
Figure 5.23 – Transmit configuration 1 – relative error associated with each trajectory type for many N_s	187
Figure 5.24 – Transmit configuration 5 – relative error associated with each trajectory type for many N_s	188
Figure 5.25 – Transmit field maps (LC 1) and their error with respect to gold standard	189
Figure 5.26 - Transmit field maps (LC 5) and their error with respect to gold standard	189
Figure 6.1 – Images obtained using the AFI sequence	199
Figure 6.2 – Schematic demonstrating the GRAPPA principle	202
Figure 6.3 – Formation of A_r	203
Figure 6.4 – The full calibration matrix	204
Figure 6.5 – Visual depiction of the matrix equation to be inverted to obtain the weights	205
Figure 6.6 – Visual impression of the eigenvalue equation given by equation 1.4.....	206
Figure 6.7 – Typical calibration dataset for a parallel transmit and receive system.....	208
Figure 6.8 – 3D depiction of k-space.....	212
Figure 6.9 – Individual transmit and receive sensitivities of simulation.....	214
Figure 6.10 – Results of simulation 1	219
Figure 6.11 – Reconstruction error verses N_{PE} for many kernel sizes and SNR levels..	220
Figure 6.12 – The gold standard (GS) and reconstructed PRIMO and IDR field maps...	222
Figure 6.13 – Results of simulation 2.....	224
Figure 6.14 – Reconstructed magnitude transmit field maps for a transverse slice through the brain.....	226
Figure 6.15 – Reconstructed magnitude transmit field maps for a sagittal slice through the brain.....	227
Figure 6.16 – IDR, PW-PRIMO and ALL-PRIMO for relative transmit field mapping	228

Figure 6.17 – IDR and ALL-PRIMO reconstructions for relative transmit field mapping 1	229
Figure 6.18 – IDR and ALL-PRIMO reconstructions for relative transmit field mapping 2	229
Figure 6.19 – Full relative transmit and receive calibration using ALL-PRIMO	230
Figure 6.20 – 2D versus 3D PRIMO	233
Table 2.1 – Human tissue relaxation times at 3T (taken from Stanisiz et al., 2005)	26
Table 3.1 – Classifications of the electromagnetic spectrum.	46
Table 3.2 – Conductivities and relative permittivities of tissues at 3T (Liu et al., 2005).	57
Table 4.1 – Summary results of ROI analysis.	103

Abbreviations

AP	Anterior-Posterior
B₀	Polarising Magnetic Field
CR	Centre Radius, or Central Reduction
CSF	Cerebrospinal Fluid
DAQ	Digital Acquisition
DCE	Dynamic Contrast Enhanced
DS	Different Sampling
ECG	Electrocardiogram
EL	Extension Level
EPI	Echo Planar Imaging
FD	Finite Difference
FDTD	Finite Difference Time Domain
FE	Frequency Encoding
FH	Foot-Head
FOV	Field of View
FSE	Fast Spin Echo
FT	Fourier Transform
GS	Gold Standard
IDR	Image Domain Ratio
IQR	Interquartile Range

LC	Linear Combination
LR	Left-Right
MRI	Magnetic Resonance Imaging
NLLS	Nonlinear Least Squares
PE	Phase Encoding
PFI	Partial Fourier Imaging
PG	Prospective Gating
PPI	Partially Parallel Imaging
PRIMO	Precise Radiofrequency Inference from Multiple Observations
PTx	Parallel Transmission
PUS	Poisson Undersampling
PW	Pairwise
NMR	Nuclear Magnetic Resonance
qMRI	Quantitative MRI
rBW	Receiver Bandwidth
RCUS	Regular Cartesian Undersampling
RF	Radiofrequency
RG	Retrospective Gating
RMSE	Root Mean Squared Error
ROI	Region of interest
RUS	Random Undersampling

SNR	Signal to Noise Ratio
SOS	Sum-of-Squares
SPGR	Spoiled Gradient Echo
SS	Same Sampling
SVD	Singular value Decomposition
TE	Echo Time
TR	Repetition Time
TV	Total Variation
VDUS	Variable Density Undersampling

Chapter 1 Overview

1.1 Motivation

Since the invention of Magnetic Resonance Imaging (MRI) in the 1970's, significant effort has been devoted to constructing systems of ever-increasing main magnetic field strength (B_0). This pursuit is primarily driven by the inherently higher signal-to-noise ratios (SNR) available at higher B_0 (Haacke et al., 1999). However, operating at higher field results in several undesirable consequences.

One of the most significant effects of high B_0 is radiofrequency (RF) transmit field inhomogeneity (Collins and Wang, 2011). This effect can severely hamper the diagnostic quality of images at 3T, and 7T imaging is virtually impossible without dedicated methods to mitigate it.

Many methods have been developed to mitigate the effects of transmit inhomogeneity (Ibrahim et al., 2001; Saekho et al., 2005; Setsompop et al., 2008). The majority of these methods require prior knowledge of the shape of the transmit field in order to operate. This knowledge is obtained through additional RF field measurement calibration scans (Insko and Bolinger, 1993; Yarnykh, 2007; Sacolick et al., 2010).

This thesis presents investigations into three aspects of RF field mapping. The first is the underlying assumption of temporal invariance of the transmit field. Once the fields have been measured, it is typically assumed that they remain the same throughout the scan session. It is shown here that this is not necessarily true – as the transmit system is electromagnetically linked to the subject, changes in the subject's position can and do lead to field changes. This is demonstrated in the case of respiration. This motivated the development of a method to measure the transmit field throughout the respiratory cycle. However, this attempt was undermined by the slow nature of transmit field mapping

sequences, which motivated the second aspect of transmit field mapping investigated in this thesis – improving efficiency of mapping.

A method was developed which achieved scan acceleration by undersampling k-space. This approach was coupled with a novel reconstruction method that promoted field map smoothness. It is shown that higher quality reconstructions can be achieved over standard approaches.

The final aspect of RF field mapping explored here concerns full RF transmit and receive calibration. The current paradigm of scanner calibration performs transmit and receive calibration sequentially. This was recognised as inefficient, motivating the development of a novel method, PRIMO. This method uses all acquired transmit and receive calibration data to estimate every possible transmit and receive field. This method is shown to be superior to standard image domain approaches.

1.2 Thesis Outline

- Chapter 2 presents a brief outline into the basic principles underlying MRI. This covers the quantum origins of the NMR signal, and how it can be exploited to generate medical images.
- Chapter 3 presents a detailed discussion on RF fields in MRI. This begins with explanations of electromagnetic theory, how fields are generated by RF coils, and how the field strength and properties of the object affect the spatial distributions of the fields. This is followed by a review of how RF fields are used to both measure signal and manipulate magnetisation. The chapter concludes by summarising the principal techniques used to obtain RF field information.
- Chapter 4 is separated into two parts. The first presents investigations on the effect of respiratory state on the RF fields observed in the liver of

normal volunteers. This is followed by the second part, which presents the work on a respiratory-resolved field mapping method.

- Chapter 5 presents research into accelerating RF field mapping by k-space undersampling. It is composed of four sections. The first outlines the mathematical framework used for field map reconstruction. The following two sections detail initial experiments using the technique. These inform the experiments performed in the final section, which demonstrates the superiority of the proposed method over standard approaches.
- Chapter 6 presents PRIMO, a comprehensive framework for mapping both transmit and receive RF fields. The chapter begins by explaining the mathematical framework underlying the technique. Then PRIMO is tested in simulations and experimentally, demonstrating its superiority over conventional techniques.
- Chapter 7 summarises the work presented in this thesis.

1.3 References

Collins, C.M., and Wang, Z. (2011). Calculation of radiofrequency electromagnetic fields and their effects in MRI of human subjects. *Magnetic Resonance in Medicine* *65*, 1470–1482.

Haacke, E.M., Brown, R.W., Thompson, M.R., and Venkatesan, R. (1999). *Magnetic Resonance Imaging: Physical principles and sequence design*.

Ibrahim, T.S., Lee, R., Baertlein, B.A., Abduljalil, A.M., Zhu, H., and Robitaille, P.-M.L. (2001). Effect of RF coil excitation on field inhomogeneity at ultra high fields: a field optimized TEM resonator. *Magnetic Resonance Imaging* *19*, 1339–1347.

Insko, E.K., and Bolinger, L. (1993). Mapping of the Radiofrequency Field. *Journal of Magnetic Resonance, Series A* *103*, 82–85.

Sacolick, L.I., Wiesinger, F., Hancu, I., and Vogel, M.W. (2010). B1 mapping by Bloch-Siegert shift. *Magnetic Resonance in Medicine* *63*, 1315–1322.

Saekho, S., Boada, F.E., Noll, D.C., and Stenger, V.A. (2005). Small tip angle three-dimensional tailored radiofrequency slab-select pulse for reduced B1 inhomogeneity at 3 T. *Magnetic Resonance in Medicine* *53*, 479–484.

Setsompop, K., Alagappan, V., Gagoski, B., Witzel, T., Polimeni, J., Potthast, A., Hebrank, F., Fontius, U., Schmitt, F., Wald, L.L., et al. (2008). Slice-selective RF pulses for in vivo B₁⁺ inhomogeneity mitigation at 7 tesla using parallel RF excitation with a 16-element coil. *Magnetic Resonance in Medicine* 60, 1422–1432.

Yarnykh, V.L. (2007). Actual flip-angle imaging in the pulsed steady state: A method for rapid three-dimensional mapping of the transmitted radiofrequency field. *Magnetic Resonance in Medicine* 57, 192–200.

Chapter 2 Magnetic Resonance Imaging

Magnetic Resonance Imaging (MRI) is a technology based on the physical mechanism of Nuclear Magnetic Resonance (NMR). This chapter provides a description of how NMR is utilised to generate medical images. It begins with a discussion of the quantum mechanical origins of the NMR mechanism. This is followed by an analysis of the Bloch equation, which describes how magnetisation behaves in the presence of magnetic fields.

The process of creating an image from the NMR signal is described next. This includes an explanation how applying additional magnetic field gradients results in Fourier encoding, and how the process of digitally sampling the signal affects the resolution and field of view of the final image. Finally, the process of generating image contrast and the detrimental effects of noise are presented.

2.1 Nuclear Magnetic Resonance

2.1.1 Spin and Magnetic Moments

The origins of NMR lie in the development of Quantum Theory at the beginning of 20th Century. Quantum Theory describes physics at atomic length scales, a regime in which all fundamental particles display both wave-like and particle-like behaviour (Rae, 2002). Early pioneering research revealed that all fundamental particles have an intrinsic property beyond their mass and charge, referred to as spin. Spin represents a particle's inherent angular momentum, and is characterised by the quantum number s . All fermions (i.e. electrons, quarks and neutrinos) have $s = \frac{1}{2}$, whilst bosons (elementary particles which carry forces, such as photons and gluons) have a whole spin number (Levitt, 2001). The spin vector of a particle (\mathbf{s} , and equation 2.1) is analogous to the angular momentum vector of a rotating body, defining the axis of rotation and its magnitude. Here, \hbar is Planck's constant and \mathbf{d} is a unit vector oriented along the spin axis.

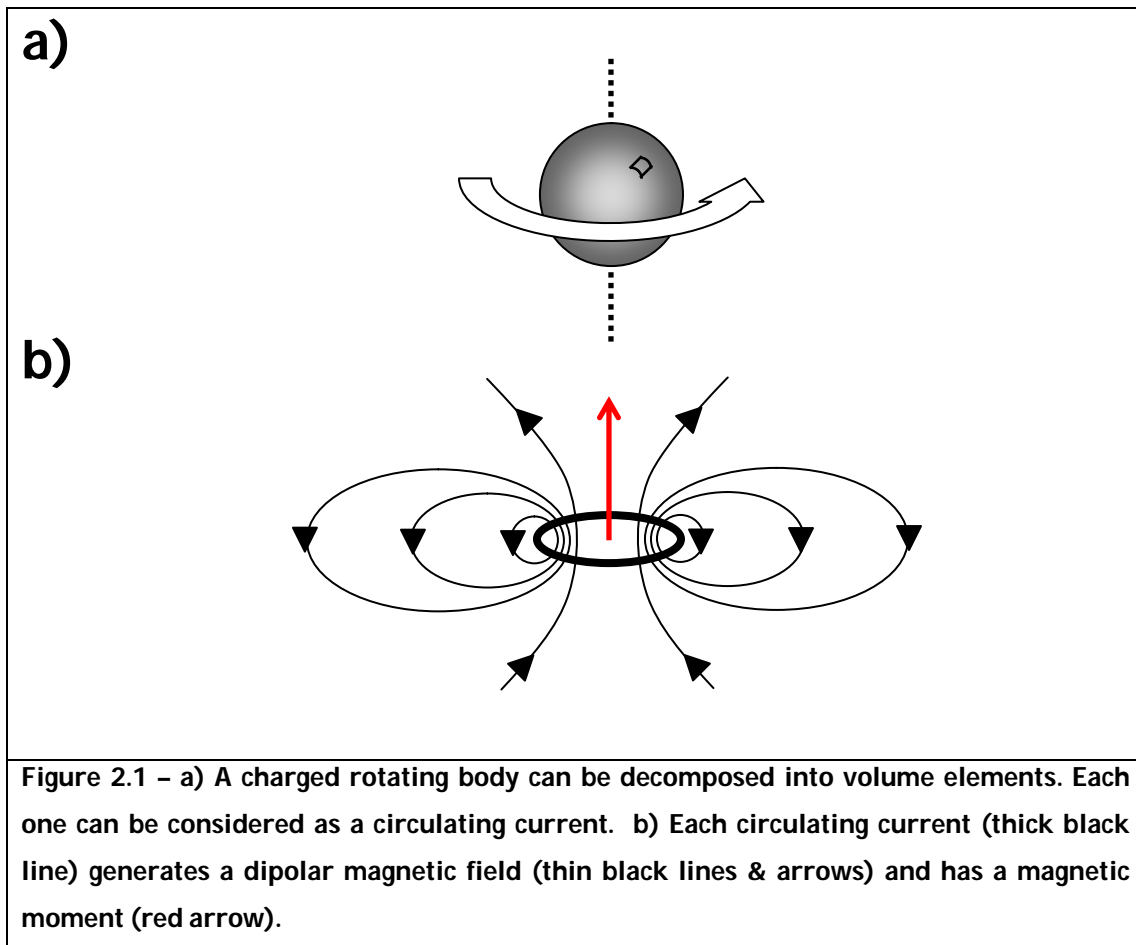
2.1

$$\mathbf{s} = \frac{h}{2\pi} \sqrt{s(s+1)} \mathbf{d}$$

Note that the magnitude of the spin vector is fixed – it is exclusively a function of s , whose value is an intrinsic property of the particle. This is in contrast to a macroscopic object, which can have any amount angular momentum.

A further parallel with classical physics can be made when considering the spin of a fundamental particle. When a charged macroscopic object rotates (Figure 2.1a), a magnetic field is generated. The origin of this field can be understood by decomposing the object into small charged volume elements on circular orbits about the axis of rotation (Figure 2.1b). Each orbit is a circulating current that generates a dipolar magnetic field (Buxton, 2002).

When immersed in an applied magnetic field, the circulating current will feel a torque so that the dipolar and applied fields align. The magnetic moment is a vector associated with the current loop, oriented perpendicularly to the plane of the circulation, whose magnitude defines the strength of the torque acting to align the fields.



Analogously, a charged fundamental particle with an intrinsic spin generates a dipolar magnetic field and has a magnetic moment. This is defined in equation 2.2, where μ is the magnetic moment vector, q is the charge of the particle, m is its mass and g is a particle-specific factor determined by how the particle interacts with its own electromagnetic field. The gyromagnetic ratio, γ , is constructed by combining the scalar factors g , q and m , and has units of radians per seconds per Tesla ($\text{rad s}^{-1}\text{T}^{-1}$).

$$2.2 \quad \mu = \frac{gq}{2m} \mathbf{s} = \gamma \mathbf{s}$$

Equations 2.1 and 2.2 are valid for elementary particles. Composite particles have properties that depend on their constituents' properties in a more complex way. For example, neutrons have a non-zero magnetic moment (Levitt, 2001), despite being electrically neutral ($q=0$), contravening equation 2.2.

In contrast, the magnetic moments of atomic nuclei can be accurately predicted by the number of protons and neutrons they contain. Atomic nuclei will only have a non-zero magnetic moment, and therefore interact with a magnetic field, if the combined number of protons and neutrons is odd (Levitt, 2001).

MRI involves the NMR of nuclei, and will therefore be the focus of the rest of this chapter. The majority of MRI performs NMR on protons (^1H , the nuclei of Hydrogen atoms in water molecules), as water is abundant in human tissues. MRI of other nuclei is performed, such as Helium (used for lung imaging, where there is low water density (Kauczor, 2003)) and Sodium (used as it provides physiological information not available from Hydrogen imaging (Nielsen-Vallespin et al., 2007)).

2.1.2 The Behaviour of Nuclei

A full quantum analysis is required to fully describe the behaviour of nuclei in a magnetic field. For the sake of brevity, the description here is purely qualitative, with the intention of providing an intuitive understanding of how NMR occurs.

All nuclei with non-zero magnetic moments interact with magnetic fields. In the absence of a field, a nucleus is free to adopt any orientation. When a polarising field is applied ($\mathbf{B}_0 = B_0\mathbf{z}$), of magnitude B_0 (T) and oriented along the Cartesian z-axis, nuclei will immediately start to precess on a cone aligned along the field axis. This motion is analogous to a spinning top, which precesses due to the action of gravity on an object with angular momentum (McCall, 2010). In the nuclear case, precession is due to the interaction of angular momentum and the magnetic force.

The polar angle of the precession cone is set by the orientation of the nucleus at the instant of the field was applied (Levitt, 2001). For example, a nucleus whose magnetisation was initially orientated perpendicular to the field direction will precess on a flat disk.

The precession occurs at a well-defined rate, named the Larmor frequency, defined in equation 2.3 (Bernstein Matt et al., 2004). The angular frequency is a linear function of both \mathbf{B}_0 and the gyromagnetic ratio.

$$2.3 \quad \omega_L = \gamma B_0$$

As described, the application of a polarising field does not align nuclei parallel to the applied field. No net magnetisation is induced, and no signal is emitted. Nuclear alignment does occur in practice, but via an additional mechanism named relaxation (Levitt, 2001).

2.1.2.1 *Polarisation and Longitudinal Relaxation*

In isolation, a nucleus in a magnetic field would undergo precession in its initial state indefinitely. However, a nucleus is not isolated in realistic circumstances. It is surrounded by a variety of atoms and molecules, each of which is undergoing random thermal motion. These particles can also carry their own magnetic field, which results in each nucleus experiencing a net magnetic field whose strength and direction is always changing. The precessional cone axis is under constant manipulation, with a long-term tendency for the nucleus to align with the field, achieving polarisation. This gradual approach to polarisation faces opposition from the thermal energy of the nuclei. The balance between the thermal and alignment effects determines the fraction of nuclei that align with the field (Haacke et al., 1999). For example, only one nucleus per 10,000 will be aligned with the field at $\mathbf{B}_0=11.7\text{T}$.

The polarisation process is named spin-lattice, or longitudinal, relaxation. It is characterised by a time constant, T_1 (s), which describes the rate at which magnetisation grows towards its equilibrium level when integrating over a large population of spins. The T_1 of a substance depends significantly on its microstructure. Consequently, human tissues display a wide range of T_1 values, making longitudinal relaxation a useful tool for differentiating between them.

2.1.2.2 *Transverse Relaxation*

A second form of relaxation exists, named spin-spin or transverse relaxation. It is a consequence of the same mechanism that causes longitudinal relaxation, but only occurs when the spin population have been previously manipulated to be in a single state.

When in thermal equilibrium, there is a small excess nuclear alignment with the field. In order to generate NMR signal, these nuclei must be perturbed from equilibrium. This is achieved by applying an RF pulse (see section 3.3.2), which rotates the nuclei's orientation so that all of their transverse directions are aligned. Immediately after the pulse, they will all precess synchronously and generate signal (see section 2.1.4).

The local environment disrupts the synchronicity of precession (Levitt, 2001). As previously discussed, the motion of nearby atoms and molecules alter the direction and amplitude of the net field that each nucleus experiences. This will lead to a nucleus-specific Larmor frequency. In time, the nuclei will gradually dephase. The net effect is for the total transverse magnetisation to decay exponentially, an effect that can be characterised by a time constant, T_2 (s).

Table 2.1 gives some example T_1 and T_2 values of human tissue at 3T (Stanisz et al., 2005). A wide range of values is seen between tissues, a consequence of microstructural differences in composition. These differences provide a primary mechanism for differentiating between tissues when performing MRI (see section 2.2.2.1).

	T1 (ms)	T2 (ms)
White Matter	1084	69
Grey Matter	1820	99
Liver	812	42
Heart	1471	47
Blood	1932	275
Muscle	1412	50

Table 2.1 - Human tissue relaxation times at 3T (taken from Stanisiz (Stanisiz et al., 2005))

2.1.3 The Bloch Equation

The behaviour of an individual nucleus is completely described by quantum mechanics. However, when considering a sufficiently large ensemble of spins, their collective behaviour can be described in a far simpler way. Consider a population of spins sufficiently large so that quantum fluctuations are averaged out. The magnetic moment arising from the net nuclear alignment of the population at thermal equilibrium can be represented by a single vector, $\mathbf{M}=[M_x, M_y, M_z]^T$. At equilibrium, it is orientated along the z-axis, and has strength M_0 , as given by $\mathbf{M}_0=M_0\hat{\mathbf{z}}$.

The behaviour of the magnetisation vector is described by the Bloch equation (Bloch, 1946), given in equation 2.4.

$$2.4 \quad \frac{d\mathbf{M}}{dt} = \gamma \mathbf{M} \times \mathbf{B} - \frac{M_x \hat{\mathbf{x}} + M_y \hat{\mathbf{y}}}{T_2} + \frac{(M_0 - M_z) \hat{\mathbf{z}}}{T_1}$$

Each term on the right-hand side of equation 2.4 corresponds to a different physical phenomenon. The first term defines how the magnetisation vector interacts with a magnetic field, \mathbf{B} . The second and third terms describe the effects of relaxation on the magnetisation vector.

The Bloch equation can be used to describe two important features of MRI: the motion of \mathbf{M} in the presence of an RF field, and the motion of \mathbf{M} in the absence of an RF field, as described in the following sections.

2.1.3.1 *Excitation*

MRI requires \mathbf{M} to be perturbed away from equilibrium in order for signal to be generated. This is achieved by applying an additional field, referred to as the transmit field, in addition to the main magnetic field, \mathbf{B}_0 . The transmit field is designed so that its direction lies predominantly in the transverse plane, as only the transmit field components orientated perpendicular to \mathbf{B}_0 can effectively manipulate the magnetisation. The z-component of the transmit field will be ignored for the remainder of the thesis.

The transmit field is designed so that its orientation precesses about the z-axis at the Larmor frequency (see section 3.2.3). In the classical picture, oscillation at the Larmor frequency can be understood in the context of the rotating frame. As soon as any transverse magnetisation has been created, it rotates about the z-axis at the Larmor frequency. When the transmit field oscillates at the same frequency, its transverse orientation remains static relative to the magnetisation's orientation. This allows a maximally efficient rotation of the magnetisation away from equilibrium.

2.1.3.2 *Precession and Relaxation*

After experiencing a perturbation away from equilibrium, \mathbf{M} has a component perpendicular to \mathbf{B}_0 , given by M_{\perp} , which can be written in complex form as given by equation 2.5. The solution of the Bloch equation of this component is given by equation 2.6. It shows that there are two determinants of its behaviour. Its magnitude will decay exponentially, controlled by decay constant $1/T_2$. Simultaneously, the transverse magnetisation will rotate about the z-axis at the Larmor frequency.

$$2.5 \quad M_{\perp}(t) = M_x(t) + iM_y(t)$$

$$2.6 \quad M_{\perp}(t) = M_{\perp}(t=0)e^{-i\omega_L t} e^{-t/T_2}$$

The behaviour of M_z is described by equation 2.7. This describes the tendency of nuclei to repolarise when out of thermal equilibrium. The z-component of the magnetisation grows towards M_0 exponentially, characterised by time constant T_1 .

$$2.7 \quad M_z(t) = M_0 - (M_0 - M_z(t=0))e^{-t/T_1}$$

2.1.4 Signal Measurement

As stated in section 2.1.3.2, the magnetisation vector will precess about the polarisation field at the Larmor frequency after being perturbed from equilibrium. The dipolar magnetic field produced by the nuclei will also rotate. A coil placed adjacent to the sample will have a voltage, V (Volts), induced in it according to Faraday's Law of Induction, given by equation 2.8.

$$2.8 \quad V \propto \frac{d}{dt} \int_A \mathbf{B}_{dipole} \cdot d\mathbf{A}$$

This equation states that the induced voltage is proportional to the rate of change of magnetic flux in the coil. Here, the magnetic flux is defined at the component of the dipolar field, \mathbf{B}_{dipole} , which is perpendicular to the plane of the coil (defined by \mathbf{A}), integrated across the entire coil area. The magnetic flux will oscillate at the Larmor frequency, and therefore the measured voltages will also oscillate.

Signal measurement in MRI is the action of recording the voltage on the RF coil. It typically involves a pre-processing step named demodulation. This is designed to remove the Larmor oscillation present in the signal. This is achieved by

multiplying the signal by a reference signal (usually a Larmor frequency sinusoid), and then repeating the process with a reference voltage 90° out of phase with the first. The signal from each of these steps is recorded, and combined into a complex number. This final quantity accurately captures the amplitude and phase of the coil voltage, whilst removing its high-frequency modulation.

2.2 Magnetic Resonance Imaging

2.2.1 Spatial Encoding

MRI requires a mechanism to distinguish between the NMR signals emitted by magnetisation at each point in space. This is achieved by applying additional spatially varying magnetic fields, referred to as gradients.

2.2.1.1 *Gradient fields*

In MRI, gradients are additional magnetic fields, referred to as \mathbf{B}_g , applied to spatially localise magnetisation. Gradient fields are oriented parallel to the polarising field (excluding concomitant field effects (Norris and Hutchison, 1990)), with a magnitude which varies as a linear function of space, as given by equations 2.9. MRI systems have three orthogonal gradient field components, providing spatial localisation capabilities along each Cartesian axis.

The steepness of each gradient field, G , can be independently modulated in time by the MRI system. The gradient fields are much weaker than the polarising field. Typical gradients along a single axis can reach $40 \times 10^{-3} \text{Tm}^{-1}$ (Glover, 2009), achieving a field strength of 20mT at the edge of a 0.5m magnet bore. This is in contrast to polarising field strengths that are routinely at and above 1.5T.

$$\begin{aligned}
\mathbf{B}_{g,x} &= (G_x x) \hat{\mathbf{z}} \\
\mathbf{B}_{g,y} &= (G_y y) \hat{\mathbf{z}} \\
\mathbf{B}_{g,z} &= (G_z z) \hat{\mathbf{z}}
\end{aligned}
\tag{2.9}$$

The net field experienced by magnetisation at position $\mathbf{r} = [x, y, z]^T$ is given by equation 2.10, where \mathbf{G} is a vector containing the spatial derivatives of the gradient fields, $\mathbf{G} = [G_x, G_y, G_z]^T$.

$$\mathbf{B}(\mathbf{r}) = \mathbf{B}_0 + (\mathbf{G} \cdot \mathbf{r}) \hat{\mathbf{z}} \tag{2.10}$$

This equation describes the mechanism underlying spatial encoding (Lauterbur, 1973). A spatially varying magnetic field leads to a spatially varying Larmor frequency. The measured signal will contain a superposition of these frequencies. Each frequency component can be isolated in post-processing, giving the NMR signal as a function of space.

2.2.1.2 Signal encoding

Further insight can be gained by considering the phase evolution of magnetisation in the presence of an arbitrary temporally varying gradients $\mathbf{G}(t)$. Equation 2.11 describes the accumulated phase of the magnetisation at position \mathbf{r} and time t , after demodulation of the Larmor frequency.

$$\phi(\mathbf{r}, t) = \gamma \int_0^t \mathbf{G}(t) \cdot \mathbf{r} dt \tag{2.11}$$

This expression can be further simplified by noting that \mathbf{r} is independent of time and can therefore be removed from the integral. A new vector, $\mathbf{k}(t)$, is defined in equation 2.12. This allows the phase to be re-expressed as equation 2.13. \mathbf{k} has units of m^{-1} , and is referred to as the spatial frequency.

$$2.12 \quad \mathbf{k}(t) = \frac{\gamma}{2\pi} \int_0^t \mathbf{G}(t) dt$$

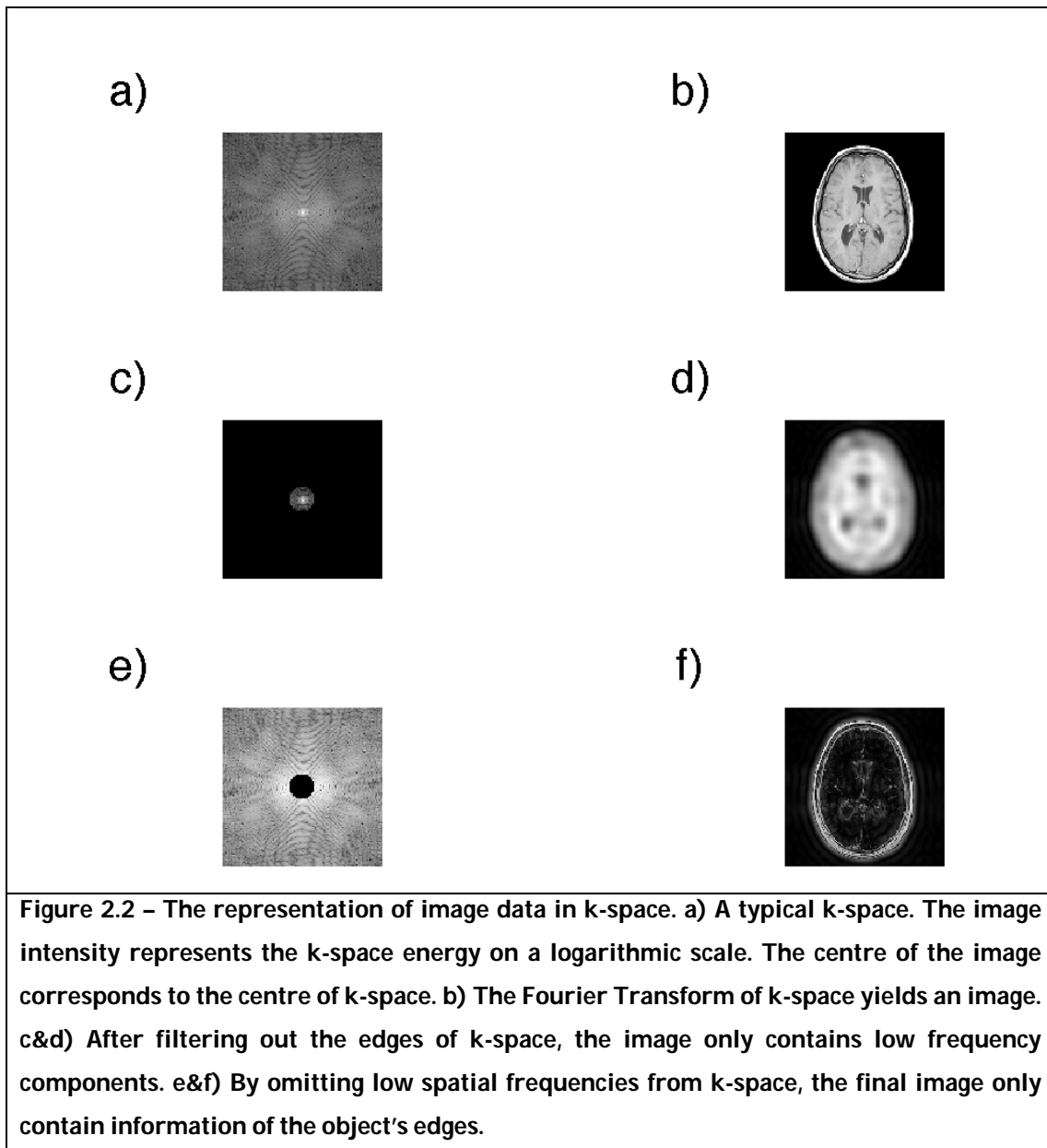
$$2.13 \quad \phi(\mathbf{r}, t) = 2\pi \mathbf{k}(t) \cdot \mathbf{r}$$

Now consider the effect on the measured signal of such a phase accumulation. After the application of an RF pulse, let the spatial distribution of transverse magnetisation be described by $\Omega(\mathbf{r})$. This is a complex quantity that defines the magnitude and orientation of the magnetisation vector at each point in space. Application of the gradient imparts an additional phase shift, $e^{i\phi(\mathbf{r},t)}$, to the magnetisation. The measured signal, $S(t)$, which contains contributions from the entire imaged volume V , is given by equation 2.14.

$$2.14 \quad S(\mathbf{k}(t)) = \int_V \Omega(\mathbf{r}) e^{2\pi i \mathbf{k}(t) \cdot \mathbf{r}} d\mathbf{r}$$

This result displays a fundamental principle behind MRI (Kumar et al., 1975). The measured signal S at co-ordinate \mathbf{k} is the Fourier Transform (FT) of the underlying magnetisation.

Equation 2.14 can be interpreted in an alternative way. The factor $e^{2\pi i \mathbf{k}(t) \cdot \mathbf{r}}$ is a Fourier harmonic, a complex oscillatory function of wavelength $2\pi \mathbf{k}(t)$. The measured value $S(\mathbf{k})$ determines how much each spatial frequency contributes towards the image. Figure 2.2 demonstrates this. Low spatial frequencies describe the large-scale structure of the image. Higher spatial frequencies define the edges of the object.



In order to create an image, the following process is performed. An RF pulse is applied, creating transverse magnetisation. Gradients are then applied through time, which defines a trajectory through k-space. The measured signal at time t is then placed at k-space location $\mathbf{k}(t)$. Taking the Fourier Transform of k-space forms an image.

2.2.1.3 Signal Sampling

Human anatomy contains structure at every length scale. Consequently, the *true* k-space representation of a medical image contains energy at every spatial

frequency - k-space is essentially infinite. It is therefore not feasible to measure all of k-space. It must be discretely sampled, which allows data to be stored and operated upon to generate an image. An important consideration is how to perform these measurements in order to guarantee that an adequate representation of the object is generated.

The vast majority of MRI utilises Cartesian sampling, an approach that produces images with well-defined characteristics. This method measures k-space by taking samples on a regular grid. There are two primary factors that affect the final image. k_{\max} defines to how high a spatial frequency is measured. Δk defines the distance in k-space between adjacent measurements. These are indicated in Figure 2.3.

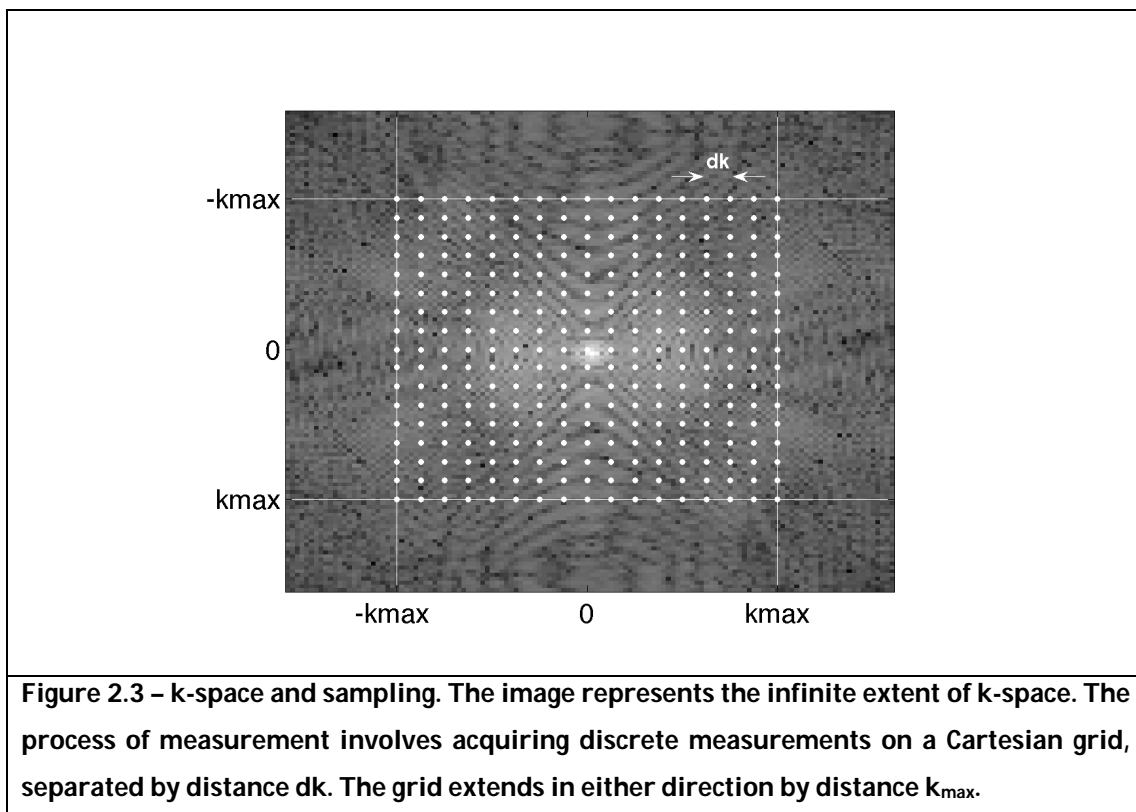


Figure 2.4 demonstrates how each parameter affects the final image in a simple 1D example. Let the full k-space of the imaged object be defined as $f(k)$. The process of sampling involves selecting points from this function every Δk , and by doing this over a rectangular region spanning $-k_{\max}$ to k_{\max} . These operations are mathematically expressed as multiplications of $f(k)$ by a Dirac comb function,

$\delta(k-n\Delta k)$ ($n = -\infty \dots -1, 0, 1, \dots \infty$), and the box function, $\text{rect}(k/2k_{\max})$. This is shown in the left hand column of the figure, with the net result of all operations displayed on the fourth row.

The image domain versions of the signal, Dirac comb and box function are shown in the first three rows of the right hand column. The FT of $f(k)$ gives a complete representation of the image at infinite resolution. The FT of the Dirac comb gives another Dirac comb, $D(x-2\pi n/\Delta k)$ whose period is inversely proportional to the k-space step size. The convolution of these two functions produces replicas separated by a distance $2\pi n/\Delta k$, referred to as the field of view, or FOV. Importantly, replicas of the object will overlap if the object is wider than the FOV. This can severely damage reconstructed images, and therefore care is taken to ensure that the k-space sampling distance is sufficiently small. In practise, the replicated versions of the object are ignored, resulting in a single image of the object.

The FT of a box function is a sinc function, given by $\text{sinc}(2k_{\max}x)$. The width of the central lobe of a sinc function is inversely proportional to k_{\max} . Therefore convolving the $F(x)$ by a sinc blurs the object. Increasing the highest spatial frequency sampled in k-space reduces the blurring in the image domain, increasing the spatial resolution. The fourth row of the right hand column shows the total effect in the image domain.

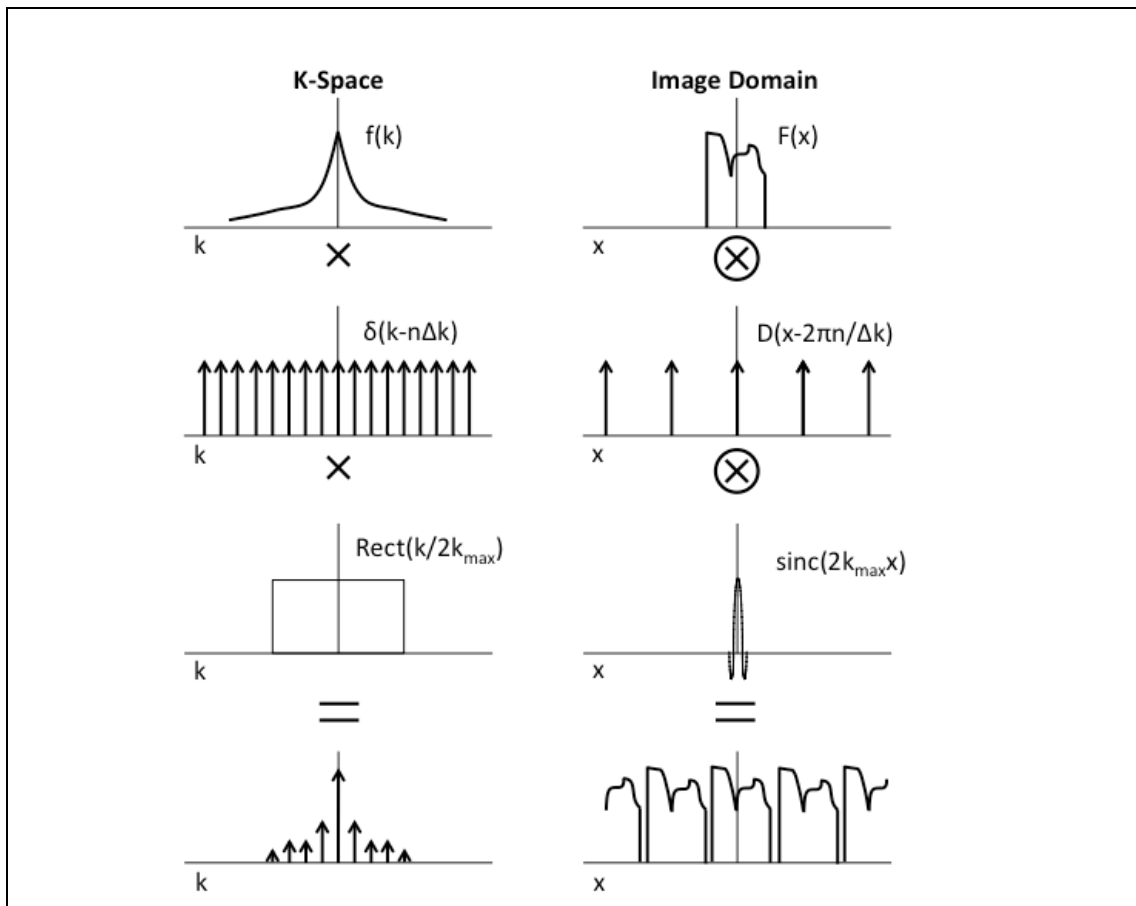


Figure 2.4 – Signal and sampling functions in both the image domain and k-space. The left hand column shows the native k-space signal, which is multiplied by a Dirac comb and rect function. The last row shows the net effect. In the image domain, the signal is convolved with a Dirac comb and a sinc function, resulting in multiple replicas of the object at reduced resolution.

2.2.2 Pulse sequences

MRI scanners have the capability of modulating the transmission field and gradient fields independently in time. This allows for a large range of possibilities when choosing how to run the system. Each mode of operation is called a pulse sequence. Pulse sequences are often constructed from repeating a basic sequence unit multiple times. These are often displayed in pulse sequence diagrams, an example of which is given in Figure 2.5.

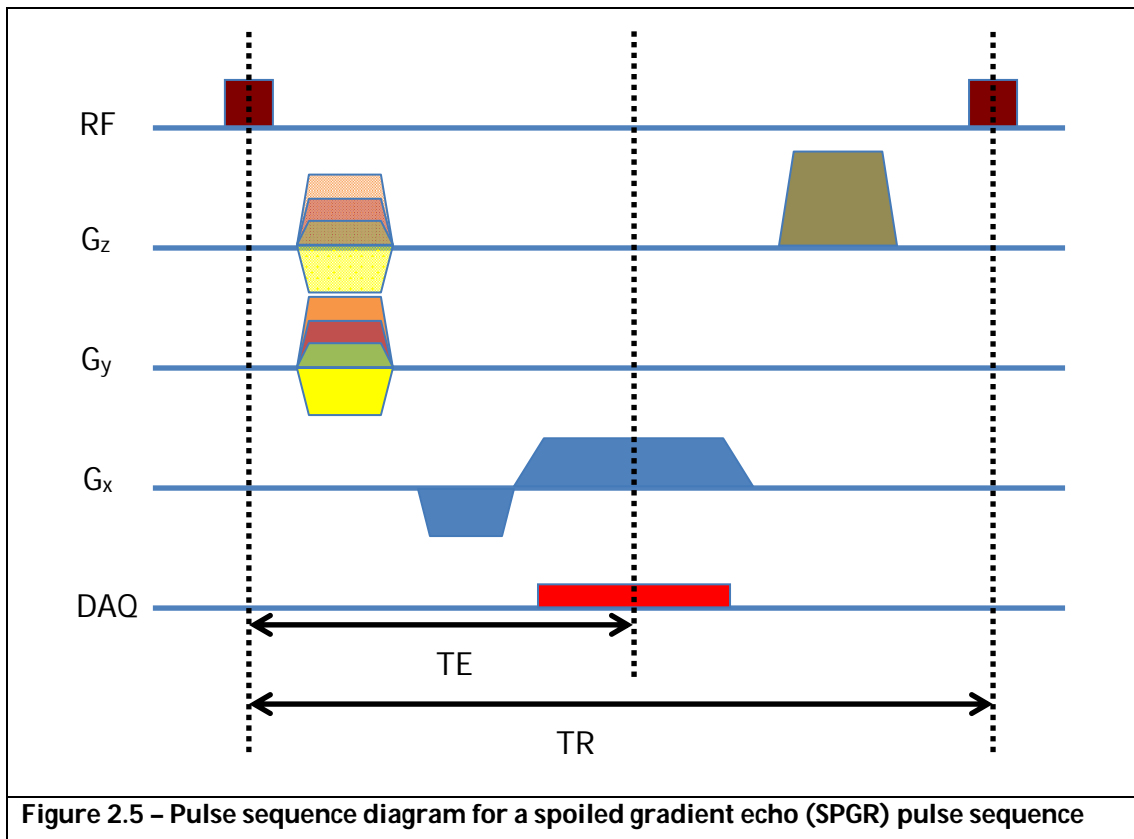


Figure 2.5 – Pulse sequence diagram for a spoiled gradient echo (SPGR) pulse sequence

Each horizontal section describes the action of one subsystem of the scanner. The first axis represents the transmit field. In this case, a field is applied for a period of time at constant amplitude. This action is then repeated every TR seconds later, where TR is the repetition time.

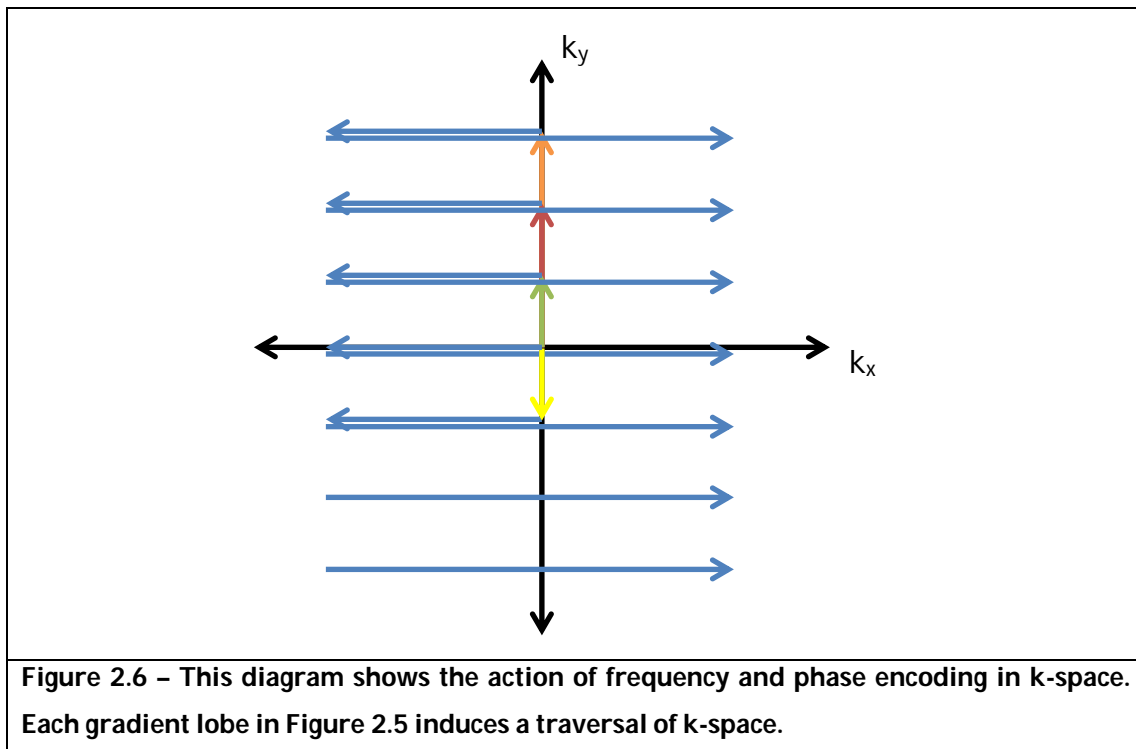
The next three axes refer to the activity of the three magnetic field gradients. The height of the blocks refer to the strength of the applied gradient. Note that each gradient lobe is trapezoidal. This is a common feature, a consequence of limited rate at which gradients can increase their strength (the slew rate) (Glover, 2009).

The activity on the x, y and z axes show the gradients applied to traverse k-space. This particular structure of gradients is commonly used for Cartesian scanning, with the x activity showing frequency encoding (FE) and y and z behaviour showing phase encoding (PE). The FE gradient defines the sequence echo time (TE).

The same FE gradients are played in every TR. In k-space, this achieves a movement in the negative k_x direction, followed by a movement in the positive k_x direction of twice the negative length. Data is acquired during the positive k_x -directed movement (as denoted by activity on the fifth axis, showing digital acquisition, or DAQ).

The PE axes show several gradient lobes of differing colour superimposed. This indicates that different lobe amplitudes are played during sequential TR periods. The action of these PE gradients is to take sequential incremental steps in the k_y and k_z directions.

The action of the FE and PE gradients is shown in Figure 2.6. Each FE acquisition samples a horizontal line of k-space. Using phase encoding, the entirety of k-space can be acquired over several TR periods. The diagram shows a single plane in the k_z direction – a full acquisition would acquire an entire 3D volume in k-space.



The final gradient axis, G_z , has an additional gradient lobe called a spoiler gradient. The spoiler gradient acts to dephase all transverse magnetisation at the end of the TR period. The sequence shown is named spoiled gradient echo (SPGR) (Haase et al., 1986; Zur et al., 1991). Here, gradient echo refers to the manner in which magnetisation is dephased and rephased due to frequency encoding.

2.2.2.1 Contrast

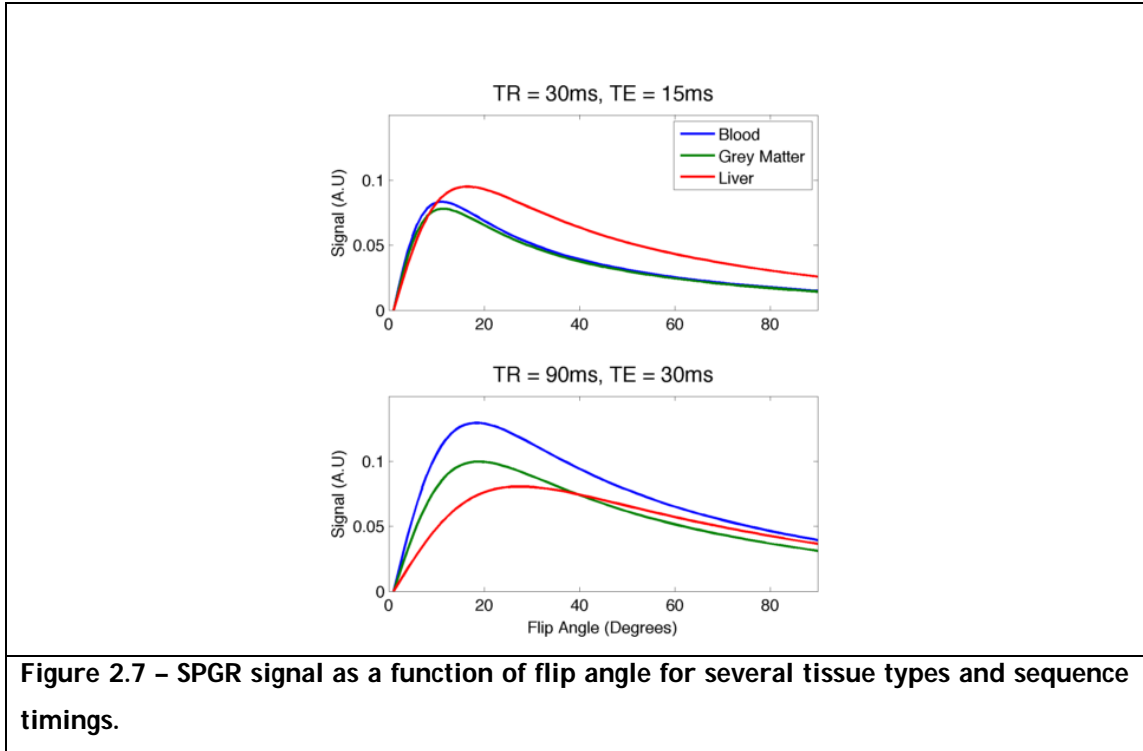
The purpose of MRI is to generate images that contain anatomical and functional information, to enable diagnosis of disease in a non-invasive way. In order to achieve this, the images have to clearly differentiate between tissues with different properties. MRI can generate contrast based on any mechanism that causes a change in the NMR signal. Examples include water diffusion (Woessner, 1961), blood flow (Moran, 1982) and brain activation (Bandettini et al., 1992). The primary MRI contrast mechanism is relaxation. Many tissues have widely varying T_1 and T_2 values, and these can be exploited.

The majority of the work in this thesis involves the SPGR sequence (Haase et al., 1986; Zur et al., 1991). Its signal is given by equation 2.15, where M_0 is the equilibrium magnetisation, R describes the spatial sensitivity of the receive coil, and θ is the flip angle, which describes the angular rotation of the magnetisation from the z-axis due to the RF pulse (see section 3.3.2). The transverse magnetisation decay constant T_2 has been replaced by T_2^* , a factor which included the signal dephasing effect from macroscopic \mathbf{B}_0 field inhomogeneities.

$$2.15 \quad S = \frac{M_0 R \sin(\theta) (1 - e^{-TR/T_1})}{1 - \cos(\theta) e^{-TR/T_1}} e^{-TE/T_2^*}$$

Figure 2.7 shows the importance of sequence optimisation for generating tissue contrast. It displays the SPGR signal for several tissue types (blood, grey matter and liver tissue, taken from Table 2.1) and several sequence timing parameters. The first plot exemplifies how different tissues can have very similar signal amplitudes. There would be very little contrast between blood and grey matter in this case. This originates from their very similar T_1 values, and the fact that the chosen TE does not allow their different T_2 values to significantly alter the signal. This is true across the range of flip angles. However, liver tissue would be significantly different for flip angles $>20^\circ$.

The second plot demonstrates a case where the parameters had been chosen to generate contrast between all tissues. At flip angles below 30° all three tissues types have very different signal amplitudes, allowing clear differentiation.



2.2.3 Noise

As with all experimental sciences, MRI measurements are corrupted by noise. There are two primary sources of noise in MRI, originating from the patient and from the receiver electronics. Both of these manifest themselves as additional Gaussian-distributed noise sources that corrupt to k-space measurements. Noise is present at all temporal frequencies. After the FT of k-space, the modulus of the resulting image is usually taken. In this case, the noise is transformed to a Rician distribution (Gudbjartsson and Patz, 1995), originating from the rectification of the negative complex noise components.

The signal to noise ratio of a 3D acquisition is given by equation 2.16, where Δx , Δy and Δz give the volume of each image voxel, N_{ave} are the number of repeats of the experiment which are averaged, N_y and N_z are the number of PE lines in k_y and k_z directions, and BW is the bandwidth of the receiver.

$$2.16 \quad SNR \propto \Delta x \Delta y \Delta z \sqrt{\frac{N_{ave} N_y N_z}{BW}}$$

The larger voxel size increases SNR as there are more spins present within the voxel, and hence a larger magnetisation vector. Increased number of averages and PE measurements (N_y and N_z) also increase SNR, but with diminishing returns due to the square root dependence on these parameters.

Minimising the receiver bandwidth (rBW) can also increase SNR. The rBW is defined as the range of NMR frequencies that contribute signal to a voxel. A steeper readout gradient will induce a wider rBW, and visa versa. Since noise is present at all frequencies, a larger rBW will allow a larger range of the noise spectrum to contribute to k-space. Hence the rBW should be kept to a minimum.

2.3 References

- Bandettini, P.A., Wong, E.C., Hinks, R.S., Tikofsky, R.S., and Hyde, J.S. (1992). Time course EPI of human brain function during task activation. *Magnetic Resonance in Medicine* 25, 390–397.
- Bernstein, M.A., King, K.F., and Zhou, X.J. (2004). *Handbook of MRI pulse sequences* (Elsevier).
- Bloch, F. (1946). Nuclear Induction. *Phys. Rev.* 70, 460–474.
- Buxton, R.B. (2002). *Introduction to functional magnetic resonance imaging: principles and techniques* (Cambridge Univ Press).
- Glover, P.M. (2009). Interaction of MRI field gradients with the human body. *Physics in Medicine and Biology* 54, R99–R115.
- Gudbjartsson, H., and Patz, S. (1995). The Rician distribution of noisy MRI data. *Magnetic Resonance in Medicine* 34, 910–914.
- Haacke, E.M., Brown, R.W., Thompson, M.R., and Venkatesan, R. (1999). *Magnetic Resonance Imaging: Physical principles and sequence design*.
- Haase, A., Frahm, J., Matthaei, D., Hanicke, W., and Merboldt, K.-D. (1986). FLASH imaging. Rapid NMR imaging using low flip-angle pulses. *Journal of Magnetic Resonance* (1969) 67, 258–266.
- Kauczor, H.U. (2003). Hyperpolarized helium-3 gas magnetic resonance imaging of the lung. *Topics in Magnetic Resonance Imaging* 14, 223.

- Kumar, A., Welte, D., and Ernst, R.R. (1975). NMR Fourier zeugmatography. *Journal of Magnetic Resonance* (1969) *18*, 69–83.
- Lauterbur, P.C. (1973). Image formation by induced local interactions: examples employing nuclear magnetic resonance. *Nature* *242*, 190–191.
- Levitt, M.H. (2001). *Spin dynamics* (John Wiley & Sons).
- McCall, M. (2010). *Classical mechanics: from Newton to Einstein: a modern introduction* (Wiley).
- Moran, P.R. (1982). A flow velocity zeugmatographic interlace for NMR imaging in humans. *Magnetic Resonance Imaging* *1*, 197–203.
- Nielsen-Vallespin, S., Weber, M.-A., Bock, M., Bongers, A., Speier, P., Combs, S.E., Wöhrle, J., Lehmann-Horn, F., Essig, M., and Schad, L.R. (2007). 3D radial projection technique with ultrashort echo times for sodium MRI: Clinical applications in human brain and skeletal muscle. *Magnetic Resonance in Medicine* *57*, 74–81.
- Norris, D.G., and Hutchison, J. (1990). Concomitant magnetic field gradients and their effects on imaging at low magnetic field strengths. *Magnetic Resonance Imaging* *8*, 33–37.
- Rae, A.I.M. (2002). *Quantum Mechanics* (CRC Press).
- Stanisz, G.J., Odobina, E.E., Pun, J., Escaravage, M., Graham, S.J., Bronskill, M.J., and Henkelman, R.M. (2005). T1, T2 relaxation and magnetization transfer in tissue at 3T. *Magnetic Resonance in Medicine* *54*, 507–512.
- Woessner, D.E. (1961). Effects of Diffusion in Nuclear Magnetic Resonance Spin-Echo Experiments. *The Journal of Chemical Physics* *34*, 2057–2061.
- Zur, Y., Wood, M.L., and Neuringer, L.J. (1991). Spoiling of transverse magnetization in steady-state sequences. *Magnetic Resonance in Medicine* *21*, 251–263.

Chapter 3 Radiofrequency Fields in MRI

This chapter presents a guide to the nature and use of RF fields in MRI. First, a qualitative description and explanation of the behaviour of RF fields is provided. This section describes how their structure is intimately connected with the architecture of the RF coil, the main field strength, and the electromagnetic properties of the object being investigated.

This is followed by a description of how RF fields are used in MRI. This includes a discussion of parallel imaging, in addition to a brief description of RF pulses and parallel transmission.

This is followed by a survey of the current methods of measuring these fields using MR. This section is composed of three parts – analytical solutions to Maxwell's equations, determining RF fields through simulations, and measuring fields using MRI.

3.1 Electromagnetic fields

MRI employs a variety of magnetic fields for the purpose of generating medical images. They can be categorised as follows: the polarising field, \mathbf{B}_0 , which induces a net magnetisation in the sample due to alignment of nuclei; gradients, which are applied to spatially localise magnetisation; and the RF field, \mathbf{B}_1 , produced by coils in order to perturb magnetisation and measure the resulting precession.

The behaviour of these fields is fully described by classical electromagnetism. The theory of electromagnetism is described by Maxwell's equations, as given in equations 3.1-3.4.

Integral Form

Differential Form

$$3.1 \quad \oint_{\text{surface}} \mathbf{E} \cdot d\mathbf{A} = \frac{q_f}{\epsilon}$$

$$\nabla \cdot \mathbf{E} = \frac{\rho_f}{\epsilon}$$

$$3.2 \quad \oint_{\text{surface}} \mathbf{B} \cdot d\mathbf{A} = 0$$

$$\nabla \cdot \mathbf{B} = 0$$

$$3.3 \quad \oint_{\text{loop}} \mathbf{E} \cdot d\mathbf{l} = -\frac{\partial}{\partial t} \int_{\text{area}} \mathbf{B} \cdot d\mathbf{A}$$

$$\nabla \times \mathbf{E} = -\frac{\partial \mathbf{B}}{\partial t}$$

$$3.4 \quad \oint_{\text{loop}} \mathbf{B} \cdot d\mathbf{l} = \mu\sigma \int_{\text{area}} \mathbf{E} \cdot d\mathbf{A} + \mu\epsilon \frac{\partial}{\partial t} \int_{\text{area}} \mathbf{E} \cdot d\mathbf{A}$$

$$\nabla \times \mathbf{B} = \mu\sigma \mathbf{E} + \mu\epsilon \frac{\partial \mathbf{E}}{\partial t}$$

The terms in these equations are described below:

- Electric and Magnetic fields
 - The vectors $\mathbf{E}(\mathbf{r},t)$ ($\text{V}\cdot\text{m}^{-1}$) and $\mathbf{B}(\mathbf{r},t)$ (T) describe the electric and magnetic fields as a function of position ($\mathbf{r} = [x, y, z]^T$) and time (t).
 - For simplicity, the positional and temporal dynamics are not explicitly included in Maxwell's equations.
- Derivative operators
 - The spatial derivative operator, ($\nabla = [\partial/\partial x, \partial/\partial y, \partial/\partial z]^T$), calculates the gradient vector of vector fields.
 - The temporal derivative, ($\partial/\partial t$), finds the rate of change of each component of a vector field.
- Integral operators
 - There are two integral operators; open (\int) and closed (\oint). An integral is closed when it includes the entirety of a geometric object (i.e. a loop or a surface) as opposed to an open integral, which includes part of a geometrical object (i.e. a line segment or a limited area).
- Charge
 - The scalar quantity $\rho_f(\mathbf{r})$ ($\text{C}\cdot\text{m}^{-3}$) describes the density of free charges of the medium at position \mathbf{r} .

- The scalar quantity $q_f(\mathbf{r})$ (C) describes the total free charge at position \mathbf{r} .
- Conductivity
 - The scalar quantity $\sigma(\mathbf{r})$ ($\text{A}\cdot\text{V}^{-1}\cdot\text{m}^{-1}$) describes the propensity of the medium to carry a current of free charges in response to an electric field. It is assumed that the medium is isotropic and linear.
 - The conductivity is frequently multiplied with the electric field to form the current density $\mathbf{J}(\mathbf{r})$ ($\text{A}\cdot\text{m}^{-2}$).
- Permittivity
 - The permittivity, $\epsilon(\mathbf{r})$ ($\text{C}\cdot\text{V}^{-1}\cdot\text{m}^{-1}$), describes the ability of a medium to polarise in response to an electric field. It is often decomposed into two components, the relative permittivity, $\epsilon_r(\mathbf{r})$, and permittivity of free space, $\epsilon_0(\mathbf{r})$, as given by the relation $\epsilon(\mathbf{r}) = \epsilon_r(\mathbf{r})\epsilon_0(\mathbf{r})$.
 - The relative permittivity of a medium is determined by its microstructure. When penetrated by an electric field, atoms and molecules can respond by distributing their positive and electric charges along the field lines. A material will have a large relative permittivity if it is polarisable in this manner. An inability of charge distributions to distort leads to a low relative permittivity.
 - The relative permittivity is often a function of the electric field oscillation frequency. This behaviour can arise from the presence of multiple contributors to polarisation, each of which elicits a different response.
- Permeability
 - The permeability of a medium, $\mu(\mathbf{r})$ ($\text{H}\cdot\text{m}^{-2}$), is the magnetic analogue to permittivity, describing the ability of a medium to magnetise in response to a magnetic field. It is commonly considered as the product of a relative permeability, $\mu_r(\mathbf{r})$, and the permeability of free space, $\mu_0(\mathbf{r})$.
 - The permeability is also a complex number, allowing lag effects to be taken into account, and is also a function of frequency, again reflecting its dependence on material microstructure.
 - Note that the magnetisation referred to here originates from many sources beyond nuclear magnetisation. Typically, the nuclear contribution is several orders of magnitude below those made by alignment of atomic electron orbits and alignment of microscopic magnetic domains.

Each Maxwell equation describes an individual electromagnetic phenomenon. Equations 3.1 are referred to as Gauss's Law. They describe how the electric field leaving any closed volume is proportional to the amount of charge it contains. In contrast, equation 3.2 shows that the magnetic fields entering and leaving any volume always balance. Alternatively, it states that there are no magnetic monopoles.

Equation 3.3, Faraday's Law, describes the relationship between time-varying magnetic fields and electric fields. An electric field will be generated around the circumference of an area when the magnetic field penetrating that area changes in time.

Finally, Ampere's Law is given by equation 3.4. This states the magnetic form of Faraday's Law: the magnetic field generated around the circumference of any closed area is a function of both the current passing through that area and any changing electric field passing through it.

3.2 Radiofrequency Fields in MRI

3.2.1 The Electromagnetic Spectrum

A broad class of solutions to Maxwell's equations are oscillatory. These can be classified according to their frequency, as given in Table 3.1.

Classification	Frequency Range (Hz)
Radio Waves	$<10^9$
Microwaves	$10^9 - 10^{12}$
Infrared	$10^{12} - 10^{14}$
Visible	$4 \times 10^{14} - 8 \times 10^{14}$
Ultraviolet	$10^{15} - 10^{17}$
X-Ray	$10^{17} - 10^{19}$
Gamma	$> 10^{19}$

Table 3.1 – Classifications of the electromagnetic spectrum.

RF fields refer to electromagnetic radiation whose frequency lies below 1GHz. The NMR Larmor frequency, which typically spans 64MHz to 469MHz (corresponding to field strengths from 1.5T to 11T for ^1H), lies within this range. Therefore, the applied \mathbf{B}_1 field will be an RF electromagnetic wave.

3.2.2 The \mathbf{B}_1 Field

The \mathbf{B}_1 field is generated by driving an RF coil with a current, as given in equation 3.1, where $A(t)$ gives the strength of the current in time, ω is the oscillation frequency and ϕ is the phase of the oscillation. The \mathbf{B}_1 field is composed of two parts: reactive fields and radiative fields. The majority of RF coils (with recent exceptions (Brunner et al., 2009)) are designed to minimise the radiative field component, and it is therefore ignored for the remainder of this thesis.

$$I(t) = A(t)\cos(\omega(t)t + \phi)$$

3.5

Consider a simple current of constant amplitude I_0 and frequency ω . The magnetic field produced will oscillate synchronously with the applied current, and will vary in magnitude and orientation throughout space, as given by equation 3.6. The magnitude of each field component is proportional to the current.

$$\mathbf{B}_1(\mathbf{r}, t) = \cos(\omega t + \phi) (B_{1,x}(\mathbf{r})\mathbf{x} + B_{1,y}(\mathbf{r})\mathbf{y} + B_{1,z}(\mathbf{r})\mathbf{z})$$

3.6

Although usually expressed in a Cartesian basis, the \mathbf{B}_1 field can be decomposed into two counter-rotating components: clockwise ($T(\mathbf{r})$) and counter-clockwise ($R(\mathbf{r})$). These are obtained by taking the dot product with CW and CCW unit vectors, $\mathbf{a}_{\text{CW}} = (\cos(\omega t)\mathbf{x} - \sin(\omega t)\mathbf{y})$ and $\mathbf{a}_{\text{CCW}} = (\cos(\omega t)\mathbf{x} + \sin(\omega t)\mathbf{y})$. These are described by equations 3.7 and 3.8. This alternative basis isolates the component of the applied \mathbf{B}_1 field that remains static in relative to precessing magnetisation. It therefore rotates the magnetisation towards the transverse plane (see section 2.1.3.1). It is named the excitation, or transmit field, $T(\mathbf{r})$, and the current applied to the coil is referred to as an RF pulse.

$$3.7 \quad T(\mathbf{r}) = \mathbf{a}_{CW} \cdot \mathbf{B}_1(\mathbf{r}) = (\cos(\omega t)B_{1,x}(\mathbf{r}) - \sin(\omega t)B_{1,y}(\mathbf{r}))\cos(\omega t + \phi)$$

$$3.8 \quad R(\mathbf{r}) = \mathbf{a}_{CCW} \cdot \mathbf{B}_1(\mathbf{r}) = (\cos(\omega t)B_{1,x}(\mathbf{r}) + \sin(\omega t)B_{1,y}(\mathbf{r}))\cos(\omega t + \phi)$$

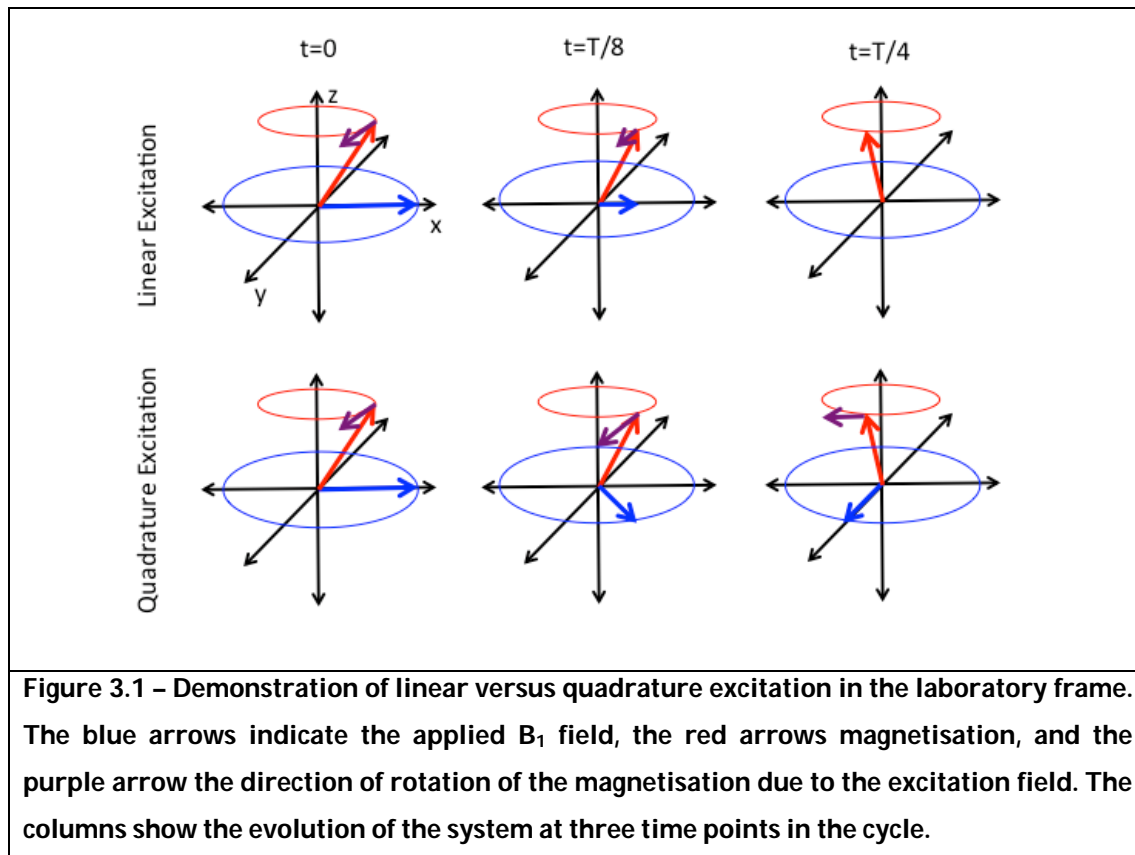
The CCW component of the \mathbf{B}_1 field oscillates at twice the Larmor frequency when viewed from the rotating frame of the magnetisation vector. Consequently, it does not effectively manipulate the magnetisation and is excluded from the excitation field. However, the CCW component of the \mathbf{B}_1 field does play an important role in MRI signal detection.

The precession of the magnetisation vector induces a current in any RF coils in its vicinity. The strength of this current is determined by the magnetic flux density that intersects the surface of the RF coil, as given by Faraday's Law. However, the sensitivity of the RF coil is proportional to the CCW component of the magnetic field of the RF coil when driven by a current, as in equation 3.9. $R(\mathbf{r})$ is therefore referred to as the receive field.

$$3.9 \quad signal \propto -\frac{d}{dt} \int_{volume} \mathbf{M}(\mathbf{r}) \cdot \mathbf{R}(\mathbf{r}) d\mathbf{r}^3$$

3.2.3 Quadrature

An important consideration when designing an RF system is the concept of quadrature (Glover et al., 1985). Consider a coil that produces a field that lies solely in the x-direction, $\mathbf{B}_1 = B \cos(\omega t) \mathbf{x}$, as indicated in the top row of Figure 3.1. As the magnetisation precesses, the amplitude of the torque it experiences oscillates due to the oscillation in the amplitude of the \mathbf{B}_1 field. By equation 3.7, the net excitation field is $T = B \cos^2(\omega t)$. Averaged over the course of a cycle, the rotating frame transmit field is half of the amplitude of the total field applied.



Maximally efficient excitation can be achieved by generating a quadrature transmit field. This is achieved by constructing a transmission system that can produce a \mathbf{B}_1 field containing orthogonal and equal-amplitude components, driven 90° out of phase with each other, $\mathbf{B}_1 = B(\cos(\omega t)\mathbf{x} + \sin(\omega t)\mathbf{y})$. This is shown in the second row of Figure 3.1. Substitution into equation 3.7 and the use of the trigonometric identity $\cos^2(a) + \sin^2(a) = 1$ demonstrates that the resulting transmit field has strength B , as opposed to $B/2$ in the linear case.

Similarly, quadrature-capable coils increase the measured signal by a factor of $\sqrt{2}$ when used for reception. This is because the magnetisation will induce a current in the RF coils throughout its precessional cycle.

3.2.4 Phase

The notion of phase appears widely across MRI. It refers to the orientation of a vector in the transverse plane, defined by the azimuthal angle, ϕ . For example, *phase* encoding is

named such since the PE gradient imparts a phase accrual to magnetisation before frequency encoding.

It has also been referred to previously as the phase of the current in RF coils. Although different to the previous description, it is intrinsically linked to it. Consider a coil with generates a quadrature \mathbf{B}_1 field, as in the second row of Figure 3.1. At $t=0$, one component of the field is at its maximum, with the other component at zero.

Now consider altering the phase of the currents of each component of the field. A delay of $\phi=T/4$ alters the initial orientation of the \mathbf{B}_1 field. The current phase shift has been mapped onto the \mathbf{B}_1 vector phase.

There is one further contributor to the phase of the \mathbf{B}_1 field. RF coils themselves generate fields whose orientation varies as a function of space. This will translate into a relative phase in magnetisation, since the axis of rotation during excitation will vary at different positions.

3.2.5 RF Coils

RF coils are a prerequisite on all MRI scanning. Significant effort has been devoted to MRI coil development since the inception of MRI, and improved designs still emerge today. There are two broad categories of RF coils: volume coils and surface coils. Both can be used for both transmit and receive, and have their own positive and negative aspects which need to be considered.

RF coils are mostly based on common design features that are required for high-quality performance. These will now be introduced in the context of surface coils.

3.2.5.1 Surface Coils

The surface coil has been utilised since the inception of MRI. It is the most basic form of RF coil, and is still used widely in current clinical practice. The most elementary form of surface coil is shown in Figure 3.2. It consists of a loop of conductor with two capacitors

embedded within it. The coil is connected to the transmit/receive electronics via port V. This configuration can be alternatively represented by the circuit given in Figure 3.2b. The shape of the conductor gives the coil an inductance L , which is in series with the tuning capacitor C_T .

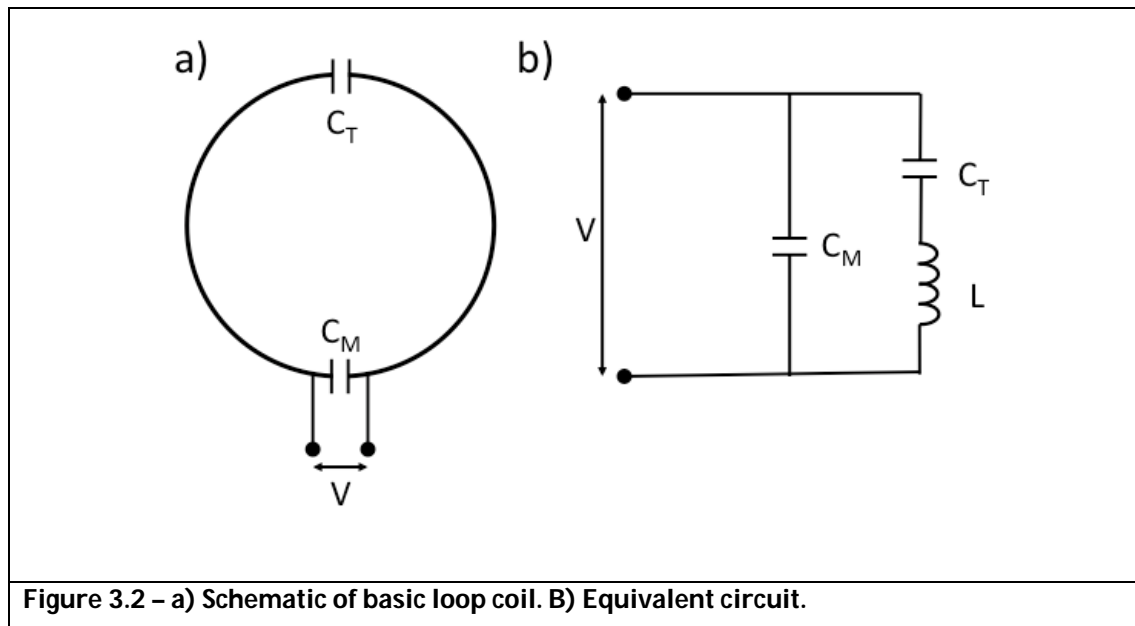
These two components give the surface coil the ability to resonate. This is an important property of all RF coils. At resonance, the coil can generate maximum voltage when driven by precessing magnetisation. This increases the SNR of the receiver system. When transmitting, resonance generates the maximum excitation field per unit drive. This minimises the burden on RF amplifiers in generating current in the coil.

The resonant frequency of the coil is given by equation 3.10. This is required to be the Larmor frequency. As the inductance is fixed by the coil geometry, the value of tuning capacitance is refined to give the desired response.

3.10

$$\omega = \sqrt{\frac{1}{LC_T}}$$

The surface coil is connected to the transmission or measurement system via the port bridged across a capacitor, C_M . This capacitor is selected so that the total impedance of the coil matches that of the connecting cable, which is typically 50Ω . This is necessary to allow efficient transfer of current between the coil and the connected systems.



The magnetic field produced by a surface coil is inherently localised. Furthermore, the direction of field produced by a surface coil changes with position. This is demonstrated in Figure 2.1, which shows the field produced by a current loop.

Loop coils have positive and negative properties. Simple loop coils do not produce quadrature fields, hence reducing the receive SNR and transmit efficiency. However, their localisation restricts the region of the patient that can contribute noise to the coil, increasing the SNR.

The inhomogeneous \mathbf{B}_1 field leads to a spatially varying flip angle in transmission and receive field. This is useful when a restricted FOV is desired, such as in spine imaging. However, the resulting images have spatially varying contrast and intensity, which can reduce image quality.

3.2.5.2 Volume Coils

Volume coils provide an alternative to surface coils. The most prominent design, the birdcage, is shown in Figure 3.3. Its name originates from its structural similarity to a birdcage. It is constructed from two circular end-rings, which are bridged by several legs. Several designs of birdcage coils exist, which place capacitors either on the legs (low-pass), end-rings (high-pass), or both (band-pass).

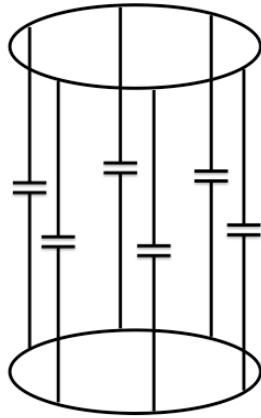


Figure 3.3 – A birdcage coil is built from two end-rings, with several legs running between them. This figure displays a low-pass birdcage.

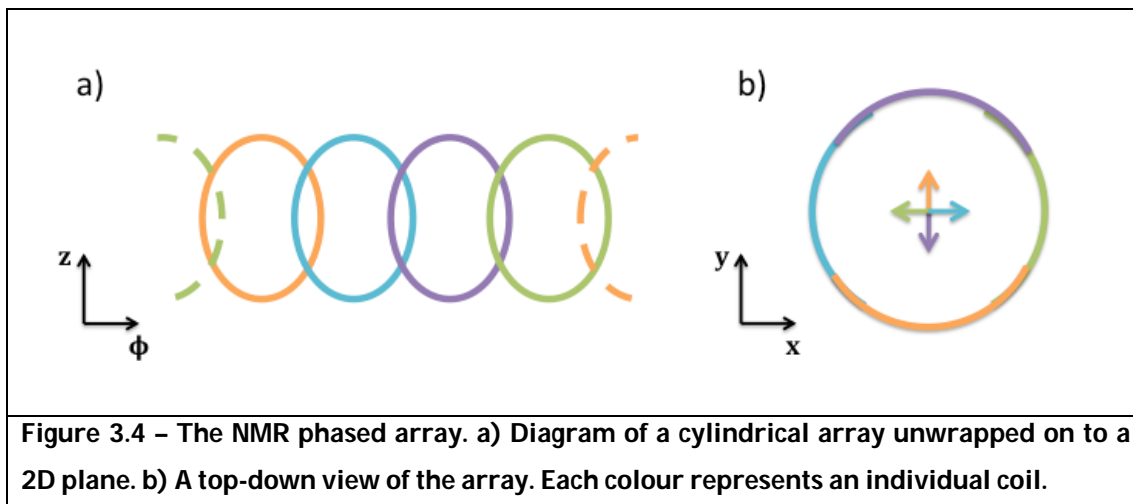
The periodic structure of the birdcage coil allows it to support many linearly independent solutions (Jin, 1998). Careful construction of the birdcage allows it to support a current pattern that mimics the ideal current required to generate a perfectly homogeneous quadrature field. This approximation improves as the number of legs increases.

Birdcages are the primary coil used for transmission on all modern clinical scanners. They are embedded directly into the bore of the magnet, allowing them to be used on any anatomical region. However they are rarely used for signal reception due to their diminished SNR, originating for their sensitivity to thermal noise from the entire body of the patient.

3.2.5.3 Coil Arrays

Although the birdcage dominates for transmission, surface coils and volume coils represent opposing philosophies when constructing receive coils. Volume coils offer large FOVs and quadrature fields, with sensitivity to thermal noise; surface coils offer small FOVs, linear fields but less sensitivity to thermal noise.

The NMR phased array (Roemer et al., 1990) presents a receive structure which uses the positive aspects of both approaches. A volume coil is built from multiple individual surface coils. The entire FOV is covered, each element is less noise-sensitive, and quadrature is achieved by aligning each element so that every Cartesian axis has a coil whose field is aligned with it.



An example schematic of the NMR phased array is provided in Figure 3.4. Four individual surface coils enclose a cylindrical surface, with each element overlapped with its neighbour. Each coil provides an orthogonal \mathbf{B}_1 component, allowing quadrature reception.

The use of multiple receiver coils presents unique challenges. The precession of magnetisation will induce simultaneous oscillating currents in all coils simultaneously. These will then in turn generate their own oscillating magnetic fields. These will induce currents in all other coils in the array. This effect, known as coupling, causes the coils to resonate away from the Larmor frequency, reducing the sensitivity of the receive system to the true NMR signal.

Employing two complementary strategies solved this problem. The first strategy employs overlapped coils, as shown in Figure 3.5. When coil 1 supports a current, it generates a magnetic field whose direction lies into the page within the coil, and out of the page outside it. When overlapped, the magnetic flux through coil 2 has opposing contributions from inside the overlap area and outside it. When the overlap is chosen

correctly, they exactly balance, and currents in either coil do not induce currents in the other.

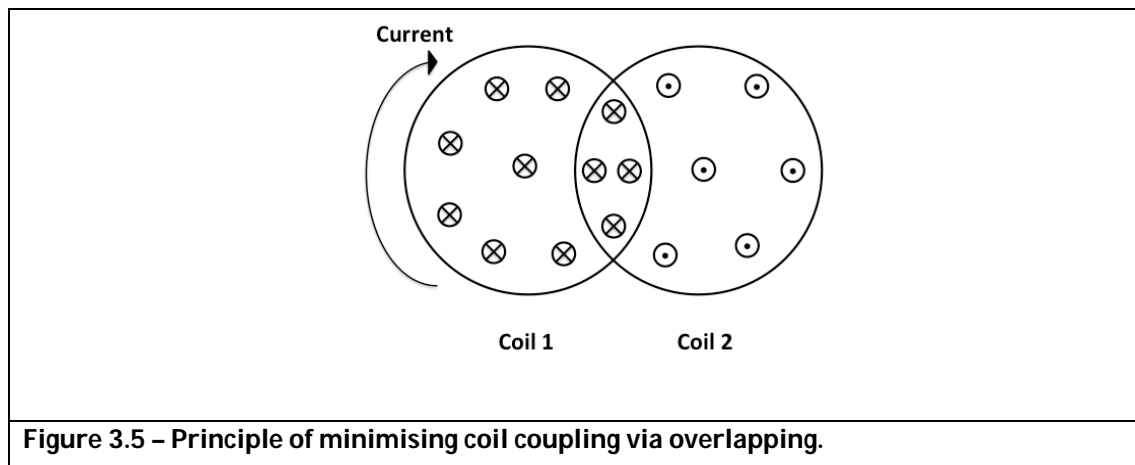


Figure 3.5 – Principle of minimising coil coupling via overlapping.

The second strategy employs low-impedance pre-amps, which effectively act as a short circuit. When combined with quarter-wavelength cables to each coil, the coil's port acts as an open-circuit, which minimises the current which flows on the coil, and therefore minimising coupling.

The use of receive arrays provide benefits beyond favourable SNR. These are discussed in section 3.3.1. Furthermore, recent work has shown that transmit arrays (Katscher et al., 2003; Zhu, 2004; Grissom et al., 2006) also bring further benefits (section 3.3.2.4). However, these approaches require knowledge of the fields produced by each element. This is discussed in section 3.4.

3.2.6 The Spatial Distribution of B_1 Field

The shape of the B_1 field plays an important role in MRI. This section outlines the factors that influence it.

3.2.6.1 Coil architecture

The architecture of the RF coil has a strong effect on the shape of the B_1 field. An empty birdcage coil produces a highly homogeneous quadrature field by design.

Many other alternative coil structures have been proposed, each with its own characteristic \mathbf{B}_1 footprint. For example, the butterfly coil (Kumar and Bottomley, 2008) is a composite surface element constructed from two coils - a standard loop coil, overlaid by a larger 'twisted' loop (i.e. a figure of eight). Analysing the coil currents reveals that a quadrature field is beneficially produced a distance away from the coil.

3.2.6.2 Dependence of the electric properties of tissue

The \mathbf{B}_1 field produced in-vivo can often significantly differ from that produced by an isolated coil. This originates from the interaction of the \mathbf{B}_1 field with the electromagnetic properties of tissue under examination.

Inspection of Maxwell's equations reveals their dependence on the conductivity, permittivity and permeability. These properties affect the \mathbf{B}_1 field produced in two distinct ways.

3.2.6.2.1 Speed of light and interference

All electromagnetic waves travel at the speed of light, c (ms^{-1}). This speed is defined as the product of the wavelength, λ (m) and frequency f (s^{-1}), and is determined by the permittivity and permeability of the propagating medium, as in equation 3.11. As the frequency is fixed at the Larmor frequency, the wavelength of the radiation varies as a function of the underlying electromagnetic properties.

$$3.11 \quad c = \frac{1}{\sqrt{\epsilon_r \epsilon_0 \mu_r \mu_0}} = \lambda f$$

In a vacuum, the wavelength of Larmor frequency radiation at 3T is approximately 2.3m. However, this reduces to approximately 26-33cm in human tissue, assuming relative permittivities of $\epsilon_r = 50-80$ (Liu et al., 2005) (note that at RF frequencies, the relative permeability does not significantly vary from unity).

When the size of the body is approximately the RF wavelength, the field will have several spatial cycles across the anatomy. Therefore fields generated by different parts of the RF coil will combine either constructively or destructively. The amount of interference will vary in space, leading to \mathbf{B}_1 field inhomogeneity.

This effect increases in severity at higher \mathbf{B}_0 field strengths (Collins and Smith, 2001). This is as the Larmor frequency is greater, making the RF wavelength shorter. The effect is negligible at field strengths lower than 1.5T.

3.2.6.2.2 *Electric interaction effects*

The second interaction effect arises from the electromagnetic response of human tissue. The electromagnetic field produced by an RF coil contains both magnetic and electric components. Although human tissue has a very small magnetic response to the RF magnetic field (hence $\mu_r=1$), the electric field couples strongly to tissues. Most tissue can support ionic currents, and hence are conductive. Furthermore, many tissues can polarise, giving them a high relative permeability. Table 3.2 has a selection of these values taken from literature (Liu et al., 2005).

Tissue	Conductivity (Sm^{-1})	Relative Permittivity
Skin	0.48	54.2
Muscle	0.82	77.2
Fat	0.03	6.0
Grey Matter	0.70	78.3
White Matter	0.39	55.5
Liver	0.55	63.4
CSF	2.27	72.4

Table 3.2 – Conductivities and relative permittivities of tissues at 3T (Liu et al., 2005)

The consequences of these mechanisms can be understood in the context of Faraday's Law. Any current driven by the \mathbf{B}_1 field will induce an additional magnetic field that is partially out of phase with the original. This will alter the total \mathbf{B}_1 field by changing its

amplitude and direction. Again, this strength of this mechanism will vary spatially, creating an inhomogeneous \mathbf{B}_1 field.

3.3 Utilisation of RF Fields in MRI

The \mathbf{B}_1 field is of fundamental importance to MRI. As discussed so far, it allows magnetisation manipulation and measurement. In this section the uses of the \mathbf{B}_1 field are discussed in depth.

3.3.1 Receive Field

The receive component of the \mathbf{B}_1 field is a passive ‘virtual’ field. It manifests itself in the MRI signal equation multiplicatively, as in equation 3.12. Here, $R_r(\mathbf{r})$ is the complex receive field of the r^{th} receiver, $I_r(\mathbf{r})$ is the image intensity at position \mathbf{r} of the r^{th} receive coil, $\rho(\mathbf{r})$ is the underlying magnetisation. The contribution of the magnitude and the phase (ϕ^R) of the receive field have been separated to emphasise that the measured image is weighted by the amplitude variation and phase variation of the receiver.

$$3.12 \quad I_r(\mathbf{r}) = |R_r(\mathbf{r})| e^{i\phi_r^R(\mathbf{r})} \rho(\mathbf{r})$$

In the case where a single coil is used, the receive field does not offer any flexibility which can be exploited. However, the introduction of multiple receivers revolutionised MRI data acquisition, as described below.

Roemer et. al. (Roemer et al., 1990) initially proposed the use of multiple surface receivers in MRI, allowing high SNR and large FOV imaging. This paper addressed how to optimally combine the images acquired by each coil. An SNR optimal reconstruction could be performed with knowledge of the receive field of each coil. However, the images could alternatively be combined by taking their sum-of-squares (SOS) to form I_{SOS} , as in equation 3.13, where N_R is the number of receivers. This approach offered a near optimal combination without the need for receive field maps. This approach was

widely adopted, as the time penalty of acquiring receive field maps was not worth the marginal SNR increase.

$$3.13 \quad I_{SOS} = \sqrt{\sum_{r=1}^{N_R} I_r I_r^*}$$

The process of MRI data acquisition was revolutionised in 2001 by the invention of partially parallel imaging (PPI). Sodickson (Sodickson and Manning, 1997) and Pruessman (Pruessmann et al., 1999) demonstrated that receive coils could be used to spatially encode magnetisation, in a manner analogous to gradient encoding. Sodickson used RF sensitivities directly to synthesise Fourier harmonics across the FOV, allowing unsampled k-space positions to be synthesised from linear combinations of its neighbours from different coils. Pruessman demonstrated a more generalised approach, SENSE, described below.

The SENSE mechanism is demonstrated in Figure 3.6. Consider the scenario where data is acquired with two receive coils, as in Figure 3.6a. Each coil measures the true signal, I , weighted by the receive sensitivities, C_1 and C_2 .

Now consider the effect of only sampling every other phase encode line (here, the PE direction is left-right). The FOV is halved, causing aliasing, as shown by the images from each coil, U_1 and U_2 . Each pixel contains the superposition of two pixels that are separated by $FOV/2$.

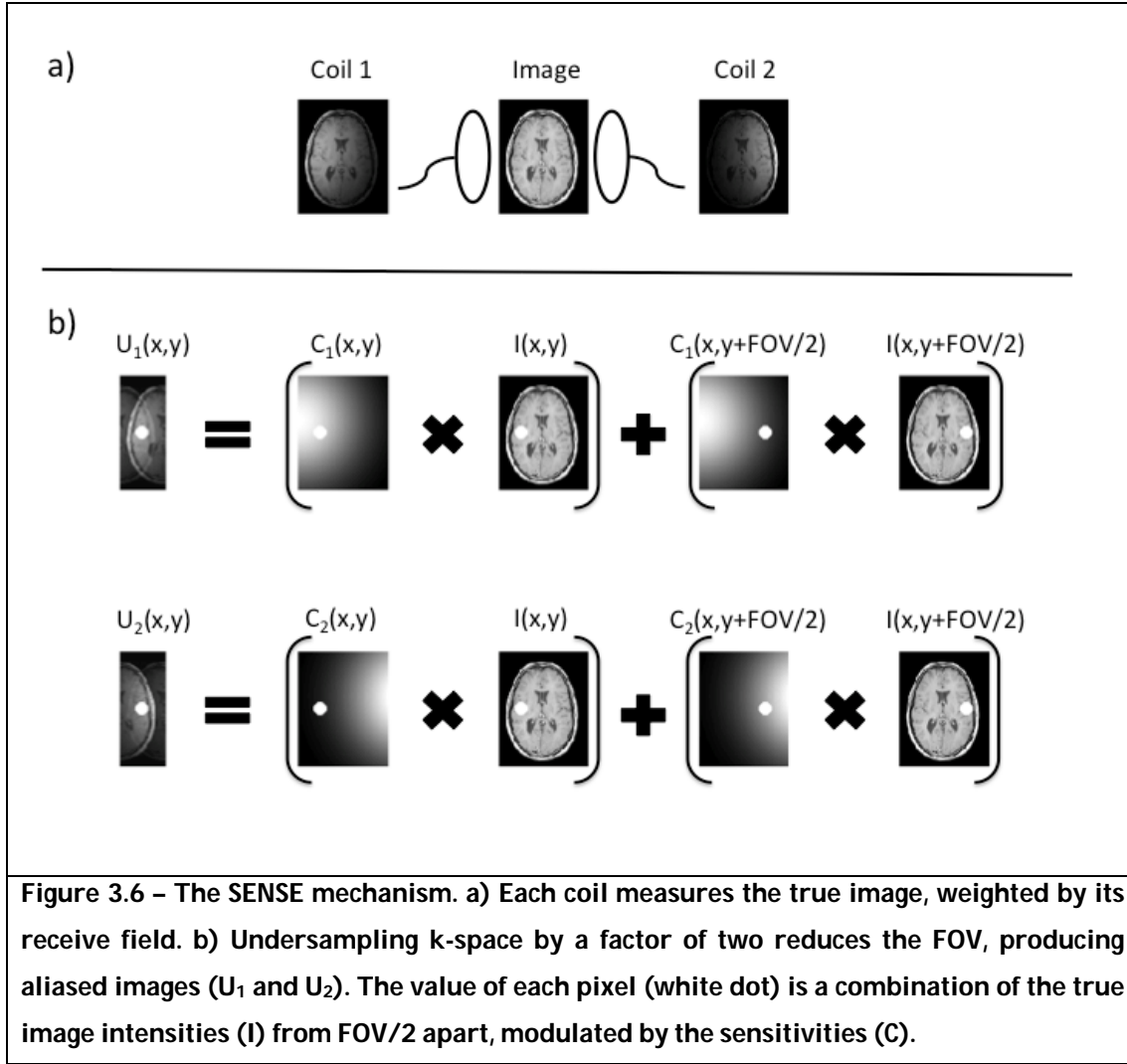


Figure 3.6 – The SENSE mechanism. a) Each coil measures the true image, weighted by its receive field. b) Undersampling k-space by a factor of two reduces the FOV, producing aliased images (U_1 and U_2). The value of each pixel (white dot) is a combination of the true image intensities (I) from $FOV/2$ apart, modulated by the sensitivities (C).

However, it is possible to undo the aliasing by utilising the fact that the different coil sensitivities offer unique measurements of the pixels. The aliasing can be written in matrix form as in equation 3.14. The unaliased pixel intensities can be obtained by inverting the matrix containing the coil sensitivities. This can be done for every image pixel sequentially, yielding an unaliased image.

$$3.14 \quad \begin{bmatrix} U_1(x,y) \\ U_2(x,y) \end{bmatrix} = \begin{bmatrix} C_1(x,y) & C_1(x,y+FOV/2) \\ C_2(x,y) & C_2(x,y+FOV/2) \end{bmatrix} \begin{bmatrix} I(x,y) \\ I(x,y+FOV/2) \end{bmatrix}$$

It is important to note that the coil sensitivity matrix wholly determines the quality of the unaliasing. The matrix inversion is improved by increasing the number of receivers,

and by having receiver sensitivities that are as distinct as possible. The quality of the inversion is wholly defined by the g-factor (Pruessmann et al., 1999).

Most importantly, SENSE requires knowledge of the receive field of each RF coil element. Without the receive fields, the coil sensitivity matrix could not be formed and inverted. The issue of receive mapping is addressed in section 3.4.3.1.

Other PPI approaches have been proposed which operate in the frequency domain ((Griswold et al., 2002),(Lustig and Pauly, 2010)). These do not require explicit receive field measurements, as they extract it directly from k-space data. This comes at the expense of a reduced SNR.

3.3.2 Transmit Fields

The transmit field provides a means of manipulating magnetisation beyond using gradient fields. The transmit field is applied in short bursts, named RF pulses. There are many types of RF pulses, the most common of which are described below.

3.3.2.1 Excitation Pulses

The most elementary RF pulse is the excitation pulse. The purpose of this pulse is to generate transverse magnetisation by rotating the magnetisation vector away from equilibrium. The amount of induced rotation is quantified by the flip angle, $\theta(\mathbf{r})$ (degrees or radians), as defined in equation 3.15, where T_{RF} is the length of the pulse. The flip angle can be increased by either increasing the length of the pulse or increasing the strength of the transmit field. Note that the net flip angle is inherently modulated by the spatial distribution of the transmit field.

$$3.15 \quad \theta(\mathbf{r}) = \gamma \int_{t=0}^{T_{RF}} T(\mathbf{r}, t) dt$$

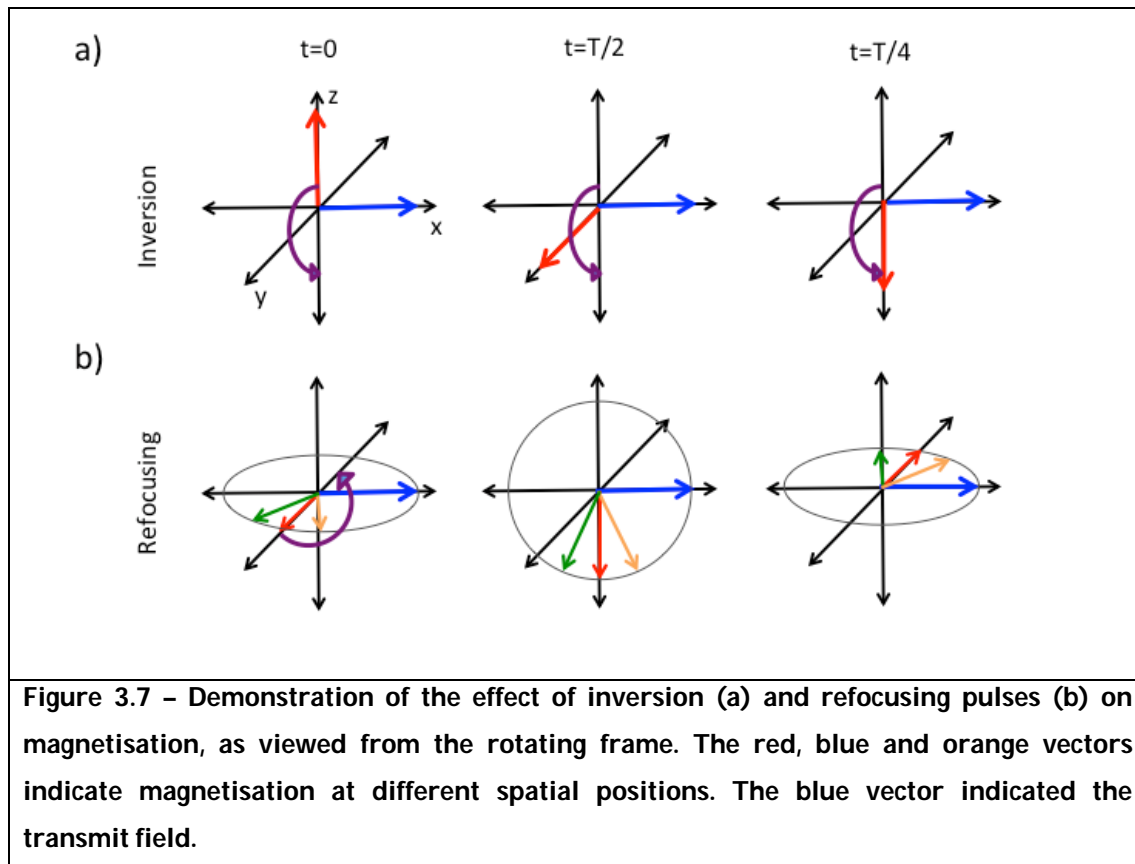
The strength of the transmit field can change in time. This can serve two purposes. The temporal profile of the pulse is related to its frequency profile by the Fourier transform. For example, consider a hard pulse for which the transmit amplitude remains constant over its duration. The frequency profile is defined by a sinc function (the FT of a rect) of width inversely proportional to the T (Bernstein et al., 2004).

Temporal modulation of the pulse can also serve a further purpose. The simultaneous application of field gradients can spatially encode the flip angle. This is most commonly seen in slice-selective pulses. A sinc-shaped pulse is played in the presence of a constant field gradient. The frequency content of the pulse is a rect function; hence the spins whose resonant frequency lies within the frequency band of the pulse rotate towards the transverse plane. The result is a slice of excited magnetisation. The width of the slice is defined by the magnitude of the gradient and the frequency content of the sinc. The slice's orientation is defined by the direction of the field gradient, i.e. a z-gradient produces a slice that lies in the x-y plane.

3.3.2.2 Inversion & Refocusing pulses

Inversion and refocusing pulses are RF pulses that cause the magnetisation to rotate by 180° . They differ due to their specific purpose. Inversion pulses are applied in order to reverse the orientation of a z-aligned magnetisation vector, as in Figure 3.7a. Refocusing pulses are applied to rotate magnetisation already in the transverse plane, as shown in Figure 3.7b.

Refocusing pulses demonstrate the importance of phase of the transmit field. As indicated in the diagram, the x-oriented field inverts the y-component of the magnetisation. However, the effect of a y-oriented transmit field would lead to a significantly different resulting magnetisation distribution, where the red vector would be unperturbed and the orange and green vectors interchanged. Careful consideration is given to both the amplitude and phase of all the RF pulses used in pulse sequences.



3.3.2.3 Adiabatic pulses

Adiabatic pulses offer an alternative strategy to achieving the magnetisation excitation, inversion or refocusing. They work by modulating the frequency of the pulse in addition to its phase and amplitude.

Consider the transmit field in a rotating frame rotating at the Larmor frequency, referred to here as Ω_L . The transmit field vector remains static in this frame when it the driving coil current oscillates at the Larmor frequency. When this carrier frequency changes to frequency ω , the transmit vector precesses about z-axis at frequency $\omega - \omega_L$, again when viewed from Ω_L . In essence, changing the frequency of the transmit field is equivalent to the addition of a transmit field component in the z-direction. Using this effect, the effective transmit field can be designed to be directed in any direction, about which the magnetisation will precess.

This behaviour allows more advanced magnetisation trajectories to be designed. Furthermore, adiabatic pulses are inherently insensitive to inhomogeneous transmit

fields. This is because the behaviour of the magnetisation does not critically depend on the amplitude of the transmit field.

However, adiabatic pulses have two major drawbacks. They are typically much longer than standard excitation pulses, as they need the rate of change of direction of the transmit vector to be slow. Secondly, they deposit high amounts of energy, as they require a high magnitude transmit field.

3.3.2.4 Multi-channel Transmission

The use of multiple transmit coils has recently been proposed by Katscher (Katscher et al., 2003) and Zhu (Zhu, 2004). This provides an additional level of flexibility over the standard single transmitter architecture. In single channel transmission, the only degrees of control are the temporal profile of the amplitude and frequency of the current passed through the coil. However, the spatial profile of the transmit field remains dependent on the RF coil and its interaction with the object being scanned. In contrast, each coil in a multi-coil system has its own transmit field shape, and controlling their drives allows for control of how they constructively and destructively interfere, changing the net transmit field shape. Furthermore, the relative channel drives can change in time, allowing for the total field shape to vary temporally.

There are two forms of multi-channel transmission: RF shimming, and full parallel transmission (PTx). RF shimming is the most basic form, in which the same shaped RF pulse is played through each transmitter, but with the ability to alter the relative current amplitudes and phases. Full PTx utilises the full flexibility of the system, driving each channel with an independent waveform.

3.3.2.4.1 RF Shimming

RF shimming was first demonstrated by Ibrahim (Ibrahim et al., 2001) in 2001 as a means of reducing RF inhomogeneity artefact at ultra-high field (UHF). Ibrahim realised that the amplitude and phase of the current in each rod of a TEM resonator (equivalent

to each leg of a birdcage) can be optimised to deviate from the normal quadrature drive to maximise the homogeneity of the overall field.

Several methods have been proposed to calculate the appropriate weights for each transmit element. The most basic approach (Metzger et al., 2008), phase shimming, calculates the phase of each channel so that the transmit fields constructively interfere. This approach has been successfully applied to methods that require homogeneity over small regions, such as the prostate. Optimising for phase coherence in a small region of interest (ROI) allows for successful imaging, at the expense of total image quality. Furthermore, this method does not require full knowledge of the transmit field of each element, just their relative phases.

A more widely adopted approach is to utilise explicitly measured field maps, providing control of the actual transmit field produced. The shim weights are obtained by minimisation of a least-squares cost function, as in equation 3.16. Here, \mathbf{w} is an $N_T \times 1$ vector containing the complex weights of all N_T channels which is to be found, \mathbf{T} is an $N_p \times N_T$ matrix which contains the transmit field maps of every channel for all N_p pixels inside the desired ROI, and \mathbf{D} is an $N_p \times 1$ vector containing the desired net transmit field. The weights that minimise the difference between \mathbf{D} and $\mathbf{T}\mathbf{w}$ are found by minimising the l_2 norm of the difference.

$$3.16 \quad \min_{\mathbf{w}} \Phi = \|\mathbf{D} - \mathbf{T}\mathbf{w}\|_2^2$$

This approach has been superseded by a method that accounts for two important factors. First, many applications of RF shimming do not require control of the phase of the total transmit field. Equation 3.16 attempts to find the superposition of fields whose amplitude and phase match those of \mathbf{D} . The Magnitude Least-Squares (MLS) approach modifies the cost function as in the first term of equation 3.17 (Katscher et al., 2007). Here, \mathbf{D} describes the desired total field amplitude, and modulus of $\mathbf{T}\mathbf{w}$ is taken before subtraction. The cost function can be minimised by any field superposition whose magnitude matches the desired magnitude, with full flexibility with phase.

3.17

$$\min_{\mathbf{w}} \Phi = \|\mathbf{D} - \mathbf{T}\mathbf{w}\|_2^2 + \lambda \|\mathbf{w}\|_2^2$$

The minimisation of equation 3.17 requires more advanced optimisation methods as it is no longer a least squares problem. An efficient approach (Setsompop et al., 2008b) utilises multiple sequential least squares minimisations. The first minimisation solves equation 3.7 without taking the modulus of $\mathbf{T}\mathbf{w}$ to directly obtain \mathbf{w}_1 . The phase of $\mathbf{T}\mathbf{w}_1$ is then assigned to \mathbf{D}_2 and equation 3.7 is solved again to obtain the new weights \mathbf{w}_2 . This process is repeated until convergence.

The second term in equation 3.17 provides control of the amplitude of the weights. This controls the total RF pulse power. The relative importance of the two terms in the cost function is defined by the regularisation parameter λ .

Many more RF shimming methods have been developed, optimising for criteria such as transmit field efficiency (Deniz et al., 2012) or satisfaction of the adiabatic condition (Setsompop et al., 2007). However, RF shimming only provides a limited amount of control over the homogeneity of the transmit field (Mao et al., 2006). In contrast, full PTx can achieve better results.

3.3.2.4.2 *Parallel Transmission*

PTx refers to the utilisation of independent temporal multi-channel waveform control in synergy with field gradients. The first implementations of PTx (Katscher et al., 2003; Zhu, 2004; Grissom et al., 2006) directly drew from insights gained from parallel imaging.

When operating in the small flip-angle regime (i.e. $\theta < 5^\circ$), it is possible to utilise the concept of transmit k-space. The gradients played during a pulse define the k-space trajectory, and the amplitude and phase of the RF pulse is deposited at each k-space location as it is played. The overall excitation is the Fourier transform transmit k-space.

Spatially selective pulses can be designed with this framework. However, these pulses have not been widely adopted, as the time taken to sufficiently traverse k-space is typically too long. The first PTx methods successfully allowed the shortening of the transmit k-space trajectory, in the same way as parallel imaging works for data acquisition.

Several more advanced applications have also been developed. Significant effort has been devoted to using PTx and gradient encoding to mitigate RF inhomogeneity (Malik et al.; Setsompop et al., 2008a). The effects of \mathbf{B}_0 inhomogeneity have also been successfully mitigated using PTx (Malik et al.).

As with receive parallel imaging, multi-coil transmission fundamentally requires the transmit fields of each transmit element. This is the topic of the next section.

3.4 Determination of RF Fields

There are many situations that require knowledge of the \mathbf{B}_1 field. This information can be obtained in many ways. The main methods in current use are described below.

3.4.1 Analytical Solutions to Maxwell's Equations

The earliest work on \mathbf{B}_1 mapping used a set of simplifying approximations that allowed Maxwell's equations to be solved analytically. Both Keltner (Keltner et al., 2005) and Carlson (Carlson, 1988) modelled the imaging of a uniform conducting sphere using a single loop coil. In this scenario, the overall \mathbf{B}_1 field can be expressed as a superposition of Legendre polynomials. This approach allowed several qualitative statements to be made about the nature of the \mathbf{B}_1 field distributions at a range of frequencies.

This approach is fundamentally limited to simplistic geometries, as analytic \mathbf{B}_1 field solutions are only possible when basic symmetries are adhered to. It is very difficult to model humans and retain any symmetries, so these approaches were abandoned for alternative approaches.

3.4.2 RF Simulations

Analytical solutions to Maxwell's equations only exist for very simplistic coil-object geometries. Solutions do exist in more complicated scenarios; but they cannot be expressed in a functional form.

General solutions are obtained by solving Maxwell's equations numerically (Collins and Wang, 2011). This is achieved by approximating the spatial and temporal derivatives of the equations with finite differences. This allows Maxwell's equations to be expressed so that any field vector component can be determined by the vector fields in neighbouring locations at the previous time-point (Hand, 2008).

First, the physical space is segmented into a 3D grid of cubes. Each is assigned the appropriate electromagnetic properties so that the subject, the coil system and magnet are faithfully represented. The boundary of the volume is typically set to be fully absorbing in order to minimise unrealistic reflections back into the space.

The RF simulation is initiated by generating an electric field across the port of the RF coil. A series of incremental steps forward in time are taken. At each time step, every field component is determined. The RF simulation is terminated when the fields have reached a steady state.

The described approach is the Finite Difference Time Domain (FDTD) method. Other approaches have been applied, using either the integral forms of Maxwell's equations of operating in the frequency domain. However, FDTD is by far the most widely used.

The method has several drawbacks that require special consideration to mitigate. Realistic objects have curved surfaces that cannot be accurately represented using a grid of cubes. Furthermore, fine detail; such as coil capacitors and other components, are often smaller than the native grid resolution. Both of these problems can be solved by using localised high-resolution meshing, but further increased the memory requirements of an already highly demanding computational problem (Hand, 2008). Often simulations take several hours to complete.

RF simulations have been used extensively to study the behaviour of RF fields at all B_0 field strengths and for a wide range of RF coil configurations (Collins and Smith, 2001). RF simulations also calculate electric fields, which in conjunction with knowledge of tissue conductivity, provides a means of estimating induced tissue currents and in turn the local and global power deposition. These are important measures of RF safety (Collins et al., 2005).

However, RF simulations also have severe limitations. As described previously in section 3.2.6.2, the behaviour of fields is intimately tied to the underlying anatomy of the subject being scanned. The diverse range of subject shapes, sizes, and internal tissue distributions means that simulation results from generic human models (as are frequently used for RF simulations) do not necessarily correlate to the actual fields produced.

Several advancements are required for RF simulations to become a valid tool for subject-specific field prediction. First, accurate subject-specific models are needed. Recent research (Homann et al., 2011) has attempted to use whole-body MRI scans to generate simplistic water/fat/air models, but then accuracy of this approach is yet to be verified. Second, the speed of RF simulations needs to be accelerated, so that patient-specific fields can be generated and used during a single scan session.

3.4.3 Measurement of fields using MRI

The final approach is direct measurement using MRI. The RF fields affect the measured signal, and therefore by appropriate sequence design and data analysis, RF field information can be obtained.

It is important to state that NMR is only responsive to the two oppositely rotating transverse RF magnetic fields. Therefore electric field information cannot be directly measured; it can only be inferred by processing measured B_1 maps and applying Maxwell's equations (Katscher et al., 2009).

RF field mapping is best understood by considering the signal equation of a general sequence utilising a multi-coil array, given in equation 3.18, where the receive field of the r^{th} receiver has magnitude $|R_r(\mathbf{r})|$ and phase $\phi_r^R(\mathbf{r})$, the transmit field of the t^{th} transmitter has magnitude $|T_t(\mathbf{r})|$ and phase $\phi_t^T(\mathbf{r})$, and the chosen pulse sequence generates a signal Ψ which is a function of the transmit field magnitude and the NMR properties of the object being imaged.

$$3.18 \quad S_{r,t}(\mathbf{r}) = |R_r(\mathbf{r})| e^{i\phi_r^R(\mathbf{r})} e^{i\phi_t^T(\mathbf{r})} \Psi \{M_0(\mathbf{r}), T_1(\mathbf{r}), T_2(\mathbf{r}), \dots, |T_t(\mathbf{r})|\}$$

This central equation underpins all field mapping. Receive and transmit mapping will be discussed in the following sections.

3.4.3.1 Receive Field Mapping

The receive field appears in the MRI signal equation in a multiplicative manner. Any measured image will be weighted by the magnitude and phase of the receiver it was measured with. Consequently, it is not possible to directly measure the receive field from images. Only relative receiver information can be obtained.

Generally, single receiver imaging does not require receive field estimation. However, there are methods where it is desirable to remove the spatial modulation imparted by the receiver. A common example is automated brain segmentation, in which different tissues are labelled in order to give a measure of their relative contribution to total brain volume (Vovk et al., 2007). The most successful approaches simultaneously estimate the smooth multiplicative receive field and tissue compartments. These methods are typically performed on magnitude images, so the receive phase is typically ignored.

Receive estimation is most commonly applied in the context of parallel imaging. The original framework set out in the SENSE paper is still widely used (Pruessmann et al., 1999). A pre-scan is performed, which acquires a low-resolution high SNR dataset, acquiring on all receivers, and if present, the body coil.

Initial estimates of the receive sensitivities are then obtained by dividing the individual coil complex images by the complex body coil image, or by an image formed by the SOS of the individual coil images. This process removes the anatomy, yielding the relative relationships. These are then typically smoothed using local low-order polynomial filtering.

The receive fields can only be estimated where there is signal. The receive fields are often slightly extrapolated outside of the object, in order to tolerate subject motion.

Very few methods have improved upon this approach. A paper by Huang (Huang et al., 2005) developed a method to fill voids inside the object, such as the lungs or abdomen. Other work has focussed on improving the filtering step by utilising more advanced models for insisting that the field maps are smooth (Lin et al., 2003; Keeling and Bammer, 2004).

The previously discussed frequency domain PPI methods infer receive field information directly in k-space. It has been recently shown how this information relates to image domain receive calibration (Lustig et al., 2011). This topic is discussed further in chapter 6.

3.4.3.2 Transmit Field Mapping

Transmit field mapping is a fundamentally different process than receive field mapping. This is because the transmit field appears in the MRI signal equation as a function of the applied pulse sequence. This allows for pulse sequence design to facilitate transmit field mapping.

Flip angle mapping methods can be classified into two classes: amplitude based, and phase based. These are discussed in the next sections. Several factors must be considered when mapping the fields of transmit arrays, as discussed in section 3.4.3.2.4. Finally, further additional considerations are discussed.

Transmit field mapping is a very active research area, with novel methods emerging frequently. Discussion of these new techniques is presented throughout the thesis at appropriate times.

3.4.3.2.1 Amplitude based methods

Amplitude based transmit field mapping sequences encode flip angle information into the magnitude of measured images. The simplest mapping sequence is the double angle method (DAM) (Insko and Bolinger, 1993). It can generate very accurate field maps at the expense of being very time consuming. The mapping sequence requires the measurement of two images, I_1 and I_2 , acquired with flip angles θ and 2θ , respectively. Both images are acquired with a very long TR ($\gg T_1$, in order to eliminate longitudinal relaxation effects) and short TE (to increase SNR). In this regime, the image intensities are $I_1 = M_0 R \sin(\theta) e^{-TE/T_2}$ and $I_2 = M_0 R \sin(2\theta) e^{-TE/T_2}$. By taking the image ratio and applying the trigonometric identity $\sin(2\theta) = 2\sin(\theta)\cos(\theta)$, the flip angle can be obtained using equation 3.19.

$$3.19 \quad \theta = \cos^{-1} \left(\frac{I_2}{2I_1} \right)$$

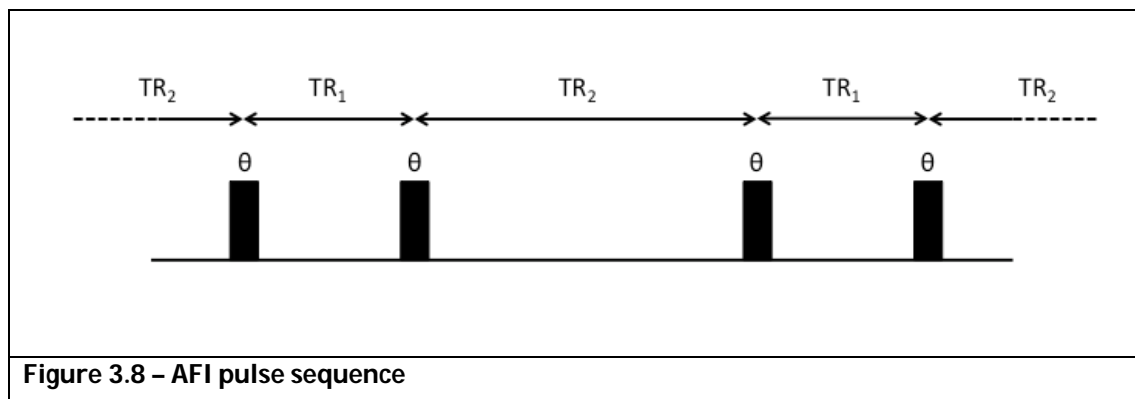
The concept of taking image ratios is commonplace in flip-angle mapping. This is because it has the favourable property of cancelling undesired signal contributions originating from the receive field and tissue contrast.

DAM is not used for in-vivo field measurement because it is too slow. Typically a TR of $5T_1$ is used, so a $32 \times 32 \times N_{FE}$ 3D field map in the brain (assuming grey matter T_1 of 1820ms, and N_{FE} can be any value defined by the FE sampling) would take over two hours. Consequently, its primary use is as a 'gold-standard' sequence for validating other methods against. Several groups have modified the DAM approach in order to increase its speed (Stollberger and Wach, 1996). The saturated (Cunningham et al., 2006) and catalysed (Wang et al., 2009) DAMs utilise additional pulses after the

acquisition of each FE line in order to put the magnetisation into a consistent state. However, these pulses need to be adiabatic, and therefore are power-intensive.

An alternative group of methods apply additional RF pulses before signal acquisition, pre-encoding the amount of the available longitudinal magnetisation so that $M_z = M_0 \cos(\theta)$ (Klose, 1992; Brunner and Pruessmann, 2009; Chung et al., 2010). Two images are again acquired, with and without the pre-pulse. These methods rely upon fast readouts that sample the centre of k-space first in order to measure M_z before it significantly returns to equilibrium or is modified by the signal generation process. These methods can be inaccurate in tissues with short T_1 .

The Actual Flip angle Imaging (AFI) technique has been adopted widely across the MRI community due to its speed and accuracy. As opposed to the pre-pulse techniques and DAMs that acquire two images serially, AFI acquires the PE lines of each image in a fully interleaved way. This is achieved by running a pulse sequence with two alternating TR periods of length TR_1 and TR_2 . This is shown in Figure 3.8. It is a fully spoiled gradient echo sequence. Both TR periods acquired at the same TE.



The signals of the acquired images are given by equations 3.20 and 3.21, where $E_{1,2} = e^{-TR_{1,2}/T_1}$.

$$3.20 \quad I_1 = RM_0 \sin(\theta) e^{-TE/T_2} \frac{1 - E_2 + (1 - E_1)E_2 \cos(\theta)}{1 - E_1 E_2 \cos^2(\theta)}$$

$$3.21 \quad I_2 = RM_0 \sin(\theta) e^{-TE/T_2} \frac{1 - E_1 + (1 - E_2)E_1 \cos(\theta)}{1 - E_1 E_2 \cos^2(\theta)}$$

In the short TR regime (i.e. $TR_1 < TR_2 < T_1$), the exponential terms can be approximated by $E_{1,2} = 1 - TR_{1,2}/T_1$. Applying this approximation and taking the ratio $r = I_2/I_1$ yield equation 3.22, where n is the ratio of TR periods, $n = TR_2/TR_1$.

$$3.22 \quad r = \frac{I_2}{I_1} = \frac{1 + n \cos(\theta)}{n + \cos(\theta)}$$

The flip angle can be obtained using equation 3.23.

$$3.23 \quad \theta = \cos^{-1} \left(\frac{rn - 1}{n - r} \right)$$

AFI performs best at large n , as this increases the method's dynamic range (see section 3.4.3.2.3). However, this must be balanced by need of both TR periods to be much shorter than T_1 . AFI accuracy also requires a unique spoiling regime that guarantees the elimination of all transverse magnetisation at the end of each TR period (Nehrke, 2009). AFI can suffer from systematic measurement errors in tissues with very short T_1 's, such as fat ($T_1 = 365\text{ms}$ at 3T, (Han et al., 2003)).

3.4.3.2.2 *Phase based methods*

An alternative approach to transmit field mapping encodes the magnitude of the transmit field into the phase of an image. One class of methods ((Morrell, 2008; Chang, 2012)) achieve this by replacing a sequence's excitation pulse by a combination of

pulses oriented along different transverse directions. The transmit field can then be extracted by processing the phase of the acquired images,

A recently developed technique, named the Bloch-Siegert (BS) method, performs the flip angle encoding in a novel way. A standard excitation pulse first generates transverse magnetisation. This is followed by a long, high amplitude off-resonance pulse. In the Larmor rotating frame, this appears as an additional z-directed field, causing the magnetisation to accrue phase proportional to the strength of the field.

The BS method acquires two images with off-resonant pulses at $+\omega$ and $-\omega$, where ω is typically several kHz. The flip angle is obtained from the phase difference of the two images.

All phase-based methods are sensitive to inhomogeneous \mathbf{B}_0 fields (referred to as off-resonance). This is because it is difficult to differentiate between phase accrual due the transmit field and phase accrual due to off-resonance. However, they do not suffer from T_1 contamination.

3.4.3.2.3 Additional considerations

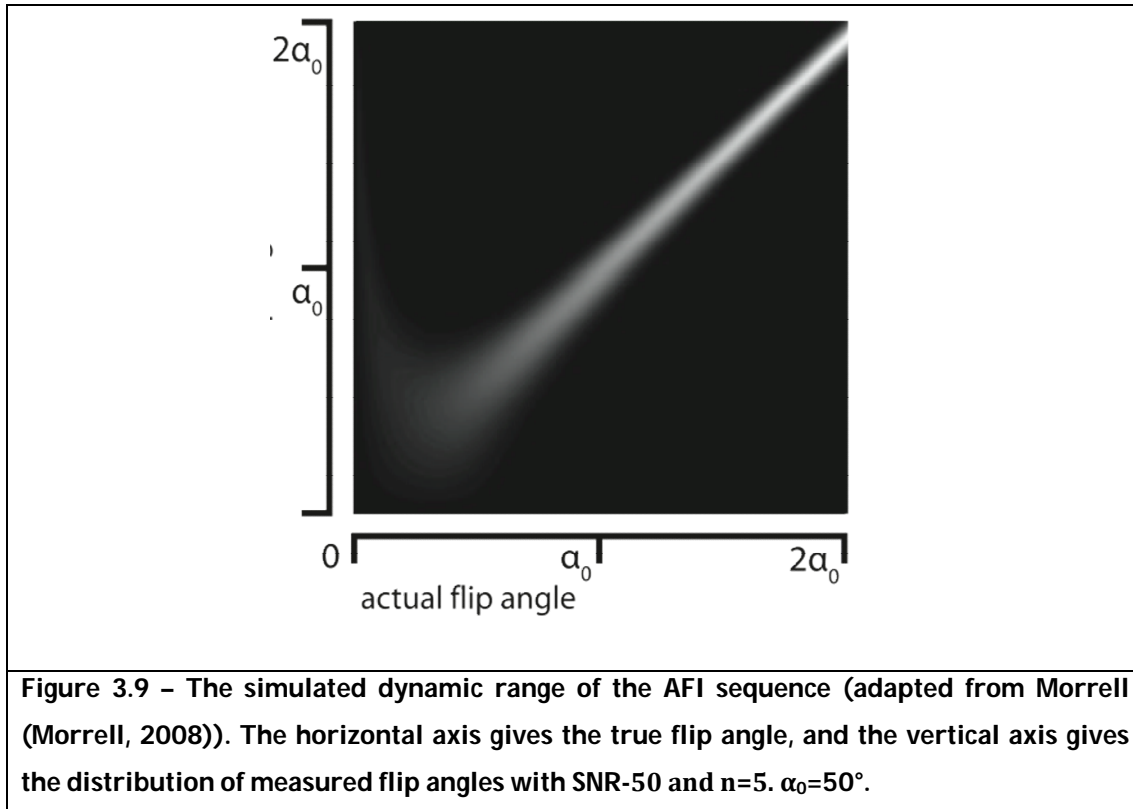
There are several other factors that must be considered when performing flip angle mapping. There are many situations for which the shape of the field is not required, but it is important that the intended global flip angle is achieved. A pre-scan calibration, referred to as power optimisation, is usually performed. This determines the relationship between the coil driving current and the flip angle. This relationship is affected by the patient interaction with the coil.

Several pre-scan methods have been developed (Perman et al., 1989; Breton et al., 2009; Sacolick et al., 2011). The method employed by the MRI systems used in this thesis employ the Perman approach, in which three identical RF pulses are applied. The correct scaling for a 90° has been found when the amplitude of the third spin echo is zero.

The methods described above must all be applied in 3D acquisitions. This is because slice selective pulses always have imperfect slice profiles, and therefore have an effective flip-angle distribution in the through-slice direction. The 2D images integrate the signal in the through slice direction, violating the signal equations derived for each method. Slice selective flip angle mapping can be performed, but special care must be taken (Brunner and Pruessmann, 2009; Malik et al., 2011).

Off-resonance can corrupt flip angle mapping in two ways. First, if RF pulses have insufficient bandwidth, spins off-resonance (either due to \mathbf{B}_0 inhomogeneity or chemical shift) will experience a different amplitude excitation field. This is not intrinsic to the shape of the transmit field, but an experimental effect which will manifest itself in field maps. Phase based methods must be also susceptible to \mathbf{B}_0 effects, and are often designed in order to reduce their effect as much as possible.

Finally, the dynamic range of a mapping method is very important. The dynamic range of a method describes its sensitivity to noise and its optimal point of operation. Consider Figure 3.9, which is taken from Morrell (Morrell and Schabel, 2010). This graph plots the quality of noise-corrupted AFI measurements versus their true value. Better estimates of the flip angle are obtained for flip angles above 50° . This criterion can be understood by considering the low flip angle case. Using small flip angles results in I_1 and I_2 being more similar. Therefore noise has a larger effect on their ratio, corrupting the measurement.



3.4.3.2.4 *Multi-transmit methods*

Multi-transmit field mapping is more problematic than single channel mapping for several reasons.

1. Individual transmit coils have localised sensitivities, with different regions of the object having either high and low magnitude transmit field. The mapping method used therefore needs to be accurate over a large dynamic range.
2. Unlike receive mapping, the transmit field of each element must be mapped serially.
3. The relative phase of the fields is also required.

Several methods have been developed to deal with these issues. Mapping the field of an individual transmit element is very difficult, as it requires a mapping method with very large dynamic range. This has been solved by mapping each element in linear combinations (LCs) (Nehrke and Bornert, 2008; Brunner and Pruessmann, 2009; Malik et al., 2009). This is demonstrated by equation 3.24.

The matrix \mathbf{E} describes the encoding used whilst transmit mapping. Each column denotes the drive applied to each transmit element. Each row corresponds to mapping of each element. \mathbf{E}_{ind} describes the mapping of each element individually: only the n^{th} coil is driven (column n) for the mapping of the n^{th} coil (row n). In contrast, \mathbf{E}_{ind} describes the use of linear combinations. All other coils are always driven with uniform weight except the mapped coil, which has weight ε . The optimal value of ε depends on the number of coils and how they interact with the subject. The individual transmit sensitivities are obtained by inverting the matrix \mathbf{E} for every pixel.

This approach is beneficial as using LCs generally produces a net transmit field which has a smaller range of flip angles across the object. Therefore the utilised mapping method can have a smaller dynamic range without affecting the overall result.

$$3.24 \quad \mathbf{E}_{ind} = \begin{bmatrix} 1 & 0 & \cdots & 0 \\ 0 & 1 & & \vdots \\ \vdots & & \ddots & \vdots \\ 0 & \cdots & \cdots & 1 \end{bmatrix}, \quad \mathbf{E}_{ind} = \begin{bmatrix} \varepsilon & 1 & \cdots & 1 \\ 1 & \varepsilon & & \vdots \\ \vdots & & \ddots & \vdots \\ 1 & \cdots & \cdots & \varepsilon \end{bmatrix}$$

The need for relative phases does not impose any restrictions on the mapping sequence used. However some methods (such as the pre-pulse approaches) do not impart the coil's phase into the acquired images, and therefore an additional set of scans to obtain the phase may be needed.

The need to map coils serially imposes a severe time penalty on transmit field mapping. This is unavoidable, but approaches have been developed to reduce its impact. The primary method chooses to only map the relative amplitude and phase relationships between transmit coils (Van de Moortele et al., 2007) by utilising small flip angle gradient echoes, a relatively fast process. Full absolute field maps for each channel can then be obtained by multiplying each map by an additionally acquired absolute field map of a single transmit configuration.

3.5 References

- Bernstein, M.A., King, K.F., and Zhou, X.J. (2004). Handbook of MRI pulse sequences (Elsevier).
- Breton, E., McGorty, K., Wiggins, G.C., Axel, L., and Kim, D. (2009). Image-guided radio-frequency gain calibration for high-field MRI. *NMR in Biomedicine* 23, 368–374.
- Brunner, D.O., and Pruessmann, K.P. (2009). B1+ interferometry for the calibration of RF transmitter arrays. *Magnetic Resonance in Medicine* 61, 1480–1488.
- Brunner, D.O., Zanche, N.D., Fröhlich, J., Paska, J., and Pruessmann, K.P. (2009). Travelling-wave nuclear magnetic resonance. *Nature* 457, 994–998.
- Carlson, J.. (1988). Radiofrequency field propagation in conductive NMR samples. *Journal of Magnetic Resonance* (1969) 78, 563–573.
- Chang, Y.V. (2012). Rapid B1 mapping using orthogonal, equal-amplitude radio-frequency pulses. *Magnetic Resonance in Medicine* 67, 718–723.
- Chung, S., Kim, D., Breton, E., and Axel, L. (2010). Rapid B1+ mapping using a preconditioning RF pulse with TurboFLASH readout. *Magnetic Resonance in Medicine* 64, 439–446.
- Collins, C.M., Li, S., and Smith, M.B. (2005). SAR and B1 field distributions in a heterogeneous human head model within a birdcage coil. *Magnetic Resonance in Medicine* 40, 847–856.
- Collins, C.M., and Smith, M.B. (2001). Signal-to-noise ratio and absorbed power as functions of main magnetic field strength, and definition of “90°” RF pulse for the head in the birdcage coil. *Magnetic Resonance in Medicine* 45, 684–691.
- Collins, C.M., and Wang, Z. (2011). Calculation of radiofrequency electromagnetic fields and their effects in MRI of human subjects. *Magnetic Resonance in Medicine* 65, 1470–1482.
- Cunningham, C.H., Pauly, J.M., and Nayak, K.S. (2006). Saturated double-angle method for rapid B1+ mapping. *Magnetic Resonance in Medicine* 55, 1326–1333.
- Deniz, C.M., Brown, R., Lattanzi, R., Alon, L., Sodickson, D.K., and Zhu, Y. (2012). Maximum efficiency radiofrequency shimming: Theory and initial application for hip imaging at 7 tesla. *Magnetic Resonance in Medicine* n/a–n/a.

Glover, G., Hayes, C., Pelc, N., Edelstein, W., Mueller, O., Hart, H., Hardy, C., O'Donnell, M., and Barber, W. (1985). Comparison of linear and circular polarization for magnetic resonance imaging. *Journal of Magnetic Resonance* (1969) *64*, 255–270

Grissom, W., Yip, C., Zhang, Z., Stenger, V.A., Fessler, J.A., and Noll, D.C. (2006). Spatial domain method for the design of RF pulses in multicoil parallel excitation. *Magnetic Resonance in Medicine* *56*, 620–629.

Griswold, M.A., Jakob, P.M., Heidemann, R.M., Nittka, M., Jellus, V., Wang, J., Kiefer, B., and Haase, A. (2002). Generalized autocalibrating partially parallel acquisitions (GRAPPA). *Magnetic Resonance in Medicine* *47*, 1202–1210.

Han, E., Gold, G., Stainsby, J., Wright, G., Beaulieu, C., and Brittain, J. (2003). In vivo T1 and T2 measurements of musculoskeletal tissue at 3 T and 1.5 T. In *Proceedings of the 11th Annual Meeting of ISMRM, Toronto, Canada*, p. 450.

Hand, J.W. (2008). Modelling the interaction of electromagnetic fields (10 MHz–10 GHz) with the human body: methods and applications. *Physics in Medicine and Biology* *53*, R243–R286.

Homann, H., Börnert, P., Eggers, H., Nehrke, K., Dössel, O., and Graesslin, I. (2011). Toward individualized SAR models and in vivo validation. *Magnetic Resonance in Medicine* *66*, 1767–1776.

Huang, F., Chen, Y., Duensing, G.R., Akao, J., Rubin, A., and Saylor, C. (2005). Application of partial differential equation-based inpainting on sensitivity maps. *Magnetic Resonance in Medicine* *53*, 388–397.

Ibrahim, T.S., Lee, R., Baertlein, B.A., Abduljalil, A.M., Zhu, H., and Robitaille, P.-M.L. (2001). Effect of RF coil excitation on field inhomogeneity at ultra high fields: a field optimized TEM resonator. *Magnetic Resonance Imaging* *19*, 1339–1347.

Insko, E.K., and Bolinger, L. (1993). Mapping of the Radiofrequency Field. *Journal of Magnetic Resonance, Series A* *103*, 82–85.

Jin, J. (1998). *Electromagnetic analysis and design in magnetic resonance imaging* (CRC).

Katscher, U., Börnert, P., Leussler, C., and Van den Brink, J.S. (2003). Transmit SENSE. *Magnetic Resonance in Medicine* *49*, 144–150.

Katscher, U., Vernickel, P., Graesslin, I., and Boernert, P. (2007). RF shimming using a multi-element transmit system in phantom and in vivo studies. In *Proceedings of the 15th Annual Meeting of ISMRM, Berlin, Germany*, p. 1693.

- Katscher, U., Voigt, T., Findekle, C., Vernickel, P., Nehrke, K., and Dossel, O. (2009). Determination of Electric Conductivity and Local SAR Via B1 Mapping. *Medical Imaging, IEEE Transactions On* 28, 1365–1374.
- Keeling, S.L., and Bammer, R. (2004). A variational approach to magnetic resonance coil sensitivity estimation. *Applied Mathematics and Computation* 158, 359–388.
- Keltner, J.R., Carlson, J.W., Roos, M.S., Wong, S.T.S., Wong, T.L., and Budinger, T.F. (2005). Electromagnetic fields of surface coil in vivo NMR at high frequencies. *Magnetic Resonance in Medicine* 22, 467–480.
- Klose, U. (1992). Mapping of the radio frequency magnetic field with a MR snapshot FLASH technique. *Medical Physics* 19, 1099–1104.
- Kumar, A., and Bottomley, P. (2008). Optimized quadrature surface coil designs. *Magnetic Resonance Materials in Physics, Biology and Medicine* 21, 41–52.
- Lin, F., Chen, Y., Belliveau, J.W., and Wald, L.L. (2003). A wavelet-based approximation of surface coil sensitivity profiles for correction of image intensity inhomogeneity and parallel imaging reconstruction. *Human Brain Mapping* 19, 96–111.
- Liu, W., Collins, C., and Smith, M. (2005). Calculations of B1+ distribution, specific energy absorption rate, and intrinsic signal-to-noise ratio for a body-size birdcage coil loaded with different human subjects at 64 and 128 MHz. *Applied Magnetic Resonance* 29, 5–18.
- Lustig, M., Lai, P., Murphy, M., Vasanawala, S., Elad, M., Zhang, J., and Pauly, J. (2011). An Eigen-Vector Approach to AutoCalibrating Parallel MRI, Where SENSE Meets GRAPPA. p. 479.
- Lustig, M., and Pauly, J.M. (2010). SPIRiT: Iterative self-consistent parallel imaging reconstruction from arbitrary k-space. *Magnetic Resonance in Medicine* 64, 457–471.
- Malik, S.J., Keihaninejad, S., Hammers, A., and Hajnal, J.V. Tailored excitation in 3D with spiral nonselective (SPINS) RF pulses. *Magnetic Resonance in Medicine*.
- Malik, S.J., Kenny, G.D., and Hajnal, J.V. (2011). Slice profile correction for transmit sensitivity mapping using actual flip angle imaging. *Magnetic Resonance in Medicine* 65, 1393–1399.
- Malik, S.J., Larkman, D.J., and Hajnal, J.V. (2009). Optimal linear combinations of array elements for B1 mapping. *Magnetic Resonance in Medicine* 62, 902–909.
- Mao, W., Smith, M.B., and Collins, C.M. (2006). Exploring the limits of RF shimming for high-field MRI of the human head. *Magnetic Resonance in Medicine* 56, 918–922.

Metzger, G.J., Snyder, C., Akgun, C., Vaughan, T., Ugurbil, K., and Van de Moortele, P. (2008). Local B1+ shimming for prostate imaging with transceiver arrays at 7T based on subject-dependent transmit phase measurements. *Magnetic Resonance in Medicine* 59, 396–409.

Van de Moortele, P., Snyder, C., DelaBarre, L., Adriany, G., Vaughan, J., and Ugurbil, K. (2007). Calibration tools for RF shim at very high field with multiple element RF coils: from ultra fast local relative phase to absolute magnitude B1+ mapping. In *Proceedings 15th Scientific Meeting, International Society for Magnetic Resonance in Medicine*, Berlin, p. 1676.

Morrell, G.R. (2008). A phase-sensitive method of flip angle mapping. *Magnetic Resonance in Medicine* 60, 889–894.

Morrell, G.R., and Schabel, M.C. (2010). An analysis of the accuracy of magnetic resonance flip angle measurement methods. *Physics in Medicine and Biology* 55, 6157–6174.

Nehrke, K. (2009). On the steady-state properties of actual flip angle imaging (AFI). *Magnetic Resonance in Medicine* 61, 84–92.

Nehrke, K., and Bornert, P. (2008). Improved B1-mapping for multi RF transmit systems. In *Proceedings of the 16th Annual Meeting of ISMRM*, Toronto, Canada, p. 353.

Perman, W.H., Bernstein, M.A., and Sandstrom, J.C. (1989). A method for correctly setting the rf flip angle. *Magnetic Resonance in Medicine* 9, 16–24.

Pruessmann, K.P., Weiger, M., Scheidegger, M.B., and Boesiger, P. (1999). SENSE: Sensitivity encoding for fast MRI. *Magnetic Resonance in Medicine* 42, 952–962.

Roemer, P.B., Edelstein, W.A., Hayes, C.E., Souza, S.P., and Mueller, O.M. (1990). The NMR phased array. *Magnetic Resonance in Medicine* 16, 192–225.

Sacolick, L.I., Sun, L., Vogel, M.W., Dixon, W.T., and Hancu, I. (2011). Fast radiofrequency flip angle calibration by Bloch–Siegert shift. *Magnetic Resonance in Medicine* 66, 1333–1338.

Setsompop, K., Alagappan, V., Gagoski, B., Witzel, T., Polimeni, J., Potthast, A., Hebrank, F., Fontius, U., Schmitt, F., Wald, L.L., et al. (2008a). Slice-selective RF pulses for in vivo B1+ inhomogeneity mitigation at 7 tesla using parallel RF excitation with a 16-element coil. *Magnetic Resonance in Medicine* 60, 1422–1432.

- Setsompop, K., Wald, L.L., and Adalsteinsson, E. (2007). Reduced-voltage RF shimming for adiabatic pulse design in parallel transmission. In Proceedings of the 15th Annual Meeting of ISMRM, Berlin, Germany, p. 1687.
- Setsompop, K., Wald, L.L., Alagappan, V., Gagoski, B.A., and Adalsteinsson, E. (2008b). Magnitude least squares optimization for parallel radio frequency excitation design demonstrated at 7 Tesla with eight channels. *Magnetic Resonance in Medicine* 59, 908–915.
- Sodickson, D.K., and Manning, W.J. (1997). Simultaneous acquisition of spatial harmonics (SMASH): Fast imaging with radiofrequency coil arrays. *Magnetic Resonance in Medicine* 38, 591–603.
- Stollberger, R., and Wach, P. (1996). Imaging of the active B1 field in vivo. *Magnetic Resonance in Medicine* 35, 246–251.
- Vovk, U., Pernus, F., and Likar, B. (2007). A Review of Methods for Correction of Intensity Inhomogeneity in MRI. *IEEE Transactions on Medical Imaging* 26, 405 –421.
- Wang, D., Zuehlsdorff, S., and Larson, A.C. (2009). Rapid 3D radiofrequency field mapping using catalyzed double-angle method. *NMR Biomed* 22, 882–890.
- Zhu, Y. (2004). Parallel excitation with an array of transmit coils. *Magnetic Resonance in Medicine* 51, 775–784.

Chapter 4 Observation and Measurement of Dynamic Changes in the Transmit Field

This chapter investigates the behaviour of the transmit field in the presence of subject motion. The motivation for this investigation is presented first. This is followed by Study 1, in which measurements are performed in order to discover how the transmit field varies as a function of respiratory state. It is shown that significant differences exist in the transmit field between subject inhalation and exhalation. An RF shimming simulation is also performed, showing that parallel transmission can mitigate the effects of respiration-induced changes in the transmit field.

Study 2 presents a novel reconstruction algorithm for mapping the transmit field throughout the respiratory cycle. The results of the study illustrate the need for an accelerated transmit field mapping technique, which will be presented in the subsequent chapter.

4.1 Motivation

4.1.1 Effect of RF Inhomogeneity on RF pulses

RF pulses are a critical component of all MR sequences. They perform a diverse range of functions, as described in section 3.3.2. Their shape, bandwidth, amplitude and phase are carefully designed in order to manipulate magnetisation in the intended manner. Transmit field inhomogeneity causes pulses to have an incorrect net effect.

Techniques have been developed to counteract the effect of transmit inhomogeneity. Adiabatic pulses (section 3.3.2.3) are designed to be robust to RF inhomogeneity, but result in high power deposition. An alternative approach is the use of spatially-selective pulses (Saekho et al., 2005), but these can require long pulse durations. Consequently, neither approach is widely adopted in

standard clinical imaging. Therefore RF inhomogeneity continues to impact upon many MR methods, as described in the next section.

4.1.2 Effects of Transmit Inhomogeneity - Imaging

At 3T, spatially varying transmit fields can cause localised shading in the image which can obscure anatomy, significantly reducing the diagnostic ability of body MR. This effect is demonstrated in Willineck et. al. (Willinek et al., 2010), in which severe transmit inhomogeneity artifacts are shown in the pelvis and liver. Similar effects have also been seen in Fast Spin-Echo (FSE) angiographic sequences in the thighs (Storey et al., 2010).

The effects of transmit inhomogeneity at 7T become even more pronounced, disrupting the ability to image the brain, and rendering body imaging impossible without using parallel transmission techniques (Vaughan et al., 2009). Shading artifacts become much more severe, completely obscuring large regions of the patient unless special efforts are made to counteract this effect (Hurley et al., 2010).

4.1.3 Effects of Transmit Inhomogeneity – Quantitative MRI

RF inhomogeneity can also negatively affect quantitative MRI (qMRI). The goal of qMRI is to discover underlying properties of imaged tissue, with the goal of using these measurements to quantitatively differentiate normal and diseased tissues (Tofts, 2005). A large range of tissue properties can be measured using qMRI, such as T_1 , T_2 , diffusion, magnetisation transfer ratios and tissue perfusion. The majority of qMRI techniques measure how the MR signal evolves as a function of a chosen variable. For example, T_1 values of tissue can be obtained by performing an inversion-recovery sequence multiple times with different inversion times (Haase, 1990). The signal model of the applied pulse sequence is then fit to the evolution curve, solving for unknown tissue properties.

Transmit inhomogeneity can interfere with qMRI as it affects all RF pulses, and hence signal evolution, in qMRI sequences. Any deviations from the assumed flip angle can impact upon the quality of the signal fit if they are not accounted for. A solution to this was presented by Treier et. al. (Treier et al., 2007), where transmit field measurements were incorporated directly into the fitting regime. An alternative approach is to solve for the inhomogeneity directly inside the fitting routine (Deoni, 2007). However, this approach requires a careful choice of parameters in order for accurate T_1 mapping over a wide range of T_1 's.

Dynamic Contrast-Enhanced (DCE) MRI has also been shown to be susceptible to transmit inhomogeneity. Azlan et. al. (Azlan et al., 2010) measured a ~40% difference in transmit field amplitude between left and right breasts and showed how this can negatively impact upon the measurement of breast tumour signal enhancement due to perfusion of a contrast agent. Roberts et. al. (Roberts et al., 2011) also demonstrated how transmit inhomogeneity can be detrimental to the estimation of arterial input functions for DCE-MRI.

Transmit field inhomogeneity can also significantly impact upon cardiac MRI. Greenman et. al. (Greenman et al., 2003) showed how it leads to spatially varying contrast across the heart at 3T when performing Double Inversion Black Blood FSE imaging. At both 1.5T and 3T, the combined effect of transmit and B_0 inhomogeneity was shown to reduce the efficiency of saturation pulses used for assessing myocardial perfusion (Kim et al., 2005), (Kim et al., 2009). Transmit field mapping sequences have been designed specifically for cardiac measurements (Sung and Nayak, 2008c), and correction methods using adiabatic pulses (Nezafat et al., 2006), (Kim et al., 2009) and tailored pulses (Sung and Nayak, 2008a), (Sung and Nayak, 2008b) have been proposed to correct for these effects.

4.1.4 Motion and RF Inhomogeneity

It is clear from the cited studies that moving organs such as the liver and heart are common targets of both standard and quantitative MRI, and that utilised

imaging techniques must therefore be motion robust. To date, this aspect of MRI has been thought of as independent of transmit inhomogeneity. This section considers how they may be interlinked.

The majority of imaging to date has adopted motion-compensation schemes that attempt to acquire all of the data in a single physiological state. Several methods have been proposed to achieve this. In the thorax and abdomen, breathholding is used extensively to mitigate respiratory motion (Treier et al., 2007). The patient is asked to perform several breathholds, inside of which multiple k-space lines are acquired. An image is formed by combining the data from all of the breathholds. This approach relies upon the patient's ability to hold their breath for long periods (up to 30s), a difficult task for many elderly or sick subjects. This approach is also sensitive to anatomical inconsistencies between breathhold states, resulting in image artifacts.

Respiratory gating can also be applied, where data is only acquired whilst the patient is in the exhalation state (Kwee et al., 2008). Whilst this approach is successful, it is inherently inefficient. It also requires a respiratory signal from which to obtain this respiratory position. This signal is often inaccurate (in the case of respiratory bellows) and can interfere with the imaging sequence (in the case of respiratory navigators).

Both respiratory and cardiac motion must be accounted for when imaging the heart. Prospective triggering and retrospective gating are common approaches for producing cardiac images throughout the cardiac cycle (Scott et al., 2009).

However, new techniques are attempting to incorporate motion directly into the reconstruction scheme. This strategy acknowledges the fact that useful information can be obtained from the body in all motion states. One strategy is to reduce the amount of acquired data by incorporating prior knowledge into the reconstruction. This would provide higher image frame rates, so that motion could be observed in real time. Promising early work in this area (Prieto et al.,

2010),(Xu et al.) has shown that DCE-MRI is can be accelerated by exploiting redundancies in the data.

Work from Atkinson et. al. (White et al., 2009), (Melbourne et al., 2007), (Hamy et al., 2012) has focused on how to robustly combine cine images of the liver during a DCE-MRI examination. By applying novel techniques from applied mathematics, they have shown greatly improved contrast enhancement curves.

A potential source of error for these emerging techniques that could affect image quality and MR quantification accuracy has so far been ignored. As discussed in section 3.2.6.2, the spatial distribution of the transmit field is inherently tied to the underlying anatomy. Therefore it might expected that tissue motion could affect the transmit field. This would result in a temporally changing transmit field. This effect could perturb the state of the MR signal, leading to previously unconsidered artifacts and errors in imaging and quantification.

4.2 Study 1: Measurement and Correction of Transmit Field Inhomogeneity in the Liver due to Respiratory Motion

4.2.1 Introduction

A preliminary study was performed in order to investigate the effect of motion on the transmit field. There are several forms of tissue motion that affect MRI, such as irregular motion, respiratory motion and cardiac motion. Whilst all could potentially affect the transmit field, this work focuses on respiratory motion in the liver. This choice was made for several reasons.

Irregular motion refers the movement of a patient's position in the scanner, such as movements of the legs, arms and head due to discomfort. This type of motion would be expected to produce large field changes, especially in cases where the motion was close to the coil (such as movement of the head in a dedicated transmit head coil or movement of the arm in a birdcage coil). However, sporadic

motion is not amenable to investigation across a range of subjects because of the difficulties associated with getting different volunteers to perform the same motion.

The heart is an attractive target organ for investigation as it moves in a highly repeatable way. As noted in Scott et. al (Scott et al., 2009), cardiac motion (specifically that of the left ventricle) can be decomposed into three components about the heart's central axis – radial, longitudinal contraction and azimuthally rotation. The net displacements are small, typically below 1.5cm. The small amplitude of the displacements are likely to induce only small RF changes, and therefore cardiac motion was not selected for investigation.

Respiratory motion has many desirable properties that make it amenable for investigation. Firstly, unlike cardiac motion, the subject can control many aspects of their respiration, such as amplitude, pace, inhalation depth and breathing type (i.e. diaphragmatic or shallow). Secondly, the tissue displacements seen in respiration are relatively large. As presented in Davies et. al. (Davies et al., 1994), the average superior-inferior diaphragm displacement during deep breathing in a cohort of ten subjects was 43 ± 10 cm. The average respiration induced liver displacement was measured as 37 ± 8 cm. Furthermore, the expansion of the chest wall will likely alter the electromagnetic coupling to the transmit coil, also potentially changing the transmit field.

These considerations led to the choice of the liver as the target organ for transmit field difference measurements. The adopted measurement protocol to investigate the field changes is described below.

An additional study was performed to test whether parallel transmission can reduce any measured dynamic field changes. By applying amplitudes and phases which vary according to the current motion state to each transmit channel, temporally and spatially uniform excitations could in principle be achieved. A simulation was performed to test this, based on in-vivo transmit field maps. The adopted methods and results are described below.

4.2.2 Methods

4.2.2.1 *Small Cohort Study – Scan Protocol*

A scanning paradigm was constructed to test for transmit field changes by direct transmit field mapping at the extremes of the respiratory cycle (inhale and exhale), the two states between which the largest difference in transmit field would be expected.

Seven healthy volunteers were scanned, one of whom was scanned three times and one of whom was scanned twice. This resulted in ten examinations in total. All scanning was performed on 3T Achieva MRI systems (Philips Medical Systems, Best, The Netherlands). The system located in the Neonatal Unit of Queen Charlotte's Hospital (referred to as the NNU system) is equipped with a standard birdcage coil. The second scanner, located in the Robert Steiner Unit of Hammersmith Hospital (referred to as the RSU system) is equipped with a eight-channel parallel transmission body coil (Vernickel et al., 2007).

The modified AFI sequence was used (Yarnykh, 2007),(Nehrke, 2009) to measure the transmit field in a single transverse slice centred on the liver. The slice position was chosen based on scout images at both inhale and exhale in order to maximise the size of the liver in the slice. An axial slice orientation was chosen as the parallel transmission (PTx) body coil primarily has sensitivity variations in the axial plane. Therefore correcting the respiratory RF field changes in the axial plane would be suited to the coil.

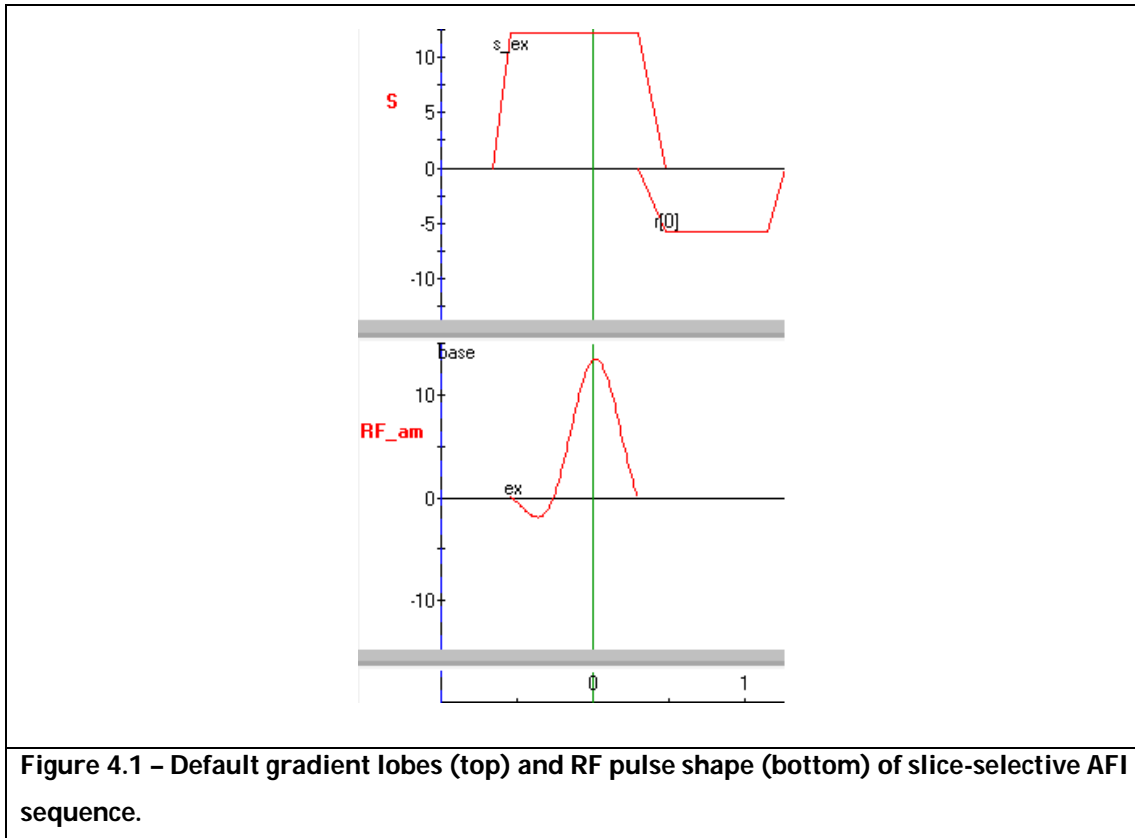
The two AFI TRs were selected as $TR_1 = 30\text{ms}$ and $TR_2 = 175\text{ms}$. This resulted in the TR ratio $n = TR_2/TR_1 = 5.8$, which lies in the range of 4-6 recommended in the source paper for favourable transmit field mapping dynamic range. A short echo time $TE = 4.6\text{ms}$ was chosen in order to increase SNR. The nominal flip angle was set at 60° .

Sequence parameters were selected to balance in-plane resolution and scan length. Two scans were tested: the first with resolution 7x7mm and 9s duration, the second with 14x14mm resolution and 4.5s duration. Both had a common FOV of 410x309mm (left-right (LR) x anterior-posterior (AP)), which was sufficiently large to image all subjects, and slice thickness of 7mm. The phase encode direction was set to AP in order to minimise scan time. A water-fat shift of two pixels was selected as a compromise between SNR and image corruption by misplaced fat signal.

Both variants provided sufficient SNR in acceptable scan times and were included in the analysis. The 7x7mm option was used on the majority of subjects (8 out of 10 datasets) in order to guarantee the field variations were adequately measured. The 14x14mm sequence was used in the remaining two datasets.

The system performs several calibration steps prior to data acquisition. These fix the centre frequency of the system, shim the \mathbf{B}_0 field to maximise \mathbf{B}_0 homogeneity, calibrate the RF power levels (see section 3.4.3.2.3) and calibrate the receive system. These were performed with the subject free-breathing.

The default slice-selective excitation of the scanner's AFI sequence was used. The bandwidth of the excitation pulse was designed to be insensitive to \mathbf{B}_0 inhomogeneity. This is important as the \mathbf{B}_0 is expected to change during respiration. Although no literature was found on \mathbf{B}_0 changes in the liver during respiration, measurements in the breast at 4T measured maximum respiratory changes of 70Hz (Bolan et al., 2004). The pulse bandwidth was maximised by selecting largest obtainable RF magnetic field magnitude, which was 13.5 μ T. This limit corresponds to the maximum current safely supported by the transmit coil. This led to a shortest pulse duration and hence broadest bandwidth. Figure 4.1 shows the pulse shape and slice selection gradient used for excitation. The bandwidth of the pulse can be approximated by the inverse of the time from its peak to the first zero crossing (which is here approximately 0.25ms) (Bernstein Matt et al., 2004). This corresponds to a bandwidth of 4kHz, which is much wider than the expected \mathbf{B}_0 variation due to respiration.



Each examination consisted of either $N_b = 5$ or $N_b = 10$ breathholds at both maximum inhale and exhale (i.e. a total of 10 or 20 scans). A single transit field map was acquired during each. Pauses were added between each individual acquisition for breathhold instruction and subject recovery.

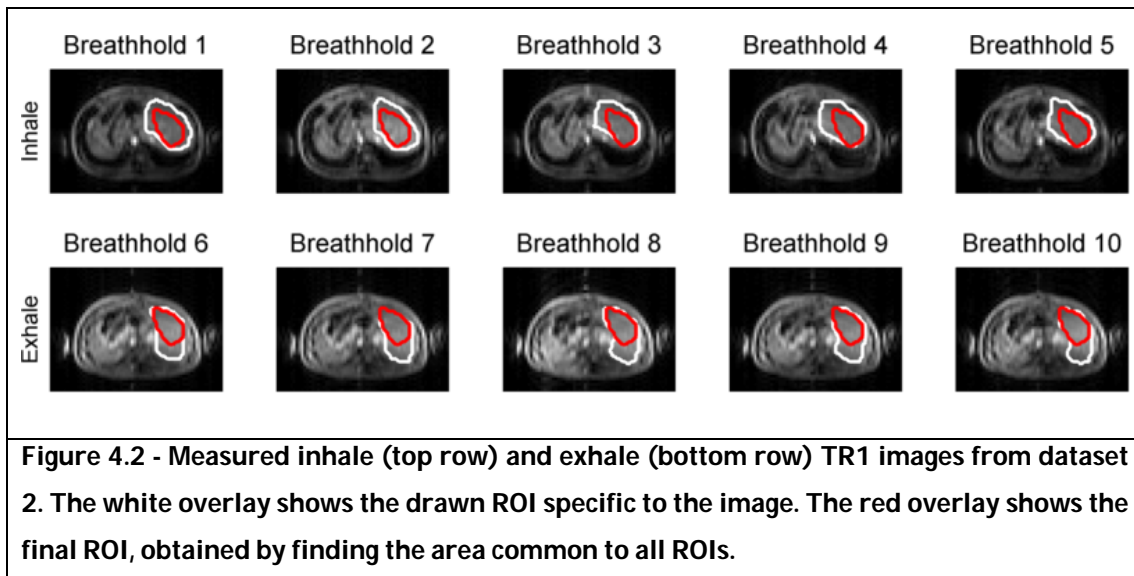
Preliminary tests with receive arrays were performed. The appropriate array, an eight-element cardiac coil, was strapped across the subject's torso. These tests found that the coil could restrict deep inhalations, so the birdcage (NNU) and PTx body coils (RSU, receiving in quadrature) were used for signal measurement. The resulting transmit field maps are not significantly corrupted by noise, despite the subsequent drop in SNR.

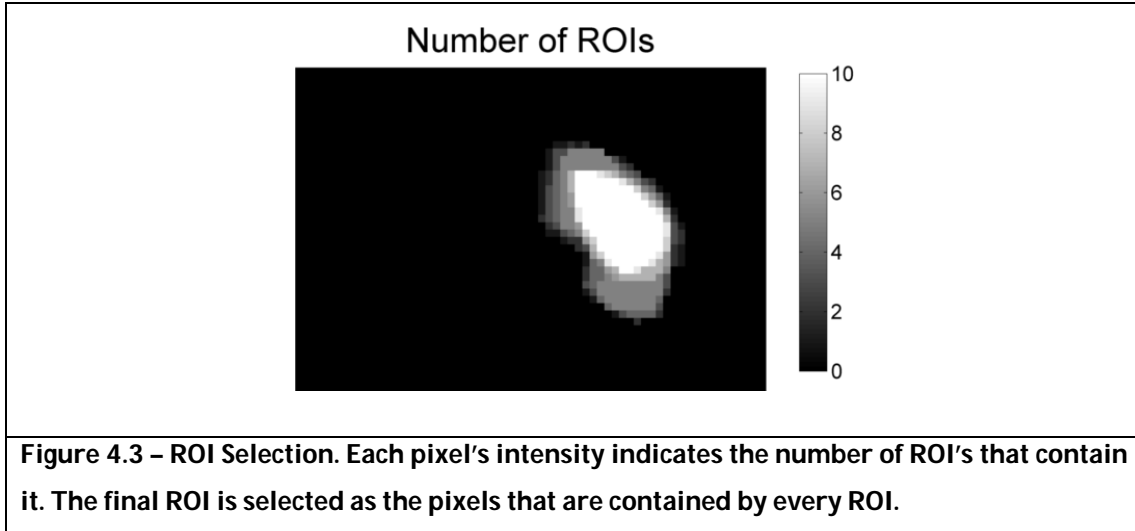
4.2.2.2 Small Cohort Study – Data Analysis

Measured data was exported from the scanner to be analysed in the MATLAB (The Mathworks, USA) scientific computing environment. The Fourier Transform (FT) of each k-space was taken to obtain both AFI images for each individual

breathhold. The magnitudes of the two AFI images were taken and were divided on a pixel-wise basis ($|I_2|/|I_1|$) and the flip angle map, $\theta_{n,b,r}$, was extracted by applying the AFI formula (equation 3.24) to the image ratio. Here, the subscripts n , b and r refer to the dataset number ($n=1-N$, N = number of datasets), breathhold number ($b=1-N_B$, N_B = number of breathholds) and respiratory state ($r = e$ or i , exhale or inhale).

A ROI analysis was performed on the acquired transmit field maps in order to test for differences between respiratory states. ROIs were manually drawn around the liver in all TR1 images of each subject. Care was taken to exclude any major blood vessels and the pulsatile flow artifact originating from the aorta. This process is shown in Figure 4.2 for a single subject. A final ROI of each dataset, ROI_n , was defined as the area common to all of the inhale and exhale ROIs. Figure 4.3 shows an overlay of all ROIs, with the final selected as the central overlapping region.





Differences between inhale and exhale respiratory states were assessed using several metrics. The first set of metrics assesses the global changes in the transmit field. This is achieved by first calculating the average flip angle inside the ROI across all breathholds, $\bar{\phi}_{n,r}$, as per equation 4.1. The error associated with this value is given by the standard deviation $\sigma_{\bar{\phi}_{n,r}}$, as per equation 4.2. The global difference between respiratory states, $\Delta\bar{\phi}_n$, can then be calculated using equation 4.3. The corresponding error, $\sigma_{\Delta\bar{\phi}_n}$, is calculated by combining errors in quadrature, as given by equation 4.4.

$$4.1 \quad \bar{\phi}_{n,r} = \frac{1}{N_B N_{ROI}} \sum_{x \in ROI} \sum_{b=1}^{N_B} \theta_{n,b,r}(x)$$

$$4.2 \quad \sigma_{\bar{\phi}_{n,r}} = \sqrt{\frac{1}{N_B N_{ROI}} \sum_{x \in ROI} \sum_{b=1}^{N_B} (\theta_{n,b,r}(x) - \bar{\phi}_{n,r})^2}$$

$$4.3 \quad \Delta\bar{\phi}_n = \bar{\phi}_{n,i} - \bar{\phi}_{n,e}$$

4.4

$$\sigma_{\Delta\phi_n} = \sqrt{\sigma_{\phi_{n,i}}^2 + \sigma_{\phi_{n,e}}^2}$$

The second set of metrics quantify the difference in the spatial distributions of the inhale and exhale transmit fields. The average inhale and exhale maps across all breathholds, $\bar{\theta}_{n,r}(x)$, are first calculated by equation 4.5.

4.5

$$\bar{\theta}_{n,r}(x) = \frac{1}{N_B} \sum_{b=1}^{N_B} \theta_{n,b,r}(x)$$

Equation 4.6 defines $\Delta\bar{\theta}_n(x)$, which gives the difference between the average inhale and exhale transmit fields, omitting the average global difference, $\Delta\bar{\phi}_n$.

4.6

$$\Delta\bar{\theta}_n(x) = [\bar{\theta}_{n,i}(x) - \bar{\theta}_{n,e}(x)] - \Delta\phi_n$$

The values of $\Delta\bar{\theta}_n(x)$ inside the ROI are then extracted. These are used to generate histograms and to calculate the interquartile range (IQR) of the distribution of differences. The IQR provides a measure of the range of local differences between the inhale and exhale states.

4.2.2.3 Individual RF Shim Study – Scan Protocol

An additional scan was performed in order to investigate the potential of RF shimming in improving transmit homogeneity across respiratory states. A single subject was scanned on the RSU system and performed two breathholds (an inhale and an exhale). During each, maps of each of the eight transmit elements were acquired with the low resolution 14x14mm resolution scan outlined above, with TR₁ and TR₂ reduced to 20ms and 117ms respectively, retaining the TR ratio of ~5.8. This parameter change allowed all coils to be mapped in 25s, an acceptable length for a breathhold for a healthy volunteer.

The transmit coils were mapped using linear combinations (see section 3.4.3.2.4) in order to improve the SNR of the obtained maps. The ‘inverted-phase’ LC (Brunner and Pruessmann, 2009) was used in this examination over the ‘all-but-one’ approach, as the condition number of the encoding matrix is lower. This leads to lower noise amplification.

4.2.2.4 Individual RF Shim Study – Data Analysis

The data was exported and processed to obtain transmit maps of each LC for each respiratory state. The phase of the n^{th} LC map was defined as the relative phase between the n^{th} and first LC map. Individual transmit maps of each channel were then obtained by inverting the LC encoding matrix at each voxel.

A ROI was drawn around the liver for both inhale and exhale states. An RF shim simulation was performed, in which the amplitude and relative phase of each channel were optimised to produce the most uniform field whose amplitude was the average of the inhale and exhale quadrature ROI averages. A Magnitude Least-Squares optimisation was employed to allow non-uniform phase across the ROI (see section 3.3.2.4.1, (Setsompop et al., 2008)). Regularisation on the total RF power was used at a range of regularisation levels between 10^{-9} and 10^2 . Both respiratory states were shimmed individually, and the drives and homogeneity were compared. The total drive power of each shim solution was calculated by applying equation 4.7, where P is the power, N_T is the transmit channel and d the drive to the channel.

$$4.7 \quad P = \sum_{t=1}^{N_T} d_t^* d_t$$

4.2.3 Results

4.2.3.1 Global Metrics

Figure 4.4 displays graphs of the average ROI flip angle of each breathhold of each dataset, $\phi_{n,b,r}$, with example inhale and exhale images. The error bars correspond to the standard deviation of the flip angle inside the ROIs, giving a measure on the level of inhomogeneity.

Strong repeatability is shown across breathholds for each subject. Dataset six shows two exceptions to this, where the first exhale and the sixth inhale display inconsistency relative to the other measurements. Visual inspection of the raw images revealed a motion artifact that propagated into the transmit maps.

The correlation between the magnitude of the respiratory motion and the flip angle difference in the ROI is not close. Datasets with the largest ROI differences (i.e. datasets 1, 3 and 6) show large respiratory changes in the raw images, but images with large respiratory changes (i.e. datasets 2, 7 and 8) do not necessarily show large ROI differences.

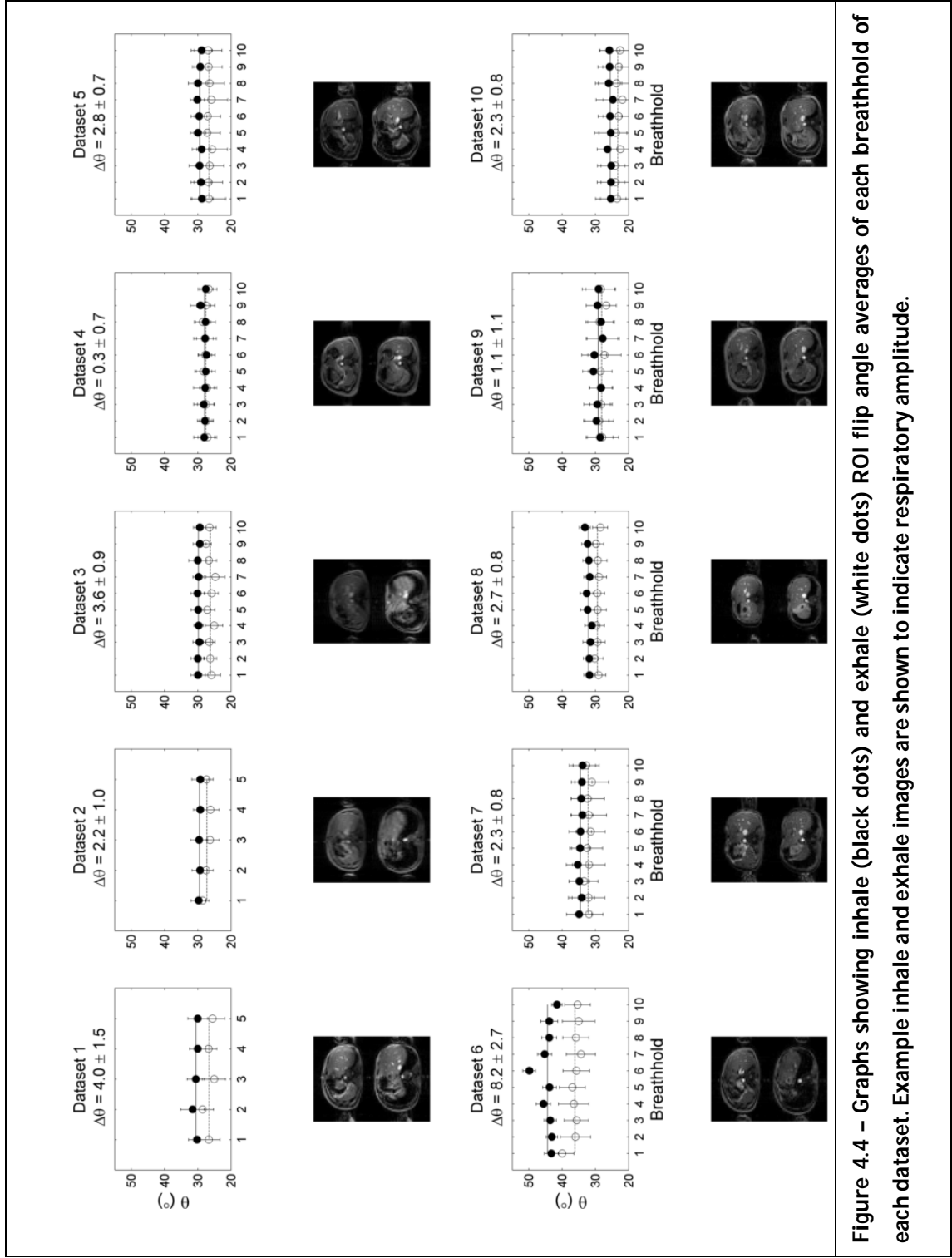
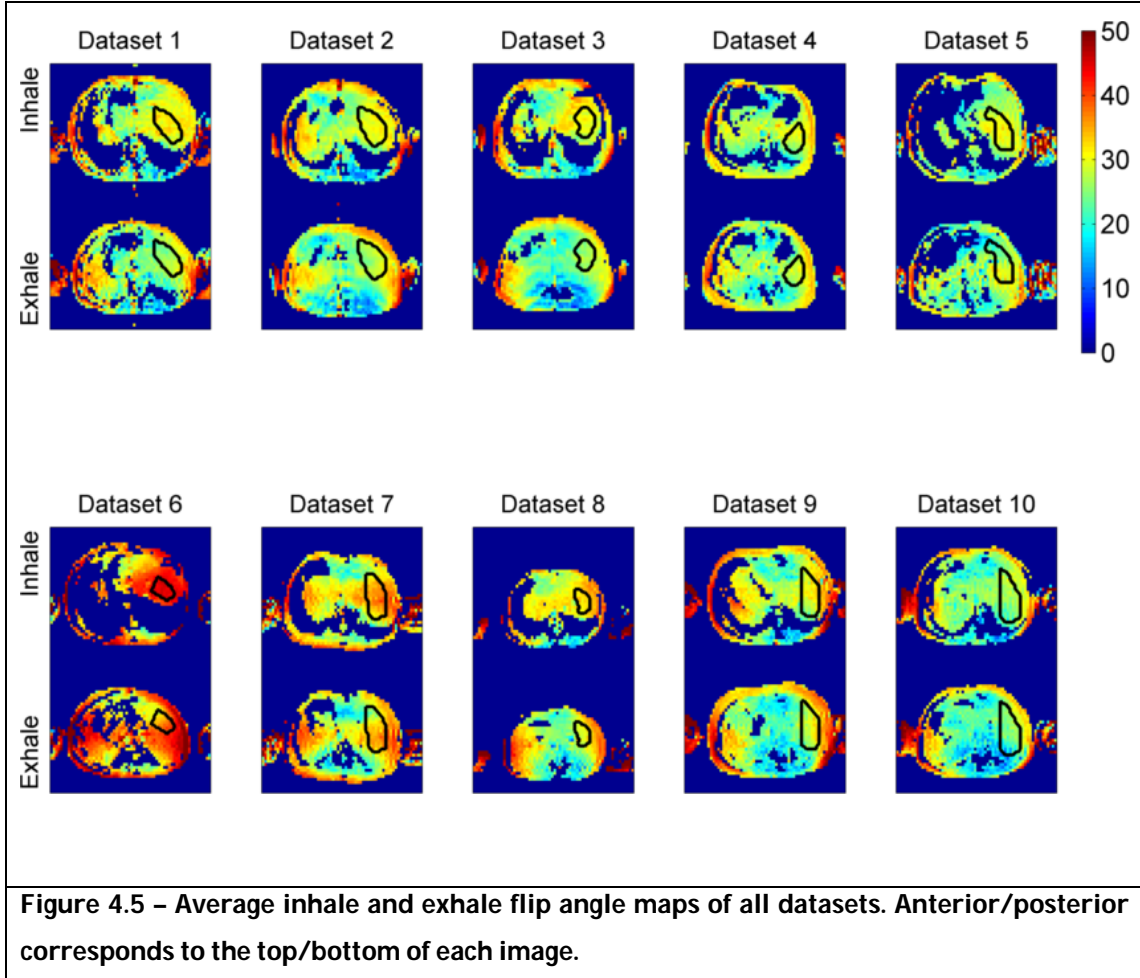


Figure 4.4 – Graphs showing inhale (black dots) and exhale (white dots) ROI flip angle averages of each breathhold of each dataset. Example inhale and exhale images are shown to indicate respiratory amplitude.

4.2.3.2 Local Metrics

Figure 4.5 shows example flip angle distributions from all ten datasets. Each image corresponds to $\bar{\theta}_{n,r}(x)$, the average over all breathholds at either inhale or exhale position. The final ROI is superimposed on each.



Transmit field inhomogeneity is present in all of the measured transmit maps. The shape of the inhomogeneity is subject dependent, but with common features across the cohort. Lower excitation is frequently exhibited at the posterior of each subject. This effect is most prominent in datasets 1, 2, 3, 4, 8, 9 and 10. Higher excitation is often seen at the subject's far left and right (i.e. datasets 2, 3, 7, 8, 9 and 10).

Differences in the transmit maps are also seen between breathing states. The bulk tissue motion due to respiration changes the signal support regions. The

inhale state often brings lungs into the imaging plane, leading to signal voids at the posterior of each subject's torso. Conversely, the inhale state can bring the gut into the imaging plane, leading to signal voids in the subject's anterior torso due to intestinal gas. The magnitude of these effects depends on the magnitude of the patient's respiratory motion and the position of the slice.

In addition to bulk tissue motion, changes in the transmit field are also observed. Although the ROI analysis focuses on the liver for quantitative assessment of this effect, changes are present across the FOV. However, the magnitude of this effect varies on a subject-by-subject basis, with dataset 4 displaying the least change between respiratory states.

The differences in the field are emphasised in Figure 4.6, in which $\bar{\theta}_{n,r}(x)$ and $\Delta\bar{\theta}_n(x)$ are shown in the ROI for all datasets. The spatially varying differences are clearly seen in difference maps.

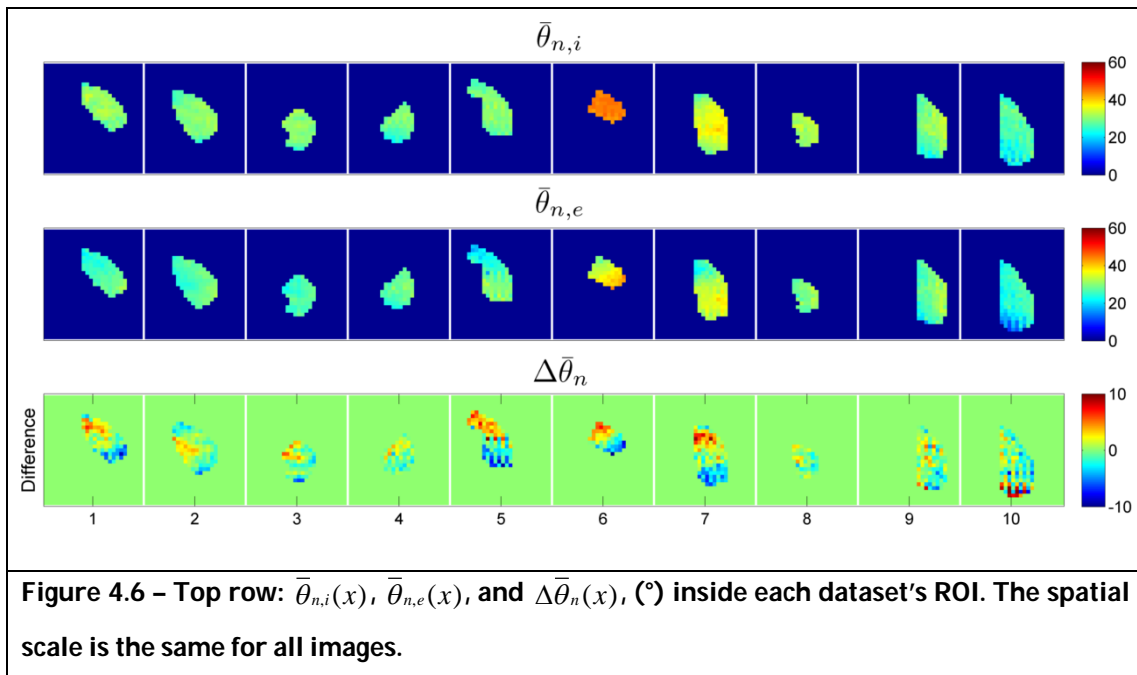
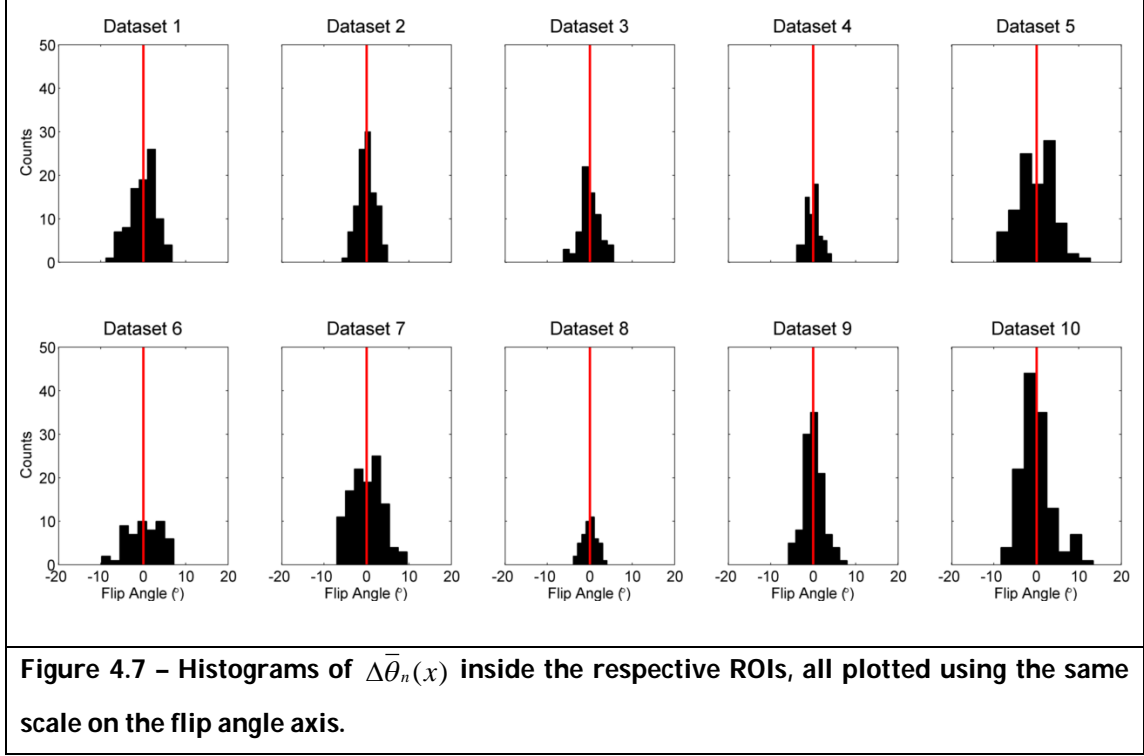


Figure 4.7 shows histograms of the values of $\Delta\bar{\theta}_n(x)$ inside the ROIs for each dataset. The total area of each histogram gives the number of pixels inside the ROI. All datasets exhibit a broad distribution of flip angle differences inside the

ROI. Wider distributions show cases where there are large local flip angle differences between inhale and exhale. The distributions are not Gaussian. Therefore the IQR is an appropriate metric for the width of the distributions.



4.2.3.3 Summary Statistics

Table 4.1 displays the summary results of the ROI analysis. The average size of the ROI across the subjects was 43.7cm², ranging from 23cm² to 63cm². This large variation is due to variation in the magnitude and particular type of physical change induced by respiration.

Columns 4 and 5 in Table 4.1 show the global inhale and exhale flip angle averages and errors, $\bar{\phi}_{n,i} \pm \sigma_{\bar{\phi}_{n,i}}$, inside the ROIs across the breathholds. The standard deviations are small, indicating consistency across breathholds.

The global flip angle differences and errors between respiratory states, $\Delta\phi_{n,i} \pm \sigma_{\Delta\phi_{n,i}}$, are shown in column 6. Significant changes in the global flip angles are seen between respiratory states for all datasets except 4 and 9. Column 7

displays the differences as a fraction of the average of inhale and exhale states. The largest fractional change occurred for dataset 6. The smallest change of 1% occurred for dataset 4.

Column 8 gives the IQR of the local flip angle differences, $\Delta\bar{\theta}_n(x)$. These numbers demonstrate that spatially varying differences in the flip angle occur between inhale and exhale states. Spatially varying changes can happen even when there is no global change, as in dataset 4.

Subject and scan number	Dataset	Size of ROI (cm ²)	$\bar{\phi}_{n,i} \pm \sigma_{\bar{\phi}_{n,i}} (^{\circ})$	$\bar{\phi}_{n,e} \pm \sigma_{\bar{\phi}_{n,e}} (^{\circ})$	$\Delta\phi_n \pm \sigma_{\Delta\phi_n} (^{\circ})$	$\frac{\Delta\phi_n}{\frac{1}{2}(\bar{\phi}_{n,i} + \bar{\phi}_{n,e})} (^{\circ})$	IQR ($^{\circ}$)
1,1	1	45	30.5 ± 0.7	26.6 ± 1.3	4.0 ± 1.5	14	3.9
1,2	2	54	29.5 ± 0.2	27.2 ± 1.0	2.2 ± 1.0	8	2.5
1,3	6	26	44.4 ± 2.2	36.2 ± 1.5	8.1 ± 2.7	21	6.3
2,1	3	34	29.8 ± 0.3	26.3 ± 0.9	3.6 ± 0.9	13	3.0
2,2	10	63	25.6 ± 0.5	23.2 ± 0.7	2.3 ± 0.8	10	3.8
3,1	4	32	28.0 ± 0.5	27.6 ± 0.5	0.3 ± 0.7	1	2.2
4,1	5	50	29.4 ± 0.5	26.6 ± 0.5	2.8 ± 0.7	10	6.1
5,1	7	56	34.5 ± 0.5	32.2 ± 0.7	2.3 ± 0.8	7	4.6
6,1	8	23	32.1 ± 0.6	29.4 ± 0.5	2.7 ± 0.8	9	2.6
7,1	9	54	29.2 ± 0.9	28.1 ± 0.7	1.1 ± 1.1	4	2.9

Table 4.1 – Summary results of ROI analysis.

4.2.3.4 RF Shimming Results

Figure 4.8 displays the amplitude and relative phase of the multi-channel transmit field maps for both inhale and exhale breathholds inside the ROI. Different transmit channels display unique spatial profiles in both amplitude and phase. The spatial profiles are different between respiratory states.

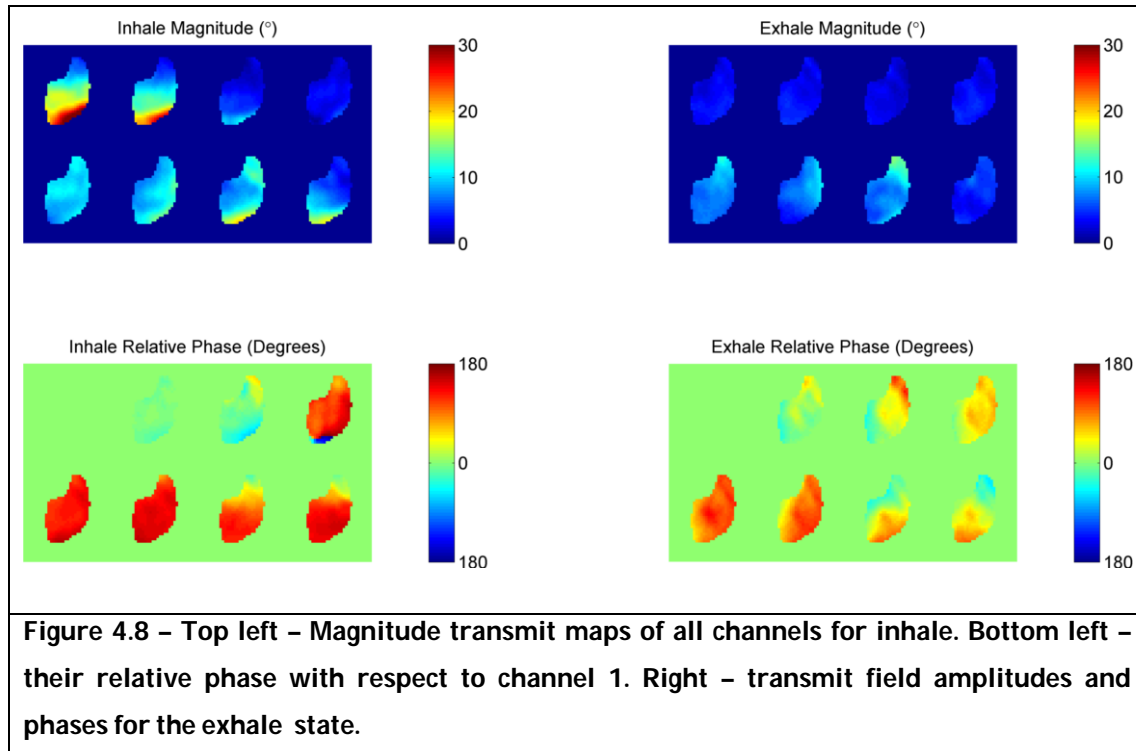


Figure 4.9 displays the total power of the drives calculated in the RF shim optimisation at each regularisation level. There are three solution regimes; no power control ($\lambda < 10^{-0.5}$), transitional power control ($10^{-0.5} < \lambda < 10^1$), and full power control ($\lambda > 10^1$). The inhale and exhale drive powers are different at low λ as the target uniform flip angle is the average of the two inhale and exhale ROI flip angle averages.

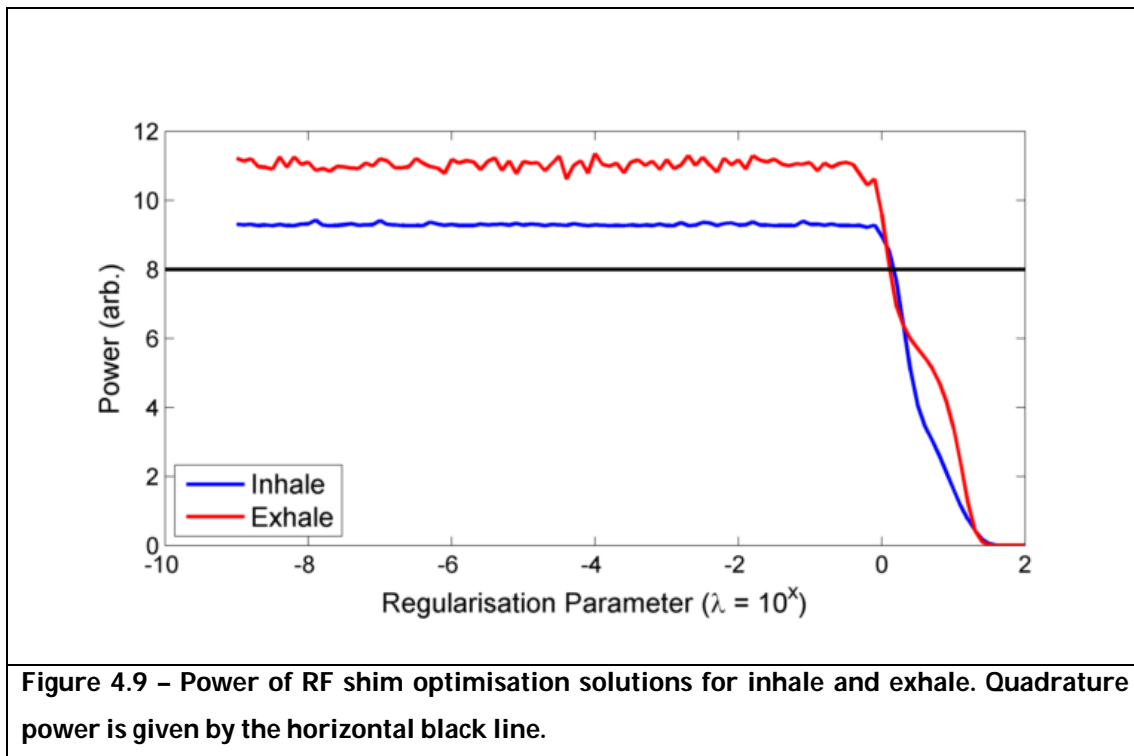


Figure 4.10 displays the RF unshimmed and several RF shimmed solutions. The left column shows the inhale and exhale ROI transmit maps when the coils are driven in quadrature. The exhale map is more uniform than the inhale map, with the difference showing local differences ranging from +5 to -5 degrees and a spatial gradient across the ROI.

Three shim solutions were selected based on their power. Both the high power ($P_{in}=9.3$, $P_{ex}=10.9$) and approximate quadrature power ($P_{in}=8.5$, $P_{ex}=8.1$) solutions achieve significant improvements in homogeneity of both respiratory states and reduce the spatial differences in the achieved excitation. There are small differences (of amplitude $<1^\circ$) between these solutions that are not visible in the figure. The results demonstrate that RF shimming could correct for the effect of respiration of the transmit field in this subject. Further reducing the power to approximately half that of quadrature ($P_{in}=4.1$, $P_{ex}=4.2$) introduces significant error into the excitations.

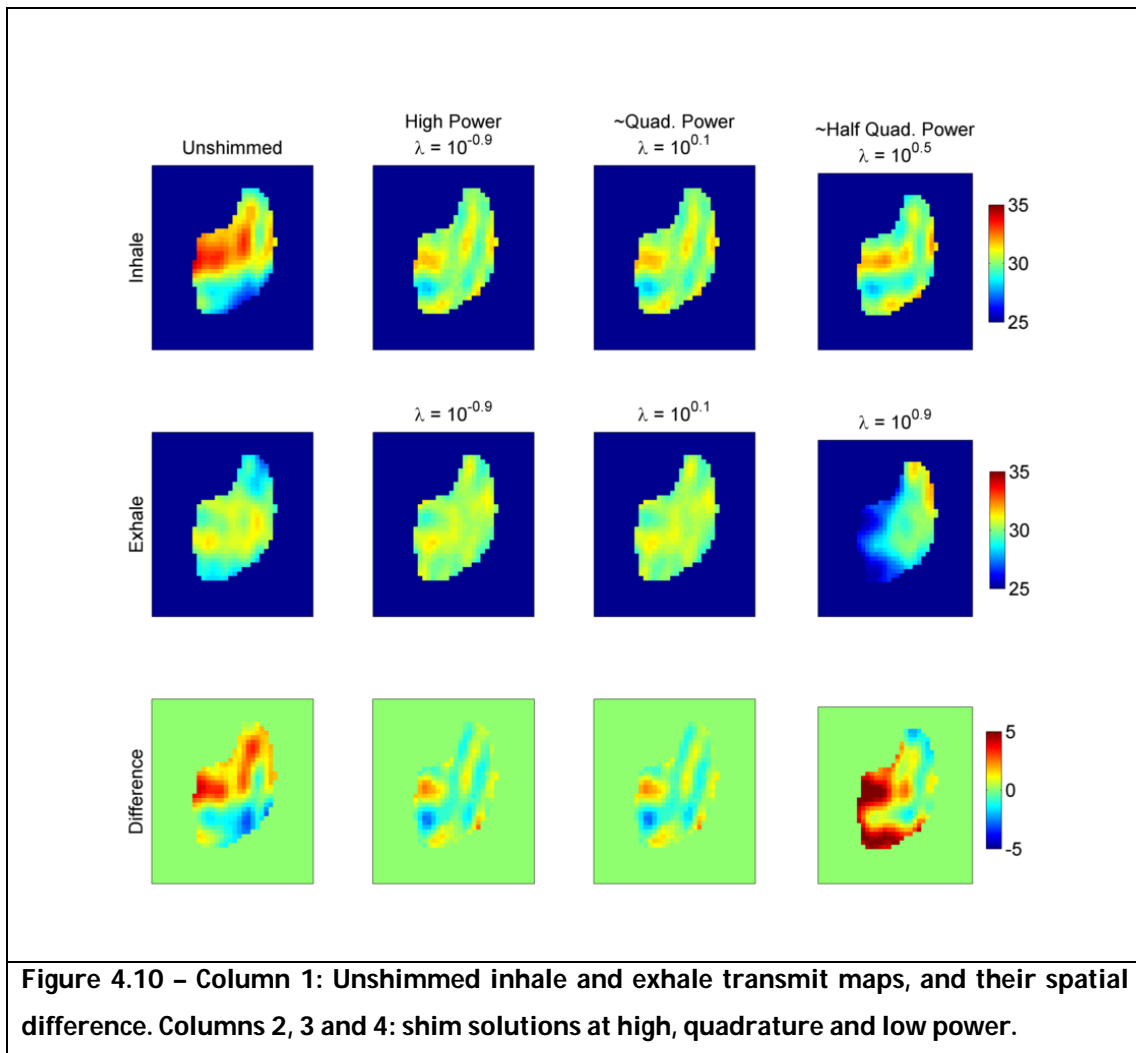


Figure 4.11 shows the nominal quadrature and shim-optimised drives to all eight transmit channels. Quadrature drives have a $2\pi/8$ relative phase difference and normalised scaling of unity. The RF shim solutions deviate from this solution in order to improve homogeneity, changing both the amplitude and phases. It is also evident that the shim solutions are different for the inhale and exhale states.

Increasing the level of power regularisation reduces the power. This is seen in this figure by the movement of the shim solutions inwards towards the origin. The strongest demonstration of this effect is by channel 2 and 3 in the exhale case.

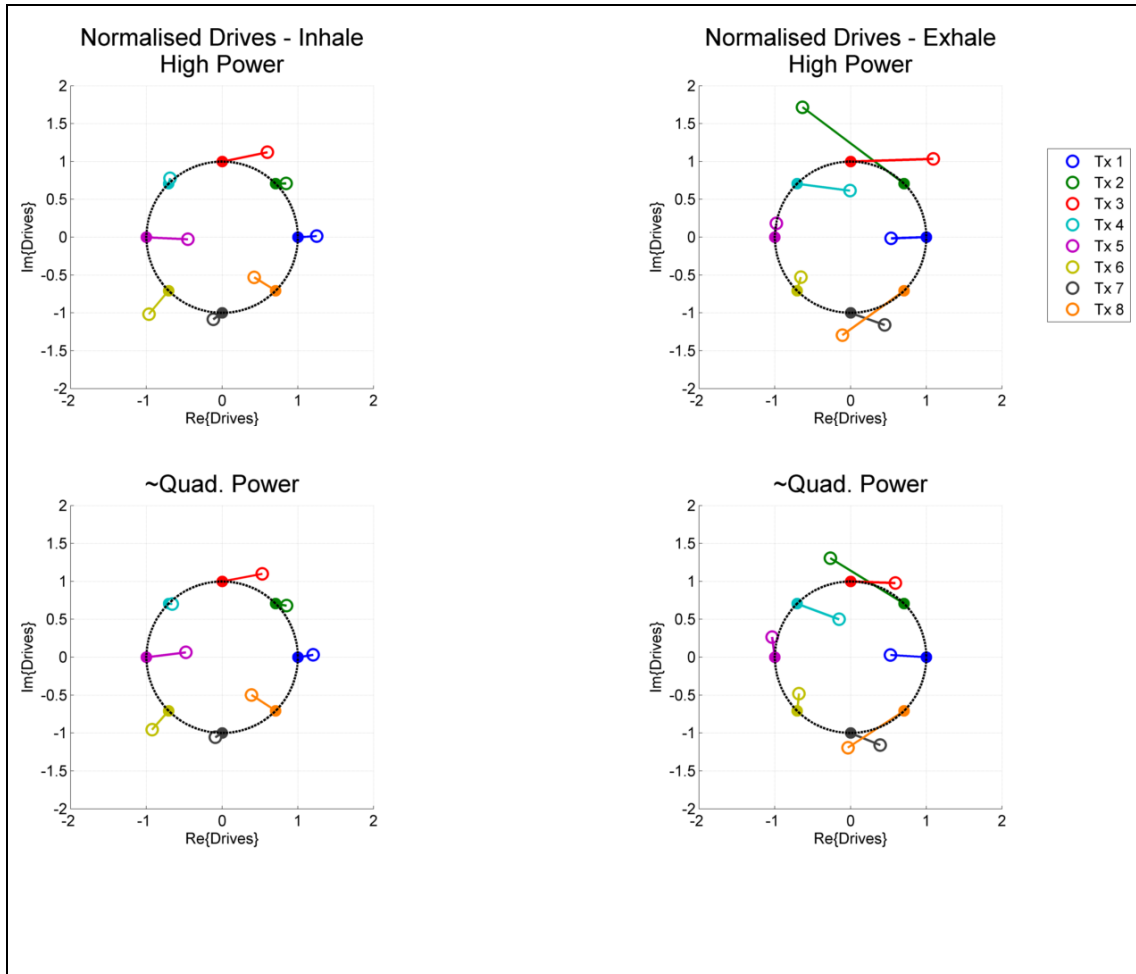


Figure 4.11 – Relative transmitter drives. Nominal quadrature is displayed by solid dots, with a 45° phase difference between channels and unit amplitude (black circle). The RF shim solutions are given by the hollow dots. Inhale and exhale results are shown on the left and right, respectively. The first and second rows give the high and approximately quadrature powered solutions, respectively.

4.2.4 Discussion

The results from this study demonstrate that changes in the transmit field do occur due to subject motion. The extent of this change is variable, ranging from no change (i.e. dataset 4) to a large change (i.e. dataset 6).

Both qualitative and quantitative comparisons between inhale and exhale maps were performed. The qualitative comparison showed that changes in the transmit field occurred across the anatomy. However, due to the changing composition of the slice from subject to subject, a quantitative ROI analysis could only be performed in the common organ, the liver. Consequently, changes in field

outside of the liver did not appear in the quantitative results. Despite this, the liver ROI analysis provided a systematic method of assessing the size of the changes.

The size of the field amplitude change did not always correlate with the visual change in the anatomy. Large changes in field did correlate with large changes in the shape of the subject. However, it is important to remember that the measurements are limited to a thin transverse slice. In reality, respiratory motion is a complicated three-dimensional process that displaces and deforms the entire torso. Therefore any attempts to correlate visual changes in the measured images to the measured change in field will always neglect the complex real change occurring. A 3D acquisition would be required in order to characterise the true change in fields and correlate the changes to movement of anatomy. At the time this research was conducted, transmit field mapping techniques were too slow to fit such a measurement into a breathhold, and thus a 2D acquisition was chosen. For example, a 3D AFI sequence with a FOV of 410x310mm in two PE directions and a resolution of 10x10mm with parameters $TR1/TR2 = 20/100\text{ms}$ would take three minutes.

Special care must be taken when performing slice-selective transmit field mapping. Slice-selective excitation pulses have imperfect slice profiles, leading to a flip angle distribution in the through-slice (z) direction. During the pulse sequence, each location in z exists in its own flip-angle specific steady-state. The measured signal is the integrated signal through the slice. However, the AFI signal equation assumes the signal at any pixel exists in a single steady state. This mismatch leads to systematic errors in the calculated flip angles. This effect (Wu et al., 2009) has been shown to reduce the measured flip angle. It was subsequently shown that this effect could be corrected for using Bloch simulations and look-up tables (Malik et al., 2011a).

The slice profile effect partially accounts for the systematically lower measured flip angles in-vivo as compared to the selected nominal flip angle of 60°. It was shown (Malik et al., 2011a) that the two-lobe sinc pulse used in these

experiments underestimates the flip angle to ~75% of the true value when imaging a phantom with the T_1 of liver ($T_1=812\text{ms}$ (Stanisz et al., 2005)). Therefore one would expect to measure flip angles of approximately 45° in this study. The remaining underestimation (flip angles of approximately 30° are obtained) is likely to originate from the nature of the power calibration performed by the system. The calibration sequence scales the power in order to achieve the desired flip angle throughout the volume of interest. This includes the arms and rest of the abdomen. Higher flip angles are measured in the arms, as partially indicated in Figure 4.5, which will balance the lower flip angles seen in the ROIs in the liver.

It is important to note that these considerations do not invalidate the work performed here, as this study is investigating *changes* in the field, and not the absolute magnitude of the field.

This study also demonstrates that RF shimming could correct for transmit variation in the liver due to respiratory motion. By optimising the drives to each channel, a clear reduction in the spatial difference between two respiratory states was shown. This solution could be attained at the same power level as transmitting in quadrature.

Whilst it was possible to correct transmit field changes at the extremes of the breathing cycle, the mapping strategy employed in this study does not provide information on the transmit field between these states. In order to correct for changes in the transmit field due to respiration using parallel transmission or by any other method, a transmit field mapping method is needed which can spatially and temporally measure the transmit field. A method to achieve this is proposed and tested in the next study.

4.3 Study 2: Respiratory-Resolved Transmit Field Measurements

4.3.1 Introduction

The previous study demonstrated how the shape of the transmit field is a function of respiratory status of the subject under examination. This effect was measured by mapping the transmit field in the liver when subjects were holding their breath at maximum inhale and exhale positions. A retrospective RF shim simulation showed how optimising the drives of each element of a parallel transmission body coil could eliminate this effect.

The results of Study 1 have two significant implications. Firstly, if the maximum inhale and exhale fields are different, it follows that a transition between the states must occur at intermediate respiratory positions. The previous study provided no insights into the nature of the transmit field during this transition. Many possibilities exist, as shown in Figure 4.12. This figure shows the hypothetical amplitude of the transmit field in a voxel throughout the respiratory cycle. The different curves represent different possible transition types, such as a linear transition (red curve), a sharp transition (green curve), or a general transition (blue curve). The actual in-vivo transition will be determined by the specific interaction between the fields generated by the RF coil and the composition and motion of the subject.

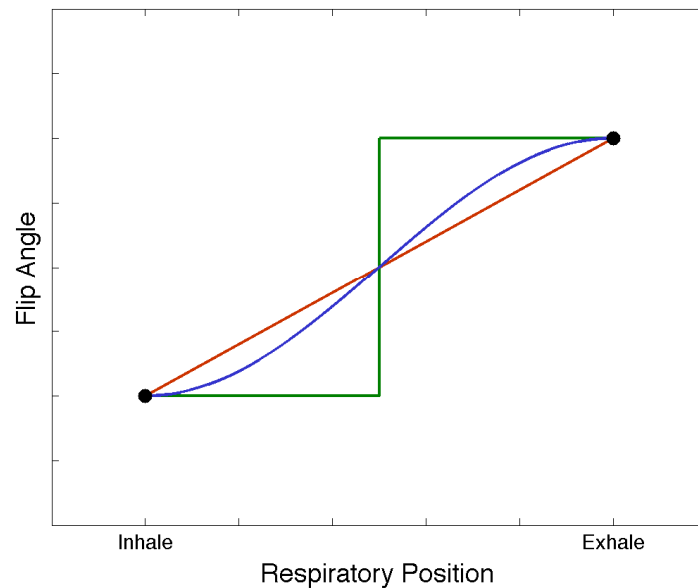


Figure 4.12 – Possible transmit field transitions between inhale and exhale respiratory states.

Study 1 also implies the following: as the maximal respiratory states can be successfully RF shimmed, one might expect the intermediate states to also be amenable to RF shimming. This would require transmit maps for each channel throughout the respiratory cycle.

Determination of the dynamic respiratory-induced variations of the transmit field requires a MR method of obtaining transmit field information throughout the respiratory cycle. Until very recently (Nehrke and Börnert, 2012), no transmit field mapping techniques were sufficiently fast to enable real-time measurements. Therefore alternative approaches were considered.

A simple way of measuring multi-phase respiratory field information is by extending the breathhold methodology of Study 1. This would involve the subject holding their breath at many different respiratory positions, with a transmit map acquisition at each location. This approach is limited by the variable nature of respiratory motion. The physical positions at the extremes of the respiratory cycle are consistently reproducible, since the subject is either at full lung

expansion or contraction. However, at intermediate positions, it is difficult for volunteers to control the balance between diaphragmatic and chest breathing. Therefore inconsistent results would be expected.

An alternative approach would be to use electromagnetic simulations to determine how the fields change in time. This approach would provide insight into the full temporal field dynamics, but only for a single body model. This approach could not be used in actual in-vivo scenarios. Furthermore, this method would require a body model that can adopt multiple realistic respiratory positions. Although models have been developed which have freely moving limbs (Wang et al., 2008), this has not been extended to altering respiratory states.

Since using breathholding and FDTD simulations are not feasible, the method developed in this section attempts to reconstruct dynamic transmit field maps in an alternative way. The basis of the method used here, retrospective gating, is used widely in cardiac imaging, as described below.

It is clinically useful to have the ability to observe pulsatile motion of the heart. In order to achieve this, images throughout the cardiac cycle are required. Fast MRI techniques have been developed to achieve this in real-time (Nayak et al., 2004),(Usman et al., 2011), but these methods require compromises on contrast and SNR. The alternatives, prospective and retrospective gating (PG and RG), fill each k-space over multiple cardiac cycles. Both monitor the electrocardiogram (ECG) trace, which gives an accurate measure of the instantaneous cardiac phase.

A PG MRI acquisition waits for the ECG trace to detect an R-wave, which triggers the acquisition of data. This is repeated over the course of several cardiac cycles. The data is then sorted according to the cardiac phase it was acquired in, filling each temporal k-space location, allowing temporally-resolved images to be formed.

RG does not use the ECG trace to trigger data acquisition. Instead, the trace and MR data is recorded continuously. Each PE position in k-space is typically

recorded for a certain fraction ($\sim 20\%$) longer than the expected cardiac cycle in order to ensure that all of required data is acquired.

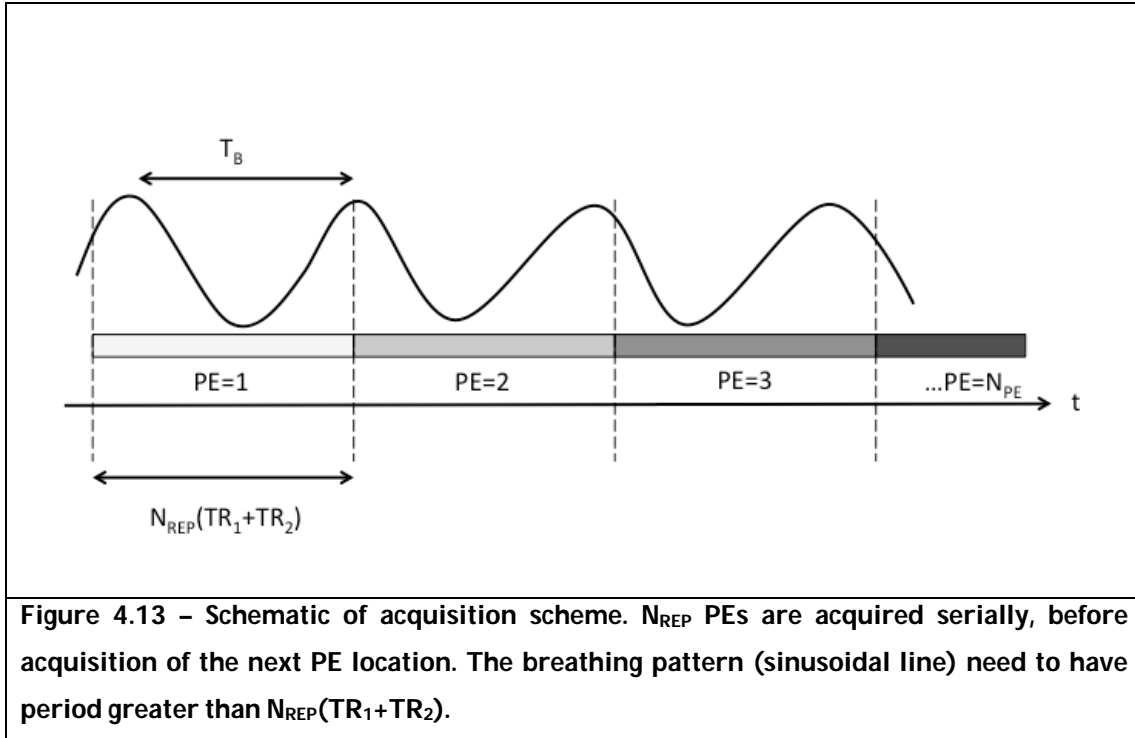
4.3.2 Methods

The use of retrospective gating for transmit field mapping is described in this section. The proposed method is composed of two parts. The first component of the method (section 4.3.2.1) concerns the specific implementation of the AFI sequence for use with RG. This details how the AFI sequence was adapted to run continuously whilst the volunteer breathed under the guidance of an audio track to ensure consistency. This allowed data to be acquired across the full range of respiratory states.

The second component of the proposed method (section 4.3.2.2) describes how the acquired data is reconstructed to visualise dynamic changes in the transmit field. This details how measured k-space data was binned according to its respiratory phase, averaged, and then processed for transmit field map extraction.

4.3.2.1 Scan Paradigm

The adopted scan strategy is outlined in Figure 4.14. The 2D AFI sequence was again utilised due to its speed. The respiratory pattern of the patient under examination is represented by the oscillatory trace. This pattern is characterised by period T_B . Data is acquired concurrently with the patient's breathing, as illustrated with the solid bars below the respiratory trace. Each block lasts for $N_{REP}(TR_1 + TR_2)$, where N_{REP} denotes the number of repeated PE samples in each block.

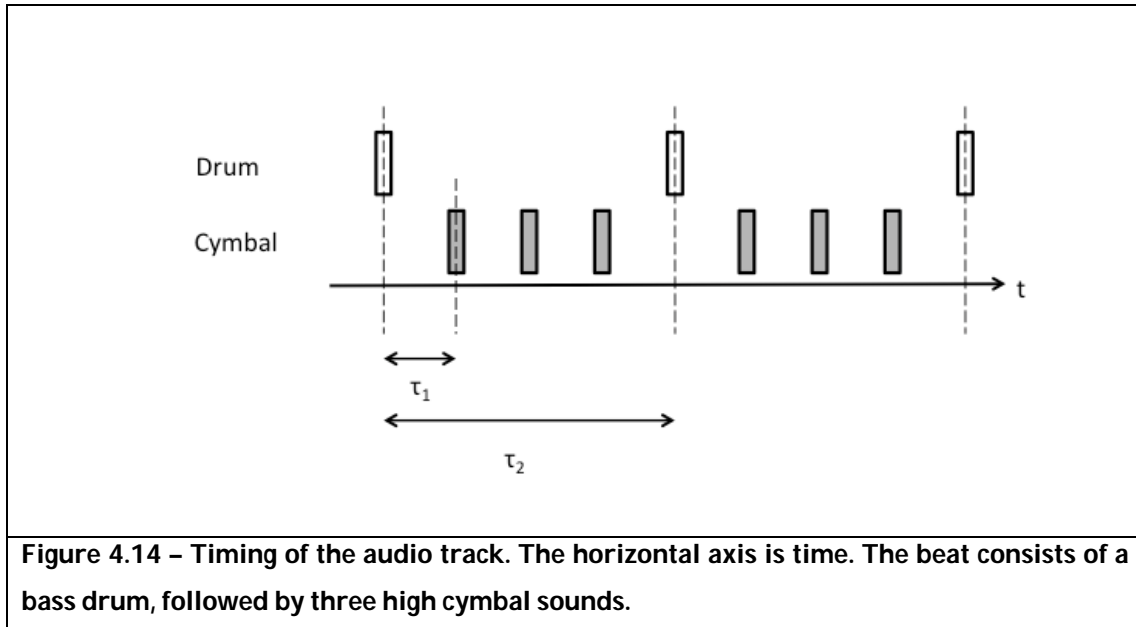


Two requirements must be fulfilled for successful respiratory gating reconstructions. First, each PE acquisition block must acquire PEs at a rate sufficient to characterise the respiratory motion. Secondly, the length of each PE block must be greater than half the respiratory period (i.e. $N_{\text{REP}}(TR_1+TR_2) > T_B/2$), to ensure that there is a PE measurement at all respiratory positions.

The most stringent limitation is the breathing period of the subject, T_B . This has to be chosen so that the subject can breathe at the same rate over an extended period of time comfortably. Preliminary experiments revealed that the default mode of free breathing in several volunteers has a degree of irregularity in both amplitude and frequency. If left uncontrolled, this could potentially cause certain positions in k-space to not contain samples across all respiratory states. Therefore a method was developed to promote regular breathing.

An audio track was played to the volunteers in order to encourage regular breathing at the correct frequency. The track was created using proprietary software (Apple GarageBand). It contains two sounds played at regular intervals, as in Figure 4.14. Pilot experiments showed that $T_B = 5.6\text{s}$ was a comfortable breathing period. This was replicated in the software using a bass drum sound

followed by three cymbal sounds, all separated by time $\tau_1=0.7s$. This is then repeated for the duration of the scan. The subject was instructed to time their breathing so that they reached either maximum inhale and exhale at the sound of the drum.



The second requirement is limited by MRI system software. The maximum N_{REP} is 32. Using standard AFI TR lengths ($TR_1/TR_2=30/175ms$), $N_{REP}(TR_1+TR_2)=6.6s$, well above the breathing cycle limit. N_{REP} could be reduced to 14 and still satisfy $N_{REP}(TR_1+TR_2)>T_B/2$. However N_{REP} was set at 32 as this provided more data for the reconstruction process, at the expense of longer scan time (4.14m).

Several volunteers were scanned. Each was placed in the scanner wearing sound-insulating headphones through which sound could be played to the subject. A respiratory bellows was also strapped to their chest wall at the level of the diaphragm, which recorded the breathing pattern throughout the acquisition.

The following sequence parameters were used: transverse slice orientation, resolution=7x7mm, slice thickness=7mm, FOV=450x309mm (RLxAP), #PEs=44 (AP direction), $\theta=60^\circ$, $TR_1/TR_2=30/175ms$, TE=4.6ms, Number of Signal Averages (NSA)=32, SMART Averaging= OFF.

4.3.2.2 Reconstruction

The raw k-space data was exported from the scanner for reconstruction. The physiological log file was also exported. This contains the output of the respiratory bellows sampled every 2ms, in addition to labels which mark when each pair of PE lines (corresponding to TR_1 and TR_2) were acquired. An example of the contents of the physiological log file is shown in Figure 4.15.

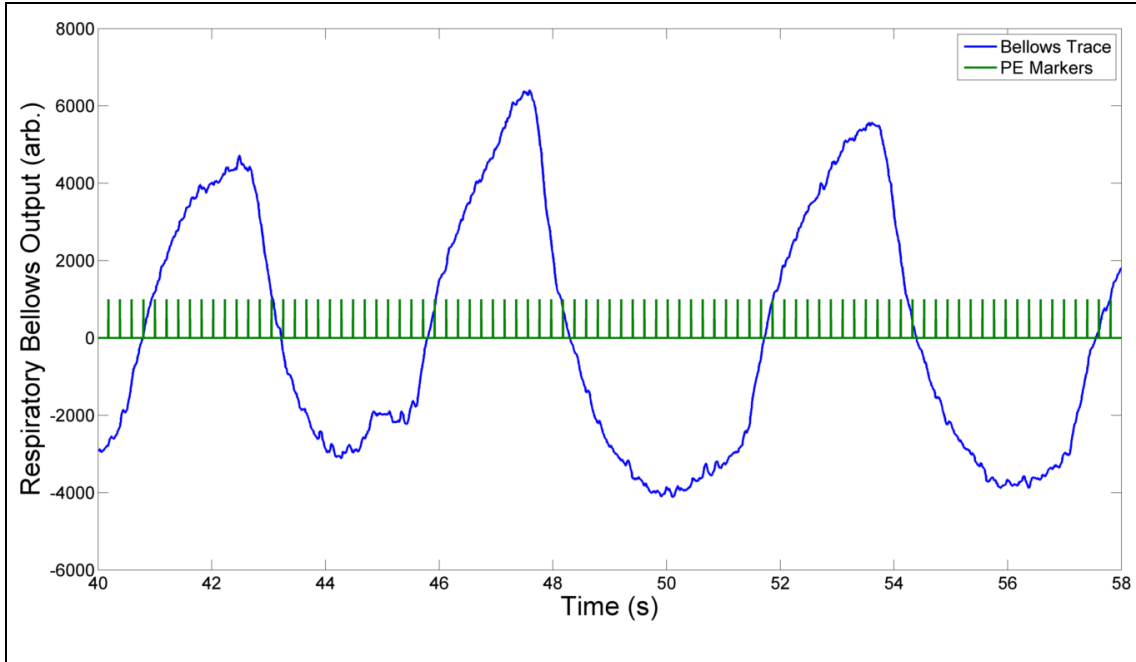


Figure 4.15 – Example respiratory bellows output (blue), and the corresponding PE acquisition markers.

The physiological data was then processed so that each PE pair was assigned the respiratory bellows amplitude at its time of acquisition. The pairs were then binned according to their respiratory trace amplitude. This was achieved by first extracting the maximum and minimum respiratory values, R_{\max} and R_{\min} . Bin boundaries were defined by segmenting the respiratory range $R_{\max}-R_{\min}$ into N_b bins. Each PE pair was then placed into the appropriate bin.

Data in the same respiratory bin and at the same k-space location were averaged, and then Fourier Transformed to the image domain. The two AFI images were then processed to obtain a transmit field map for each respiratory bin. This process was repeated for 1 to 6 bins.

4.3.3 Results

4.3.3.1 *Bellows traces and binning*

Figure 4.16 shows example respiratory patterns of six volunteers for a 200s period during the scan. There is significant variability between the traces. The first volunteer misunderstood the given instructions and breathed at twice the desired frequency. However, the breathing was consistent during the course of the scan. Volunteer 2 initially breathed at a consistent rate, but with variable amplitude and with short periodic anomalies (i.e. 180s, 260s). Furthermore, their breathing became more irregular towards the end of the acquisition (not shown). Volunteers 3 and 5 showed consistent frequency and amplitude breathing. However, the traces from volunteers 4 and 6 show poor consistency across the period.

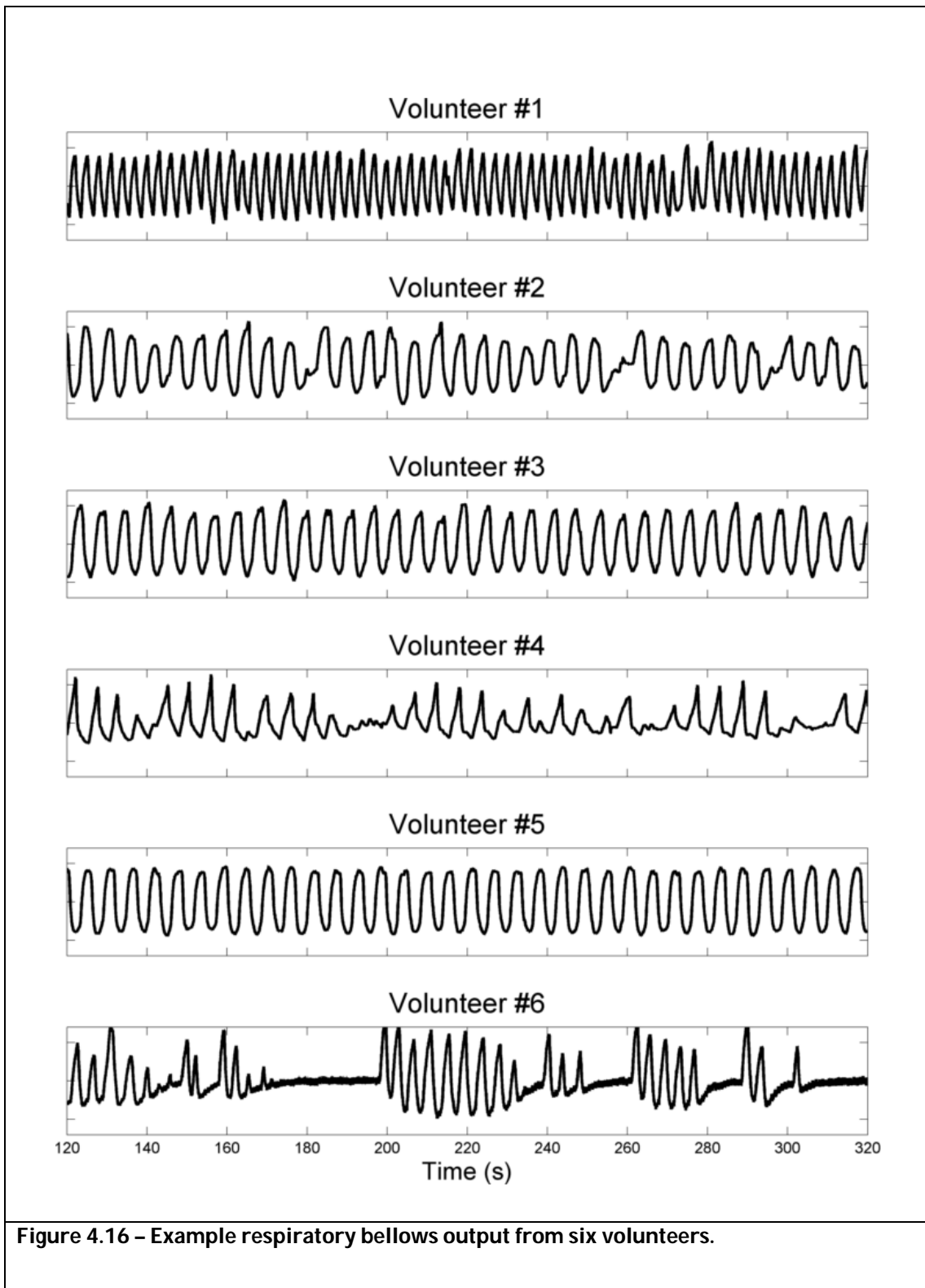


Figure 4.16 – Example respiratory bellows output from six volunteers.

Figure 4.17 shows the number of PEs in each bin for all volunteers and N_b . In the case of a single bin, all k-space positions have 32 PEs inside them. Increasing the number of bins to two generates two possible situations. Firstly, an approximate

50% split into each bin can be achieved, as for volunteers 1, 3 and 5. This is a consequence of their consistent respiratory traces. Volunteer two also achieved an approximately equal split, but late-acquisition irregular breathing manifests itself by perturbed PE distributions. For example second respiratory bin is empty at k-space location 11 and 12. The irregular breathing of volunteers 4 and 6 results in very unequal bin distributions. The first bin has the majority of entries, with large gaps existing in the second bins.

The difference between regular and irregular breathing becomes more apparent for larger N_b . Volunteer 1 has the most equally distributed PE lines. Volunteers 3 and 5 again show consistency across PE positions, but at the expense of an unequal bin distribution. The centre bin, corresponding to the transition between inhale and exhale has far fewer entries. This is because the respiratory transition is very fast. Despite this, these three volunteers have very few empty PE locations for $N_b < 6$. At $N_b = 6$, more empty PE locations begin to emerge. In contrast, the binning procedure fails for the remaining volunteers for $N_b > 2$. Several empty PE locations exist.

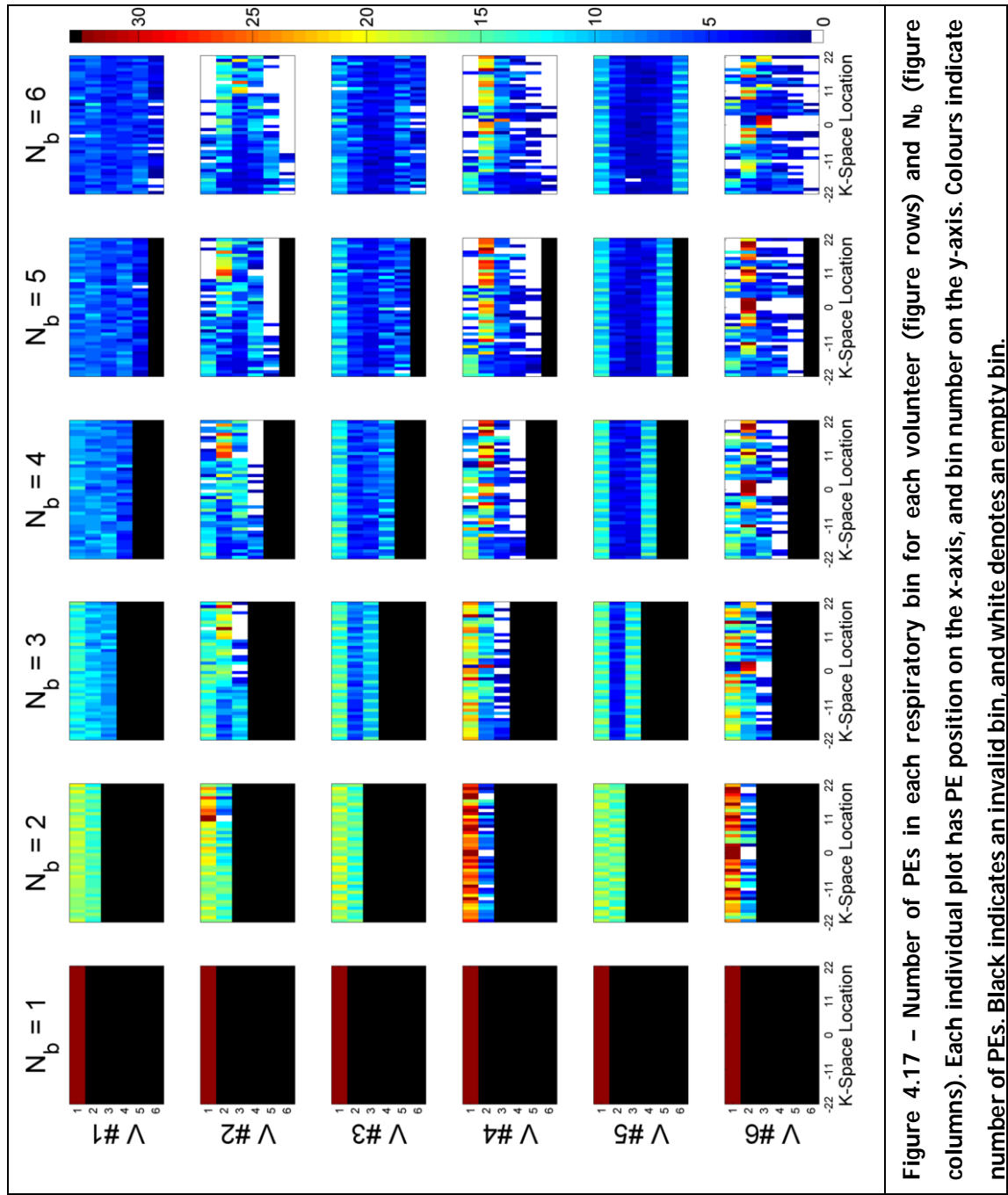


Figure 4.17 – Number of PEs in each respiratory bin for each volunteer (figure rows) and N_b (figure columns). Each individual plot has PE position on the x-axis, and bin number on the y-axis. Colours indicate number of PEs. Black indicates an invalid bin, and white denotes an empty bin.

4.3.3.2 *Reconstructed Images and Field Maps*

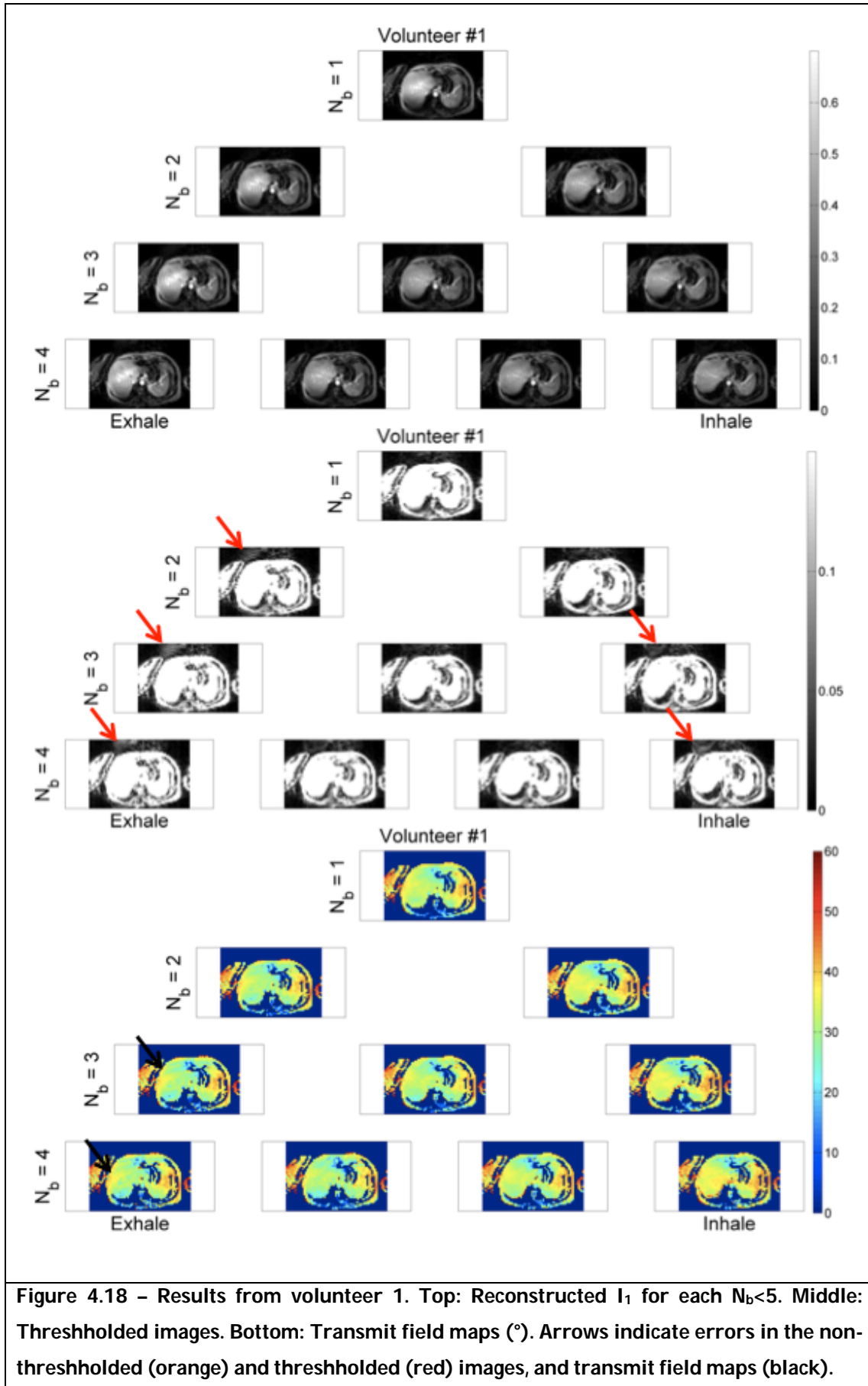
Figure 4.18Figure 4.21 display the results from four volunteers (V1, V3, V5 & V6) in order to display typical results seen across the volunteer cohort. Each figure contains the reconstructed images from the first TR period (top), the same images, thresholded to 15% of the maximum image pixel intensity (middle), and the reconstructed transmit field maps (bottom). Volunteers 1, 3 and 5 have respiratory traces that are consistent. Volunteer 6 has a low-consistency respiratory trace.

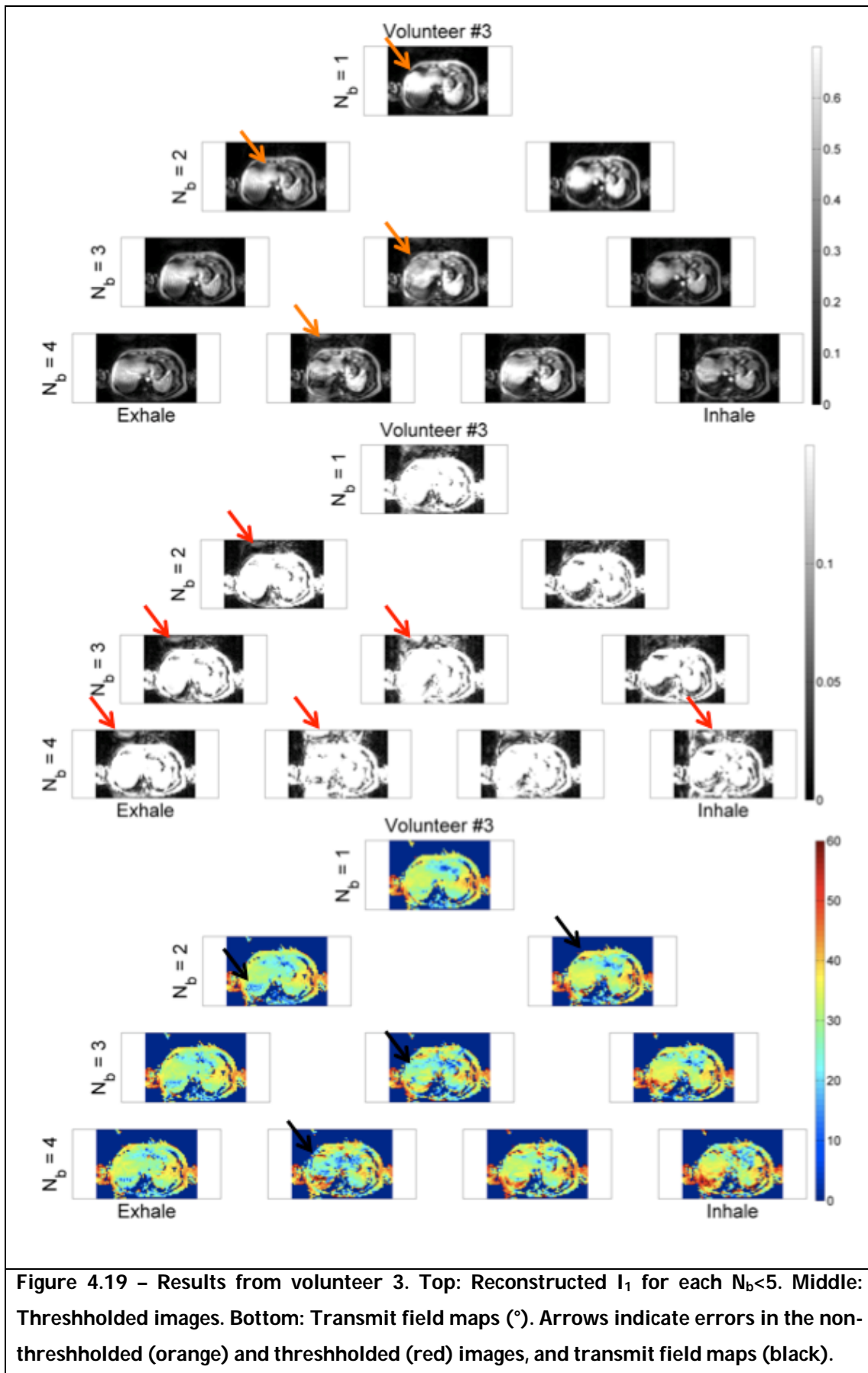
Three types of behaviour are observed: consistent respiratory traces with un-artifacted images; consistent respiratory traces with artifacted images; and inconsistent respiratory traces with un-artifacted images.

The first behaviour is only seen in V1. The non-thresholded images do not display overt artifacts. The thresholded images do reveal low-level artifacts (some of which are highlighted by red arrows). The reconstructed transmit field maps are generally visually uncorrupted, but unphysical (i.e. non-smooth) fields are seen in some images across the liver (some examples indicated by black arrows).

Volunteers 3 and 5 showed consistent respiratory cycles, but the image and field reconstructions displayed artifacts. The non-thresholded images of V3 contained visible artifacts (examples given by orange arrows), and thresholding revealed further lower-level artifacts (red arrows). This higher artifact level compared to V1 resulted in transmit field maps which contained stronger artifacts (black arrows). Similar behaviour is seen for V5.

Volunteer 6 displays an example of an unrecoverable reconstruction. The images are fundamentally undermined by the irregularity of the breathing. Large errors appear in the non-thresholded and thresholded images and the transmit field maps.





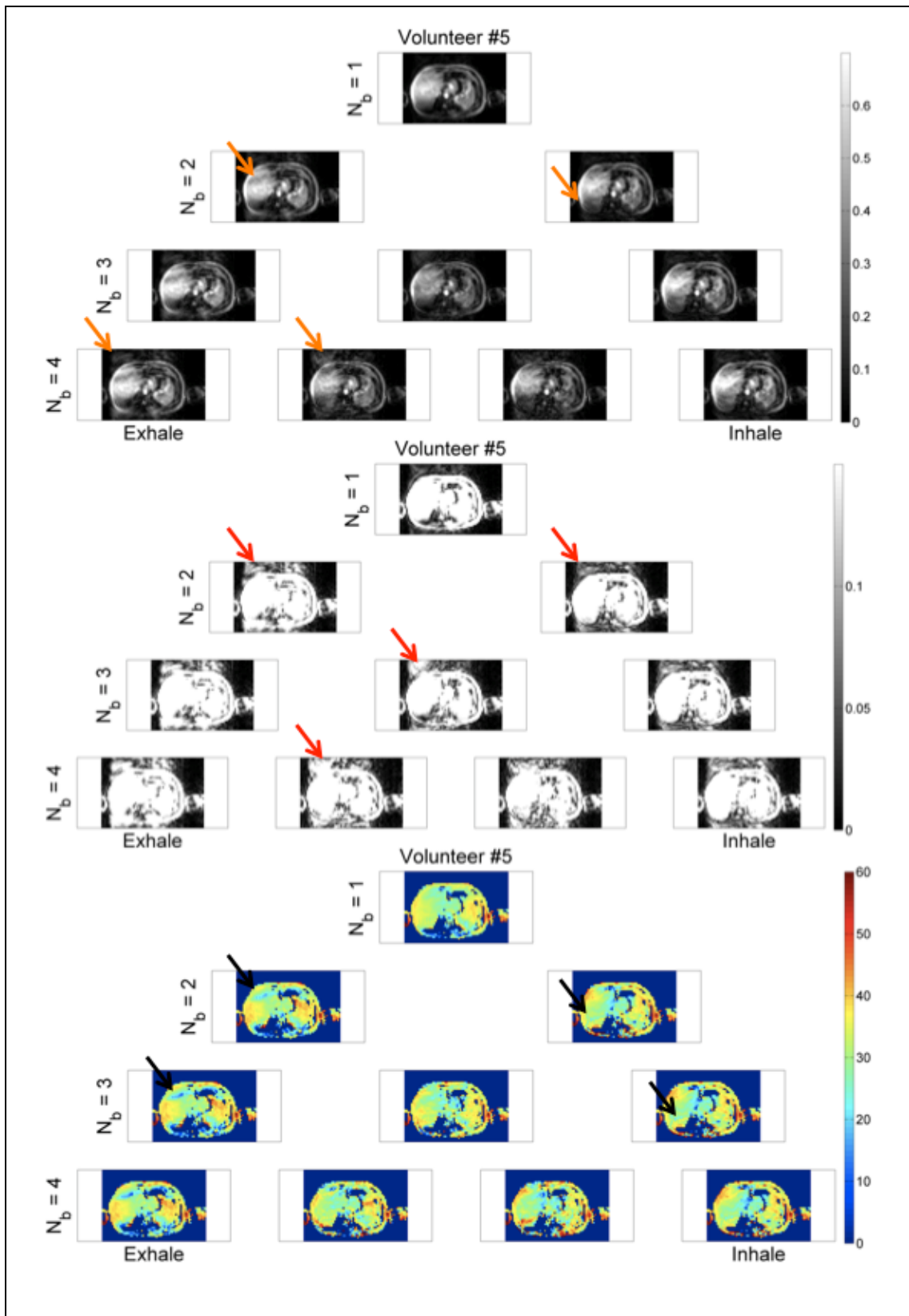


Figure 4.20 – Results from volunteer 5. Top: Reconstructed I_1 for each $N_b < 5$. Middle: Thresholded images. Bottom: Transmit field maps (°). Arrows indicate errors in the non-thresholded (orange) and thresholded (red) images, and transmit field maps (black).

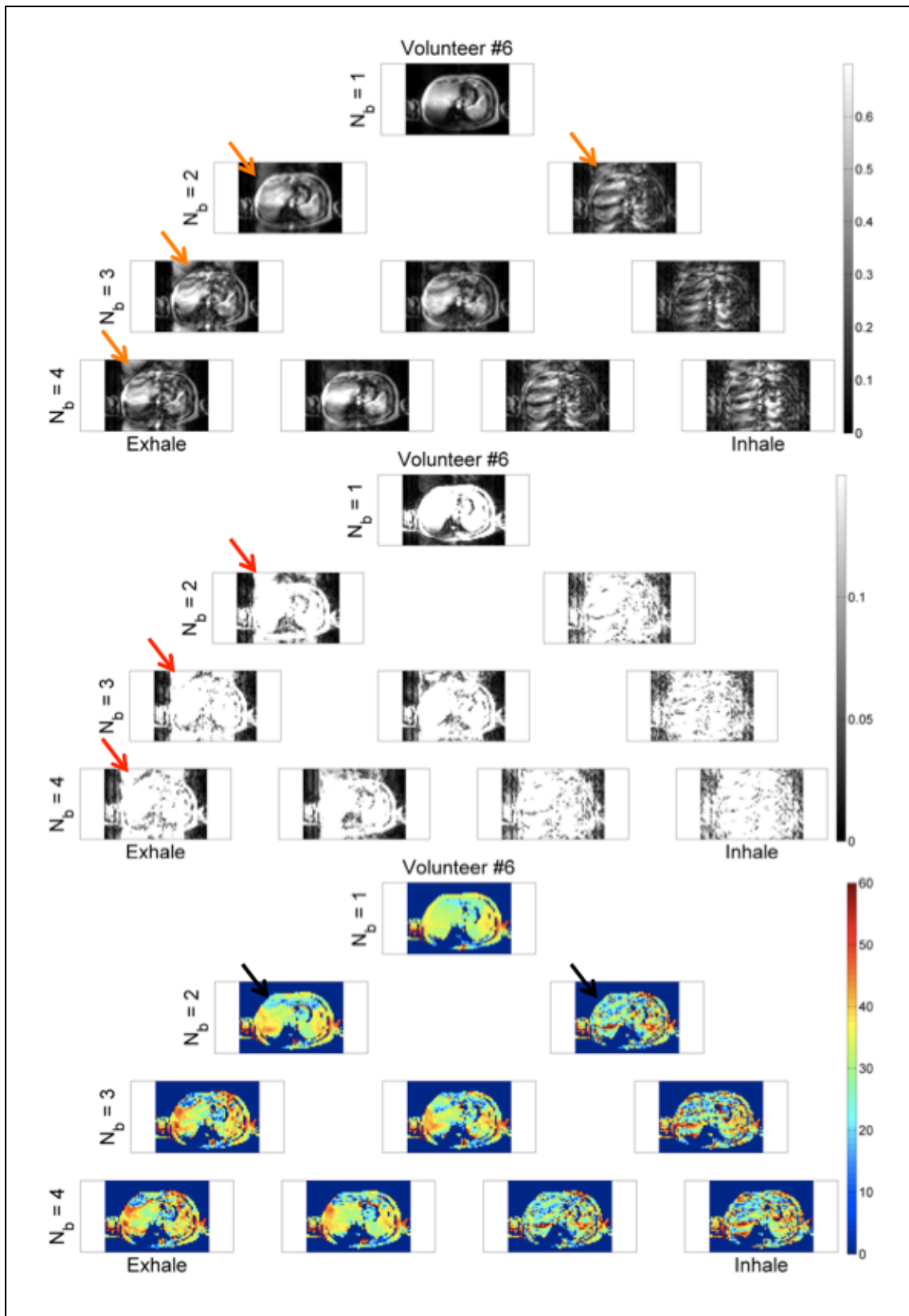


Figure 4.21 – Results from volunteer 6. Top: Reconstructed I_1 for each $N_b < 5$. Middle: Thresholded images. Bottom: Transmit field maps ($^{\circ}$). Arrows indicate errors in the non-thresholded (orange) and thresholded (red) images, and transmit field maps (black).

4.3.4 Discussion

This study investigated the use of retrospective gating to reconstruct respiratory resolved transmit field maps.

Several issues with this methodology became apparent during the investigation. The first limitation was the variable ability to breathe as required by the sequence. Although volunteers reported the ability to breathe at the correct frequency, they all experienced discomfort due to the need to focus of breathing for an extended period, and from the consequent increased blood oxygenation. Many reported feeling slightly light-headed towards the end of the scan. This effect could be reduced by further shortening scan length, but this would in turn reduce the amount of data in each bin, possibly leading to more holes in k-space.

A more significant issue with the proposed technique is the artifacted nature of the images used to calculate the transmit field. All show some level of artifact. These errors propagate through to transmit field maps, undermining their utility for field measurement. Substantial artifacts even appeared for volunteers who had reliable respiratory traces. Having fewer numbers of bins reduced the artifacts, but this comes at a high price. Wider bins reduced aliasing by averaging incoherent artifacts, but this in turn means that the transmit field is an average of a larger fraction of the respiration cycle. There is an inherent trade-off between resolving field changes and artifact level.

Further work was performed with the goal of minimising artifacts using an adaptive RG technique. This approach trialled several candidate PE measurements at each k-space location, and selected the line that improved the image according to two criteria: image entropy (Atkinson, 2006) (a surrogate measure for image quality) and total signal outside of a predefined mask of the object. Although improved artifact minimisation was achieved (Padormo et al., 2009), this research area was abandoned for the reasons described below.

The artifacts potentially originate from multiple sources. Although the steady-state nature of the sequence is robust to changes in the amplitude of the field

(Malik et al., 2011b), a more pronounced effect is likely to be the movement of tissue perpendicular to the slice. As liver tissue moves out of plane, previously excited regions become unaffected by the excitation pulse, and begin relaxing towards equilibrium. As they return into the imaging plane, the magnetisation begins to return to the steady-state (Scheffler, 1999), which takes approximately T_1 seconds ($T_1 = 812\text{ms}$ in the liver, (Stanisz et al., 2005)). This data will still be acquired despite having these undesirable (non-steady-state) signal amplitudes. This will cause image artifacts.

Altering the acquisitions geometry could reduce these effects. Respiratory motion is primarily in the FH (liver) and AP (chest wall) directions, therefore favouring a sagittal acquisition. Despite this potential modification, the proposed method was abandoned. The demand on the volunteer of mapping a single transmit field is too high. Extending this to a parallel transmission system for total field homogeneity correction is not feasible.

An alternative mapping sequence, DREAM (Nehrke and Börnert, 2012), has been presented in the literature since this work was performed. A study of abdominal field changes (Nehrke and Börnert, 2012) using this technique revealed respiratory field amplitude changes of up to 20° . Field changes were also measured in the lung due to inflation at 1.5T and 3T (Wild et al., 2011). No variation was seen at 1.5T, and a small variation of 5% was seen at 3T.

There is still a significant need for faster transmit field mapping, both for standard scanner calibration, and for more advanced needs such as for monitoring field dynamics. Therefore alternative approaches were considered, as presented in the following chapters.

4.4 References

- Atkinson, D. (2006). Incoherent artefact correction using PPI. *NMR in Biomedicine* 19, 362–367.
- Azlan, C.A., Di Giovanni, P., Ahearn, T.S., Semple, S.I.K., Gilbert, F.J., and Redpath, T.W. (2010). B1 transmission-field inhomogeneity and enhancement ratio errors in dynamic contrast-enhanced MRI (DCE-MRI) of the breast at 3T. *Journal of Magnetic Resonance Imaging* 31, 234–239.
- Bernstein, M.A., King, K.F., and Zhou, X.J. (2004). *Handbook of MRI pulse sequences* (Elsevier).
- Bolan, P.J., Henry, P.-G., Baker, E.H., Meisamy, S., and Garwood, M. (2004). Measurement and correction of respiration-induced B0 variations in breast 1H MRS at 4 Tesla. *Magnetic Resonance in Medicine* 52, 1239–1245.
- Brunner, D.O., and Pruessmann, K.P. (2009). B1+ interferometry for the calibration of RF transmitter arrays. *Magnetic Resonance in Medicine* 61, 1480–1488.
- Davies, S.C., Hill, A.L., Holmes, R.B., Halliwell, M., and Jackson, P.C. (1994). Ultrasound Quantitation of Respiratory Organ Motion in the Upper Abdomen. *Br J Radiol* 67, 1096–1102.
- Deoni, S.C.L. (2007). High-resolution T1 mapping of the brain at 3T with driven equilibrium single pulse observation of T1 with high-speed incorporation of RF field inhomogeneities (DESPOT1-HIFI). *Journal of Magnetic Resonance Imaging* 26, 1106–1111.
- Greenman, R.L., Shirosky, J.E., Mulkern, R.V., and Rofsky, N.M. (2003). Double inversion black-blood fast spin-echo imaging of the human heart: A comparison between 1.5T and 3.0T. *Journal of Magnetic Resonance Imaging* 17, 648–655.
- Haase, A. (1990). Snapshot flash mri. applications to t1, t2, and chemical-shift imaging. *Magnetic Resonance in Medicine* 13, 77–89.
- Hamy, V., Melbourne, A., Tremoulheac, B., Punwani, S., and Atkinson, D. (2012). Registration of DCE-MRI using Robust Data Decomposition. In *Proceedings 20th Scientific Meeting, International Society for Magnetic Resonance in Medicine, Melbourne*.

Hurley, A.C., Al-Radaideh, A., Bai, L., Aickelin, U., Coxon, R., Glover, P., and Gowland, P.A. (2010). Tailored RF pulse for magnetization inversion at ultrahigh field. *Magnetic Resonance in Medicine* 63, 51–58.

Kim, D., Cernicanu, A., and Axel, L. (2005). B0 and B1-insensitive uniform T1-weighting for quantitative, first-pass myocardial perfusion magnetic resonance imaging. *Magnetic Resonance in Medicine* 54, 1423–1429.

Kim, D., Oesingmann, N., and McGorty, K. (2009). Hybrid adiabatic-rectangular pulse train for effective saturation of magnetization within the whole heart at 3 T. *Magnetic Resonance in Medicine* 62, 1368–1378.

Kwee, T.C., Takahara, T., Koh, D., Nievelstein, R.A.J., and Luijten, P.R. (2008). Comparison and reproducibility of ADC measurements in breathhold, respiratory triggered, and free-breathing diffusion-weighted MR imaging of the liver. *Journal of Magnetic Resonance Imaging* 28, 1141–1148.

Malik, S.J., Kenny, G.D., and Hajnal, J.V. (2011a). Slice profile correction for transmit sensitivity mapping using actual flip angle imaging. *Magnetic Resonance in Medicine* 65, 1393–1399.

Malik, S.J., Padormo, F., and Hajnal, J.V. (2011b). Steady-State B1 Mapping of Dynamically Changing RF Fields. In *Proceedings 19th Scientific Meeting, International Society for Magnetic Resonance in Medicine, Montreal*, p. 645.

Melbourne, A., Atkinson, D., White, M.J., Collins, D., Leach, M., and Hawkes, D. (2007). Registration of dynamic contrast-enhanced MRI using a progressive principal component registration (PPCR). *Physics in Medicine and Biology* 52, 5147–5156.

Nayak, K.S., Cunningham, C.H., Santos, J.M., and Pauly, J.M. (2004). Real-time cardiac MRI at 3 tesla. *Magnetic Resonance in Medicine* 51, 655–660.

Nehrke, K. (2009). On the steady-state properties of actual flip angle imaging (AFI). *Magnetic Resonance in Medicine* 61, 84–92.

Nehrke, K., and Börnert, P. (2012). Free-Breathing Abdominal B1 Mapping at 3T Using the DREAM Approach. In *Proceedings 20th Scientific Meeting, International Society for Magnetic Resonance in Medicine, Melbourne*, p. 3356.

Nehrke, K., and Börnert, P. DREAM—a novel approach for robust, ultrafast, multislice B1 mapping. *Magnetic Resonance in Medicine*.

Nezafat, R., Stuber, M., Ouwerkerk, R., Gharib, A.M., Desai, M.Y., and Pettigrew, R.I. (2006). B1-insensitive T2 preparation for improved coronary magnetic resonance angiography at 3 T. *Magnetic Resonance in Medicine* 55, 858–864.

Padormo, F., Larkman, D.J., and Hajnal, J.V. (2009). Reducing artefacts in respiratory resolved MRI field measurements. In *Proceedings of the ESMRMB 2009*, p. 529.

Prieto, C., Uribe, S., Razavi, R., Atkinson, D., and Schaeffter, T. (2010). 3D undersampled golden-radial phase encoding for DCE-MRA using inherently regularized iterative SENSE. *Magnetic Resonance in Medicine* 64, 514–526.

Roberts, C., Little, R., Watson, Y., Zhao, S., Buckley, D.L., and Parker, G.J.M. (2011). The effect of blood inflow and B1-field inhomogeneity on measurement of the arterial input function in axial 3D spoiled gradient echo dynamic contrast-enhanced MRI. *Magnetic Resonance in Medicine* 65, 108–119.

Saekho, S., Boada, F.E., Noll, D.C., and Stenger, V.A. (2005). Small tip angle three-dimensional tailored radiofrequency slab-select pulse for reduced B1 inhomogeneity at 3 T. *Magnetic Resonance in Medicine* 53, 479–484.

Scheffler, K. (1999). A pictorial description of steady-states in rapid magnetic resonance imaging. *Concepts in Magnetic Resonance* 11, 291–304.

Scott, A.D., Keegan, J., and Firmin, D.N. (2009). Motion in Cardiovascular MR Imaging. *Radiology* 250, 331–351.

Setsompop, K., Wald, L.L., Alagappan, V., Gagoski, B.A., and Adalsteinsson, E. (2008). Magnitude least squares optimization for parallel radio frequency excitation design demonstrated at 7 Tesla with eight channels. *Magnetic Resonance in Medicine* 59, 908–915.

Stanisz, G.J., Odobina, E.E., Pun, J., Escaravage, M., Graham, S.J., Bronskill, M.J., and Henkelman, R.M. (2005). T1, T2 relaxation and magnetization transfer in tissue at 3T. *Magnetic Resonance in Medicine* 54, 507–512.

Storey, P., Atanasova, I.P., Lim, R.P., Xu, J., Kim, D., Chen, Q., and Lee, V.S. (2010). Tailoring the flow sensitivity of fast spin-echo sequences for noncontrast peripheral MR angiography. *Magnetic Resonance in Medicine* 64, 1098–1108.

Sung, K., and Nayak, K.S. (2008a). B1+ compensation in 3T cardiac imaging using short 2DRF pulses. *Magnetic Resonance in Medicine* 59, 441–446.

- Sung, K., and Nayak, K.S. (2008b). Design and use of tailored hard-pulse trains for uniformed saturation of myocardium at 3 Tesla. *Magnetic Resonance in Medicine* 60, 997–1002.
- Sung, K., and Nayak, K.S. (2008c). Measurement and characterization of RF nonuniformity over the heart at 3T using body coil transmission. *Journal of Magnetic Resonance Imaging* 27, 643–648.
- Tofts, P. (2005). *Quantitative MRI of the brain: measuring changes caused by disease* (Wiley).
- Treier, R., Steingoetter, A., Fried, M., Schwizer, W., and Boesiger, P. (2007). Optimized and combined T1 and B1 mapping technique for fast and accurate T1 quantification in contrast-enhanced abdominal MRI. *Magnetic Resonance in Medicine* 57, 568–576.
- Usman, M., Prieto, C., Schaeffter, T., and Batchelor, P.G. (2011). k-t group sparse: A method for accelerating dynamic MRI. *Magnetic Resonance in Medicine* 66, 1163–1176.
- Vaughan, J.T., Snyder, C.J., DelaBarre, L.J., Bolan, P.J., Tian, J., Bolinger, L., Adriany, G., Andersen, P., Strupp, J., and Ugurbil, K. (2009). Whole-body imaging at 7T: Preliminary results. *Magnetic Resonance in Medicine* 61, 244–248.
- Vernickel, P., Röschmann, P., Findelee, C., Lüdeke, K. -m, Leussler, C., Overweg, J., Katscher, U., Grässlin, I., and Schünemann, K. (2007). Eight-channel transmit/receive body MRI coil at 3T. *Magnetic Resonance in Medicine* 58, 381–389.
- Wang, Z., Penney, C.W., Luebbbers, R.J., and Collins, C.M. (2008). Poseable Male and Female Numerical Body Models for Field Calculations in MRI. In *Proceedings 16th Scientific Meeting, International Society for Magnetic Resonance in Medicine, Toronto*, p. 75.
- White, M.J., Hawkes, D.J., Melbourne, A., Collins, D.J., Coolens, C., Hawkins, M., Leach, M.O., and Atkinson, D. (2009). Motion artifact correction in free-breathing abdominal MRI using overlapping partial samples to recover image deformations. *Magnetic Resonance in Medicine* 62, 440–449.
- Wild, J.M., Deppe, M.H., Ajraoui, S., Marshall, H., Norquay, G., Lanz, T., Behr, M., Padormo, F., Parra-Robles, J., and Koezerke, S. (2011). Sensitivity of transmit coil

B1+ to lung inflation in hyperpolarised ^3He MRI. In Proceedings 19th Scientific Meeting, International Society for Magnetic Resonance in Medicine, Montreal,.

Willinek, W.A., Gieseke, J., Kukuk, G.M., Nelles, M., König, R., Morakkabati-Spitz, N., Träber, F., Thomas, D., Kuhl, C.K., and Schild, H.H. (2010). Dual-Source Parallel Radiofrequency Excitation Body MR Imaging Compared with Standard MR Imaging at 3.0 T: Initial Clinical Experience. *Radiology* 256, 966–975.

Wu, X., Deelchand, D., Yarnykh, V., Ugurbil, K., and Van de Moortele, P. (2009). Actual flip angle imaging: from 3D to 2D. In Proceedings of the 17th Annual Meeting of ISMRM, Honolulu, HA, USA, p. 372.

Xu, B., Spincemaille, P., Chen, G., Agrawal, M., Nguyen, T.D., Prince, M.R., and Wang, Y. Fast 3D contrast enhanced MRI of the liver using temporal resolution acceleration with constrained evolution reconstruction. *Magnetic Resonance in Medicine*.

Yarnykh, V.L. (2007). Actual flip-angle imaging in the pulsed steady state: A method for rapid three-dimensional mapping of the transmitted radiofrequency field. *Magnetic Resonance in Medicine* 57, 192–200.

Chapter 5 Accelerated Transmit Field Measurement using a Model-Based Reconstruction

5.1 Introduction

Chapter 4 presented an investigation into the response of the transmit field to a change in the respiratory state of the subject under examination. It was shown that the transmit field, measured at maximum inhale and maximum exhale, could significantly change, and that the size of change was variable across a cohort of several volunteers.

A proof-of-principle examination was performed to demonstrate the potential use of RF shimming to correct for such differences. A volunteer performed two individual breathholds (one in each respiratory state), during each of which field maps of all eight transmit channels of a PTx system were acquired. It was shown that the average and spatially varying flip angle differences in the liver could be reduced by RF shimming each respiratory state individually.

Differences in the transmit field at the extremes of the respiratory cycle implied that a dynamic transition must occur throughout it. Furthermore, the RF shim calculation suggested that the dynamic field changes could be corrected. However, any real-time correction would require knowledge of the transmit fields in time. An approach utilising retrospective binning was developed to measure this information.

The AFI sequence was adapted so that each PE line was measured serially 32 times whilst the patient was performing controlled breathing. The PE lines were grouped according to the position of the chest wall at the time they were acquired. This allowed transmit maps to be calculated for multiple respiratory positions.

The reconstructed field maps were of insufficient quality for further use. The resulting images contained respiratory artifacts that propagated through to the resulting flip angle maps. Furthermore, the method was time-consuming and the controlled breathing paradigm was too demanding for the subjects.

The use of a retrospective reconstruction was necessarily adopted due to the limited speed of transmit field mapping techniques. Only very recently has a transmit field mapping technique emerged (Dual Refocusing Echo Acquisition Mode, or DREAM (Nehrke and Börnert, 2012)) which is sufficiently fast to capture respiration-induced field changes (Nehrke and Börnert, 2012). This method is a pre-pulse based mapping technique. It accelerates the mapping process by utilising two key features. Firstly, it uses a very fast readout with a very short TR ($\sim 3\text{ms}$), which allows a 64 PEs to be acquired in under 200ms. Secondly, it measures two echoes during each FE gradient readout. This allows two images (each with different flip angle encoding) to be measured from a single acquisition.

DREAM demonstrates the state-of-the-art in transmit field mapping. Whole brain field maps can be obtained in 3s, and abdominal transmit field mapping can be achieved in under 9s, which is amenable for use within a single breathhold. However, the method does have limitations.

The DREAM implementation for real-time respiratory monitoring can measure the transmit field in a single slice in 270ms, effectively freezing respiratory motion within the acquisition. However, an immediate reacquisition of the same slice to monitor field dynamics is not possible. This is because an inter-shot delay time for longitudinal magnetisation recovery has to be inserted into the sequence. This is needed as otherwise the magnetisation will drive towards a steady-state in which the signal does not correctly encode the flip angle. In the specific implementation presented (Nehrke and Börnert, 2012), a delay time, and hence image frame-rate, of 2s was used. This is only sufficient for very slow breathing cycles. This problem is exacerbated in the case of parallel transmission systems, where the acquisition time scales linearly with the number of channels.

Furthermore, DREAM is inherently slice-selective, and is therefore not suitable for multi-slice volume acquisitions in the presence of motion due to cross-talk.

These considerations demonstrate the need for further increases in the speed of transmit field mapping. The majority of research into area this has focussed on sequence development. This chapter adopts an alternative approach, seeking acceleration through applying an advanced reconstruction technique.

5.1.1.1 Accelerated MRI for faster transmit field mapping

Accelerating MRI has always been a goal of the research community. Faster imaging increases clinical patient throughput and provides a means of viewing the dynamic processes in the human body, such as cardiac dynamics or functional brain activation. Consequently, a multitude of methods have been proposed to allow faster imaging.

The primary of method of acceleration is to acquire more data per unit time. A conceptually simple solution is reducing the TR. This approach has been successful, with many steady-state sequences allowing minimum TRs approaching 1ms. However, there is limited potential to reduce the TR further. Faster scanning would require gradients of with higher slew rates and larger maximum amplitudes. This is a difficult engineering problem, with costs rising prohibitively for small gains in performance. Furthermore, the current gradient systems achieve switching rates that are on the limits tolerable by the human nervous system (Glover, 2009). Reducing TR also imposes restrictions on achievable tissue contrast, and SSFP sequences are also restricted by power deposition limits.

TR-minimisation has been widely employed to accelerate transmit field mapping. For example, the speed improvement offered by AFI stems from its steady-state nature. However, transmit field mapping sequences require signal equations that allow the flip angle to be extracted in a manner independent from any relaxation

effects. This is only true for certain sequences, and no methods apart from AFI have been built around ultra-fast sequences.

An alternative speedup approach involves utilising alternative k-space sampling schemes, referred to as trajectories. These attempt to sample more of k-space per excitation pulse. A vast array of trajectories have been developed, such as echo-planar imaging (EPI), spiral, rosette and radial (Bernstein Matt et al., 2004). These techniques have been employed successfully in many scenarios, but not widely in transmit mapping. This is because this method of acceleration has consequences that can corrupt the flip angle measurement.

For example, EPI allows very fast image acquisition but is very sensitive to \mathbf{B}_0 inhomogeneity. This can cause image distortions and signal dropout. Spiral and radial approaches typically suffer from the characteristic image artifacts of blurring and streaking, respectively. These advanced trajectories have been employed for transmit field mapping with mixed success. Additional post-processing was required for a 3D EPI sequence to correct for distortions, and a systematic bias was also seen when compared to the gold standard (Lutti et al., 2010). A spiral trajectory has been used in conjunction with a Bloch-Siegert sequence, but displayed errors in regions of \mathbf{B}_0 inhomogeneity (Khalighi et al., 2011).

Beyond employing the above techniques, the primary alternative for imaging acceleration is reducing the amount of data collected. Under normal circumstances this will either reduce the FOV or resolution of the final image. The aim of accelerated imaging is to generate an image of equivalent or improved quality with less data without making this sacrifice.

Perhaps the simplest approach to acquisition acceleration is Partial Fourier Imaging (PFI (Feinberg et al., 1986)). This technique exploits the fact that the background phase of an image is typically a smooth function of space. This consideration implies that k-space has a conjugate symmetry, which is broken by a convolution by a small kernel that represents the phase variation. This

knowledge is exploited by PFI to accelerate imaging. A PFI acquisition samples over 50% of k-space, and uses the fully sampled centre to estimate the convolution kernel. The remaining empty k-space areas can then be estimated using the data from the opposite quadrant and the estimated kernel.

This approach is widely used in standard imaging. However it cannot be successful when k-space contains sharp phase variations (such as in flow imaging or in areas of high B_0 inhomogeneity). Furthermore, it only provides a moderate speedup factor. PFI has been used successfully by amplitude-based transmit field mapping methods ((Lutti et al., 2010; Eggenschwiler et al., 2011), which sample 3/4^{ths} of a full k-space, providing a 1.33 speedup factor), but PFIs applicability for phase-based methods has not been investigated.

The most common MRI acceleration method is the use of parallel imaging (section 3.3.1, (Pruessmann et al., 1999; Griswold et al., 2002)). PPI provides a method to increase scan speed without imposing any limitations on the pulse sequence itself. All that is required is a scanner architecture with multiple independent receive channels, as is commonly found in all modern clinical scanners, and knowledge of the receive fields of each channel. The degree of acceptable acceleration depends on the number of receive channels and the k-space sampling pattern used. At field strengths up to 3T, speedup factors ≤ 3 are achievable with acceptable degradation in SNR. Larger speedup factors can be achieved at higher field strengths (Wiesinger et al., 2006), with acceptable with acceleration factor of 4 being demonstrated at 7T with only a small decrease in SNR.

PPI has been used for a range of transmit mapping methods, but generally with a maximum acceleration factor of 2 ((Lutti et al., 2010; Eggenschwiler et al., 2011)). A study has investigated the effect of using GRAPPA to accelerate AFI with speedup factors up to 4, but the resulting maps were of degraded quality (Brenner et al., 2009). This behaviour would be expected, as PPI amplifies noise. Mapping sequences that involve taking image ratios are very sensitive to noise,

which will further reduce map quality. Therefore PPI cannot be used for transmit mapping to significantly improve speed.

An alternative approach to scan acceleration employs prior knowledge of the features the reconstructed images are expected to have. It adopts the philosophy that the measured data can be represented by model, and that the image can be reconstructed by finding the best fit to that model. This is achieved by using a cost-function, where the optimal solution is the location where the value of the cost-function is minimised.

Consider the acquisition of a 2D k-space (\mathbf{K}). Its value is the FT (F) of the 2D image (\mathbf{I}), plus an additional contribution from random Gaussian-distributed noise, as in equation 3.1.

$$\mathbf{K} = F\{\mathbf{I}\} + \varepsilon \quad 5.1$$

A standard MRI reconstruction procedure applies an inverse 2D FT to the two dimensional k-space data. However, this procedure can be expressed in another way. The 2D inverse FT is equivalent to minimising the cost function $\Psi(\mathbf{I})$, given in equation 5.2. The optimal image \mathbf{I}' minimises the least-squares of the difference between the data and FFT of the image. Here, the least-squares is achieved by taking the square of the Frobenius norm, $\|\mathbf{X}\|_2 = \sqrt{\sum_i \sum_j X_{ij}^* X_{ij}}$.

$$\Psi(\mathbf{I}) = \|\mathbf{K} - F\{\mathbf{I}\}\|_F^2 \quad 5.2$$

The ability to minimise the cost function Ψ becomes compromised in the presence of undersampling. This can be understood by considering the Fourier Transform as a matrix. For an $N \times N$ k-space and image, the FT can be expressed as an $N^2 \times N^2$ matrix whose inverse is well defined. Undersampling reduces the number of rows of this matrix, and hence it becomes underdetermined. It cannot be inverted, and hence an image cannot be formed from undersampled data.

However, undersampled data can still produce useful images when used in conjunction with regularisation, as in equation 5.3. The cost function here includes an additional term, $R(\mathbf{I})$, weighted by the regularisation parameter λ . $R(\mathbf{I})$ is a function which incorporates the prior knowledge into the reconstruction process. The regularisation parameter controls the balance between data consistency (DC) and regularisation.

$$\Psi(\mathbf{I}) = \|\mathbf{K} - F\{\mathbf{I}\}\|_2^2 + \lambda R(\mathbf{I}) \quad 5.3$$

Many forms of regularisation have been used in MR reconstruction methods. The simplest form used is Tikhonov regularisation, as given by equation 5.4. This function has the tendency to produce images with uniform contrast. This is not widely used in MR reconstruction (Van De Walle et al., 2000) as MR images do not readily fit the prior knowledge it imposes.

$$R(\mathbf{I}) = \|\mathbf{I}\|_F^2 \quad 5.4$$

A more popular regularisation method is Total Variation (TV). The functional form of TV is given in equation 5.5. This term minimises the absolute difference of intensities between a pixel (I_n) and its neighbours (I_j , where j is an index which labels adjacent pixels which comprise the set Ω). This function promotes a piecewise constant image, where there are regions of uniform intensity separated by sharp transitions. This has been successfully applied in MR (for example, in the brain (Block et al., 2007) and heart (Uecker et al., 2010)), but careful control of the regularisation parameter is needed as excessive regularisation promotes images that have a 'blocky' appearance.

5.5

$$R_{TV}(\mathbf{I}) = \sum_{n=1}^N \sum_{j \in \Omega} |I_n - I_j|$$

The TV function is a specific case of a more general class of reconstruction approach known as Compressed Sensing (CS) (Lustig et al., 2007). CS leverages the ability to transform an image to an alternative domain in which it is sparse. When this sparsity is used in conjunction with random k-space sampling, high-quality reconstructions can be achieved with a small amount of data (Candes and Wakin, 2008).

The concept of sparsity can be understood by considering the following example. Consider the FT of an MR image – typically, all Fourier coefficients contain energy, and therefore the image cannot be considered to be sparse in the Fourier domain. In contrast, it has been shown that transforming an image to the Wavelet domain achieves sparsity – a large fraction of Wavelet coefficients contain virtually no energy. In the same way, TV ‘transforms’ the image to a new domain of pixel differences, where sparsity is achieved when an image is piecewise constant.

The concept of sparsity is utilised using a regularisation term that uses an l_1 as opposed to an l_2 -norm (Candes and Wakin, 2008), as given by equation 5.6. Here, H is a function that performs the transform to the sparse domain. The l_1 -norm promotes a solution in which only few coefficients have non-zero amplitudes.

5.6

$$R_{CS}(\mathbf{I}) = \|\mathbf{H}(\mathbf{I})\|_1$$

CS also relies upon random k-space sampling, as the undersampling artifacts appear as random noise in both the image and transform domain. The CR reconstruction can effectively suppress the artifact, recovering the true image.

CS has been shown to allow vast undersampling rates. However, these can only be realised if the suitable transform domain is known beforehand. How to choose the transform domain is still an open problem, with the very latest methods attempting to estimate the domain directly from the data whilst reconstructing an image (Aharon et al., 2006; Ravishankar and Bresler, 2011).

Model-based reconstruction techniques have not been widely employed for transmit field mapping acceleration. A single study (Funai et al., 2008) considered the case of performing DAM in a multi-transmit scenario. The standard DAM approach would involve acquiring $2N_T$ images to recover N_T field maps, one for each transmit coil. The novel approach allowed good estimation of all fields with only N_T+1 images. This was achieved by exploiting the structure of the DAM signal equations. All the images could be modelled as the product of an underlying magnetisation distribution and the sine of the flip angle. This allowed a cost function to be created which directly estimated the object and the field maps from the data, with the imposition of field smoothness as regularisation. However, this approach is only applicable to multi-transmit cases.

The work in the following sections considers a more flexible and direct approach which performs undersampling of the k-space to speed up transmit field mapping. The undersampled data is then reconstructed using a model-based approach which ensures that the transmit field map is a smooth function of space.

5.2 Theory

This section presents a detailed description of the proposed reconstruction method. It begins with a discussion on the general structure of the cost-function to be minimised. This is followed by a description of the optimisation routine used to minimise the cost function, and how the cost function is expressed mathematically for use with this routine.

5.2.1 Strategy

5.2.1.1 *Mapping method selection*

As discussed in the introduction, there is potential for transmit field mapping to be accelerated by employing ideas from constrained reconstruction. This approach requires image reconstruction to be posed as an optimisation problem, in which a cost function reflecting known properties of the data is minimised.

As outlined in section 3.4.3.2, there is a multitude of field mapping methods. These can be broadly classified into amplitude-based and phase-based encoding methods. Furthermore, methods can either acquire two images and extract the flip angle from their ratio, or more than two images are acquired from which the flip angle is extracted by performing a fit to the signal.

This work focuses on two-image amplitude-based mapping methods, and uses AFI as a specific exemplar. This selection was made due to several reasons. Using a dual-image method is also favourable as it limits the size of the optimisation problem. AFI has been widely adopted by the research community due to its speed and robustness, and is the mapping method used within our group. Therefore any advances made in this work would have wide applicability.

5.2.1.2 *Reconstruction Formulation*

There are two properties of the reconstruction problem that need to be expressed in the cost function.

The first is DC. All reconstructed variables have to be consistent with the measured k-space data, else they do not necessarily reflect the true state of magnetisation of the subject being imaged.

Further prior knowledge is required to constrain the reconstruction in the presence of undersampling. This knowledge is the spatial smoothness of the transmit field. This property has been widely observed across MRI (Wiesinger et

al., 2004), and was used by Funai (Funai et al., 2009) in the previously discussed DAM acceleration approach.

With these considerations in mind, the following cost function is proposed. It contain four terms: the first two ensure DC, and the last two ensure field smoothness. Note that this framework assumes a 2D acquisition, and the expressions can easily be generalised to 3D.

$$\Psi(\mathbf{I}_1, r) = \|\mathbf{k}_1 - \mathbf{S}_1 \times (\mathbf{F}\mathbf{I}_1\mathbf{G})\|_F^2 + \|\mathbf{k}_2 - \mathbf{S}_2 \times (\mathbf{F}(\mathbf{r} \times \mathbf{I}_1)\mathbf{G})\|_F^2 + \lambda \|\nabla_x \{\mathbf{r}, \mathbf{M}\}\|_F^2 + \lambda \|\nabla_y \{\mathbf{r}, \mathbf{M}\}\|_F^2$$

5.7

Given below is a list of quantities involved:

- Measured k-space data
 - The variables \mathbf{k}_1 and \mathbf{k}_2 are $N_x \times N_y$ matrices which contain the complex k-space measurements from a 2D acquisition. For AFI, they correspond to the first and second TR periods, respectively. Unsampld locations contain a Fourier coefficient of zero amplitude.
- Images
 - The image \mathbf{I}_1 is a 2D $N_x \times N_y$ complex matrix reflecting the signal intensity and phase of the image from the first TR period. \mathbf{I}_2 is defined in in the same manner.
- Fourier Matrices
 - \mathbf{F} and \mathbf{G} are $N_x \times N_y$ and $N_x \times N_y$ 2D matrices that transform any $N_x \times N_y$ image to the frequency domain.
- Sampling Matrices
 - \mathbf{S}_1 and \mathbf{S}_2 are k-space sampling matrices. Sampled k-space ordinates have value 1, and unsampled ordinates contain 0.
- Mask

- The $N_x \times N_y$ matrix \mathbf{M} is an image domain mask. It has value 1 inside the object and 0 outside the object. This is pre-defined before each reconstruction is performed.
- Image ratio
 - The image ratio \mathbf{r} is a real 2D matrix, representing the division of the magnitudes of the image matrices, $\mathbf{r} = \sqrt{(\mathbf{I}_2 \times \mathbf{I}_2^*)} / \sqrt{(\mathbf{I}_1 \times \mathbf{I}_1^*)}$.
- Operators
 - The $/$ and \times symbols represent image division and multiplication on a pixelwise basis, respectively.
- Norms
 - The Frobenius norm applied to matrix \mathbf{A} , $\|\mathbf{A}\|_F$, is given by equation 5.8, where a_{ij} is the complex number located in the i^{th} row and j^{th} column.

5.8

$$\|\mathbf{A}\|_F = \sqrt{\sum_{j=1}^{N_y} \sum_{i=1}^{N_x} a_{ij}^* a_{ij}}$$

- Regularisation parameter
 - The real number λ controls the balance between DC and smoothness terms. Larger λ assigns more significance to field smoothing and visa versa.
- Gradient Operators
 - The ∇_x and ∇_y operators represents first-order difference operators. When ∇_x acts on an $N_x \times N_y$ matrix, it returns an $(N_x - 1) \times N_y$ matrix \mathbf{D} , as defined in equation 5.9. The difference between neighbouring pixels is only nonzero when both pixels are inside the mask. ∇_y is defined in the same way, but acting in the y direction.

$$5.9 \quad \nabla_x \{\mathbf{A}, \mathbf{M}\} = \mathbf{D}, \quad \text{where} \quad D_{i,j} = M_{i,j} M_{i+1,j} (A_{i+1,j} - A_{i,j})$$

Note that the cost function does not convert the ratio of images into flip angle before applying the gradient operators. This simplification is valid, as a smooth ratio of images will translate to a smooth flip angle distribution. This is because the AFI ratio to flip angle conversion formula (equation 3.23) is smooth (figure 2 in (Yarnykh, 2007)).

Equation 5.7 is minimised by solving for \mathbf{l}_1 and the ratio \mathbf{r} . The DC term for the second TR period forms \mathbf{l}_2 by taking the product $\mathbf{r} \times \mathbf{l}_1$. It is also possible to solve for the ratio only inside the mask area. This is favourable as it reduces the number of variables. Consequently, $(2+m)N_x N_y$ variables are solved for, where m denotes the fraction of FOV covered by the mask. The ratio is forced to equal zero outside of the mask.

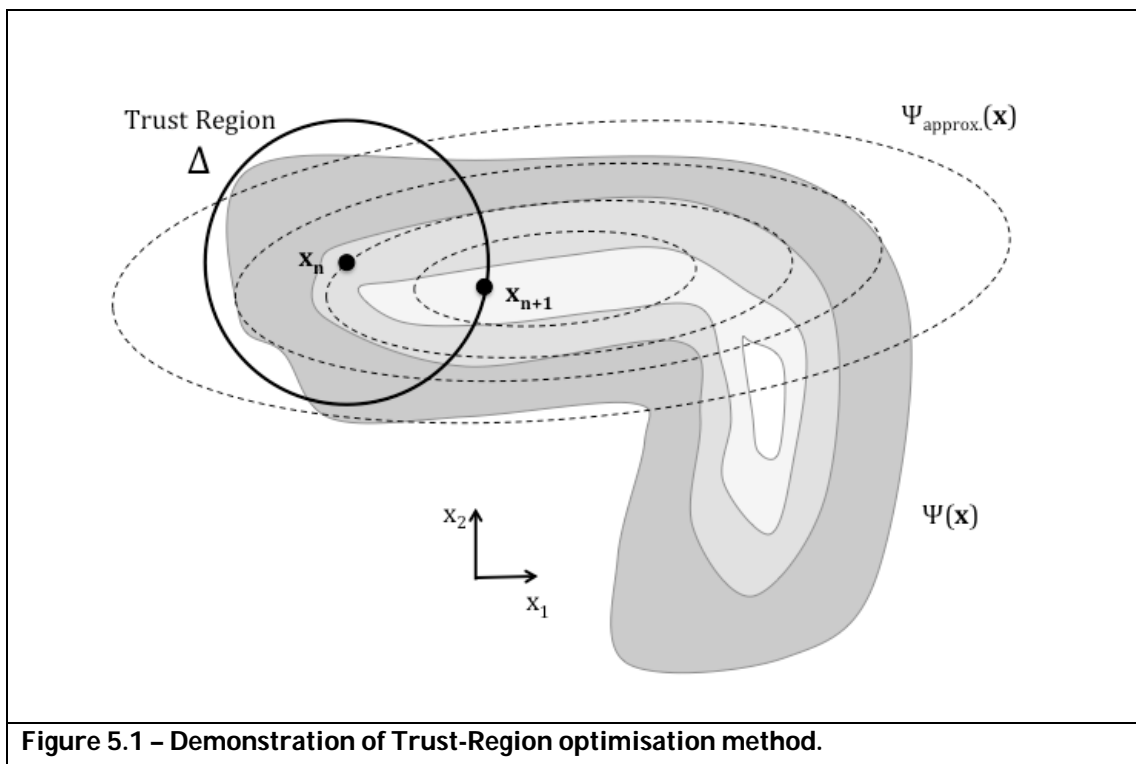
5.2.1.3 Cost Function Minimisation Method

A diverse range of methods have been developed to solve numerical optimisation problems. These methods are typically designed to efficiently solve individual classes of problems, based on the nature of the cost function. The proposed cost function (equation 5.7) has several properties that need to be taken into account so that the appropriate solver can be chosen.

The proposed cost function is primarily a least-squares problem. This is because each term involves the square of the l_2 -norm. Linear least-squares problems can be very efficiently solved, and the obtained solution can be guaranteed to converge towards the global minimum of the cost function [18]. However, these methods cannot be applied here. This is because the cost function is nonlinear. The nonlinearity originates from the second term of the cost function, in which the product between the image and ratio variables is taken. This property is referred to as bilinearity.

These two properties make the cost function suitable for non-linear least-squares (NLLS) solvers. Such a solver, the `lsqnonlin` function, is provided in Matlab Scientific Computing Environment and was used for the optimisations performed in this chapter.

The Matlab NLLS algorithm is a trust-region method. The basis of this technique is demonstrated in Figure 3.1. The shaded contours represent the value of a fictitious cost function, $\Psi(\mathbf{x})$, that is the function of two variables, x_1 and x_2 . Consider a trial solution, given by \mathbf{x}_n . First, a circle of radius Δ is defined around this position. This is the trust region. The cost-function is approximated in this area using a second-order Taylor expansion, $\Psi_{\text{approx}}(\mathbf{x})$, as given by the dashed ellipses. The minimum of the Ψ_{approx} in the trust region can be easily found (\mathbf{x}_{n+1}), and this is selected to be the next trial solution of the optimisation. This process is repeated until convergence.



An important aspect of trust region methods is how to adapt the size of the trust region. When the approximation is a good fit to the true cost function, the size of

the area is increased for the next iteration. Conversely, the trust region is shrunk when the approximation is poor.

5.2.1.4 *Mathematical expression of cost-function for use with optimisation routine*

The Matlab implementation of the NLLS algorithm requires equation 5.7 to be expressed in an alternative form. The method minimises cost functions of the form given by equation 5.10, where \mathbf{x} is a real vector containing all of the cost-function variables and $\Phi(\mathbf{x})$ is a function which outputs a vector \mathbf{y} of which the l_2 -norm is taken, so that equations 5.7 and 5.10 are equivalent.

$$5.10 \quad \Psi(\mathbf{x}) = \|\Phi(\mathbf{x})\|_2^2$$

The optimisation variables \mathbf{I}_1 and \mathbf{r} must first be mapped into \mathbf{x} , as shown in equation 5.11. The $N_x \times N_y$ matrix \mathbf{I}_1 (where each complex valued pixel at the x^{th} row and y^{th} column is given by $I_{x,y}^r + iI_{x,y}^c$) is separated into real and imaginary components which are individually vectorised and then concatenated. A vector containing the mN_xN_y ratio values is then appended to the vector to complete the construction of \mathbf{x} .

$$5.11 \quad \mathbf{x} = \begin{bmatrix} I_{1,1}^r & I_{2,1}^r & \cdots & I_{N_x,N_y}^r & I_{1,1}^c & I_{2,1}^c & \cdots & I_{N_x,N_y}^c & r_1 & r_2 & \cdots & r_{mN_xN_y} \end{bmatrix}^T$$

The function $\mathbf{y} = \Phi(\mathbf{x})$ must also be defined explicitly for input into the NLLS algorithm. The vector \mathbf{y} comprises of four concatenated individual vectors \mathbf{d}^{DC1} , \mathbf{d}^{DC2} , \mathbf{d}^{FDx} and \mathbf{d}^{FDy} , as in equation 5.12, with the appropriate weighting from the regularisation parameter.

$$5.12 \quad \mathbf{y} = \Phi(\mathbf{x}) = \begin{bmatrix} \mathbf{d}^{\text{DC1}} \\ \mathbf{d}^{\text{DC2}} \\ \lambda \mathbf{d}^{\text{FDx}} \\ \lambda \mathbf{d}^{\text{FDy}} \end{bmatrix}$$

The vectors \mathbf{d}^{DC1} and \mathbf{d}^{DC2} correspond to the first and second DC terms. The vectors \mathbf{d}^{FDx} and \mathbf{d}^{FDy} correspond to the first and second gradient (or finite difference, FD) terms. These terms are defined as follows.

5.2.1.4.1 Data Consistency Terms

The first DC term can be expressed as squared Frobenius norm of an $N_x \times N_y$ residual matrix \mathbf{R}^{DC1} , as defined in equation 5.13.

$$5.13 \quad \mathbf{R}^{\text{DC1}} = \mathbf{k}_1 - \mathbf{S}_1 \times (\mathbf{F}\mathbf{I}_1\mathbf{G})$$

The value of each element of \mathbf{R}^{DC1} is given by equation 5.14, where the subscript letters refer to the matrix elements row and column positions, and subscript has been removed from \mathbf{I}_1 for simplicity. All quantities, except \mathbf{S} , are complex.

$$5.14 \quad R_{ab}^{\text{DC1}} = k_{1,ab} - S_{1,ab} \sum_{c=1}^{N_x} \sum_{d=1}^{N_y} f_{ac} I_{cd} g_{db}$$

This expression is further manipulated to form the vectors $\mathbf{R}^{\text{DC1},r}$ and $\mathbf{R}^{\text{DC1},c}$. These are defined in equation 5.15, and reflect the real (superscript r) and complex (superscript c) components of the data consistency residual.

$$\begin{aligned}
5.15 \quad R_{v\{a,b\}}^{\text{DC1},r} &= k_{1,ab}^r - S_{1,ab} \sum_{c=1}^{N_x} \sum_{d=1}^{N_y} \alpha_{abcd} I_{cd}^r - \beta_{abcd} I_{cd}^c \\
R_{v\{a,b\}}^{\text{DC1},c} &= k_{1,ab}^c - S_{1,ab} \sum_{c=1}^{N_x} \sum_{d=1}^{N_y} \beta_{abcd} I_{cd}^r + \alpha_{abcd} I_{cd}^c
\end{aligned}$$

The function $v\{a,b\}$ transforms the 2D matrix indices a and b into vector indices. The rows in which $k_{1,ab}$ and $S_{1,ab}$ are zero (due to undersampling) are removed. The coefficients α_{abcd} and β_{abcd} are defined by equations 5.16 and 5.17.

$$5.16 \quad \alpha_{abcd} = f_{ac}^r g_{db}^r - f_{ac}^c g_{db}^c$$

$$5.17 \quad \beta_{abcd} = f_{ac}^r g_{db}^c + f_{ac}^c g_{db}^r$$

The final \mathbf{d}^{DC1} vector is formed by vertically concatenating the vectors $\mathbf{R}^{\text{DC1},r}$ and $\mathbf{R}^{\text{DC1},c}$, as in equation 5.18.

$$5.18 \quad \mathbf{d}^{\text{DC1}} = \begin{bmatrix} \mathbf{R}^{\text{DC1},r} \\ \mathbf{R}^{\text{DC1},c} \end{bmatrix}$$

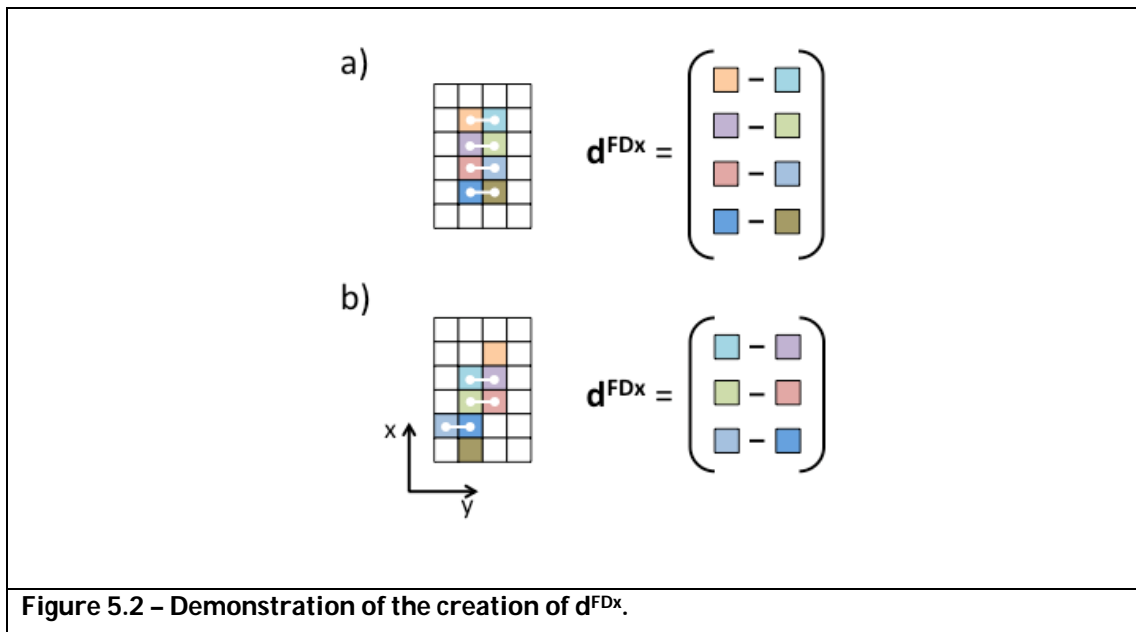
The second data consistency term is similar to first, but with slight modifications to account for the pixelwise product with the ratio, as in equation 5.19. The quantity r_{cd} outside of the mask is defined to equal zero.

$$\begin{aligned}
5.19 \quad R_{v\{a,b\}}^{\text{DC2},r} &= k_{2,ab}^r - S_{2,ab} \sum_{c=1}^{N_x} \sum_{d=1}^{N_y} (\alpha_{abcd} I_{cd}^r - \beta_{abcd} I_{cd}^c) r_{cd} \\
R_{v\{a,b\}}^{\text{DC2},c} &= k_{2,ab}^c - S_{2,ab} \sum_{c=1}^{N_x} \sum_{d=1}^{N_y} (\beta_{abcd} I_{cd}^r + \alpha_{abcd} I_{cd}^c) r_{cd}
\end{aligned}$$

The final \mathbf{d}^{DC2} vector is formed by vertically concatenating the vectors $\mathbf{R}^{\text{DC2},r}$ and $\mathbf{R}^{\text{DC2},c}$, as for the DC1 case.

5.2.1.4.2 Finite Difference Terms

The finite difference terms apply exclusively to the ratio variables. Each element of the residual vectors \mathbf{d}^{FDx} and \mathbf{d}^{FDy} contain the differences between neighbouring pixels in the x or y direction inside the object mask \mathbf{M} . The process is shown diagrammatically in Figure 5.2 for the case of FD in the x-direction. Two example masks are shown on the LHS. White pixels are outside of the mask, and coloured pixels are inside the object. The x-direction finite difference can only be calculated where the mask has x-adjacent pixels. The number of these, and hence the length of the finite difference vector, depends on the shape of the mask. This is demonstrated by comparing Figure 5.2a and Figure 5.2b. The two masks have the same number of non-zero elements. However, their different shapes lead to four and three differences being taken, respectively.



The FD process can be expressed mathematically as in equations 5.20 and 5.21. Here, the function $\xi_{x/y}\{a,b\}$ selects b^{th} element of the a^{th} pair of all possible $N_{\text{FDx/y}}$ neighbours in the x/y direction.

5.20

$$\mathbf{d}^{\text{FD}_x} = \begin{bmatrix} r_{\xi_x\{1,1\}} - r_{\xi_x\{1,2\}} \\ r_{\xi_x\{2,1\}} - r_{\xi_x\{2,2\}} \\ \vdots \\ r_{\xi_x\{N_{\text{FD}_x},1\}} - r_{\xi_x\{N_{\text{FD}_x},2\}} \end{bmatrix}$$

5.21

$$\mathbf{d}^{\text{FD}_y} = \begin{bmatrix} r_{\xi_y\{1,1\}} - r_{\xi_y\{1,2\}} \\ r_{\xi_y\{2,1\}} - r_{\xi_y\{2,2\}} \\ \vdots \\ r_{\xi_y\{N_{\text{FD}_y},1\}} - r_{\xi_y\{N_{\text{FD}_y},2\}} \end{bmatrix}$$

5.2.1.5 Cost Function Gradient

The NLLS method approximates the cost function in the trust region using a Taylor expansion. This typically requires knowledge of the cost function's first and second order derivatives. The specific NLLS algorithm utilised here ((Coleman and Li, 1994, 1996)) requires knowledge of the Jacobian, \mathbf{J} . This is a matrix that gives the partial derivatives of each element of \mathbf{y} with respect to every variable. \mathbf{J} is shown in equation 5.22, where each partial derivative represents a block of entries.

5.22

$$\mathbf{J}(\mathbf{x}) = \begin{bmatrix} \frac{\partial \mathbf{R}^{\text{DC1,r}}}{\partial I_{\gamma\delta}^r} & \frac{\partial \mathbf{R}^{\text{DC1,r}}}{\partial I_{\gamma\delta}^c} & \frac{\partial \mathbf{R}^{\text{DC1,r}}}{\partial r_\varepsilon} \\ \frac{\partial \mathbf{R}^{\text{DC1,c}}}{\partial I_{\gamma\delta}^r} & & \vdots \\ \frac{\partial \mathbf{R}^{\text{DC2,r}}}{\partial I_{\gamma\delta}^r} & & \vdots \\ \frac{\partial \mathbf{R}^{\text{DC2,c}}}{\partial I_{\gamma\delta}^r} & \ddots & \vdots \\ \lambda \frac{\partial \mathbf{d}^{\text{FDx}}}{\partial I_{\gamma\delta}^r} & & \vdots \\ \lambda \frac{\partial \mathbf{d}^{\text{FDy}}}{\partial I_{\gamma\delta}^r} & \square & \lambda \frac{\partial \mathbf{d}^{\text{FDy}}}{\partial r_\varepsilon} \end{bmatrix}$$

The structure of the Jacobian reflects the structure of the cost function. The structure of the proposed cost function results in Jacobian structure shown in equation 5.23. Several areas of the Jacobian are empty. The four blocks in the bottom-left region always equal zero as the finite difference cost function term is not a function of the image pixel intensities (i.e. $\partial \mathbf{d}^{\text{FDx}} / \partial I_{\gamma\delta}^r = 0$, $\partial \mathbf{d}^{\text{FDx}} / \partial I_{\gamma\delta}^c = 0$, $\partial \mathbf{d}^{\text{FDy}} / \partial I_{\gamma\delta}^r = 0$ and $\partial \mathbf{d}^{\text{FDy}} / \partial I_{\gamma\delta}^c = 0$). Similarly for the two blocks in the top-right of the Jacobian – these terms always equal zero as the first data consistency term is not a function of the ratio (i.e. $\partial \mathbf{R}^{\text{DC1,r}} / \partial r_\varepsilon = 0$ and $\partial \mathbf{R}^{\text{DC1,c}} / \partial r_\varepsilon = 0$).

$$\mathbf{J}(\mathbf{x}) = \begin{bmatrix} \frac{\partial \mathbf{R}^{\text{DC1,r}}}{\partial I_{\gamma\delta}^r} & \frac{\partial \mathbf{R}^{\text{DC1,r}}}{\partial I_{\gamma\delta}^c} & 0 \\ \frac{\partial \mathbf{R}^{\text{DC1,c}}}{\partial I_{\gamma\delta}^r} & \frac{\partial \mathbf{R}^{\text{DC1,c}}}{\partial I_{\gamma\delta}^c} & 0 \\ \frac{\partial \mathbf{R}^{\text{DC2,r}}}{\partial I_{\gamma\delta}^r} & \frac{\partial \mathbf{R}^{\text{DC2,r}}}{\partial I_{\gamma\delta}^c} & \frac{\partial \mathbf{R}^{\text{DC2,r}}}{\partial r_\varepsilon} \\ \frac{\partial \mathbf{R}^{\text{DC2,c}}}{\partial I_{\gamma\delta}^r} & \frac{\partial \mathbf{R}^{\text{DC2,c}}}{\partial I_{\gamma\delta}^c} & \frac{\partial \mathbf{R}^{\text{DC2,c}}}{\partial r_\varepsilon} \\ 0 & 0 & \lambda \frac{\partial \mathbf{d}^{\text{FDx}}}{\partial r_\varepsilon} \\ 0 & 0 & \lambda \frac{\partial \mathbf{d}^{\text{FDy}}}{\partial r_\varepsilon} \end{bmatrix}$$

The values of the non-zero partial derivatives remaining in \mathbf{J} are now given below. Equations 5.24 give the partial derivatives for the first data consistency term.

$$\begin{aligned}
\frac{\partial R_{v\{a,b\}}^{\text{DC1,r}}}{\partial I_{\gamma\delta}^r} &= -S_{1,ab} \alpha_{ab\gamma\delta} \quad , \quad \frac{\partial R_{v\{a,b\}}^{\text{DC1,r}}}{\partial I_{\gamma\delta}^c} = S_{1,ab} \beta_{ab\gamma\delta} \\
\frac{\partial R_{v\{a,b\}}^{\text{DC1,c}}}{\partial I_{\gamma\delta}^r} &= -S_{1,ab} \beta_{ab\gamma\delta} \quad , \quad \frac{\partial R_{v\{a,b\}}^{\text{DC1,c}}}{\partial I_{\gamma\delta}^c} = S_{1,ab} \alpha_{ab\gamma\delta}
\end{aligned}$$

Equations 5.25 give the partial derivatives for the first data consistency term.

$$\begin{aligned}
\frac{\partial R_{v\{a,b\}}^{\text{DC2,r}}}{\partial I_{\gamma\delta}^r} &= -S_{2,ab} \alpha_{ab\gamma\delta} r_{\gamma\delta} \quad , \quad \frac{\partial R_{v\{a,b\}}^{\text{DC2,r}}}{\partial I_{\gamma\delta}^c} = S_{2,ab} \beta_{ab\gamma\delta} r_{\gamma\delta} \quad , \quad \frac{\partial R_{v\{a,b\}}^{\text{DC2,r}}}{\partial r_\varepsilon} = S_{2,ab} \left(-\alpha_{ab\gamma\delta} I_{\gamma\delta}^r + \beta_{ab\gamma\delta} I_{\gamma\delta}^c \right) \\
\frac{\partial R_{v\{a,b\}}^{\text{DC2,c}}}{\partial I_{\gamma\delta}^r} &= -S_{2,ab} \beta_{ab\gamma\delta} r_{\gamma\delta} \quad , \quad \frac{\partial R_{v\{a,b\}}^{\text{DC2,c}}}{\partial I_{\gamma\delta}^c} = S_{2,ab} \alpha_{ab\gamma\delta} r_{\gamma\delta} \quad , \quad \frac{\partial R_{v\{a,b\}}^{\text{DC2,c}}}{\partial r_\varepsilon} = S_{2,ab} \left(-\alpha_{ab\gamma\delta} I_{\gamma\delta}^c - \beta_{ab\gamma\delta} I_{\gamma\delta}^r \right)
\end{aligned}$$

Equations 5.26 and 5.27 give the partial derivatives for the finite difference terms.

$$5.26 \quad \frac{\partial d_{\sigma}^{FDx}}{\partial r_{\varepsilon}} = \begin{cases} 1 & r_{\varepsilon} = r_{\xi_x\{\sigma,1\}} \\ -1 & r_{\varepsilon} = r_{\xi_x\{\sigma,2\}} \\ 0 & otherwise \end{cases}$$

$$5.27 \quad \frac{\partial d_{\sigma}^{FDy}}{\partial r_{\varepsilon}} = \begin{cases} 1 & r_{\varepsilon} = r_{\xi_y\{\sigma,1\}} \\ -1 & r_{\varepsilon} = r_{\xi_y\{\sigma,2\}} \\ 0 & otherwise \end{cases}$$

5.2.1.6 How well-posed is the optimisation?

The suitability of the optimisation can be understood by comparing the number of constraints (i.e. the number of elements in \mathbf{y}) to the number of variables (i.e. the number of variables in \mathbf{x}). The number of constraints is given by $4U_s N_x N_y + N_{FDx} + N_{FDy}$, where U_s is the fraction of each k-space sampled. The number of variables is given by $(2+m)N_x N_y$.

The balance between these two factors depends both on the object mask and the undersampling rate. The optimisation cannot be reliably solved in cases where the problem is underdetermined.

5.2.1.7 Optimisation Scheme

The solution obtained by the optimisation will rely heavily on the size of the regularisation parameter. It is difficult to anticipate the optimal amount of regularisation, so the reconstructions in this chapter will be performed for a range of regularisation parameter amplitudes. The optimisations are performed sequentially, starting from small values regularisation parameter values upwards (i.e. $\lambda=10^{-9}$ to $\lambda=10^{-1/2}$ in 50 equal steps in the exponent).

The first optimisation is seeded from the zero-filled FT of the undersampled k-space data. The result of the first optimisation is then used at the starting point of the next optimisation. This forward seeding process is then repeated. This technique is widely used [18]. The default parameters of the NLLS algorithm were used, except for the termination criteria tolerance ($[\Psi(x_{n+1}) - \Psi(x_n)] / \Psi(x_n)$), which was increased from 10^{-6} to 10^{-4} . Again, this was found in pilot data to not effect of the results.

The NLLS algorithm has the added ability to constrain the size of the optimisation variables. This feature was utilised for the ratio variables, which should always lie in the range of 0 to 1, as defined by AFI. The bounds of $0 < r < 1.5$ were used to allow tolerance in the presence of undersampling.

5.3 Experimental Methods and Results

5.3.1 Structure

The experimental methods and results are presented in this section. The research is comprised of three sequential studies, each motivated by the previous. An outline of the three studies is provided below in order to help navigate through the studies and their conclusions.

Study 1

The first study investigated the ability of the reconstruction method to accurately reconstruct transmit field maps in the presence of k-space undersampling. This included the testing of four different sampling approaches: Cartesian Undersampling (CUS), random undersampling (RUS), Poisson undersampling (PUS) and Variable Density Undersampling (VDUS). The study also tested whether the two AFI images should use the same or different sampling patterns, and the effect of the regularisation parameter on reconstruction quality. The results from this study demonstrated that the proposed reconstruction scheme is able to reconstruct smooth transmit field

maps from undersampled k-space data. However, the quality of reconstructions did not strongly reduce as undersampling increased. This indicated that the central region of k-space contributed more information to the reconstruction than the edges of k-space.

Study 2

Study 2 was performed to further probe the results from the first study. The simulation dataset was modified to minimise data redundancy, so that k-space contained information at all frequencies. This was achieved by tightly cropping the FOV, choosing an anatomical location that contained significant transmit field inhomogeneity, and truncating k-space to minimise the resolution. The results from this study indicated that the quality of the reconstruction was highly dependent on the amount of data sampled at the centre of k-space.

Study 3

Study 3 approached the question of optimal k-space sampling from an alternative perspective. Study 2 assumed that maximally truncating k-space minimised data redundancy. Although this is valid, the act of truncating itself introduced errors with respect to the *true* gold standard transmit field. Therefore study 3 tested the proposed reconstruction scheme by prioritising data at the centre of k-space and testing the results against the *true* gold standard. This study demonstrated that the proposed scheme could robustly outperform standard reconstruction approaches.

5.3.2 Study 1

This section details the first set of experiments performed to test the proposed reconstruction method. These experiments explore the choice of sampling pattern, the level of undersampling and the choice of regularisation parameter.

5.3.2.1 *Methods*

5.3.2.1.1 Dataset

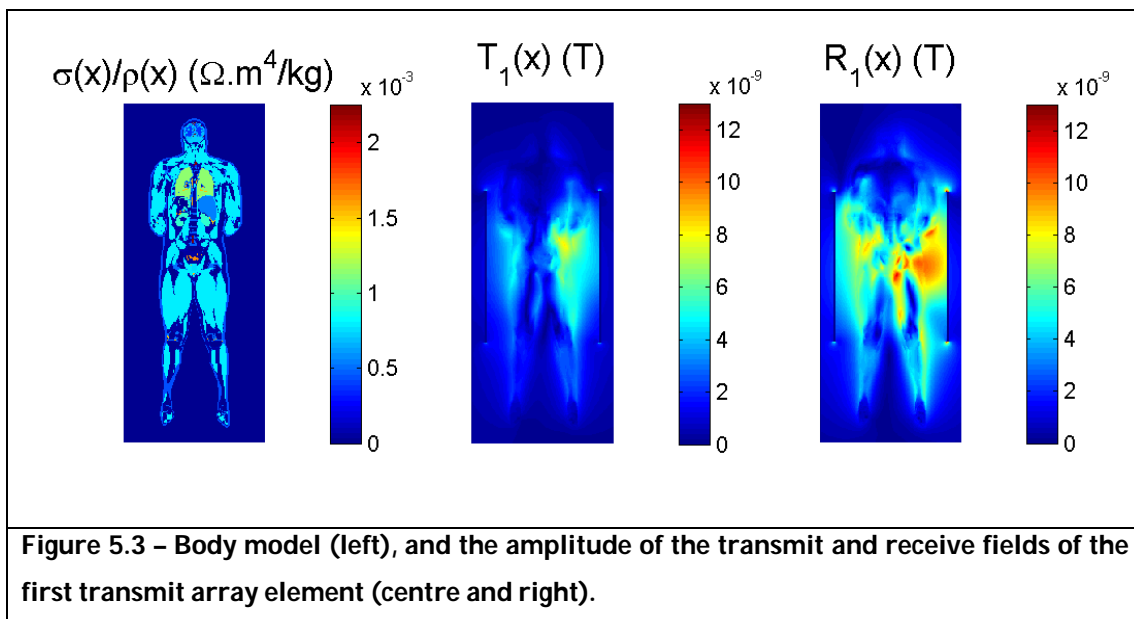
A rigorous testing framework was constructed so that systematic evaluations of each reconstructed field map could be performed. A fundamental part of this framework is the choice of gold standard field map to which all reconstructions should be compared. There are two possible approaches. First, a gold standard dataset could be constructed from actual measured MRI data. The second approach involved creating a gold standard dataset from a FDTD simulation (section 3.4.2).

Using a measured dataset as a gold standard presents several problems. The primary issue is that measurements are corrupted by noise. This can be mitigated to a certain extent by averaging repeated acquisitions, but this requires extended scan times. This is problematic for in-vivo scans, but could be circumvented using a phantom. However, long scan times also makes the data susceptible to \mathbf{B}_0 drift (caused by the heating of gradient coils). Furthermore, a phantom does not have the spatial detail of human anatomy, detaching the method from realistic in-vivo scenarios.

The second option of using an FDTD simulation eliminates almost all of these issues. This approach first requires the FDTD body model to be segmented into distinct tissue areas, which are then assigned appropriate relaxation times. Using this information and the calculated RF fields, a set of field map data can be generated by applying the signal equations of the field mapping method. This method is noise-free and allows the use of realistic fields. However, the true complexity of the in-vivo data is not recreated as the body model only has a finite number of segmented tissues. The FDTD method was adopted for this work, and implemented as described below.

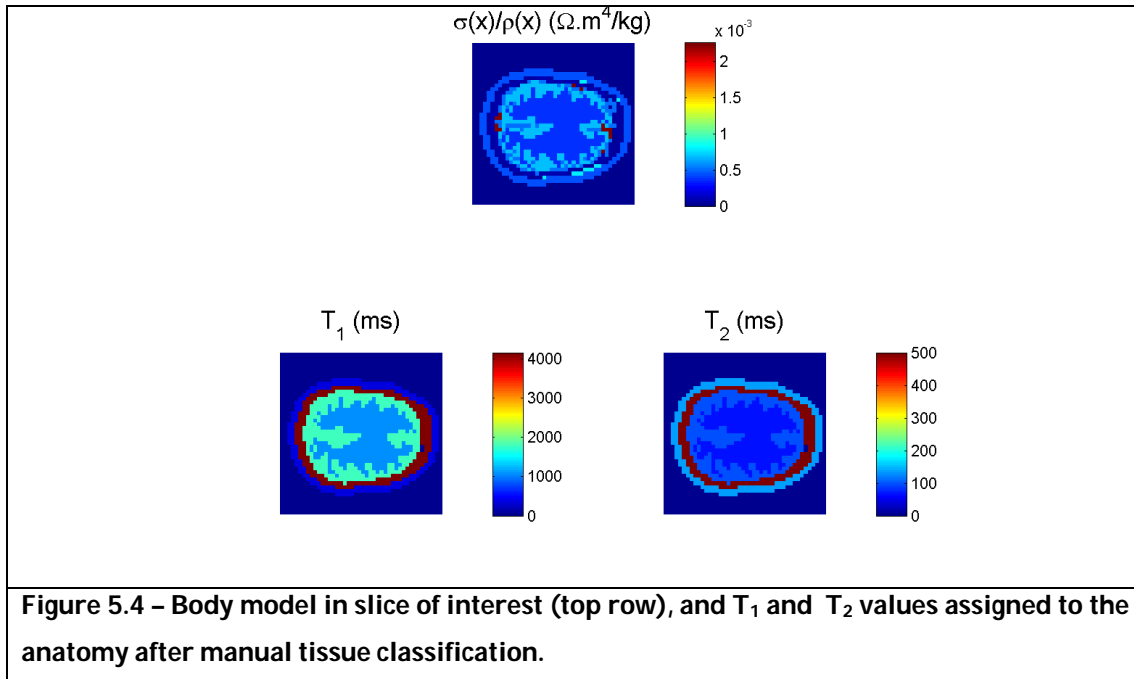
A RF field simulation of the Visible Human Duke body model was performed using proprietary software (XFDTD, Remcom Inc., State College, PA) by collaborators at Philips Medical Systems. This simulation was performed to

provide insight into power deposition using the parallel transmission system installed locally (Vernickel et al., 2007). The model consists of a 171x171x405 3D array of voxels of size 5x5x5mm, each assigned with the ratio of tissue conductivity to tissue mass density. A coronal slice through the body model is shown on the left of Figure 5.3. The RF simulation used this information in addition to a digital representation of the transmit array to generate the electric and magnetic fields throughout the volume. This process is performed for each transmit element. The transverse magnetic field components are then combined as per equations 3.7 and 3.8 to synthesise the transmit and receive fields of each element of the transmit array. The centre and right images in Figure 5.3 show the amplitude of the transmit and receive fields of the first transmit array element in the slice.



The dataset is then reduced to a single transverse slice through the brain. The resulting matrix is of size 44x44, corresponding to a realistic set of imaging parameters (FOV = 220x220mm, resolution = 5x5mm). The top row of Figure 5.4 shows the native body model in the chosen slice. It is manually segmented into four tissue regions: subcutaneous fat ($T_1=365\text{ms}$, $T_2=133\text{ms}$), cerebrospinal fluid (CSF, $T_1=4163\text{ms}$, $T_2=500\text{ms}$), grey matter ($T_1=1820\text{ms}$, $T_2=99\text{ms}$), and white matter ($T_1=1084\text{ms}$, $T_2=69\text{ms}$). These values are obtained from experimentally

determined literature values at 3T ([18–20], except T_2 of CSF which is assumed to have approximately the same T_1/T_2 ratio as blood from (Stanisz et al., 2005)).



The calculated fields from the FDTD simulations are added together to create quadrature transmit and receive fields. These are then normalised. Quadrature transmission is scaled so that the position of maximum transmit field amplitude has a flip angle of 60° . This scaling is then applied to all individual transmit channels. Similarly, the quadrature receive field is scaled so that it maximum has unit amplitude, with individual channels again given the same scaling. The amplitude and phase of the transmit and receive fields of each element in the selected slice are given in Figure 5.5.

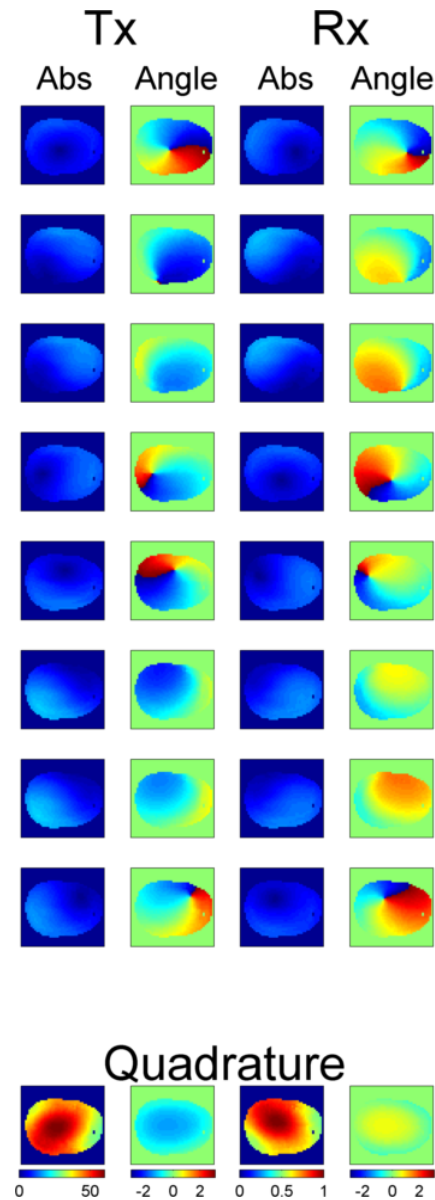


Figure 5.5 – Individual transmit and receive fields (amplitude (transmit units = degrees, receive has arbitrary units) and phase (units = radians)) in the anatomy, and the net quadrature fields.

The experiments in this study models the scenario of mapping the quadrature transmit field whilst receiving in quadrature. Complex image domain signals for I_1 and I_2 were generated by applying the full AFI signal equations (equations 3.20 and 3.21) using $n=4$. The FT of the image domain signals were taken to generate the corresponding k-space data. Figure 5.6 displays the native image magnitudes,

their ratio, their signal along an AP profile (indicated by the white line in the ratio image), and the k-space data.

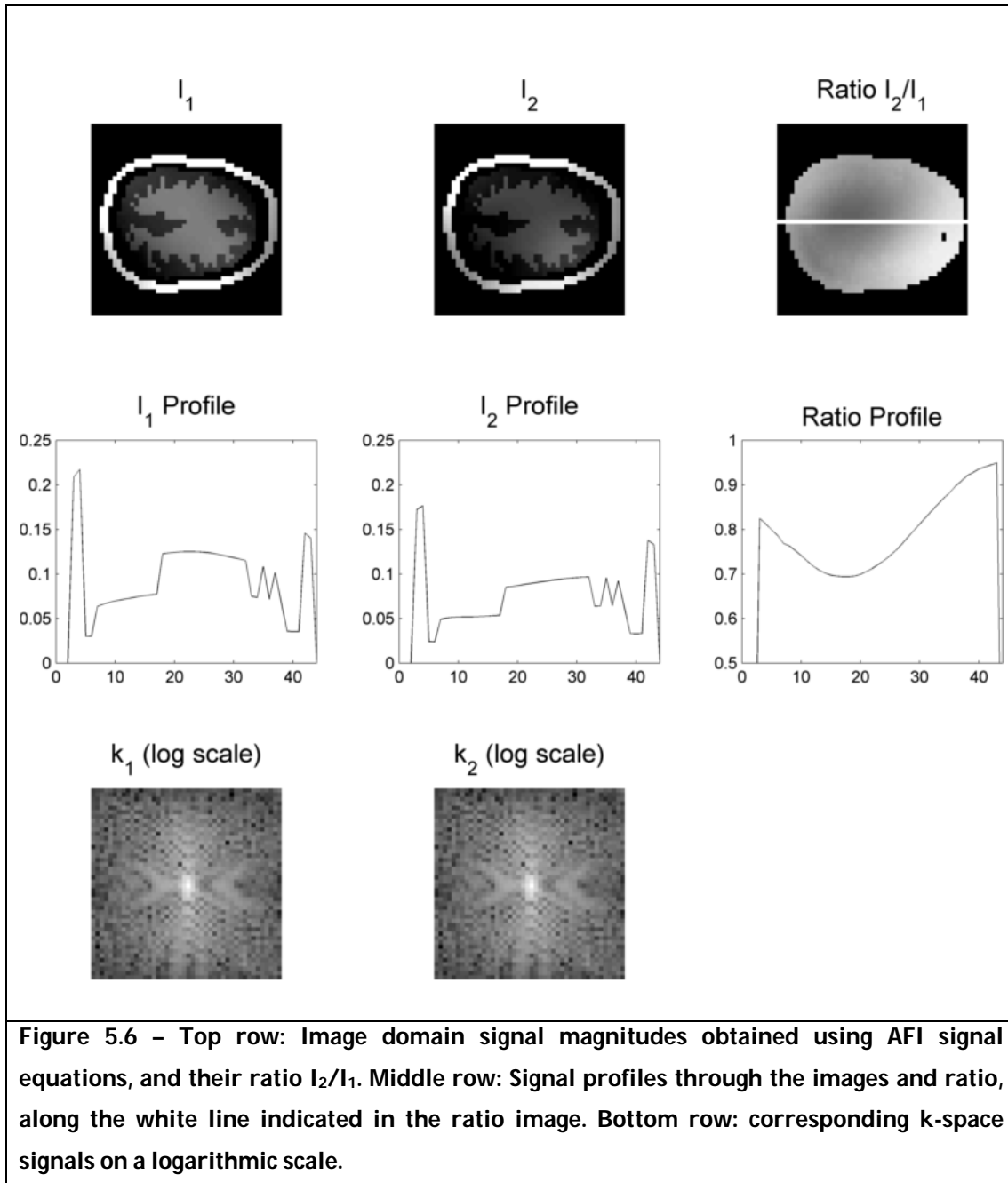


Figure 5.6 – Top row: Image domain signal magnitudes obtained using AFI signal equations, and their ratio I_2/I_1 . Middle row: Signal profiles through the images and ratio, along the white line indicated in the ratio image. Bottom row: corresponding k-space signals on a logarithmic scale.

5.3.2.1.2 Sampling Patterns

A primary goal of this study is to investigate how to optimally sample k-space. There are many candidate strategies, all of which can be classified as either Cartesian or non-Cartesian. Cartesian approaches restrict k-space sampling to

regular grid. Non-Cartesian approaches can place samples at any location and may offer speed advantages, but can also introduce unpredictable artifacts into transmit mapping reconstruction. Therefore only Cartesian approaches are considered here.

It is normally desirable to know the transmit field throughout the imaging volume, and hence this chapter considers 3D acquisitions. Solving for the image and ratio in 3D significantly increases the size of optimisation problem over a 2D problem. Therefore the problem considers k-space data that has previously been Fourier Transformed in the FE direction. This results in a 2D k-space where both directions are PE directions. Both PE directions can be undersampled, so 2D undersampling patterns are used.

The various ways that the base Cartesian grid can be undersampled are now described. The level of undersampling is given by U_s , which is a multiplicative factor that can lie between 0 (no sampling) and 1 (full sampling).

The first approach, Regular Cartesian Undersampling (RCUS), omits k-space samples in a regular manner. This method is typically adopted by PPI, where every $(1/U_s)^{\text{th}}$ k-space sample is left unmeasured.

The remaining alternative approaches are stochastic. The most basic approach is Random Undersampling (RUS). Each k-space location is assigned a random number p such that $0 < p < 1$. All locations for which $p < U_s$ are sampled. Although the RUS approach is easy to implement, it frequently leaves localised patches of k-space empty.

A proposed alternative is Poisson Undersampling (PUS) (Yellott, 1983; Nayak and Nishimura, 1998). This is still random, but is designed to sample k-space with a uniform sampling density. This approach starts with an initial randomly placed sample – a second randomly located sample is then added, and if it lies within a certain distance (r_p) of the first sample it is rejected, else it is accepted. The third point in turn must lie more than distance r_p to both the prior points.

This process is repeated for until no more suitable candidate locations exist, at which point the radius is shrunk. This process continues until the correct fraction of k-space has been sampled.

The final approach, as proposed by Lustig (Lustig et al., 2007) in the context of CS, is Variable Density Undersampling, (VDUS). This method recognises the fact that low-frequency k-space data contains higher amplitude coefficients, and therefore chooses to sample them more frequently. This is achieved by creating a probability density function whose amplitude decays from the centre of k-space, as per equation 5.28, where \mathbf{k} is the k-space position, and p is a positive number, which was here set to 4.

$$5.28 \quad P(\mathbf{k}) = \left(1 - \frac{1}{N_x N_y} \sqrt{\mathbf{k}^T \mathbf{k}} \right)^p$$

The presence of a fully sampled centre of k-space was also provided to the RCUS, PUS and RUS patterns. The central 3% of k-space was fully sampled in all trajectories.

Several variants of the proposed trajectories types were created:

- Sampling patterns of each trajectory class were created with the following undersampling rates: $U_s = [1, 0.75, 0.5, 0.25, 0.125, 0.1]$ (see Figure 5.7).
- At each undersampling rate, two sets of sampling patterns were made:
 - Different samples for different AFI images – referred to as Different Samples, (DS).
 - Same samples for different AFI images – referred to as Same Samples (SS).
- Finally, four versions of each sampling pattern were created to ensure robustness against the random nature of the stochastic trajectories. In the case of RCUS, different regular sampling patterns were created (see Figure 5.8).

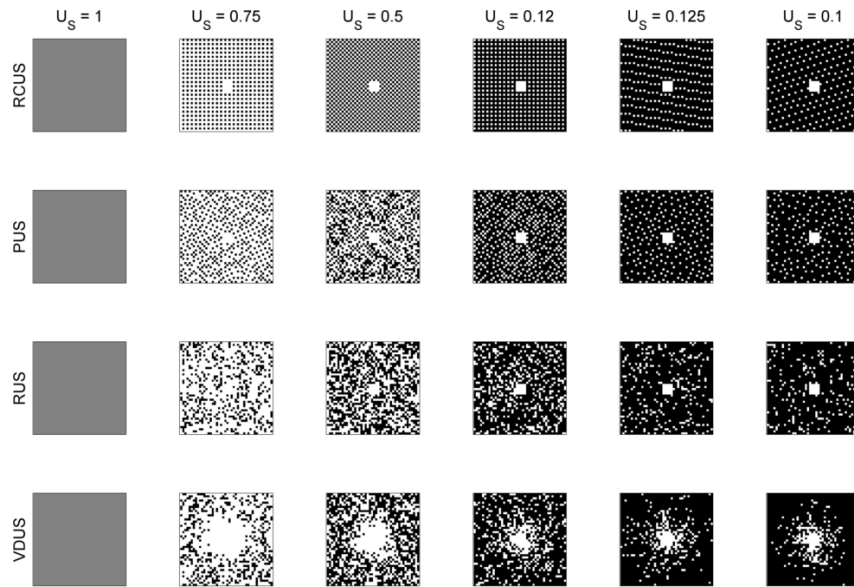


Figure 5.7 – Sampling patters for each trajectory class at many undersampling rates. Each axis is a PE direction.

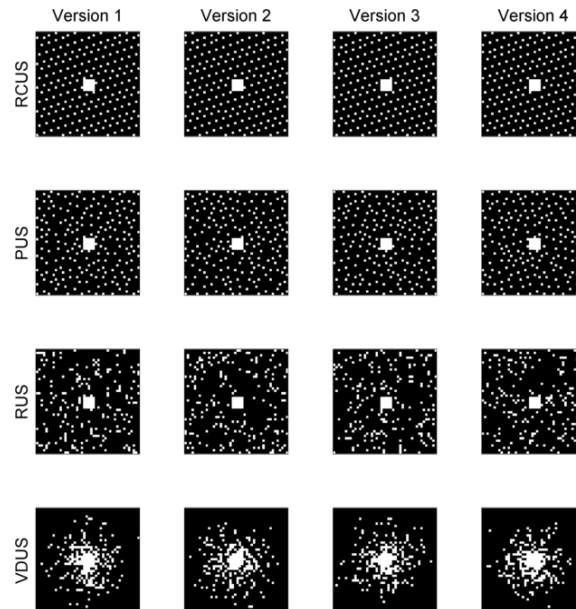


Figure 5.8 – Four versions of each sampling pattern. This example corresponds to $U_s = 0.1$. Each axis is a PE direction.

5.3.2.1.3 Data Reconstruction and Analysis

The synthetic sampled k-space data was inserted into the reconstruction algorithm, which performed reconstructions at each regularisation level. The obtained ratios were extracted and processed to form transmit field maps, $\theta_R\{\lambda, v, s, t, U_S\}$. Here, λ gives the regularisation parameter, v is a variable which denotes which of the four instances of each trajectory is used, s is a label denotes whether the same ($s=1$) or different ($s=0$) sampling of k_1 and k_2 was used, and t denotes which class of trajectory was used. These reconstructions were then assessed against the gold standard, θ_{GS} , using equation 5.29.

$$5.29 \quad E_{all}(\lambda, v, s, t, U_S) = \frac{1}{N_{mask}} \sum_{mask} \left| \theta_R(\lambda, v, s, t, U_S) - \theta_{GS} \right|$$

5.3.2.2 Results

Figure 5.9 shows the reconstruction error versus regularisation parameter value for each trajectory class (columns) and undersampling rate (rows), after averaging across all versions of each trajectory. The blue and red curves denote the SS and DS, respectively. The error bars give the standard deviation across the four versions of the trajectory.

For $U_S = 1$, the reconstruction error remains small for all regularisation levels. There is a small increase in reconstruction error for $\lambda > 10^{-2}$, reaching a maximum of 0.08° at $\lambda = 10^{-2}$. This behaviour reflects the increased emphasis on smoothing over data consistency.

The remaining curves in the presence of undersampling display many similar features. Erroneous reconstructions are found at low regularisation levels, reflecting the underdetermined nature of the unregularised reconstruction. For

intermediate regularisation levels ($\sim 10^{-5} < \lambda < \sim 10^{-3}$), the reconstruction error reduces to a minimum, reflecting the best possible reconstruction. Further increasing the regularisation causes the error to diverge.

This behaviour is seen for both SS and DS. However, the magnitude of the errors differ significantly. In the low regularisation regime, DS achieves reconstruction errors of approximately 20° , as opposed to same sampling, which achieves errors of approximately 2° across U_s levels. Regularisation can significantly improve upon the DS error, but cannot reduce it to below the best error of the SS approach.

The reconstruction consistency of SS is superior to that of DS. This is shown by the width of the error bars at each regularisation level.

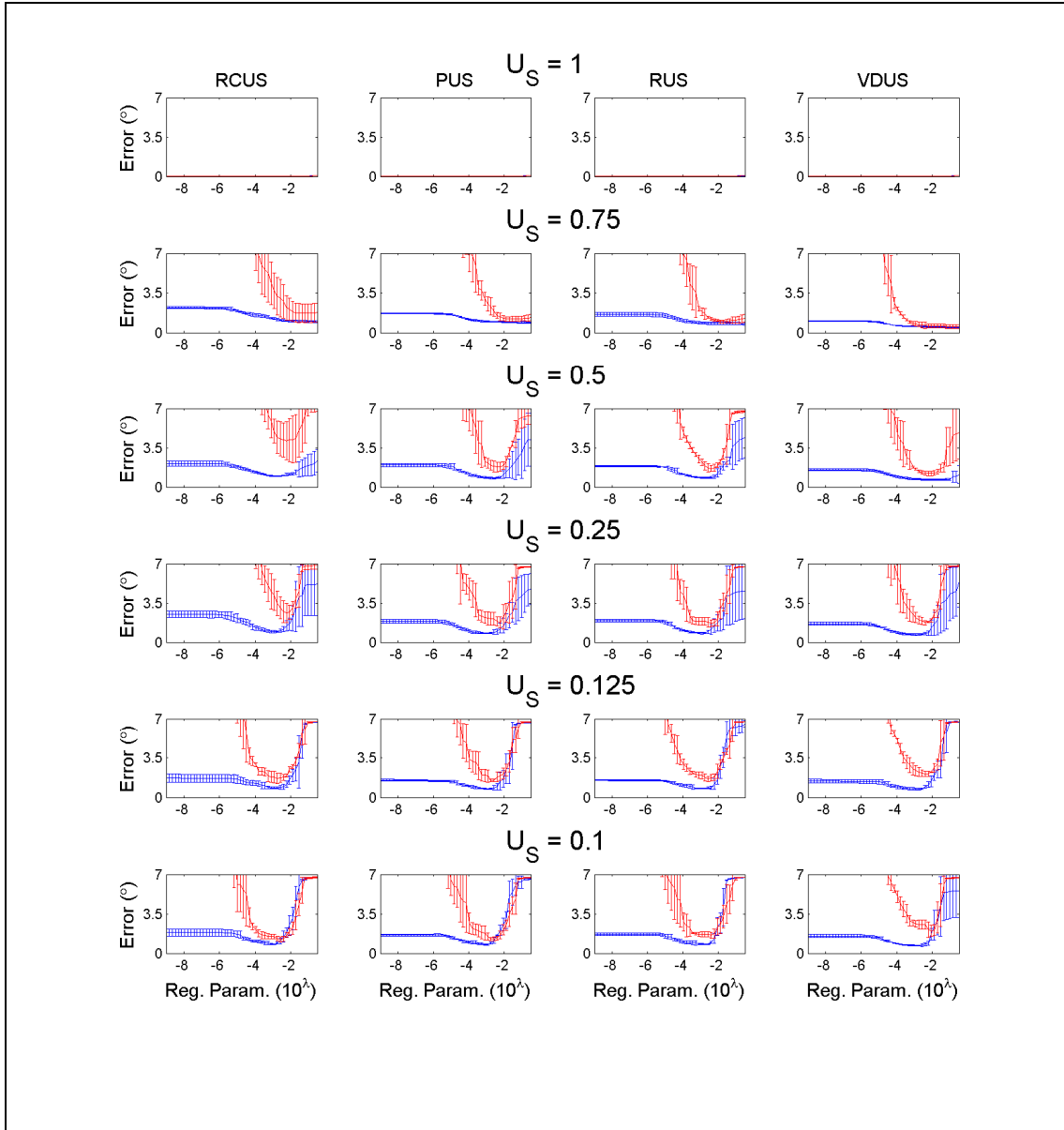
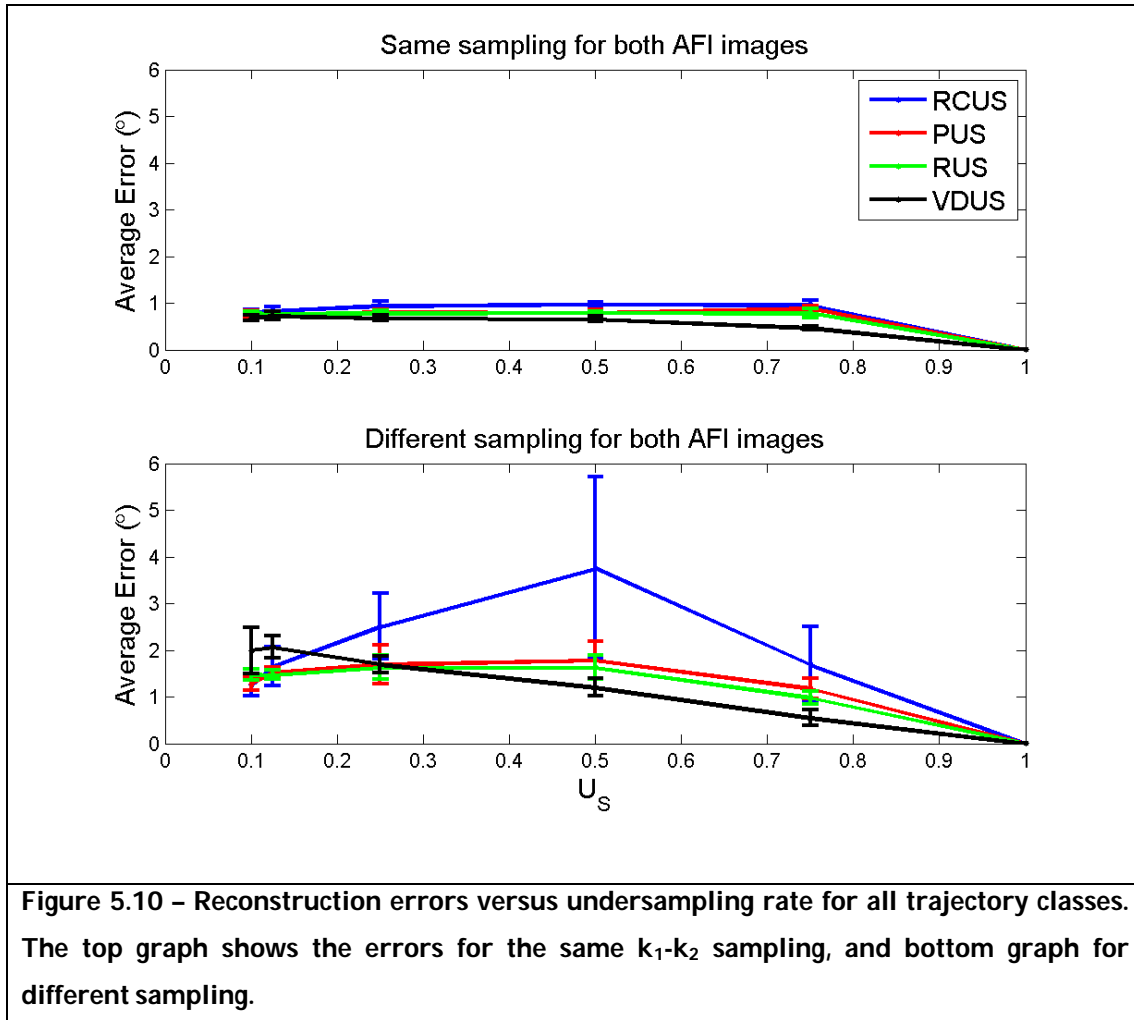


Figure 5.9 – Field map error versus regularisation parameter for all undersampling rates and trajectory types. SS is given by the blue curves, and DS given by the red curves. Each error bar corresponds to the standard deviation of the errors of each individual example of each trajectory.

Figure 5.10 displays the minimum error achieved by each trajectory type at each undersampling rate. The data points correspond to the average of the minimum errors achieved by each trajectory version. The error bars correspond to the standard deviation of the minimum errors of each version.

Using SS for both AFI images significantly improves the quality of the reconstructions. SS errors plateau at a level of approximately 1° for

undersampling rates of $U_s < 0.75$. Different versions of each trajectory are consistent, indicated by the very small error bars. The lowest errors are achieved by VDUS, followed by PUS and PUS. RCUS achieves the highest error for all US rates.



In contrast, DS results in higher average error reconstructions, and more variability between different trajectory versions. The errors for RCUS peaks at $U_s = 0.5$, and then falls to a minimum at $U_s = 0.1$, outperforming all other trajectories. PUS and RUS also peak at $U_s = 0.5$ and fall, but by a lesser degree. VDUS shows a gradual increase in reconstruction error as undersampling increases.

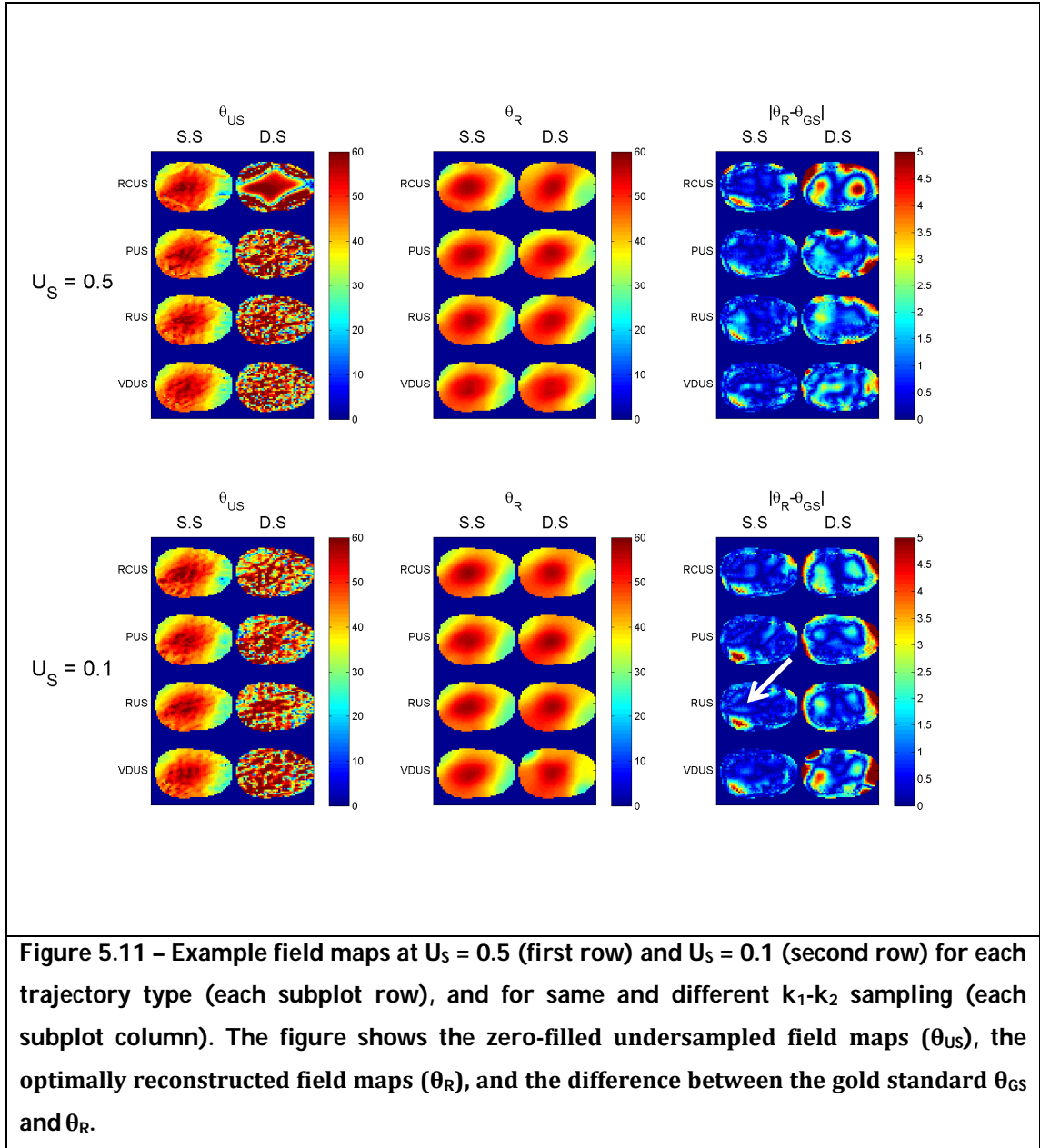


Figure 5.11 shows transmit the zero-filled and reconstructed field maps for both $U_s = 0.5$ and $U_s = 0.1$. It also gives the difference between the reconstructed field maps and the gold standard. The zero-filled maps are both of very low quality, displaying strong undersampling artifacts. However, using SS generates an undersampled field map vastly better than the DS case. The random trajectories display a similar pseudo-random artifact structure. In contrast, RCUS $U_s=0.5$ undersampling generates strong overlapping interference artifacts. This effect is weaker at $U_s=0.1$.

The optimal reconstructed field maps are all smoothly varying functions of space, and have a global shape similar to the gold standard field. The difference images clearly show that the sampling both AFI TR datasets with SS pattern improves the quality of the reconstruction.

5.3.2.3 *Discussion*

These simulations demonstrate that the proposed reconstruction framework can in principle accelerate transmit field mapping. The results highlight the importance on choosing an appropriate sampling strategy.

It was initially expected that DS patterns would yield results superior to SS. This is because more spatial frequency content would be measured, which would in turn feed through to better inform the reconstruction. In practice, using SS outperformed DS. This behaviour can be understood by examining the zero-filled field maps. Using the same sampling yields initial estimates of the field that are far less corrupted than DS. This means that the reconstruction starts at a location closer to the global minimum of the cost function, and hence the optimisation is more likely to converge to a correct solution.

The field maps produced with same sampling accurately replicate the gold standard map. The remaining errors appear diffusely across the object, but can have local regions of higher error. At $U_s = 0.1$, local errors of up to 5° were seen in a bottom left of the field map (white arrow).

The obtained results also display an important counter-intuitive feature. Reducing the number of samples should increase the error of the reconstructed field map. However, the average error of all sampling patterns with SS remains approximately constant at 1° for undersampling rates $U_s < 0.75$. This behaviour indicates that the data at the edges of k-space contributes less information relative to the data at the centre of k-space. This is because undersampling reduces the density of samples everywhere except at the very centre. This observation is further explored in the next section.

5.3.3 Study 2

The results presented in the previous section imply that accurate transmit field maps can be produced using a small amount of data from the centre of k-space. This study investigates this property by altering the dataset to maximise the information content across all spatial frequencies. This was achieved by selecting an anatomical region with strong transmit field inhomogeneity, choosing a very tight FOV, and selecting an image resolution that is just sufficient to capture the field dynamics.

5.3.3.1 *Methods*

5.3.3.1.1 **Dataset**

An anatomical location with the highest degree of RF inhomogeneity was selected. The pelvis showed the highest degree of inhomogeneity, and was therefore chosen. This is the case as the anatomy is large relative to the RF wavelength, and therefore field interference occurs.

After cropping the model to a tight FOV, the data matrix was of size 88x54, corresponding to a FOV of 440x270cm at a resolution of 0.5mm. The anatomy was again manually segmented into separate tissue regions: subcutaneous fat ($T_1=365\text{ms}$, $T_2=133\text{ms}$), cerebrospinal fluid in the spinal canal (CSF, $T_1=4163\text{ms}$, $T_2=500\text{ms}$), skeletal muscle ($T_1=1412\text{ms}$, $T_2=50\text{ms}$), spinal cord ($T_1=993\text{ms}$, $T_2=78\text{ms}$) and blood vessels ($T_1=1932\text{ms}$, $T_2=275\text{ms}$) ((Han et al., 2003; Stanis et al., 2005)). The individual transmit and receive fields corresponding to this location were also extracted and normalised, as before.

The AFI equation was again used to generate images I_1 and I_2 . The transmitters were driven in 'leave-one-out' LCs, as this further increased the field inhomogeneity. Each image was then Fourier Transformed to generate high-resolution k-space datasets.

Finally, the following procedure was then performed to determine the minimum appropriate resolution of k-space.

1. Take the high-resolution k_1 and k_2 of a single k-space configuration.
2. Truncate both k-spaces by factor U_T , where $U_T=100$ corresponds to no truncation and $U_T=0$ corresponds to full truncation (i.e. no data left in k-space)
3. Zero-fill and again take the FT of each k-space. Calculate the flip angle from the images.
4. Calculate the error with respect to the full resolution transmit field using equation 5.29.
5. Repeat procedure for each transmit configuration.

The results of this process are given by Figure 5.12. As the level of truncation increases, the error gradually increases across all channels. The error increases at a greater speed for $U_T < 36$, and therefore this is the chosen truncation level. This corresponds to a k-space and image size of 32×20 , which corresponds to a resolution of 1.4×1.4 cm (the FOV remains the same).

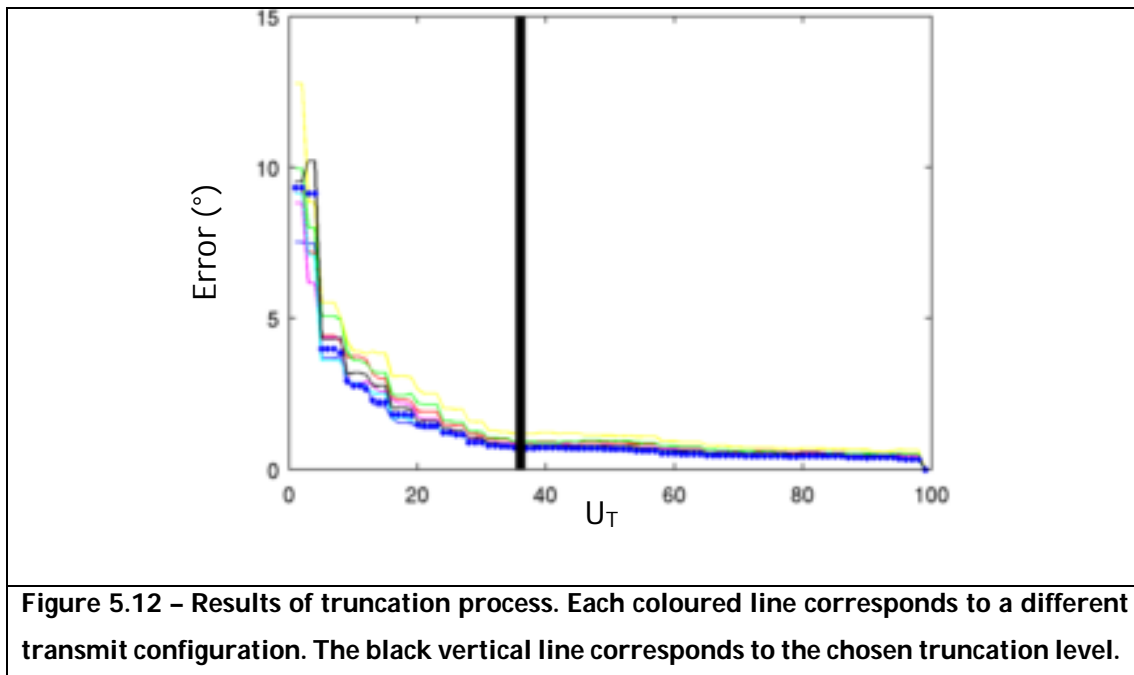


Figure 5.12 – Results of truncation process. Each coloured line corresponds to a different transmit configuration. The black vertical line corresponds to the chosen truncation level.

This truncated dataset is then defined as the gold standard, as it does not contain redundant spatial information.

5.3.3.1.2 *Sample Generation*

A set of sampling patterns was generated in order to test the contribution to reconstruction quality of central and non-central k-space data. The Poisson sampling strategy was chosen as it allows for well-defined definition of the centre mask. RUS performed equally as well as Poisson, and would also have been a valid choice. VDUS was not used, as it requires choosing an appropriate value of parameter p . The sampling patterns of TR1 and TR2 were selected to be the same, as indicated by the superior quality reconstructions offered by SS in Study 1.

The following undersampling rates were used: $U_s = [1, 0.5, 0.45, 0.4, 0.35, 0.3]$. Seven patterns were created at each undersampling rate, each with a different size centre radius (CR). The seven sizes of centre radius sampled 0%, 0.1%, 0.8%, 1.4%, 2%, 3.3% and 4% of k-space, respectively. The sampling patterns generated are shown in Figure 5.13.

5.3.3.1.3 *Reconstruction and Analysis*

The generated k-space measurements and sampling patterns were reconstructed and analysed in the same manner as before. The range of regularisation parameters were extended from $\lambda=10^{-9}$ - $10^{-0.5}$ to $\lambda=10^{-9}$ - 10^1 .

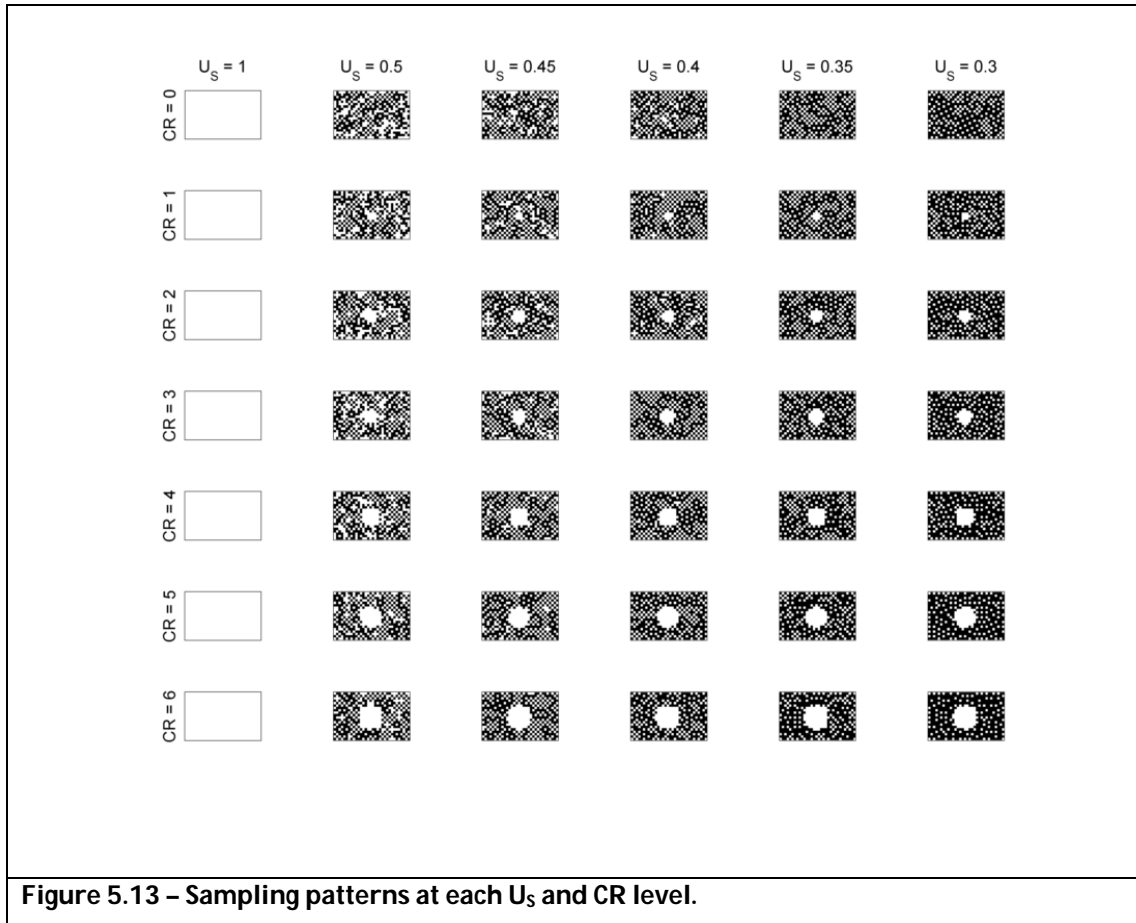
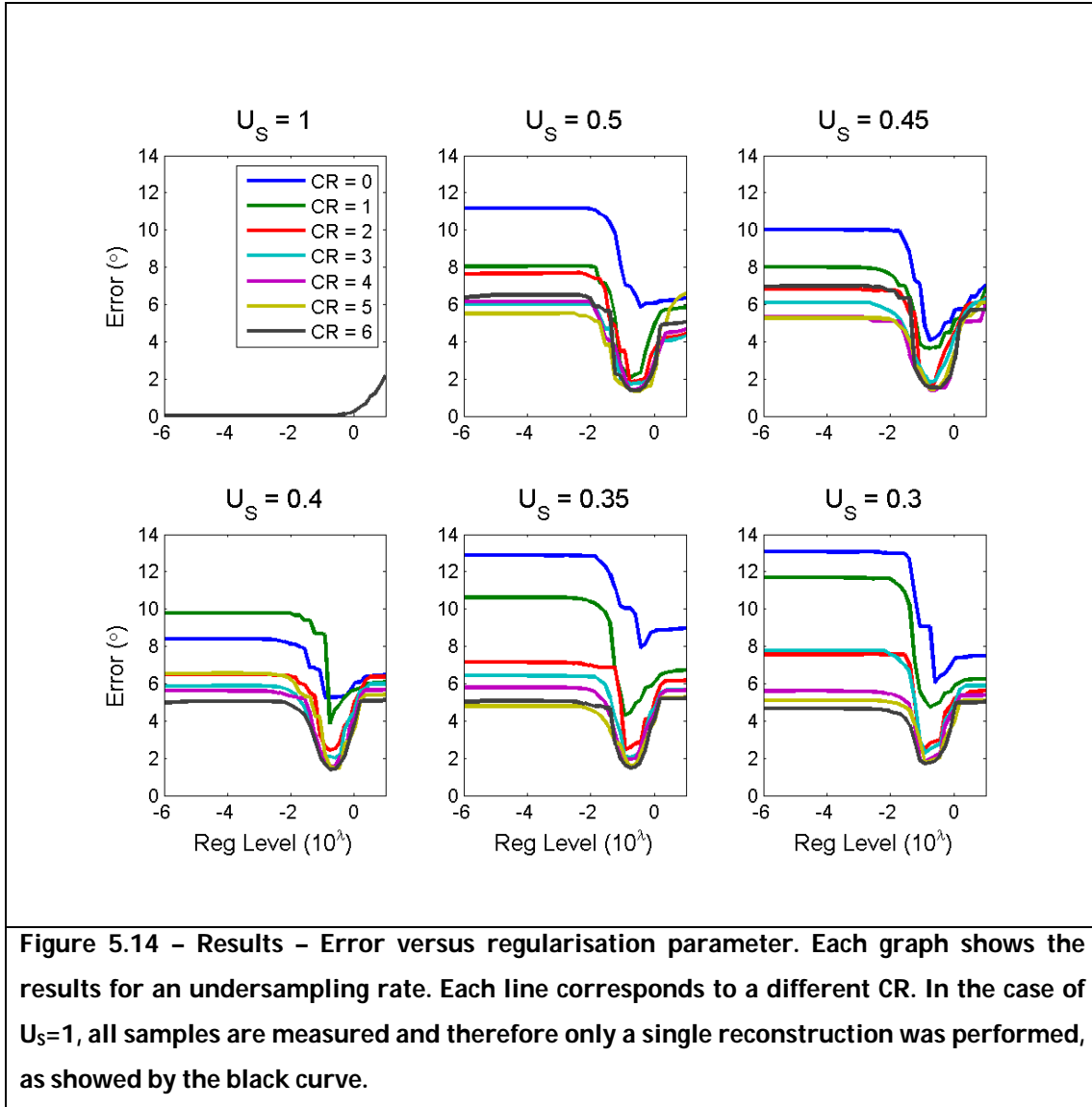


Figure 5.13 – Sampling patterns at each U_S and CR level.

5.3.3.2 Results

Figure 5.14 and Figure 5.15 display the field map errors as a function of regularisation parameter for all CR and U_S . All curves show the expected behaviour of high error for low λ , low error for appropriate λ and increasing error for high λ . The optimal regularisation level lies in the range $10^{-1} < \lambda < 10^0$.



The results in Figure 5.14 reveal two categories of solution. The CR= 0 and CR=1 sampling strategies consistently perform worse than larger CR patterns. The CR=1 case can only match the larger CR schemes for $U_s=0.5$. For $CR>1$, they all perform consistently across U_s rates.

This is further demonstrated in Figure 5.15. The CR=0 case shows erratic results. The error of the optimal reconstructions at each U_s does not correlate with U_s (i.e. one would expect the best reconstructions to be for $U_s=1$, then $U_s=0.5$, $U_s=0.45$, etc. The observed order is [1, 0.45, 0.4, 0.5, 0.3, 0.35]. The expected order returns for CR=1. For $CR>1$, the trend of stable reconstructions independent of undersampling rate is seen again.

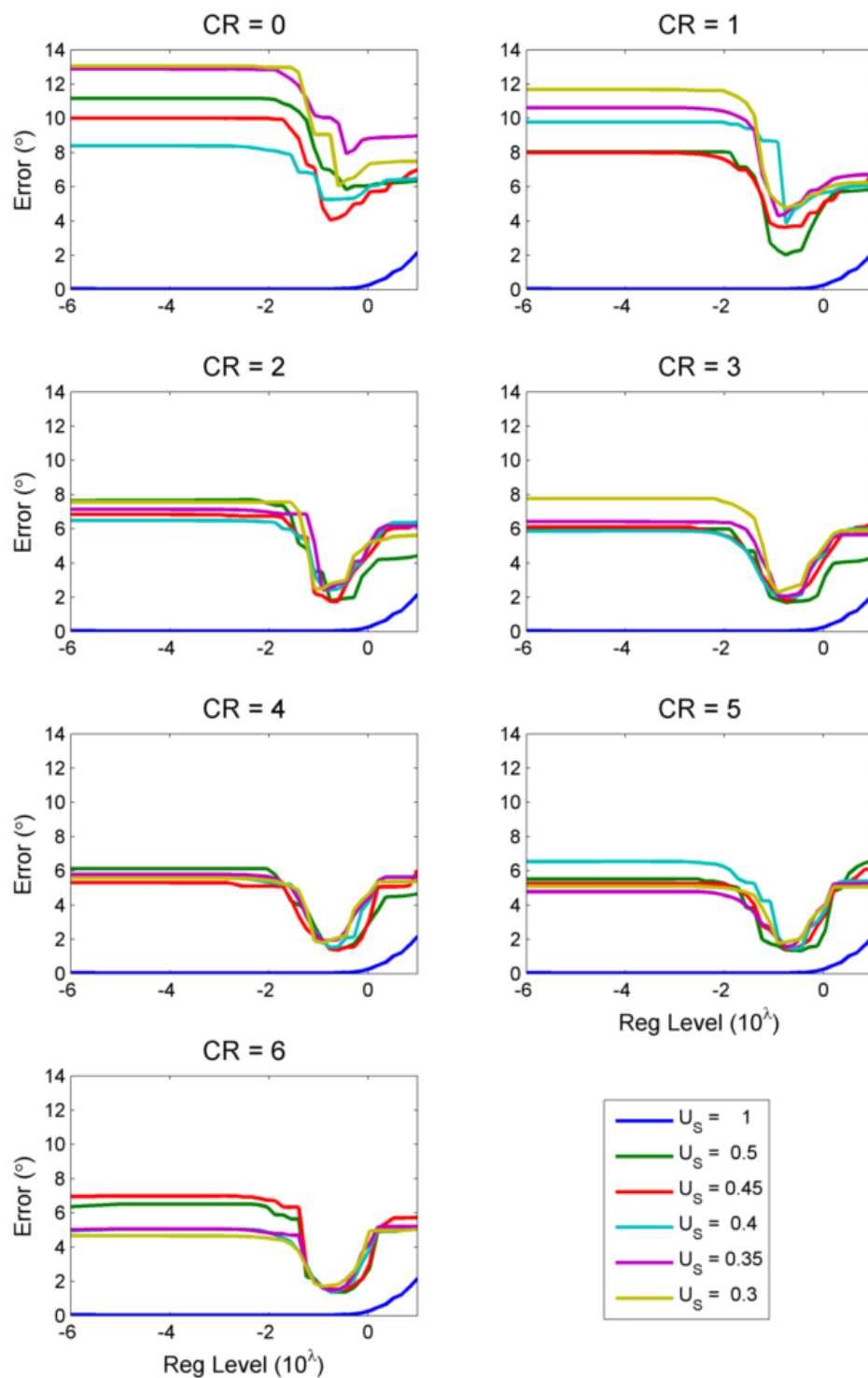


Figure 5.15 – Results – Error versus regularisation parameter. Each graph shows the results for a centre radius level. Each line corresponds to a different U_s .

This is further visualised by Figure 5.16. The error matrix demonstrates that the worst reconstructions are achieved by having low centre sampling. Increasing CR above 2 significantly improves the reconstruction. The error plot demonstrates the erratic behaviour of CR=0, and how CR>2 yields good reconstructions independently of U_s . This plot also reveals the gradual improvement of the reconstruction quality as CR increases, although the size of the improvement is marginal.

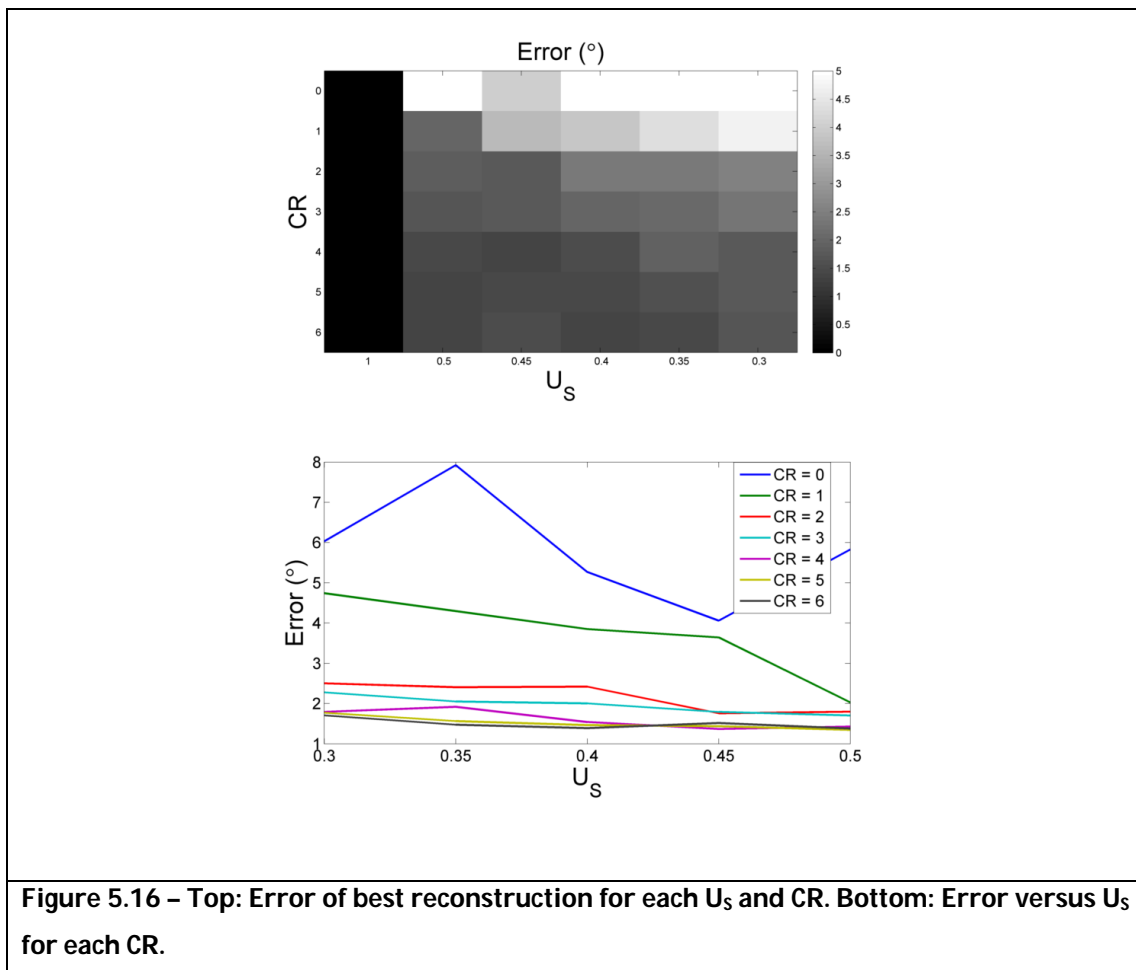
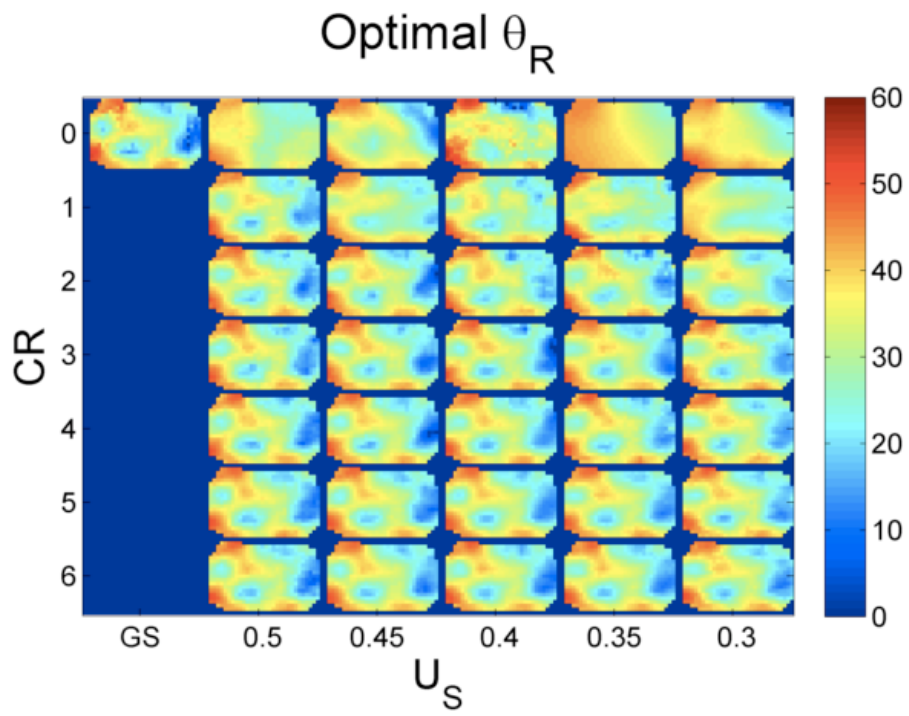


Figure 5.17 shows the reconstructed field maps and their error with respect to the gold standard. The CR=0 field maps show variable results. Reconstruction stability increases as CR increases. The reconstructed fields are smooth and have the same shape as the gold standard. Errors appear as random fluctuations, with a generally higher value in the regions of low transmit field intensity on the right of the object.

a)



b)

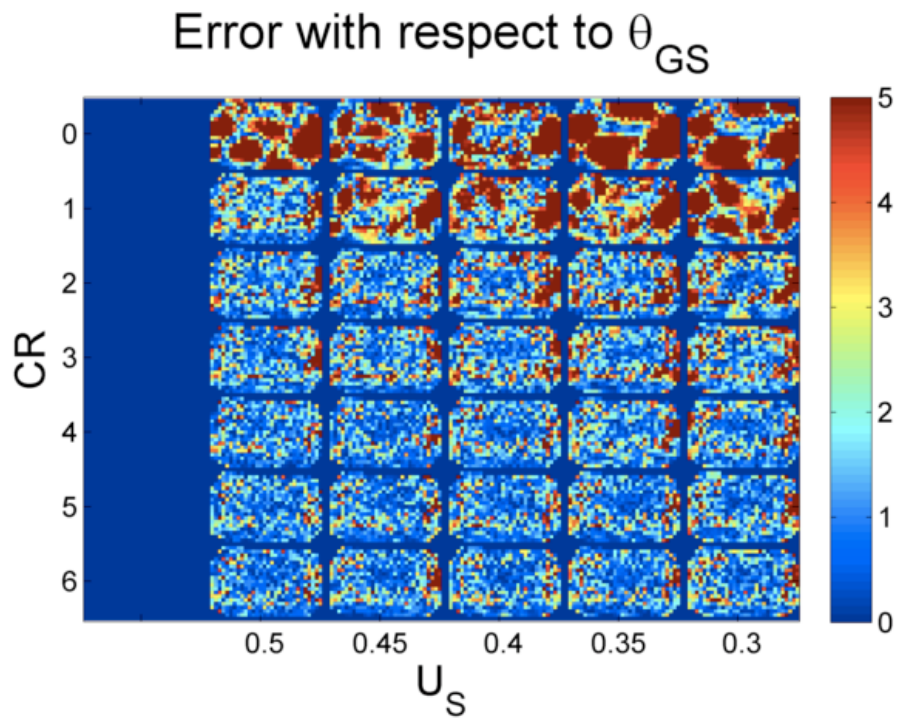


Figure 5.17 – a) Gold Standard transmit field (top left sub-image), and optimal reconstructions at all CR and U_S . b) Error maps with respect to gold standard.

5.3.3.3 Discussion

In this section the proposed reconstruction method was tested on an alternative dataset with a new range of sampling schemes. The intention was to explore the benefits of sampling the centre of k-space in contrast to sampling the outside in a random fashion.

The new dataset was created with explicit intent to ensure that it contained no redundant data. This was achieved by truncating the high-resolution k-space so that any further decreases in resolution would significantly increase the field maps error with respect to the high-resolution version.

Despite these efforts, the same behaviour as in the first study was observed. Fully sampling the centre of k-space ensured that the results were largely independent of the undersampling rate.

5.3.4 Study 3

The two previous studies have explored the relationship between the proposed reconstruction method and the how the data is sampled. Both studies demonstrated that the reconstruction scheme worked as intended. However, the studies showed that the most important factor was how the centre of k-space was sampled.

Based on this observation, this study adopts a wholly different approach to k-space sampling. The previous study began by defining the gold standard dataset. This was designed to mimic an in-vivo dataset, which would always be acquired at low-resolution. This reflects the fact that the field is expected to be smooth, and that the scan would be as fast as possible. In study 2, all further undersampling was compared to this low-resolution gold standard, referred to as $\theta_{GS,LR}$.

However, this definition does not acknowledge the fact that the k-space truncation has already introduced differences with respect to the *true* transmit

field, as calculated by the FDTD simulation. This in turn forces a change of perspective. It is invalid to ask the question of what U_s can be tolerated compared to what is typically measured when field mapping in-vivo. The appropriate question is: "We can afford to devote T amount of time acquiring a transmit field map – which samples should be acquired and how should they be reconstructed?"

This question is explored in this study.

5.3.4.1 *Methods*

5.3.4.1.1 Dataset

The FDTD pelvis dataset was used as before to generate the synthetic AFI k-space data using $n = 4$ and with the transmit field scaled so that quadrature drive achieved a 60° excitation. Eight sets of data were generated, corresponding to 'leave-one-out' LCs of transmit elements. These datasets were defined on the native FDTD high-resolution grid, with resolution of 5x5mm and FOV of 220x27cm.

5.3.4.1.2 Sampling

As discussed in the introduction, this study alternatively tries to find the optimal sampling scheme for a number of given samples, N_s .

Consider the high-resolution k-space, given by Figure 5.8a. The distance between each k-space sample defines the FOV, which is fixed. The selected image resolution is controlled by the number of samples acquired in the k_x and k_y directions. Figure 5.8b shows several possible sampling areas at the centre of k-space. A larger mask corresponds to a higher resolution. The choices of N_s in this study correspond to the number of samples of each of the sampling areas.

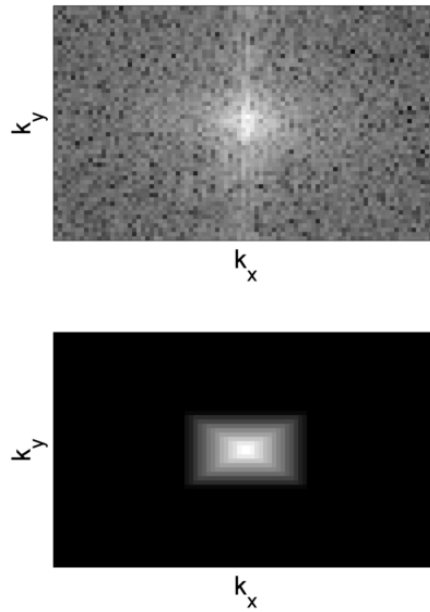


Figure 5.18 – High resolution k-space (top), and resolution masks (bottom).

The results from the previous studies are used to inform the sampling schemes here. At a given N_s level, all of the samples are first placed in the centre of k-space. This choice is then perturbed in two ways, as shown in Figure 5.19. The first alteration is to expand the allowed region in which samples can be placed. This is shown by different rows. The second adaption is to reduce the fully samples centre region at the centre of k-space. The remaining samples are placed using PUS in the allowed sampling area. The level of k-space extension is given by the Extension Level, EL, and the level of centre sampling reduction is given by the Central Reduction, CR.

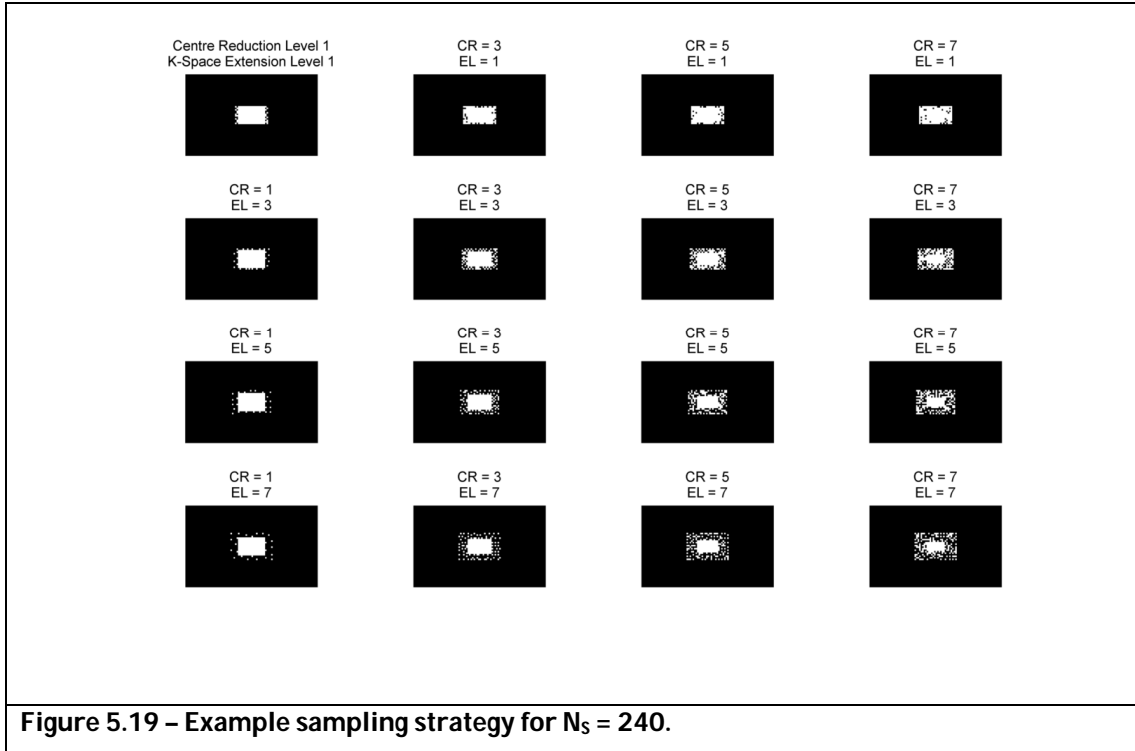


Figure 5.19 – Example sampling strategy for $N_s = 240$.

CR and EL factors of up to 8 are used in this study. Smaller CR factors are used when the centre cannot be shrunk any further. Smaller EL factors are used when further sampling area expansion causes the optimisation problem to become underdetermined. This originates from the fact that larger EL increases the resolution of image and ratio, increasing the number of variables that need to be solved for.

5.3.4.1.3 Reconstruction

Multiple reconstructions were performed, corresponding to all N_s levels, all trajectory variants at this level, and for regularisation levels ranging from $\lambda=10^{-9}$ to $10^{-0.5}$. This was repeated for each transmit configuration.

The ratio was again solved for exclusively inside the mask. Masks were generated at each resolution by generating a truncated image at each N_s . A mask was drawn manually over the regions of the image containing signal.

5.3.4.1.4 Analysis

Two sets of field maps were created. The first corresponds to the standard method of acquiring data from the centre of k-space, taking the (zero-filled) Fourier Transform and then forming field maps, θ_{ZF} . Field maps are generated for all sampling levels. The error relative to the high-resolution field map, $\Delta\theta_{ZF}$, is calculated using equation 5.29.

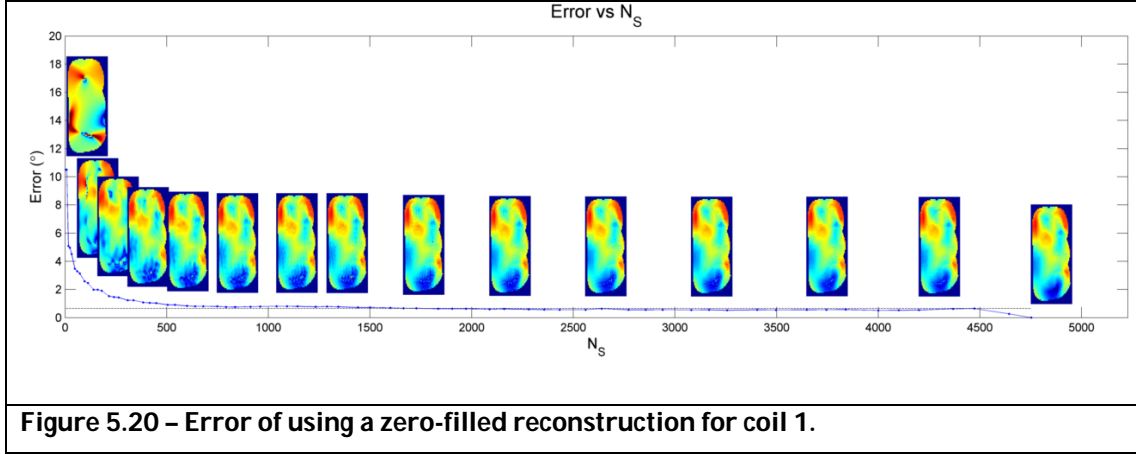


Figure 5.20 – Error of using a zero-filled reconstruction for coil 1.

Figure 5.20 demonstrates this error for the first transmit configuration. The first two truncation steps increase the error significantly to $\Delta\theta_{ref}=0.8^\circ$. These errors arise from the appearance of ringing in the calculated images. This is an artifact, originating from the specific alignment of the body model to the Cartesian grid. Further truncation does not increase the error, until $N_s \approx 1000$. Further reductions in sampling produce a faster increase in error levels.

The fields reconstructed using optimisation are analysed in a similar manner. Each reconstruction outputs image I_1 and the ratio r at the resolution corresponding to the k-space extent of the sampling pattern. Image I_2 was synthesised from the product of I_1 and r . I_1 and I_2 were then Fourier Transformed, zero-filled and inverse Fourier Transformed in order to render them at the full FDTD spatial resolution. Their ratio was taken and transmit field map calculated, θ_R . The reconstructed field map error, $\Delta\theta_R$, is then calculated relative to the true FDTD high-resolution field, again using equation 5.29. The field map of minimum error is selected from all of the reconstructions with different regularisation values.

A further error metric is defined by equation 5.30. The relative error, Err_{rel} , gives the ratio of errors of the reconstructed field maps and ZF field maps, accounting for the reference error. Reconstructed field maps which are better than the ZF equivalent yield Err_{rel} lower than 1.

$$5.30 \quad Err_{rel} = \frac{\Delta\theta_R - \Delta\theta_{ref}}{\Delta\theta_{ZF} - \Delta\theta_{ref}}$$

5.3.4.2 Results

Figure 5.21Figure 5.22 display the reconstructed and zero-filled field map errors of transmit configurations one and five, respectively. In both cases, the zero-filled error increases as the number of samples decreases. The errors achieved by using the proposed reconstruction scheme is capable of achieving both increased and reduced errors, depending on the particular sampling pattern. Improved performance can be achieved in the approximate range $32 < N_s < 400$, corresponding to scan times of 5.7s to 72s, assuming a $TR_1/TR_2=0.18s$.

Figure 5.23 and Figure 5.24 display the relative errors Err_{rel} for transmit configurations 1 and 5, respectively. A clear pattern is seen in the data. The proposed reconstruction scheme outperforms zero filling when the trajectory has a large sampling area (and therefore a high resolution) and has a significant portion of the samples at the centre of k-space.

Figure 5.25 and Figure 5.26 show the reconstructed field maps and their error with respect to the gold standard for a range of sampling levels. For low sampling ($N_s=32$), both methods have strong errors. Increasing N_s improves both methods. However, the proposed reconstruction produces field maps of lower error for fewer samples.

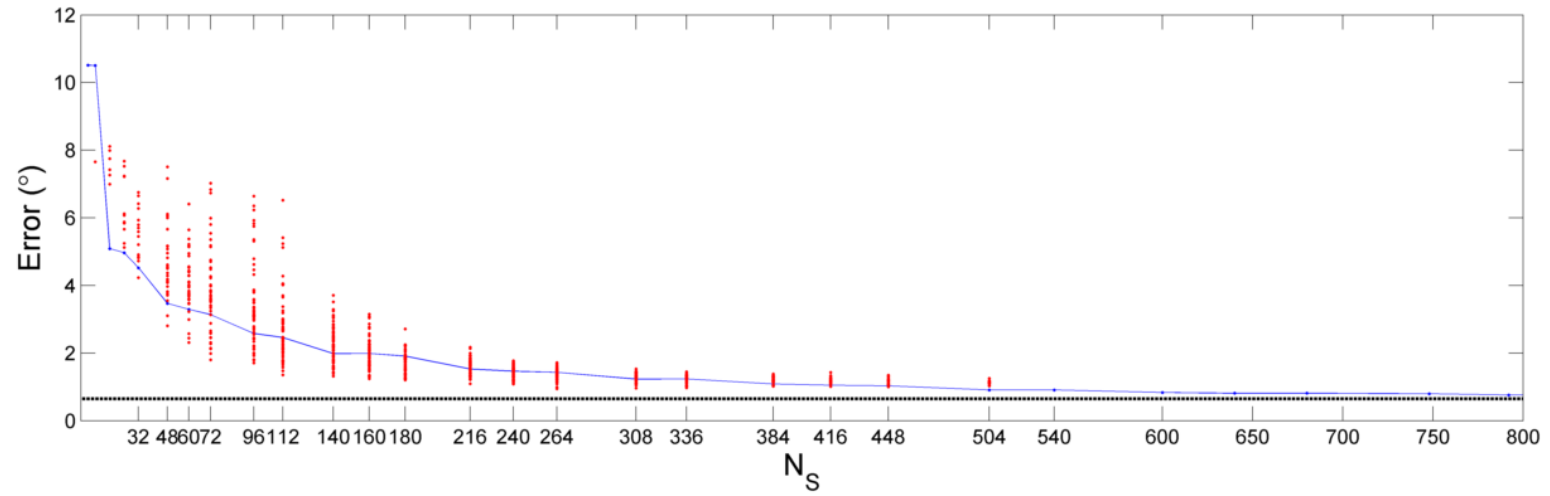


Figure 5.21 – Reconstruction error versus N_s for transmit configuration 1. The blue line gives the zero filled reconstruction error. The red dots display the error of the optimisation field maps. Each dot represents a particular trajectory at each sampling rate. The black dotted line shows $\Delta\theta_{\text{ref}}$.

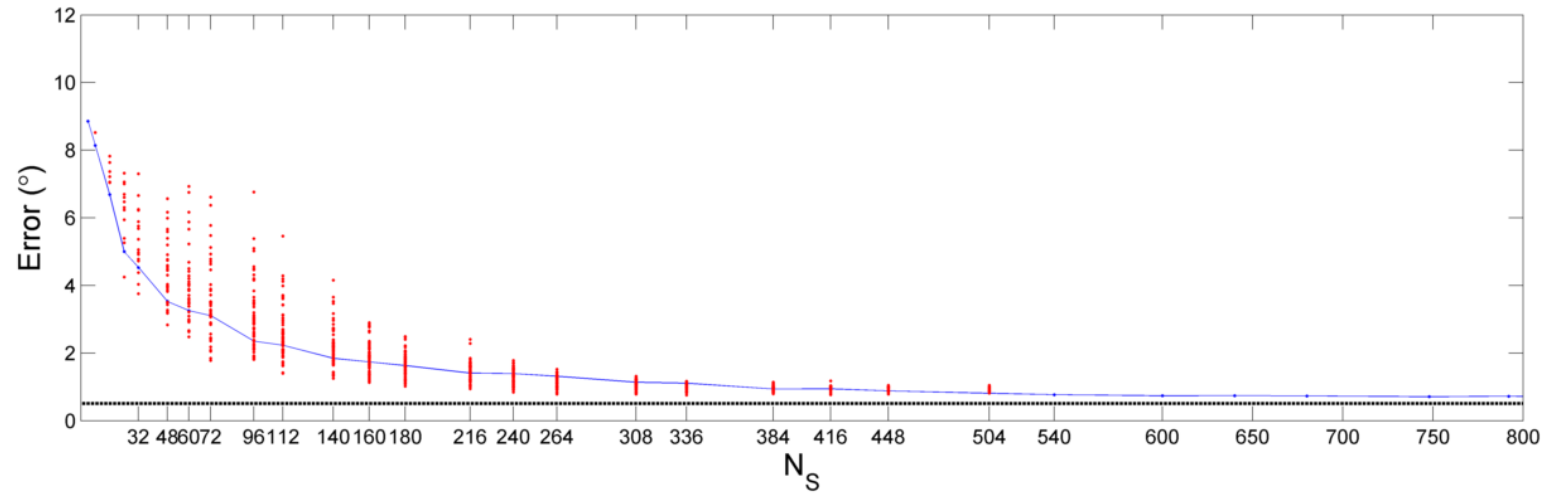


Figure 5.22 – Reconstruction error versus N_s for transmit configuration 5. The blue line gives the zero filled reconstruction error. The red dots display the error of the optimisation field maps. Each dot represents a particular trajectory at each sampling rate. The black dotted line shows $\Delta\theta_{\text{ref}}$.

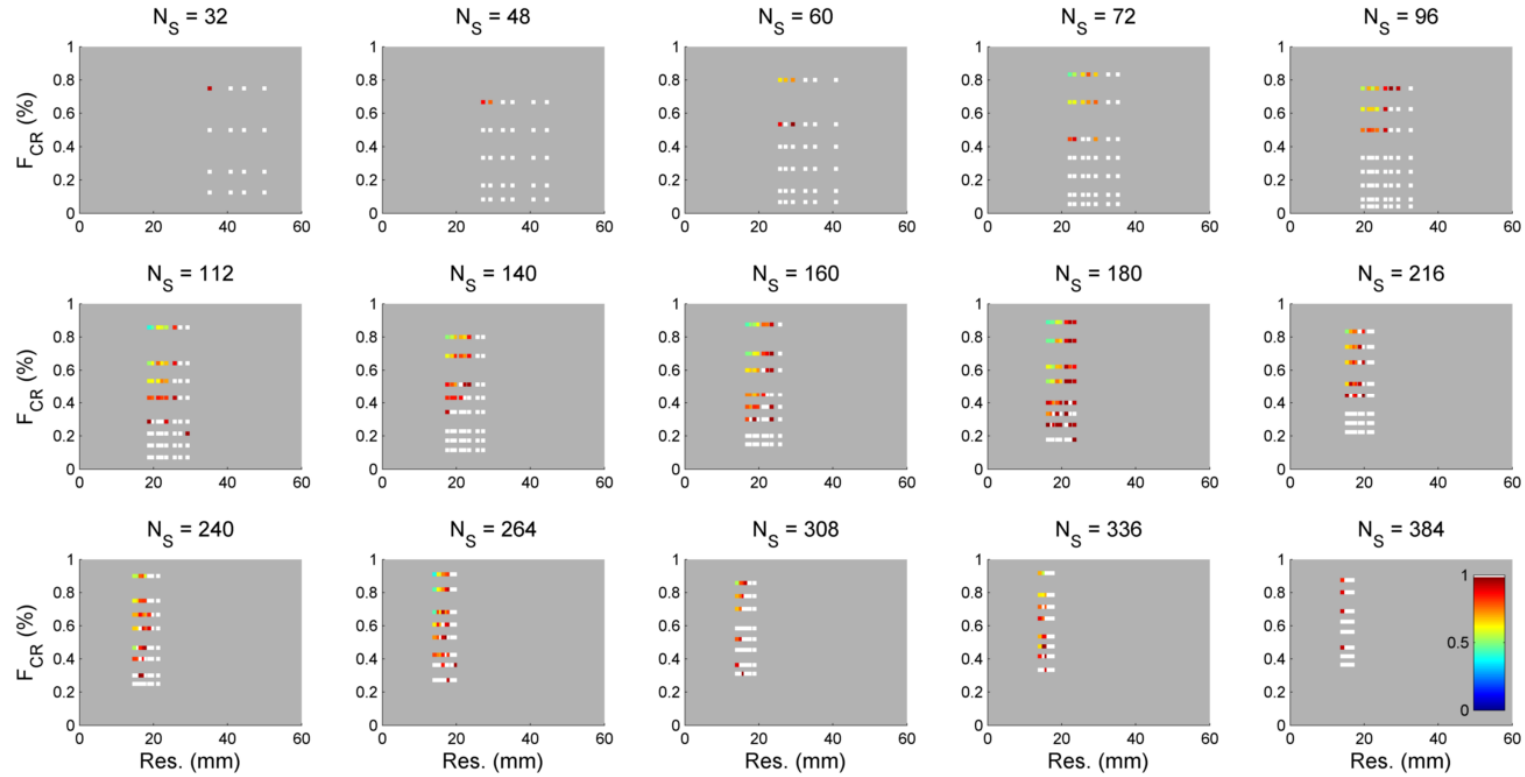


Figure 5.23 – Transmit configuration 1 – relative error associated with each trajectory type for many N_S . The x-axis of each plot corresponds to the effective resolution of the sampling pattern, and the y-axis corresponds to the fraction of samples at the centre of k-space. The colour of each dot corresponds to Err_{rel} . White dots have $Err_{rel} > 1$.

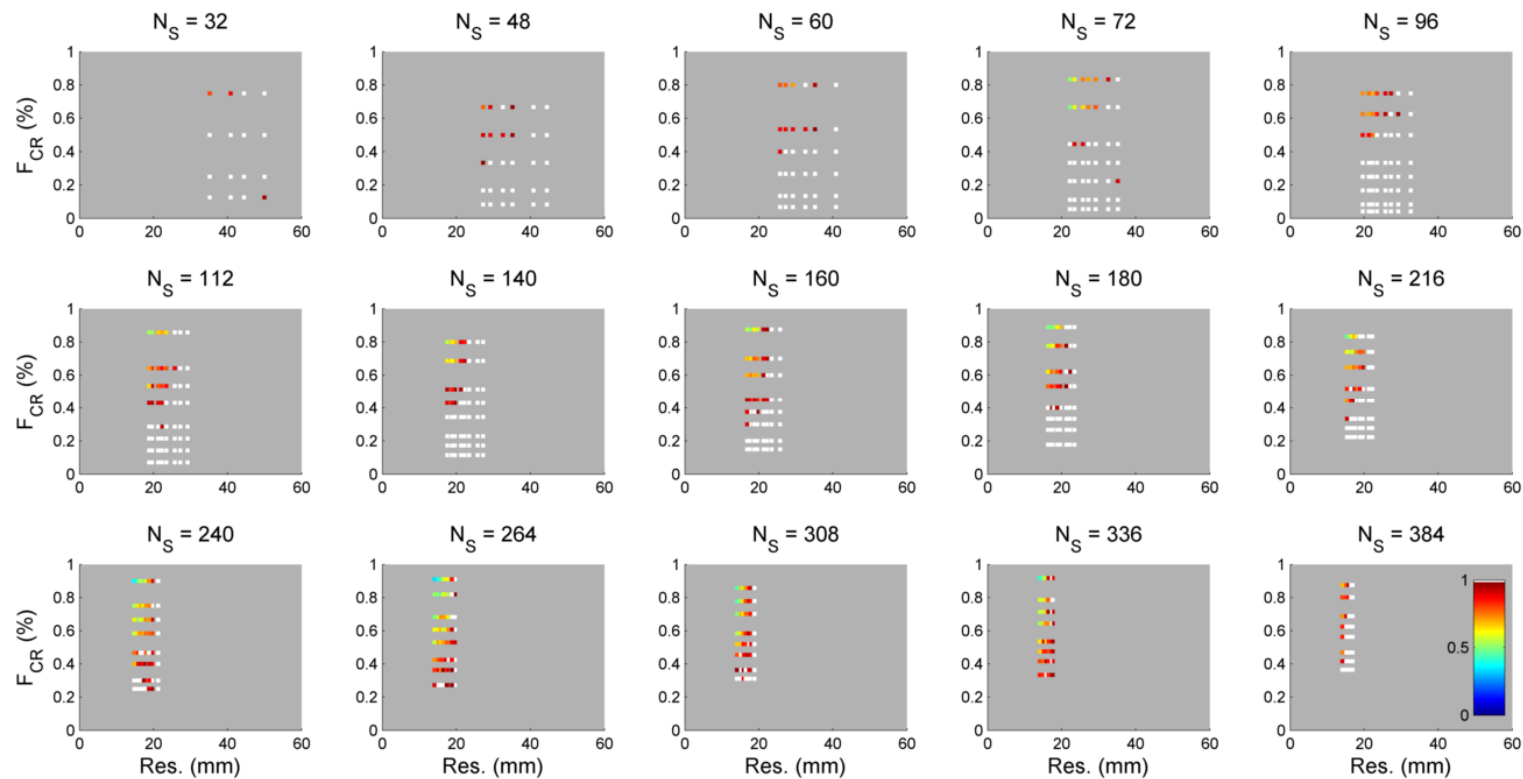


Figure 5.24 - Transmit configuration 5 – relative error associated with each trajectory type for many N_s . The x-axis of each plot corresponds to the effective resolution of the sampling pattern, and the y-axis corresponds to the fraction of samples at the centre of k-space. The colour of each dot corresponds to Err_{rel} . White dots have $Err_{rel} > 1$.

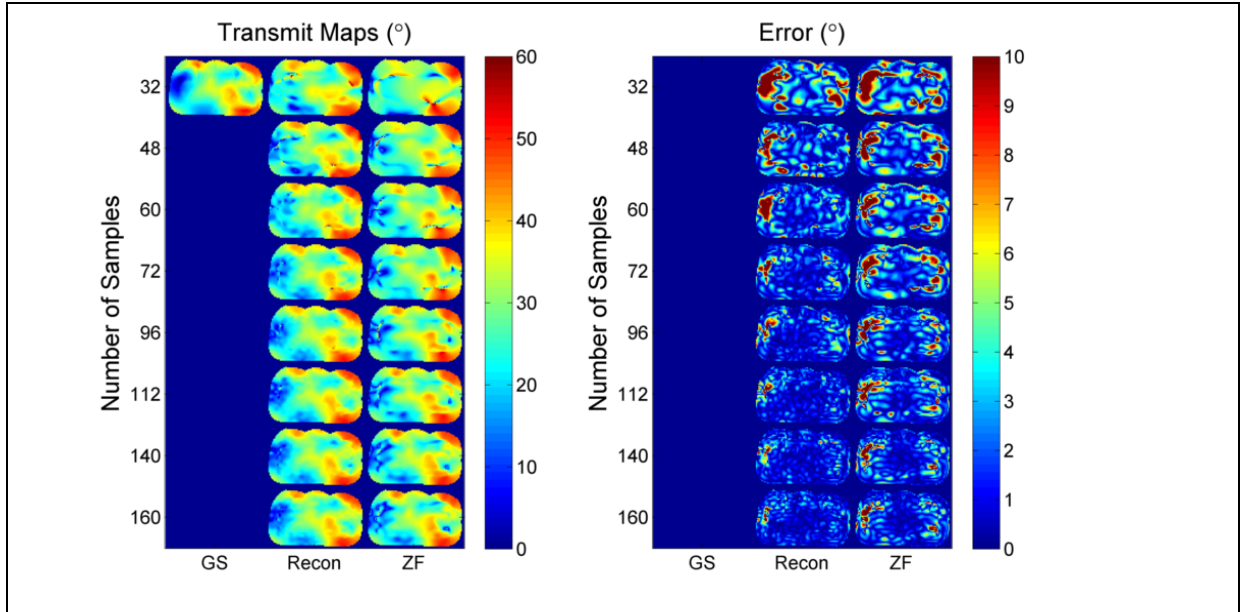


Figure 5.25 – Transmit field maps (LC 1) (left) and their error with respect to gold standard. In each image, left column has θ_{GS} , centre column has reconstructed field maps and right column has zero filled maps. Each row is a different N_s .

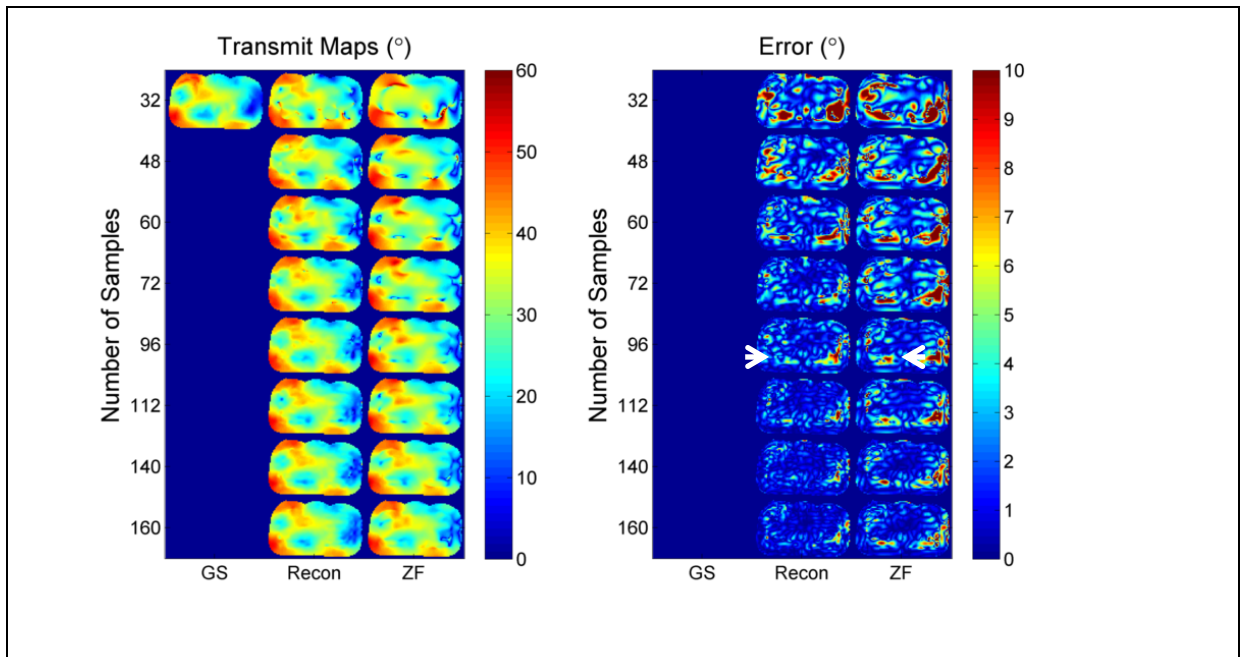


Figure 5.26 - Transmit field maps (LC 5) (left) and their error with respect to gold standard. In each image, left column has θ_{GS} , centre column has reconstructed field maps and right column has zero filled maps. Each row is a different N_s .

5.3.4.3 Discussion

The results presented in this study show that using the proposed reconstruction technique can produce superior field maps than using zero-filling. The alternative

perspective adopted in this study is not widely acknowledged by the wider MRI community. It is normally assumed that field maps are smooth, and that a low-resolution acquisition is sufficient to capture the field dynamics. The results here demonstrate that truncation inherently introduces errors, and that these can produce significant local errors in the calculated field map. Consider for example the reconstructed fields for $N_s=72$ in Figure 5.26. The ZF solution has a strong local area in the left of the object that is largely corrected by using the regularised approach (white arrows).

The sampling extension level and central sampling level determine the quality of the reconstructed maps. The required large ELs for low error reconstructions allow the finite difference regularisation term to work on a finer spatial grid, creating a finer smoothness. The lower error arising from having the majority of points at the centre of k-space agrees with the results of the previous two studies.

This analysis would benefit from two further investigations. Firstly, the effects of noise on the reconstruction have been neglected. This would affect both the ZF and regularised approaches, but how sensitive the techniques are remains to be seen. Secondly, this study did not consider the case of full centre sampling, and only altering the reconstruction resolution.

A remaining issue is how to best choose the regularisation parameter. In this work, the optimal point was chosen using knowledge of the gold standard. This isn't known when performing standard scanning. As an alternative, simulations such as those performed here can be used to find the range of optimal regularisation values that can be applied on real data. The work here also uses prior knowledge of the object mask, inside of which the ratio is solved for. In reality, this mask can either be obtained from the initial survey scan, or the ratio can be solved for across the FOV.

5.4 Discussion

The work presented in this chapter demonstrates that the proposed reconstruction scheme can produce superior field maps than the standard approach. It was shown that the notion of achieving acceleration via undersampling is a fictitious idea: the process of acquiring an image at a finite resolution is already approximating the true field. The true quantity of interest is how well can reconstructed field maps approximate this true field for a given number of samples. If you must very accurately measure the field, this can be achieved using a standard reconstruction with lots of samples. Conversely, if you can only afford the time to acquire few samples, then the approach presented here can offer a closer version of the field than via zero filling.

Similar methods to those developed here have been used in other areas of MRI, specifically parallel imaging ((Ying and Sheng, 2007; Uecker et al., 2008)). These approaches, such as JSENSE, attempt to jointly estimate the image and individual coil sensitivities of an undersampled multi-coil reconstruction. Whereas here we have two images and a single smooth relationship between them, in PPI they have a single image and multiple smooth coil sensitivities. Further work could investigate the utility of these methods for transmit field mapping.

The bilinear structure of the cost-functions proposed here (see section 5.2.1.3) and in PPI approaches have been thoroughly studied by Clason & Von Winckel (Clason and von Winckel, 2010). They highlighted that standard cost-function minimisation methods are not optimally suited to bilinear cost functions and developed a new algorithm that is more efficient and less likely to fall into local minima. A potential further step would be to use this method.

All of the methods presented in references (Ying and Sheng, 2007; Uecker et al., 2008; Clason and von Winckel, 2010) also utilise a different approach to modelling the RF fields. In the proposed cost-function here the ratio is modelled as an array of values, each of which is solved for. The other approaches use sum of polynomials, Fourier coefficients, or an alternative basis. These have the benefit of reducing the number of

variables that have to be solved for. However, care must be taken that the true field can accurately be modelled by the new basis.

Other model-based methods for accelerated transmit field mapping were developed at the same time as this work. In (Doneva et al., 2010), Doneva et. al. proposed a CS method which exploits the fact that all measured images are sparse in the same way. An undersampling factor of 0.5 was achieved.

Lee & Adalsteinsson (Lee and Adalsteinsson, 2010) developed a method in which used the total variation constraint to regularise an undersampled acquisition. Moderate acceleration was achieved, but the regularisation function promoted field maps with stepping artifacts.

The proposed method can be generalised to other mapping approaches that take image ratios. This includes phase-based techniques. For example, the Bloch-Siegert method involves the ratio of two images, and this ratio has magnitude 1 and a phase which reflects the transmit field. This can be modelled in our regime by a complex ratio, for which the real and imaginary parts are smooth.

5.5 References

- Aharon, M., Elad, M., and Bruckstein, A. (2006). K-SVD: An Algorithm for Designing Overcomplete Dictionaries for Sparse Representation. *Signal Processing, IEEE Transactions On* 54, 4311–4322.
- Bernstein, M.A., King, K.F., and Zhou, X.J. (2004). *Handbook of MRI pulse sequences* (Elsevier).
- Block, K.T., Uecker, M., and Frahm, J. (2007). Undersampled radial MRI with multiple coils. Iterative image reconstruction using a total variation constraint. *Magnetic Resonance in Medicine* 57, 1086–1098.
- Brenner, D., Vahedipour, K., Stocker, T., Pracht, E., and Shah, N.J. (2009). Accelerated actual flip angle imaging by means of parallel imaging. In *Proceedings of the ESMRMB 2009*, p. 34.

- Candes, E.J., and Wakin, M.B. (2008). An Introduction To Compressive Sampling. *IEEE Signal Processing Magazine* 25, 21–30.
- Clason, C., and Von Winckel, G. (2010). On a bilinear optimization problem in parallel magnetic resonance imaging. *Applied Mathematics and Computation* 216, 1443–1452.
- Coleman, T.F., and Li, Y. (1994). On the convergence of interior-reflective Newton methods for nonlinear minimization subject to bounds. *Mathematical Programming* 67, 189–224.
- Coleman, T.F., and Li, Y. (1996). An Interior Trust Region Approach for Nonlinear Minimization Subject to Bounds. *SIAM Journal on Optimization* 6, 418.
- Van De Walle, R., Barrett, H.H., Myers, K.J., Aitbach, M.I., Desplanques, B., Gmitro, A.F., Cornelis, J., and Lemahieu, I. (2000). Reconstruction of MR images from data acquired on a general nonregular grid by pseudoinverse calculation. *IEEE Transactions on Medical Imaging* 19, 1160–1167.
- Doneva, M., Nehrke, K., Mertins, A., and Bornert, P. (2010). Compressive B1+ mapping: Towards faster transmit coil sensitivity mapping. In *Proceedings 18th Scientific Meeting, International Society for Magnetic Resonance in Medicine, Stockholm*, p. 2833.
- Eggenschwiler, F., Kober, T., Magill, A.W., Gruetter, R., and Marques, J.P. (2011). SA2RAGE: A new sequence for fast B1+-mapping. *Magnetic Resonance in Medicine* 67, 1609–1619.
- Feinberg, D.A., Hale, J.D., Watts, J.C., Kaufman, L., and Mark, A. (1986). Halving MR imaging time by conjugation: demonstration at 3.5 kG. *Radiology* 161, 527–531.
- Funai, A.K., Fessler, J.A., and Noll, D.C. (2009). Estimating K transmit B1+ maps from K+1 scans for parallel transmit MRI. In *Proc. Intl. Soc. Mag. Reson. Med*, p. 2609.
- Funai, A.K., Fessler, J.A., Yeo, D., Olafsson, V.T., and Noll, D.C. (2008). Regularized Field Map Estimation in MRI. *IEEE Transactions on Medical Imaging* 27, 1484–1494.
- Glover, P.M. (2009). Interaction of MRI field gradients with the human body. *Physics in Medicine and Biology* 54, R99–R115.
- Griswold, M.A., Jakob, P.M., Heidemann, R.M., Nittka, M., Jellus, V., Wang, J., Kiefer, B., and Haase, A. (2002). Generalized autocalibrating partially parallel acquisitions (GRAPPA). *Magnetic Resonance in Medicine* 47, 1202–1210.
- Han, E., Gold, G., Stainsby, J., Wright, G., Beaulieu, C., and Brittain, J. (2003). In vivo T1 and T2 measurements of musculoskeletal tissue at 3 T and 1.5 T. In *Proceedings of the 11th Annual Meeting of ISMRM, Toronto, Canada*, p. 450.

- Khalighi, M.M., Glover, G.H., Pandit, P., Hinks, S., Kerr, A.B., Saranathan, M., and Rutt, B.K. (2011). Single-shot spiral based Bloch-Siegert B₁+ mapping. In *Proc Int Soc Magn Res Med*, p. 578.
- Lee, J., and Adalsteinsson, E. (2010). A Novel Compressed Sensing (CS) Method for B₁+ Mapping in 7T. In *Proceedings 18th Scientific Meeting, International Society for Magnetic Resonance in Medicine*, Stockholm, p. 4859.
- Lustig, M., Donoho, D., and Pauly, J.M. (2007). Sparse MRI: The application of compressed sensing for rapid MR imaging. *Magnetic Resonance in Medicine* 58, 1182–1195.
- Lutti, A., Hutton, C., Finsterbusch, J., Helms, G., and Weiskopf, N. (2010). Optimization and validation of methods for mapping of the radiofrequency transmit field at 3T. *Magnetic Resonance in Medicine* 64, 229–238.
- Nayak, K.S., and Nishimura, D.G. (1998). Randomized trajectories for reduced aliasing artifact. In *Proceedings of the 6th Annual Meeting of ISMRM*, Sydney, Australia, p. 670.
- Nehrke, K., and Börnert, P. (2012). Free-Breathing Abdominal B₁ Mapping at 3T Using the DREAM Approach. In *Proceedings 20th Scientific Meeting, International Society for Magnetic Resonance in Medicine*, Melbourne, p. 3356.
- Nehrke, K., and Börnert, P. DREAM—a novel approach for robust, ultrafast, multislice B₁ mapping. *Magnetic Resonance in Medicine*.
- Pruessmann, K.P., Weiger, M., Scheidegger, M.B., and Boesiger, P. (1999). SENSE: Sensitivity encoding for fast MRI. *Magnetic Resonance in Medicine* 42, 952–962.
- Ravishankar, S., and Bresler, Y. (2011). MR image reconstruction from highly undersampled k-space data by dictionary learning. *Medical Imaging, IEEE Transactions On* 30, 1028–1041.
- Stanisz, G.J., Odobina, E.E., Pun, J., Escaravage, M., Graham, S.J., Bronskill, M.J., and Henkelman, R.M. (2005). T₁, T₂ relaxation and magnetization transfer in tissue at 3T. *Magnetic Resonance in Medicine* 54, 507–512.
- Uecker, M., Hohage, T., Block, K.T., and Frahm, J. (2008). Image reconstruction by regularized nonlinear inversion—Joint estimation of coil sensitivities and image content. *Magnetic Resonance in Medicine* 60, 674–682.

- Uecker, M., Zhang, S., and Frahm, J. (2010). Nonlinear inverse reconstruction for real-time MRI of the human heart using undersampled radial FLASH. *Magnetic Resonance in Medicine* 63, 1456–1462.
- Vernickel, P., Röschmann, P., Findekle, C., Lüdeke, K. -m, Leussler, C., Overweg, J., Katscher, U., Grässlin, I., and Schünemann, K. (2007). Eight-channel transmit/receive body MRI coil at 3T. *Magnetic Resonance in Medicine* 58, 381–389.
- Wiesinger, F., Van de Moortele, P., Adriany, G., De Zanche, N., Ugurbil, K., and Pruessmann, K.P. (2004). Parallel imaging performance as a function of field strength—An experimental investigation using electrodynamic scaling. *Magnetic Resonance in Medicine* 52, 953–964.
- Wiesinger, F., Van de Moortele, P., Adriany, G., De Zanche, N., Ugurbil, K., and Pruessmann, K.P. (2006). Potential and feasibility of parallel MRI at high field. *NMR in Biomedicine* 19, 368–378.
- Yarnykh, V.L. (2007). Actual flip-angle imaging in the pulsed steady state: A method for rapid three-dimensional mapping of the transmitted radiofrequency field. *Magnetic Resonance in Medicine* 57, 192–200.
- Yellott, J. (1983). Spectral consequences of photoreceptor sampling in the rhesus retina. *Science* 221, 382–385.
- Ying, L., and Sheng, J. (2007). Joint image reconstruction and sensitivity estimation in SENSE (JSENSE). *Magnetic Resonance in Medicine*, *Magnetic Resonance in Medicine* 57, 57, 1196, 1196–1202, 1202.

Chapter 6 PRIMO - Precise Radiofrequency

Inference from Multiple Observations

6.1 Introduction

The previous two chapters have explored several different areas of transmit field mapping. The results presented in chapter 4 revealed that the transmit field changes as a result of respiration. It was also shown through simulations that these changes could in principal be eliminated by RF shimming. However, any RF shimming method which attempted to keep the transmit field temporally invariant would require measurements of the field throughout the respiratory cycle. No field mapping sequence was capable of performing real-time measurements when this research was conducted, and therefore a retrospective reconstruction method was developed. This method was unsuccessful, and motivated the development of alternative methods to accelerate transmit field mapping.

Chapter 5 explored the use of model-based reconstruction methods for accelerating transmit field mapping. Model-based reconstruction approaches increase imaging speed by allowing less data to be acquired. Although undersampling k-space would normally corrupt the resulting images, good quality reconstructions can be achieved by exploiting prior knowledge of features present in the data. The reconstruction method developed in chapter 4 utilised the prior knowledge that the field map is a smooth function of space. It was shown that the proposed method could yield field maps of superior quality than those of standard methods.

The technique presented in chapter 5 was developed for sequences which measure the magnitude of the transmit field. However, magnitude transmit field mapping represents only a small part of the whole calibration process. In this

chapter, a method is developed which considers the wider picture of total RF system calibration.

6.1.1 Current Paradigm of RF System Calibration

The current paradigm of parallel RF system calibration can be understood by considering what needs to be obtained from the process.

1. The spatial sensitivity pattern (amplitude and phase) of each receive channel, relative to either each other or a common reference configuration (such as the body coil or the sum-of-squares (SOS), see section 3.4.3.1).
2. The amplitude of the transmit field of each channel.
3. The relative phases between each transmit channel.

The standard calibration procedure addresses point 1 using a dedicated calibration sequence, performed at the beginning of the scan session (see section 3.4.3.1) (Larkman and Nunes, 2007). This is a high SNR sequence that takes approximately a minute to perform on the local Philips scanners. Standard quadrature transmission is used.

Note that frequency-domain PPI techniques do not require point 1 to be performed, as receiver channel relationships are directly estimated from measured k-space data (Griswold et al., 2002). However, point 1 needs to be addressed in order to use image-domain PPI techniques such as SENSE (Pruessmann et al., 1999), and this will be the focus for this chapter.

There are two approaches commonly used to address points 2 and 3. The first acquires an absolute transmit field map for each transmit channel. The relative channel phases are then extracted from the images acquired in each absolute field mapping sequence. The second approach only performs absolute transmit field mapping for a single channel (Van de Moortele and Ugurbil, 2009). This is then supplemented with a series of low flip angle spoiled gradient echo (SPGR)

acquisitions, each using a different transmit state. The relative magnitude and phases of transmit channels can be extracted from the SPGR data, and when combined with the single absolute map, provides absolute field maps and relative phases for every transmit channel. Both approaches can use the prior receive field maps to combine the multi-channel images.

6.1.2 Data Redundancy

Parallel receiver architectures have been commonplace in clinical scanners for the past decade. The use of parallel transmit systems has only recently been available to clinical and research scanners.

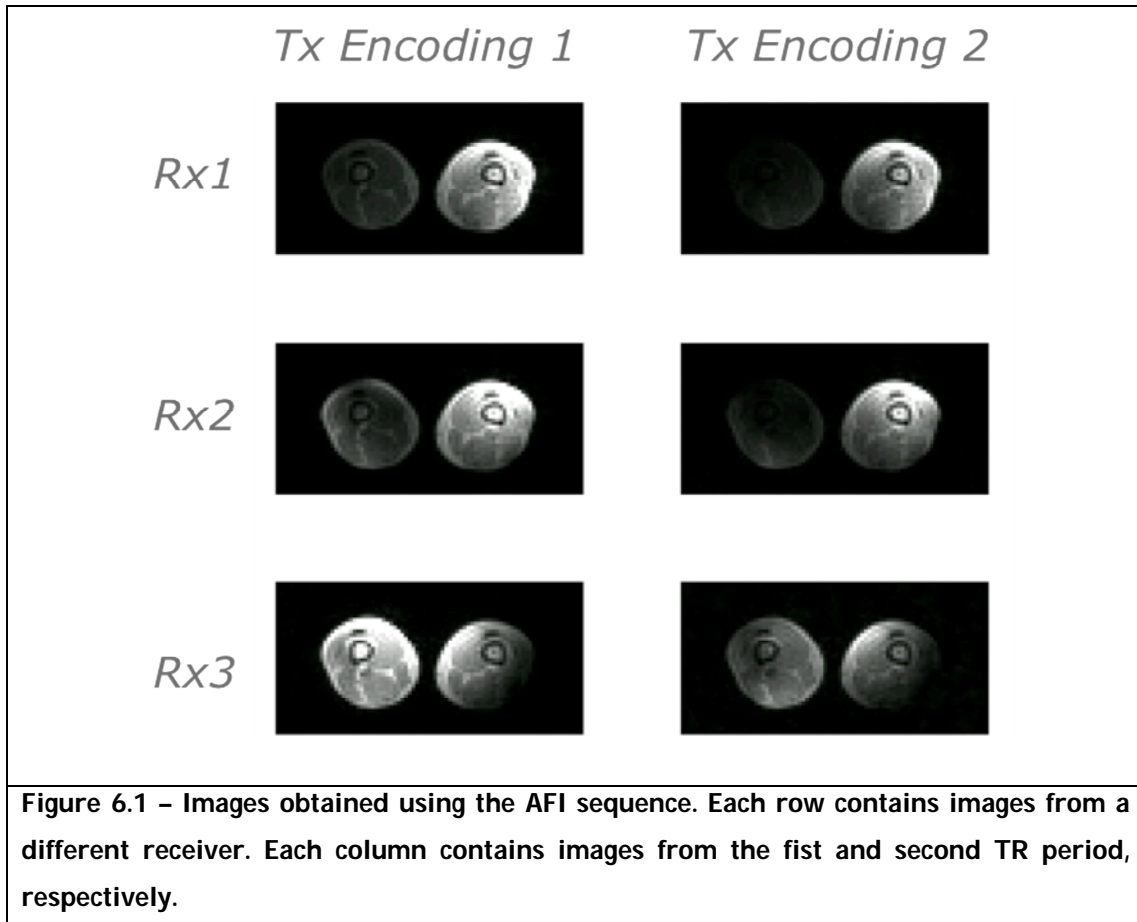
The staggered development of these subsystems has resulted in two isolated and independent calibration procedures. Receive systems are still calibrated as they have been historically, and the majority of current research into transmit methods neglect the multi-receive aspect of the data.

It is therefore likely that the current calibration regime is inefficient, containing much redundant data. This is best demonstrated by considering Figure 6.1, which contains a set of images acquired using the AFI sequence (Yarnykh, 2007) using a multi-channel receive array.

In the current paradigm of RF calibration, the images from each receiver would either be optimally combined using previously measured receive fields, or combined using the sum-of-squares (SOS). The resulting two images would then be divided to extract the transmit field.

However, this approach ignores the full information content present in the dataset: it contains both transmit and receive field information. Therefore this single dataset could be used for both receive calibration and the extraction of the AFI ratio, without the need for pre-calibration of the receive fields.

In this chapter, a reconstruction method is developed which allows full RF field information, in both transmit and receive modes, to be extracted from typical calibration datasets. The proposed strategy builds upon a common element of the majority of image domain RF calibration methods. This common link is the pixelwise division of images, which removes the signal component dependent on tissue relaxation properties, leaving a smooth ratio that reflects the sensitivity profiles of the RF coils.



6.1.3 Proposed Strategy

Again consider Figure 6.1. The aim of the proposed method is to extract the relative receive sensitivities and the ratio of two transmit encoding states. How is this best achieved? For example, consider the ratio between AFI encoding states. The ratio could be taken for each receiver, but how are these combined into a single ratio? Care must be taken, as the AFI ratio estimate will be poor in regions of low receiver sensitivity. Also consider the extraction of the relationship

between receiver 1 and 3. This can be achieved for each individual transmit encoding state, but again, how are these best combined?

The proposed formulation builds upon recent results from parallel imaging. Lustig et. al. and Tieng et. al. (Tieng et al., 2008; Lustig et al., 2011) recently demonstrated that image domain receive sensitivities could be extracted directly from k-space data. This chapter details the generalisation of these methods to full RF system calibration. This is achieved by generalising the Lustig approach, as described in the following section. The method is then tested on both simulated and in-vivo data.

6.2 Theory

Consider an MRI system consisting of N_T transmit channels and N_R receive channels. The signal of any transmit or receive calibration sequence can be described by equation 6.1. In this equation, $I_{a,r,c}(\mathbf{x})$ denotes the image measured by the r^{th} receiver, with the transmitters driven in the c^{th} of N_{LC} linear combinations. The utilised sequence generates a signal amplitude which is a function (f_a) of the transmit state $T_c(\mathbf{x})$ and the properties of the object, $\rho(\mathbf{x})$. The index $a=1-N_A$ labels the case where the sequence generates N_A images with different contrast.

$$6.1 \quad I_{a,r,c}(\mathbf{x}) = R_r(\mathbf{x}) f_a(\rho(\mathbf{x}), T_c(\mathbf{x}))$$

Standard receive calibration sequences utilise a sequence with a single contrast ($N_A=1$) in a single transmit state ($N_{LC}=1$), with an image acquired from each channel ($r = 1, 2, \dots, N_R$). Magnitude field mapping sequences (such as AFI) utilise two acquisitions ($N_A=2$, $N_{LC}=1$), again measuring on all receive channels. Finally, relative transmit field mapping methods (Van de Moortele and Ugurbil, 2009) acquire images from all receivers, repeating the sequence for each transmit state ($N_{LC}=N_T$).

The Lustig method for extracting receive sensitivities is now outlined, before generalisation to full RF calibration.

6.2.1 Receive Mapping directly from k-space

Let us again consider any receive mapping sequence in which data is measured from multiple receive channels simultaneously. As given by equation 6.1, a multiplicative relationship exists between the receive sensitivities and underlying signal. The k-space signal from the r^{th} receiver, $S_r(\mathbf{k})$, is therefore given by the convolution of the frequency representation of the magnetisation, $F(\mathbf{k})$, and the receive sensitivity, $\sigma_r(\mathbf{k})$ (Pruessmann, 2006). Note that the subscripts a and c have temporarily been dropped for simplicity. Since the invention of PPI, several methods have been developed with the goal of reconstructing undersampled data directly in k-space by exploiting this convolution relationship ((Sodickson and Manning, 1997; Griswold et al., 2002; Lustig and Pauly, 2010)).

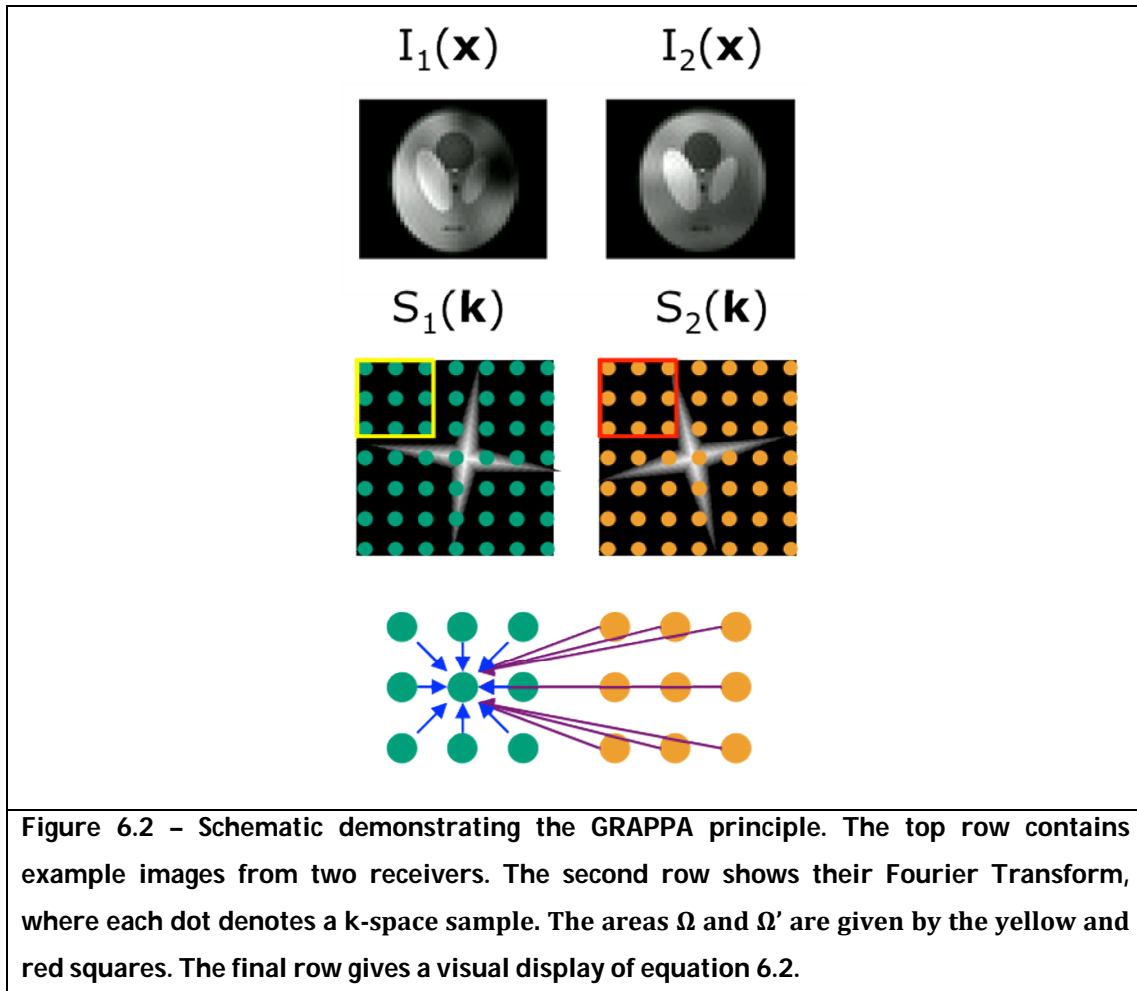
K-space PPI methods, such as GRAPPA, exploit the fact that each coil's footprint, or kernel, can generally be expressed with a relatively small number of low-order Fourier harmonics. This property originates from the smooth, generally slowly varying spatial pattern they exhibit in the image domain.

GRAPPA exploits this observation by noting that each measured point $S_r(\mathbf{k})$ can be formed by an appropriately weighted sum of the signals from all receiver coils. This is displayed diagrammatically in Figure 6.2, and further described by equation 6.2. The figure shows example images in the case of two receivers, but equally applies to more channels. The corresponding k-spaces are given in the second row. In GRAPPA, any sample in k-space (here given by the centre green sample) can be synthesised by a weighted sum (indicated by arrows) of the samples from its local neighbourhood (here a 3x3 region, given by the yellow box, denoted by Ω) and from the neighbourhood from the other channels (red box, Ω').

Equation 6.2 expresses this relationship mathematically, given the size of Ω is sufficiently large to capture all field information. The sample $S_r(\mathbf{k})$ is synthesised by taking a weighted sum of the points in its local neighbourhood (first term) and the same neighbourhood from other channels (second term). The neighbourhoods Ω and Ω' are identical, except that the centre point is excluded for the local sum. The weights are given by $w_r(\mathbf{k}')$ and $w_{r'}(\mathbf{k}')$, where \mathbf{k}' is a dummy variable over the region.

$$S_r(\mathbf{k}) = \sum_{\mathbf{k}' \in \Omega} w_r(\mathbf{k}') S_r(\mathbf{k} + \mathbf{k}') + \sum_{r' \neq r} \sum_{\mathbf{k}' \in \Omega'} w_{r'}(\mathbf{k}') S_{r'}(\mathbf{k} + \mathbf{k}')$$

6.2



In order to utilise this equation, the weights must be determined. This is achieved by following the calibration procedure described below. A fully sampled section of \mathbf{k} -space is measured on all channels. The \mathbf{k} -space

measurements ($S_r(\mathbf{k})$) from every possible kernel location are extracted by the function Ψ , as shown in Figure 6.3, and placed in the rows of data matrix \mathbf{A}_r . A full calibration matrix, \mathbf{A}^F is obtained by horizontally concatenating the matrices from all receivers, as in Figure 6.4.

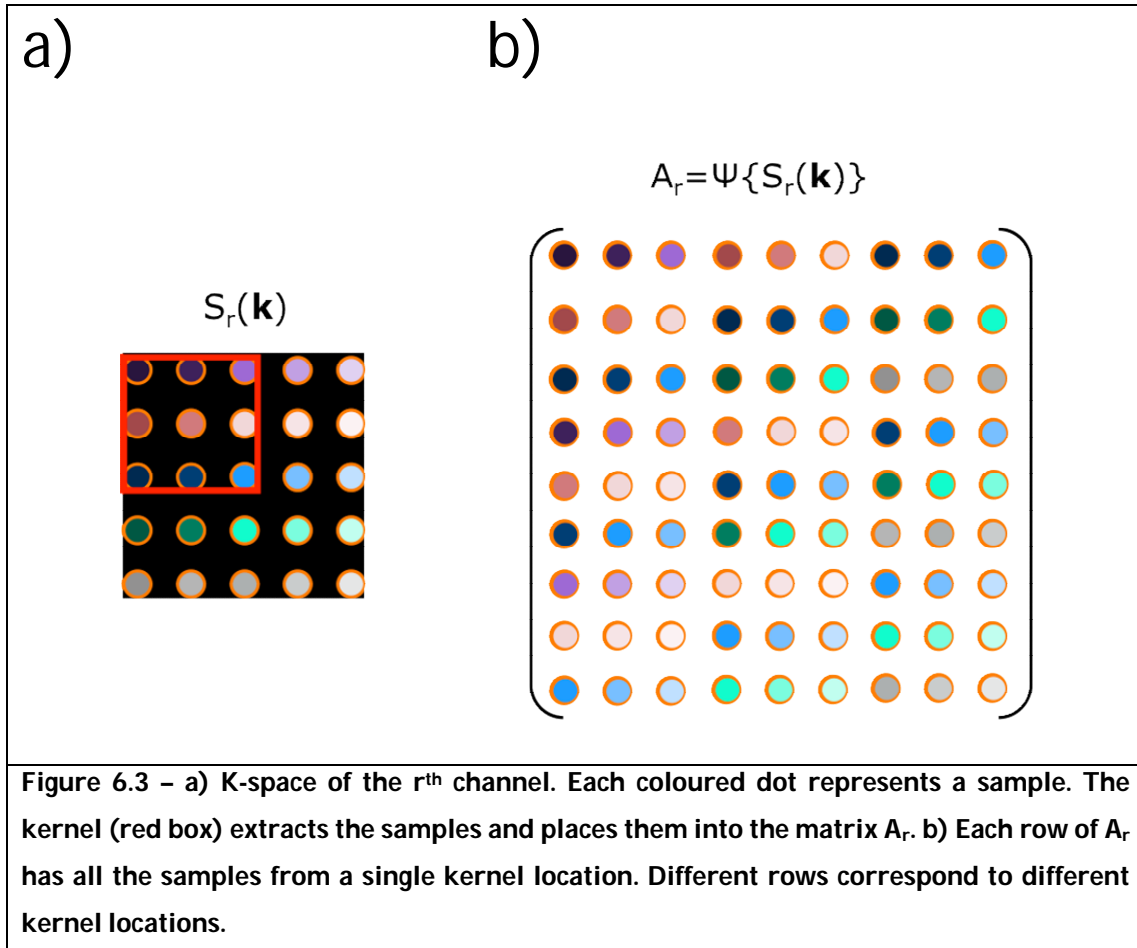


Figure 6.3 – a) K-space of the r^{th} channel. Each coloured dot represents a sample. The kernel (red box) extracts the samples and places them into the matrix \mathbf{A}_r . b) Each row of \mathbf{A}_r has all the samples from a single kernel location. Different rows correspond to different kernel locations.

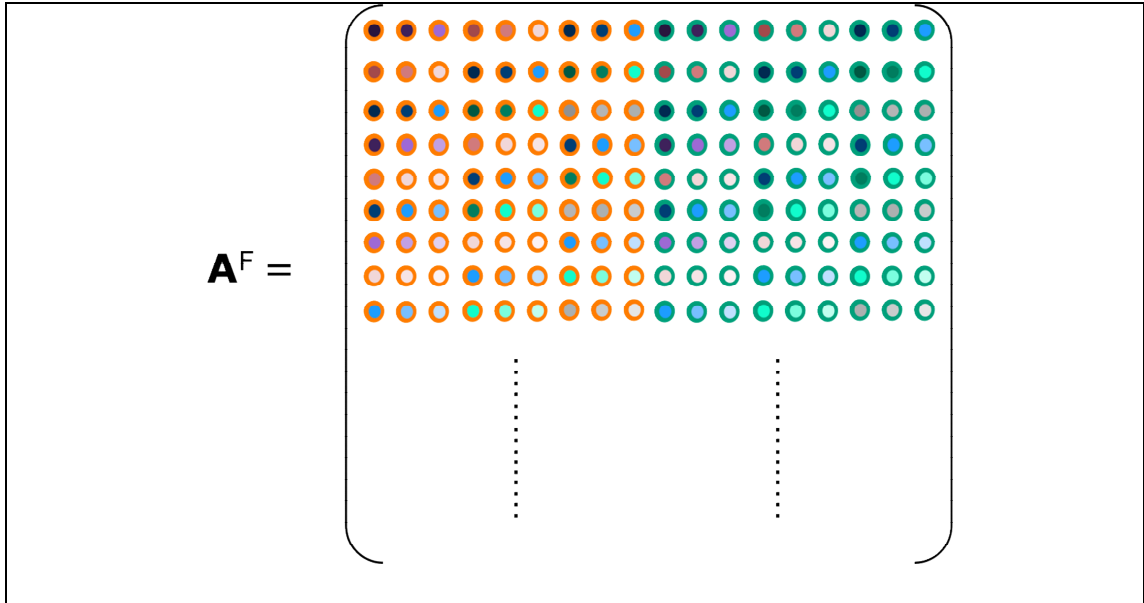
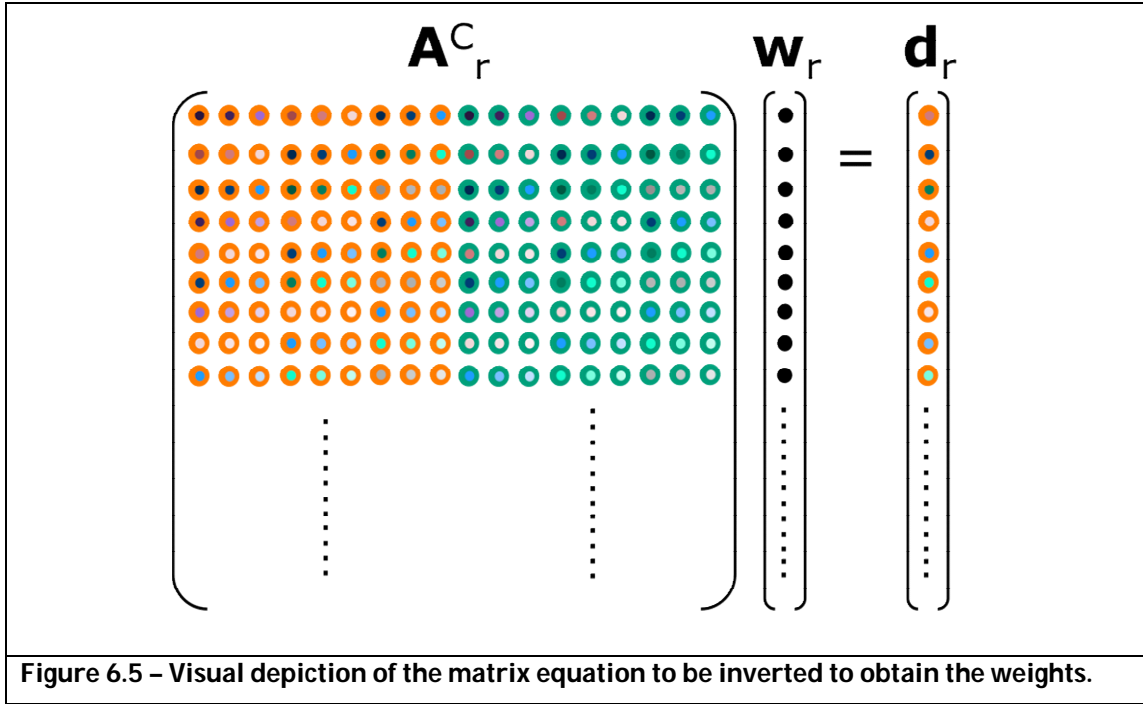


Figure 6.4 – The full calibration matrix. It is created by the horizontal concatenation of two data matrices, \mathbf{A}_1 (orange-edged samples) and \mathbf{A}_2 (green-edged samples).

The weights that allow the synthesis of the r^{th} k-space from every other are obtained by solving an over-determined inverse problem $\mathbf{A}^{\text{C}_r} \cdot \mathbf{w} = \mathbf{d}_r$, displayed in Figure 6.5 and the terms therein defined as follows. The column of \mathbf{A}^F corresponding to the centre of the r^{th} kernel is extracted into data vector \mathbf{d}_r , with the remaining entries of \mathbf{A}^F placed into \mathbf{A}^{C_r} . The weights \mathbf{w}_r are obtained by inverting the matrix \mathbf{A}^{C_r} , with the least-squares solution given by equation 6.3. This equation also includes an optional regularisation term λ , which can be used to control the magnitudes of the weights (Lin et al., 2010). This process is repeated for each receive coil, so that weights relating each coil's signal to every other's are obtained.



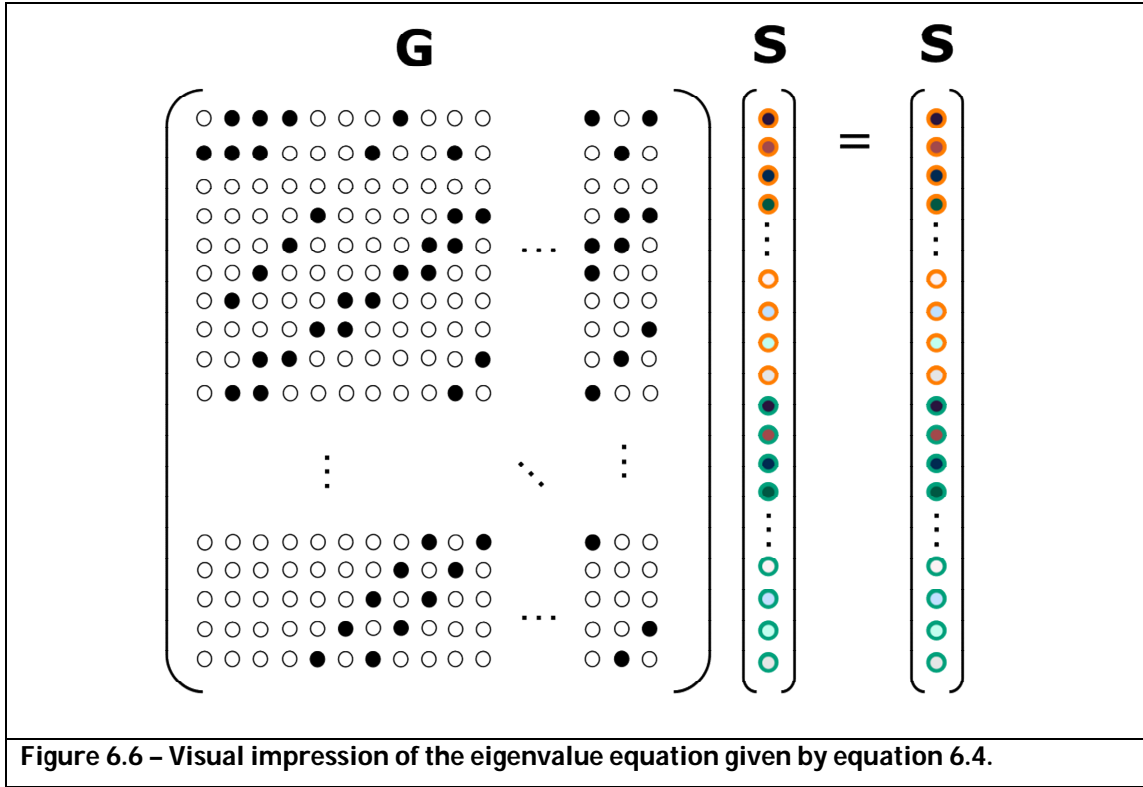
6.3

$$\mathbf{w}_r = \left(\left[\mathbf{A}_r^c \right]^* \mathbf{A}_r^c + \lambda \mathbf{I} \right)^{-1} \left[\mathbf{A}_r^c \right]^* \mathbf{d}_r$$

It was previously shown (Lustig et al., 2011) that equation 6.2 could be alternatively expressed as to highlight the underlying relationship between the measured data and the calculated weights. By concatenating all of the measured k-space signals into a single vector, \mathbf{S} , and using the weights to populate a sparse convolution matrix, \mathbf{G} , it becomes evident that their product, should equal the signal vector, \mathbf{S} , as described in equation 6.4. This is shown visually in Figure 6.6.

6.4

$$\mathbf{GS} = \mathbf{S}$$



Equation 6.4 is an eigenvalue equation whose solution is the eigenvector of \mathbf{G} corresponding to eigenvalue $\mu=1$. \mathbf{G} can be a very large matrix. For example, for a 64×64 k-space matrix size with four receivers, \mathbf{G} is $(4 \times 64^2) \times (4 \times 64^2) = 16,384 \times 16,384$. This is difficult to manipulate, and therefore a more intuitive and computationally efficient (Lai et al., 2010) expression is given by equations 6.5. This alternative expression exploits the fact that \mathbf{G} is a convolution operation. Equation 6.5 expresses equation 6.4 in the image domain, where $\mathbf{g}(\mathbf{x})$ is an $N_R \times N_R$ matrix whose element at row r and column r' contains the zero-filled Fourier Transform of the estimated kernel which synthesises the signal of coil r from the signal of coil r' at position \mathbf{x} , and $\mathbf{s}(\mathbf{x})$ is a $N_R \times 1$ vector whose r^{th} row contains the image domain signal of coil r at position \mathbf{x} .

This equation can be further simplified, as the signal $\mathbf{s}(\mathbf{x})$ is the product of the receive sensitivity and the underlying magnetisation. Cancelling the common magnetisation from both sides yields equation 6.6, where $\mathbf{r}(\mathbf{x})$ is a $N_R \times 1$ vector whose r^{th} row contains the receive sensitivity of coil r at position \mathbf{x} . This expression demonstrates how the $\mu=1$ eigenvector yields receive sensitivities.

The relative relationship of the N_R elements of the $\mu=1$ eigenvector correspond to the relative values of the receive sensitivities at position \mathbf{x} .

$$6.5 \quad \mathbf{g}(\mathbf{x})\mathbf{s}(\mathbf{x}) = \mathbf{s}(\mathbf{x})$$

$$6.6 \quad \mathbf{g}(\mathbf{x})\mathbf{r}(\mathbf{x}) = \mathbf{r}(\mathbf{x})$$

In summary, relative receive maps can be extracted by performing the following:

1. Find weights \mathbf{w}_r which allow any sample \mathbf{S}_r to be synthesised from sum of samples in its local neighbourhood across all coils. Repeat for all r .
2. Fourier Transform the kernels. Form the matrix \mathbf{g} at each position \mathbf{x} .
3. Perform an eigendecomposition of each $\mathbf{g}(\mathbf{x})$. Extract the eigenvector with eigenvalue 1.
4. The relative receive sensitivities of between the r^{th} and q^{th} coils are given by the ratio of the r^{th} and q^{th} elements of the eigenvector.

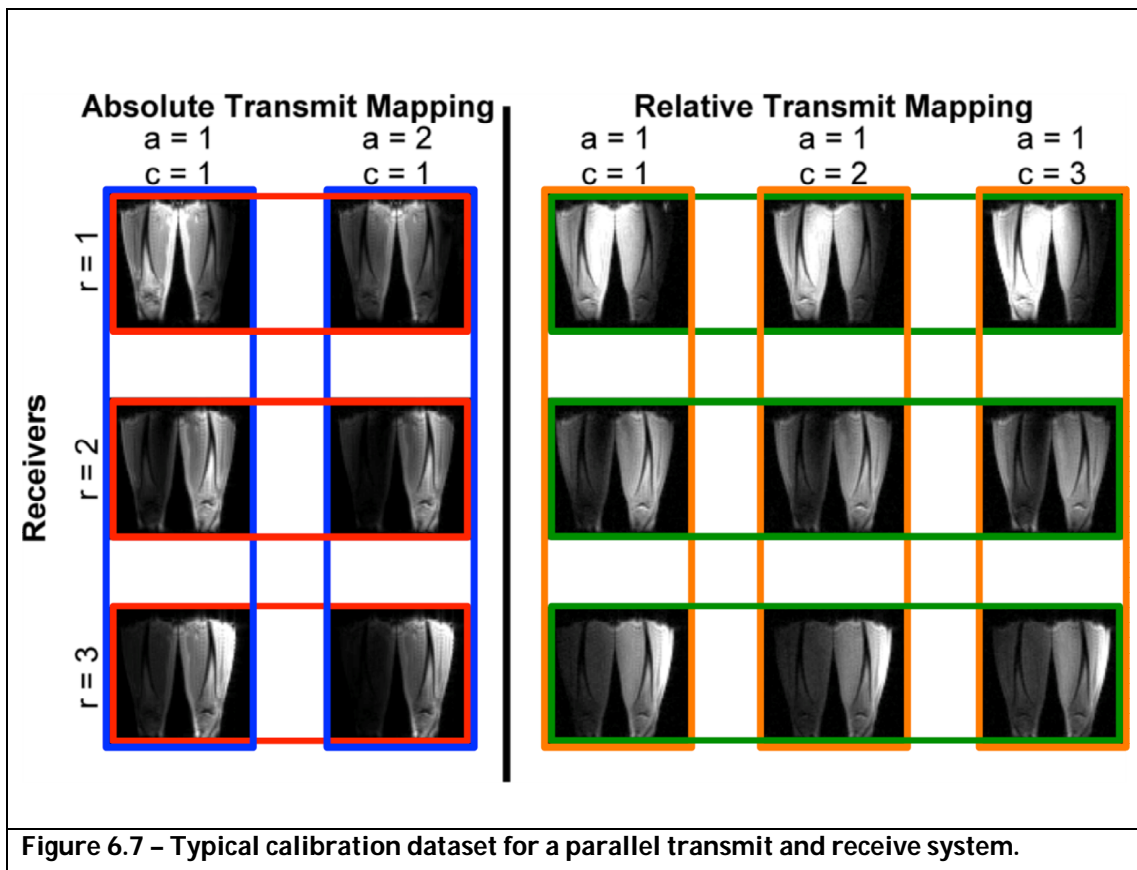
6.2.2 Application to Full RF Calibration

As stated earlier, the proposed method by Lustig (Lustig et al., 2011) is a restricted subset of a much larger calibration problem. We now describe how the described method provides an elegant framework for full RF field mapping. The proposed approach is named Precise Radiofrequency Inference from Multiple Observations, or PRIMO.

Figure 6.7 shows example images from which full RF calibration can be performed. Each row corresponds to images from each receive channel. The first two columns display two transmit field encoded images, obtained from a magnitude field mapping sequence such as AFI. The last three columns display small flip angle SPGR images, acquired in different transmit configurations.

Each individual blue or orange highlighted area contains data from which receive calibration directly from k-space, as described earlier, could be performed. It is clear that it would be equally valid to extract relative receive maps from any other column of data.

Similarly, the image ratio required for absolute transmit mapping methods can be obtained from comparing any pair of transmit encoded images, as highlighted in red. As with the receive case, the ratio between transmit contrasts is valid for all receivers. The same is true in the case of relative transmit states. These can be found by comparing images maps across transmit states, again valid for all receivers, as highlighted in green.



The proposed PRIMO framework expands upon the eigensystem approach by utilising all the available data to estimate each part of the RF system. This is achieved by modifying the weight calculation process.

As stated earlier, a general calibration sequence can be described by equation 6.1. The corresponding k-space data can be expressed as $S_{a,r,c}(\mathbf{k})$. These k-spaces can then be converted into matrix form, $\mathbf{A}_{a,r,c}$, using the kernel extractor operator Ψ .

6.2.2.1 Receive Calibration

Now consider the case of receive calibration. In the receive-only case, the full calibration matrix \mathbf{A}_F was constructed by horizontally concatenating the individual receive matrixes \mathbf{A}_r . In the full RF calibration case developed here, this process is modified as in equation 6.7.

$$6.7 \quad \mathbf{A}_F = \begin{bmatrix} \mathbf{A}_{1,1,1} & \mathbf{A}_{1,2,1} & \cdots & \mathbf{A}_{1,N_R,1} \\ \mathbf{A}_{1,1,2} & & \ddots & \vdots \\ \vdots & & & \\ \mathbf{A}_{1,1,N_{LC}} & \cdots & & \mathbf{A}_{1,N_R,N_{LC}} \\ \hline \mathbf{A}_{2,1,1} & \mathbf{A}_{2,2,1} & \cdots & \mathbf{A}_{2,N_R,1} \\ \mathbf{A}_{2,1,2} & & \ddots & \vdots \\ \vdots & & & \\ \mathbf{A}_{2,1,N_{LC}} & \cdots & & \mathbf{A}_{2,N_R,N_{LC}} \\ \hline \vdots & \vdots & & \vdots \\ \hline \mathbf{A}_{N_A,1,1} & \mathbf{A}_{N_A,2,1} & \cdots & \mathbf{A}_{N_A,N_R,1} \\ \mathbf{A}_{N_A,1,2} & & \ddots & \vdots \\ \vdots & & & \\ \mathbf{A}_{N_A,1,N_{LC}} & \cdots & & \mathbf{A}_{N_A,N_R,N_{LC}} \end{bmatrix}$$

The full calibration matrix has a more complex form. The first row of the matrix corresponds to the receive-only case, as before. The second row again corresponds to all receivers, but for the second of the N_{LC} transmit linear combinations. The remaining rows of this block correspond to the remaining linear combinations. The second block mirrors the structure of the first, but for the second transmit contrast acquisition. The remaining blocks represent the remaining transmit contrast acquisitions. \mathbf{A}_F can then be used as before to calculate weights and obtain relative receive maps.

6.2.2.2 Magnitude Transmit Field Calibration

In any ratiometric transmit mapping sequence of a particular linear combination c , all N_R receivers measure two images of different transmit contrast ($a=1,2$). Ratiometric mapping approaches rely on the function f_a in equation 6.1 simplifying into two known components which represent the transmit field and the object separately. This is shown in equation 6.8, where p and q_a are known sequence dependent functions. Since $p(\rho(\mathbf{x}))$ and $R_r(\mathbf{x})$ is common to both sequence acquisitions, the image ratio is purely a function of the transmit sensitivity, as in equation 6.9. Knowledge of Q allows for the transmit field to be obtained from the image ratio.

$$6.8 \quad I_{a,r,c}(\mathbf{x}) \approx R_r(\mathbf{x})p(\rho(\mathbf{x}))q_a(T_c(\mathbf{x}))$$

$$6.9 \quad \frac{I_{2,r,c}(\mathbf{x})}{I_{1,r,c}(\mathbf{x})} \approx \frac{q_2(T_c(\mathbf{x}))}{q_1(T_c(\mathbf{x}))} = Q(T_c(\mathbf{x}))$$

PRIMO provides the ability to obtain this ratio directly from k-space measurements. The full calibration matrix \mathbf{A}_F is constructed as in equation 6.10.

$$6.10 \quad \mathbf{A}_F = \begin{bmatrix} \mathbf{A}_{1,1,1} & \mathbf{A}_{2,1,1} \\ \mathbf{A}_{1,2,1} & \mathbf{A}_{2,2,1} \\ \vdots & \vdots \\ \mathbf{A}_{1,N_R,1} & \mathbf{A}_{2,N_R,1} \end{bmatrix}$$

Note that only a single linear combination, $c=1$, is used here. This is the case as altering the linear combination would alter the ratio, making the data inconsistent. Again, the weights can be found, and the principal eigenvector found. The relative relationship between the two components of this eigenvector reflect the ratio between the two transmit images. This ratio can then be converted into the spatial distribution of the amplitude of the transmit field.

6.2.2.3 Relative Transmit Mapping

Consider a pulse sequence for which the image signal is a linear function of the flip angle, such as a small flip angle SPGR. The signal equation for this form of sequence is given by equation 6.11.

$$6.11 \quad I_{a,r,c}(\mathbf{x}) = R_r(\mathbf{x})f_a(\rho(\mathbf{x}), T_c(\mathbf{x})) \approx R_r(\mathbf{x})p(\rho(\mathbf{x}))T_c(\mathbf{x})$$

PRIMO can be used to extract both relative transmit sensitivities and relative receive sensitivities. The calibration matrix for relative transmit extraction is given by equation 6.12. All obtained weights are processed using the eigendecomposition as before, obtaining relative transmit maps.

$$6.12 \quad \mathbf{A}_F = \begin{bmatrix} \mathbf{A}_{1,1,1} & \mathbf{A}_{1,1,2} & \cdots & \mathbf{A}_{1,1,N_{LC}} \\ \mathbf{A}_{1,2,1} & & \ddots & \vdots \\ \vdots & & & \\ \mathbf{A}_{1,N_R,1} & \cdots & & \mathbf{A}_{1,N_R,N_{LC}} \end{bmatrix}$$

6.3 Methods

The Theory section has given a general description of PRIMO approach. In this section the details of the methodology are addressed, and the simulations and experiments used to test PRIMO are described.

The results of the simulations presented here are restricted to those of absolute and relative transmit field mapping. This is for the sake of brevity, and because no further insights are gained by considering the quantitative results of receive field reconstructions. Relative receive fields are reconstructed and presented from the in-vivo data.

6.3.1 Implementation Details

6.3.1.1 Dimensionality of the Acquisition and Reconstruction

It is desirable to know the RF fields throughout the volume being imaged. Therefore a 3D acquisition is considered from the outset. If Cartesian sampling is used, each measured k-space is a volume of with two PE and a single FE direction, as shown in Figure 6.8. The FE direction will be referred to as the z-direction, and the PE directions as x and y. N_{PE} phase encode lines are acquired in each PE direction, and N_{FE} samples are acquired in the FE direction.

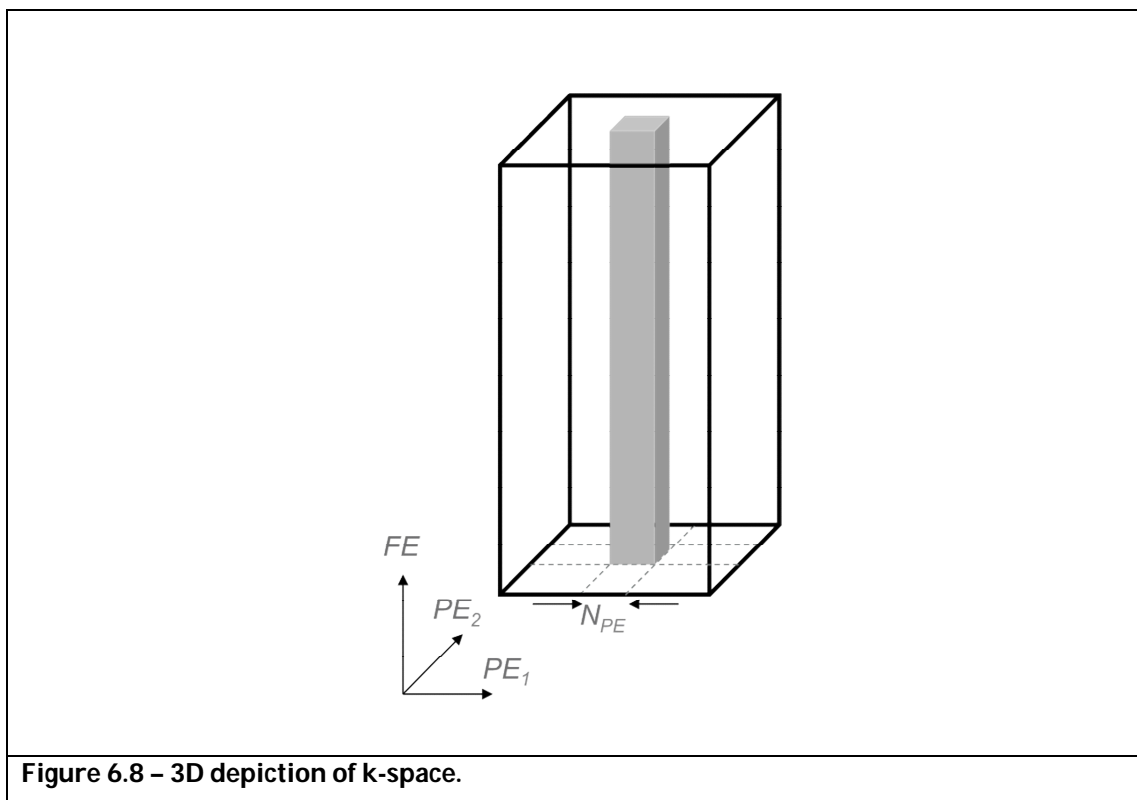


Figure 6.8 – 3D depiction of k-space.

The dimensionality of the reconstruction method does not necessarily have to be the same as that of the acquisition. Taking an initial FT in the FE direction yields a set of 2D k-spaces at each location in z. PRIMO is then implemented on a slice-by-slice basis, as pilot experiments determined that this is the better approach. This is further explained in the Discussion.

6.3.1.2 Kernel Selection

The kernel is an important component of PRIMO. It is characterised by a single parameter, the width of the kernel, N_k . The kernel width defines the spatial frequency content of the relative fields, and is investigated in simulations and experiments. The kernel is defined to be 2D.

6.3.1.3 Calibration Matrix – Size and Inversion

A vital component of PRIMO is the construction of the calibration matrices \mathbf{A}^c . As they are inverted to obtain the weights, they need to be over-determined (i.e. have more rows than columns). The size of the matrix in the case of absolute field mapping is given by equation 6.13. The number of rows is determined by the number of kernels that can fit into the $N_{PE} \times N_{PE}$ area of data, multiplied by the number of receive channels. The number of weights to be solved for is given by the $2N_k^2 - 1$.

$$6.13 \quad Size = N_R (N_{PE} - (N_k - 1))^2 \times 2N_k^2 - 1$$

The size of relative transmit mapping calibration matrix is given by equation 6.14. The number of rows is the same as for the absolute mapping case. However, the number of columns increases to account for the ability to use contributions from other linear combinations.

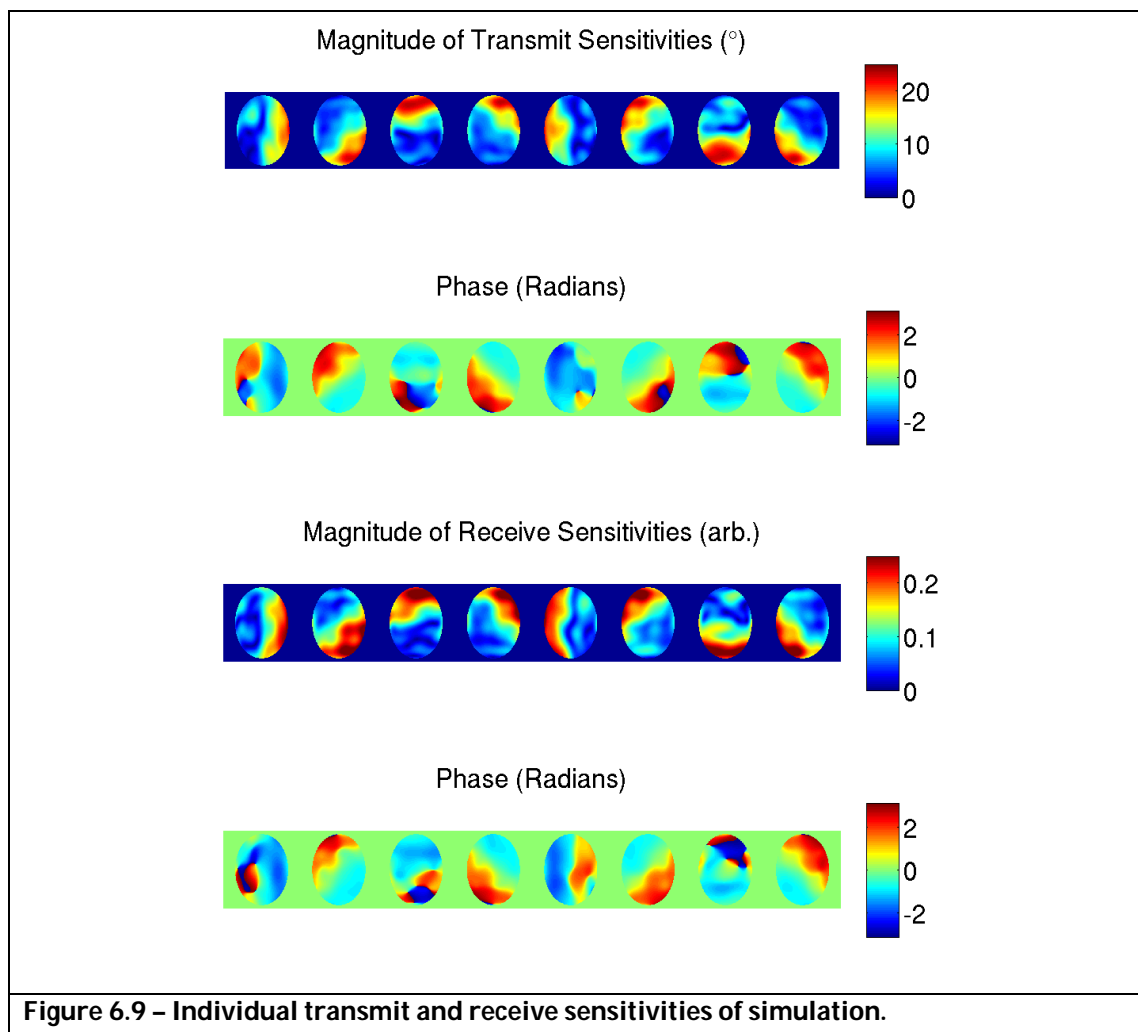
$$6.14 \quad Size = N_R (N_{PE} - (N_k - 1))^2 \times N_{LC} N_k^2 - 1$$

The simulations performed here test the effect of reducing the number of receivers, the number of PEs sampled, and size of the kernel. Furthermore, in the case of relative field mapping, two cases are tested: firstly, using all LCs to synthesise samples, and secondly, only using two LCs to synthesise samples.

The effect of using regularisation to improve the matrix inversion is also tested. The simulations are also performed at several SNR levels.

6.3.2 Simulations

Simulations were performed in order to demonstrate the utility of the PRIMO formulation. The 2D Shepp-Logan phantom was modified to model RF field mapping in the brain by assigning different compartments the T_1 and T_2 values of white matter, grey matter (Stanisz et al., 2005), and CSF (Lin et al., 2001). Eight complex transmit and eight receive sensitivities ($N_T = 8$, $N_R = 8$) were generated, with a maximum frequency component of seven spatial harmonics in both spatial directions (see Figure 6.9). The frequency encoding (FE) direction is considered as the through-plane direction, with both displayed spatial dimensions being the phase encoding (PE) directions.



6.3.2.1 *Simulation 1: Magnitude Transmit Mapping with PRIMO*

A synthetic dataset of an absolute transmit field mapping sequence was generated for testing PRIMO. Simulated AFI images for each receive channel were created using the full signal equations described previously (see equation 3.7 and 3.8), with the simulated transmit fields driven in quadrature. The following sequence parameters were used: $TR_1/TR_2/TE = 30/150/4.5\text{ms}$, nominal flip angle = 80° . The images were Fourier Transformed and truncated from matrix size 256^2 to matrix size 46^2 . Noise was added to the data so that the SNR was either 1x, 0.5x or 0.2x the level as measured in an in-vivo dataset (SNR_{REF}).

The data was processed using PRIMO with varying levels of regularisation and with kernel sizes of 3, 5, 7 and 9. These simulations were repeated for several levels of k-space truncation in both PE directions. The relative values of the elements of each pixel's primary eigenvector were processed using equation 3.23 in order to extract the magnitude of the transmit field.

Standard reconstructions were performed with the same data for comparison. Datasets from each receiver were truncated to the same level as the input to PRIMO, and zero filled and Fourier Transformed to the image domain. The images from each receiver were then combined using the Sum-Of-Squares (SOS), their ratio was taken, from which the transmit field amplitude could be obtained. We refer to this approach as the 'Image Domain Ratio' method, or IDR.

The IDR and PRIMO reconstructions (T_{RECON}) were assessed for error with respect to magnitude of the noise-free gold standard transmit map (T_{GS}). The root mean square error (RMSE), as defined in equation 6.15, was used as the error metric, utilising a mask defined as the area inside the object.

6.15

$$RMSE = \sqrt{\frac{1}{N_{mask}} \sum_{\mathbf{x} \in mask} (T_{GS}(\mathbf{x}) - T_{RECON}(\mathbf{x}))^2}$$

6.3.2.2 Simulation 2: Relative Transmit and Receive Mapping with PRIMO

Simulated images of a 2D low-flip angle SPGR sequence (Bernstein Matt et al., 2004) were also generated in order to test PRIMO formulation for relative transmit and receive mapping. The following sequence parameters were chosen: TR/TE = 5/2.3ms, amplitude of transmit fields scaled for quadrature transmission to achieve 3° excitation. N_T+1 linear combinations were chosen – quadrature, in addition to inverted phase linear combinations of transmitters (Brunner and Pruessmann, 2008). Noise was added to the simulations at the same levels as simulation 1, with SNR_{REF} measured from an in-vivo experiment. The data was processed using PRIMO with data from all eight receivers, varying regularisation, kernel size and noise level parameters as in simulation 1. Two versions of PRIMO reconstruction were tested: firstly, a data matrix was constructed so that weights relating every transmit dataset to every other were obtained by a single inversion (onwards referred to as ALL-PRIMO). The second approach, Pairwise PRIMO (PW-PRIMO), sequentially found weights relating each transmit configuration individually to quadrature. For both approaches, individual transmit field maps were formed by multiplying the relative maps obtained by ALL-PRIMO or PW-PRIMO by the low-resolution gold standard quadrature field map. The magnitude of the individual transmit states were compared to the gold standard, again using equation 6.15 as an error metric. The individual channel errors were combined by averaging to produce a single figure error value. Note that whilst PRIMO produces field relationships with both amplitude and phase, IDR loses phase information due to the SOS. Therefore average error across all transmitters was used to compare IDR and PRIMO.

6.3.2.3 In-Vivo Experiments

PRIMO for absolute and relative field mapping was tested in the head and thighs of a volunteer. All scans were performed on a 3T Philips Achieva, modified with

an eight channel parallel transmit body coil (Vernickel et al., 2007). Data was acquired using either a six-channel torso receive array or a 6 channel head coil. All data was initially Fourier Transformed in the FE direction (always the foot-head direction), then truncated by discarding several PE lines, and reconstructed using PRIMO and standard image domain pixelwise division on a slice-by-slice basis.

3D AFI (Yarnykh, 2007) with transmit channels driven in quadrature was performed in the head with the following sequence parameters: $TR_1/TR_2/TE = 30/150/4.6\text{ms}$, resolution = $5\times 5\times 5\text{mm}$, flip angle = 80° , maximum $B_1 = 5\mu\text{T}$, FOV = $200\times 200\times 400\text{mm}$ (APxRLxFH), scan duration 4m50s.

A 3D low flip-angle spoiled gradient echo sequence was also performed in order to demonstrate PRIMO for relative mapping. The following sequence parameters were used: FOV = $210\times 420\times 340\text{mm}$ (APxRLxFH), resolution = $5\times 5\times 5\text{mm}$, $TR/TE = 5/2.3\text{ms}$, water-fat shift = 0.89 pixels, maximum $B_1 = 5\mu\text{T}$, and the flip angle set so that quadrature excitation mode achieves a 3° flip angle. This scan was performed sequentially eight times, with transmitters driven in inverted-phase linear combinations. Each acquisition took 18s, resulting in a total scan time of 2m21s.

6.4 Results

6.4.1 Simulation 1

Figure 6.10 presents the numerical results of simulation 1, and provides insight into the behaviour of the IDR and PRIMO reconstruction methods.

First consider the results of the IDR approach. IDR performs poorly at all SNR levels for N_{PE} 's below ~ 10 -15. This is because k-space is truncated to the level at which coil sensitivity information is lost. The behaviour above this level is SNR dependent. All SNR levels see an increase in error as N_{PE} increases. The rate at which the error increases is greater for lower SNR levels. This behaviour reflects corruptive influence of noise.

The PRIMO error curves display similar features as that of the IDR error. The error steeply increases at low N_{PE} . This critical N_{PE} threshold varies for different kernel sizes; for $N_k=5$, threshold ≈ 18 ; for $N_k=7$, threshold ≈ 21 ; for $N_k=9$, threshold ≈ 25 . This behaviour reflects the suitability of the calibration matrix for inversion. Higher kernel widths require more variables to be solved for, and therefore require more data in order to achieve the same quality of inversion. Note that $N_k=3$ has been omitted from these results. This is because the error is much larger than those for $N_k \geq 5$. However, field maps from $N_k=3$ PRIMO are displayed later.

Regularisation only provides improved reconstructions below the critical threshold. This is best demonstrated in the case of $N_k = 5$ at $SNR = SNR_{REF}$. Using no regularisation causes unpredictable and large errors below the critical N_{PE} level (blue curve and blue arrow). Adding a small amount of regularisation ($\lambda=10^{-8}$ and 10^{-7} , red line and red arrow) controls this behaviour. Further increasing the regularisation increases the error at all N_{PE} (purple line and purple arrow). This effect less prominent at $SNR = 0.5 \times SNR_{REF}$, and is not present at $SNR = 0.2 \times SNR_{REF}$. This is as the contribution of noise effectively acts as regularisation, as described by Lin. et. al. (Lin et al., 2010). Regularisation is omitted from further PRIMO reconstructions presented in this chapter. This is because it is not favourable to be in the regime where regularisation improves the reconstruction.

PRIMO performs favourably in comparison to IDR. It results in lower error field maps relative to the gold standard at the majority of N_{PE} . IDR does outperform PRIMO at very low N_{PE} , but in this regime neither IDR nor PRIMO produce maps of good quality (black arrow).

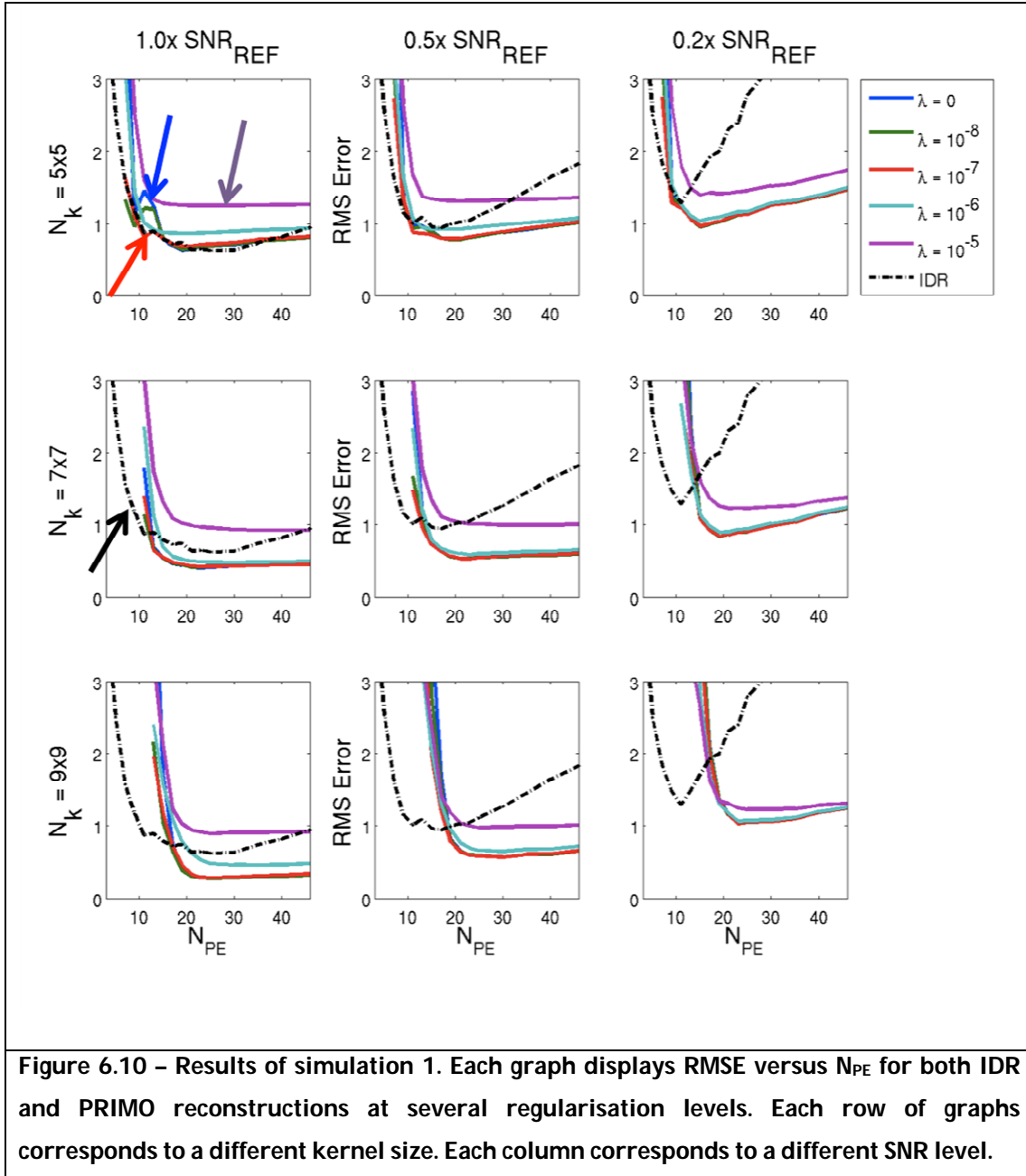


Figure 6.11 displays the reconstruction error of unregularised PRIMO versus IDR for all SNR levels and kernel sizes. The quality of the reconstruction depends both on the kernel size and the SNR level.

At $\text{SNR} = \text{SNR}_{\text{REF}}$, $N_k = 9$ achieved the lowest error reconstruction, followed by $N_k = 7$ and $N_k = 5$. IDR achieves an error at the same level as $N_k = 5$. This order reflects the ability of larger kernels to account for more spatial harmonics present in the field. However, this comes at the expense of a higher critical N_{PE} threshold.

Decreasing the SNR to $0.5 \times \text{SNR}_{\text{REF}}$ results in $N_k=7$ PRIMO achieving the minimum reconstruction error. This behaviour reflects the inherent trade-off in the choice of kernel-size versus SNR. Larger kernels provide an ability to model higher spatial harmonics, but this comes at the cost of needing to estimate more weights.

At $\text{SNR} = 0.2 \times \text{SNR}_{\text{REF}}$, $N_k=7$ again achieves the minimum reconstruction error, followed by $N_k=5$ and then $N_k=9$. This result shows that it is better to knowingly restrict the kernel size (and hence ignore present spatial harmonics) than to attempt to accurately model the field variation.

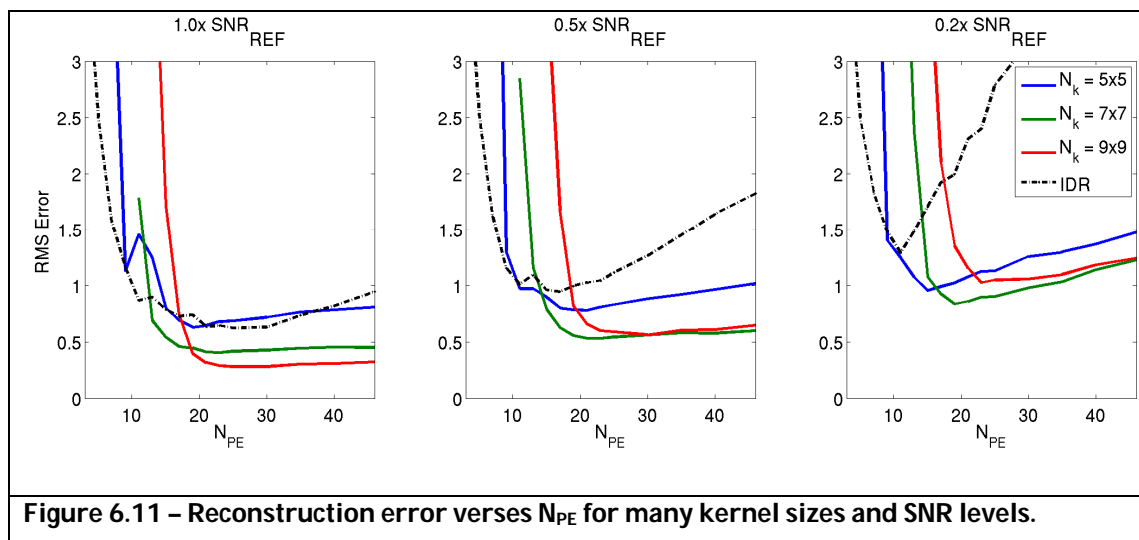


Figure 6.11 – Reconstruction error versus N_{PE} for many kernel sizes and SNR levels.

Figure 6.12 displays the reconstructed field maps of both IDR and PRIMO (using no regularisation) at many kernel sizes, N_{PE} 's and SNR levels. The displayed IDR results show how increasing N_{PE} can reduce the quality of the field map. This is because higher frequency k-space data primarily contributes noise over field information. This is most clearly seen in the case of lowest SNR (see white box in Figure 6.12).

The $N_k=3$ PRIMO field maps demonstrate why the errors for small kernel sizes are significantly greater than for higher kernel sizes. The $N_k=3$ field map does reproduce the larger-scale shape of the field, but none of the detail. The small kernel cannot capture the full frequency content of the field map, and therefore produces the best approximation it can. This effect is indicated by white arrows

(a feature of the GS map that is reproduced by the PRIMO map) and the red arrows (a feature of the GS map that is not reproduced by the PRIMO map).

The remaining PRIMO fields explain the behaviour seen in Figure 6.11 (see red box). At low N_{PE} , both the $N_k=5$ and $N_k=7$ fields produce good reconstructions. However, the $N_k=7$ result is better as it can capture more of the field's frequency content. The $N_k=9$ result is poor as too little PE data is provided. Increasing N_{PE} allows all PRIMO reconstructions to achieve superior fields as compared to IDR, given sufficient kernel size (see green box). This behaviour is true across SNR levels.

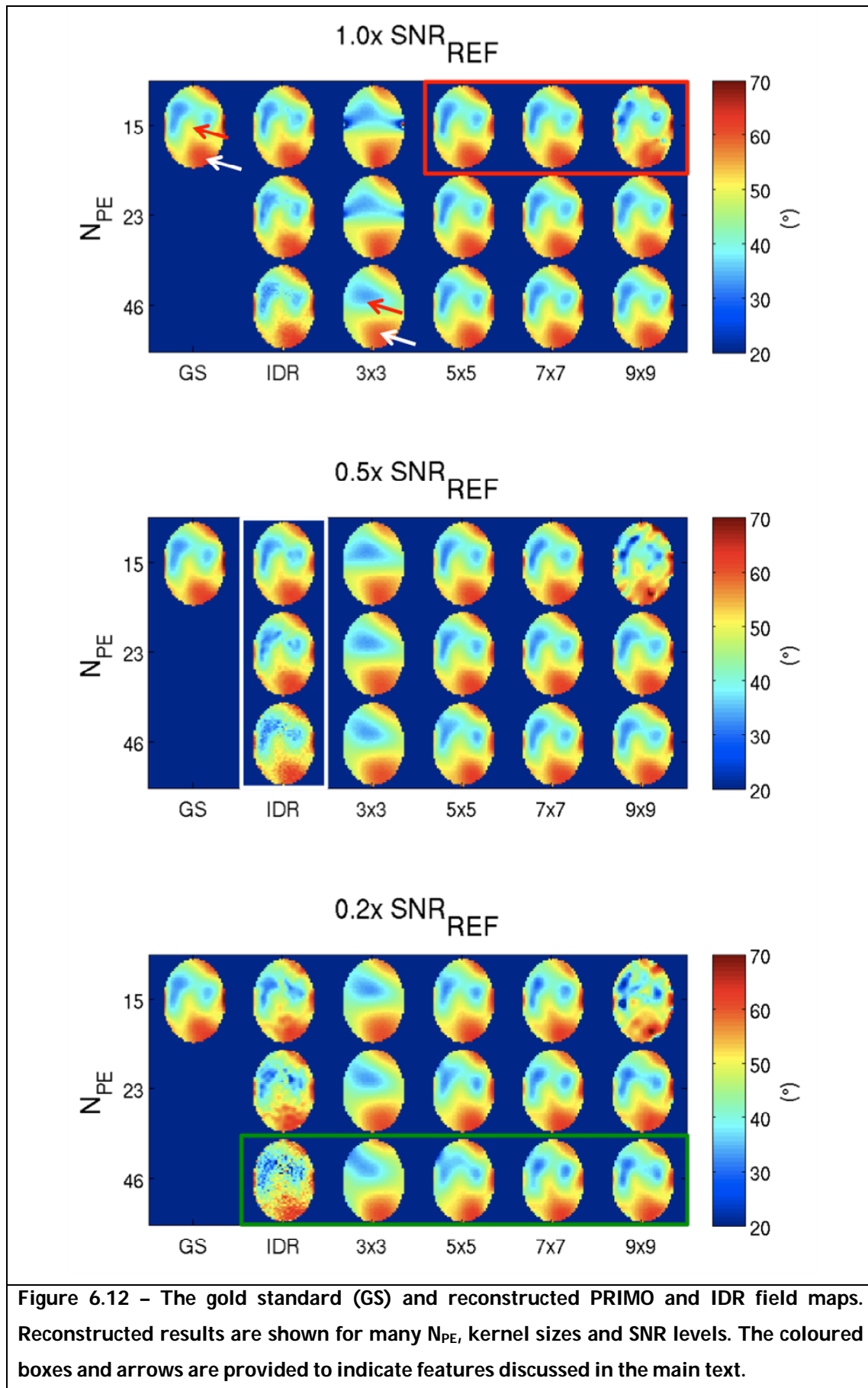


Figure 6.12 – The gold standard (GS) and reconstructed PRIMo and IDR field maps. Reconstructed results are shown for many N_{PE} , kernel sizes and SNR levels. The coloured boxes and arrows are provided to indicate features discussed in the main text.

6.4.2 Simulation 2

Figure 6.13 shows the results from the second simulation, applying PRIMO to relative transmit mapping. The error curves broadly display similar features as seen in simulation 1. The IDR curves have higher error at low and high N_{PE} . PRIMO error curves have high error at low N_{PE} , and a gradually increasing error as N_{PE} increases.

PW-PRIMO and ALL-PRIMO display different characteristics. In all cases, PW-PRIMO has a lower critical N_{PE} level. This is because PW-PRIMO requires fewer weights to be estimated than ALL-PRIMO. The reconstruction errors of ALL-PRIMO and PW-PRIMO above the critical N_{PE} level depend on the kernel size. For $N_k > 5$, PW-PRIMO and ALL-PRIMO produce very similar reconstruction errors. These errors always outperform IDR.

In contrast, ALL-PRIMO and PW-PRIMO behave differently at $N_k=3$ and $N_k=5$. PW-PRIMO produces a reconstruction with a higher error compared to ALL-PRIMO. This is behaviour, which has been observed in other studies (Bauer et al., 2011), can be explained as follows. PW-PRIMO produces poor results, as the kernel is too small to model the full spatial frequency profile of the relative coil profile. However, for ALL-PRIMO, the reconstruction algorithm can use k-space samples from any other transmit dataset to synthesise a point in the desired dataset. Therefore ALL-PRIMO will be more successful, as it is more likely that another coil will have a relative relationship which can be modelled by a small kernel.

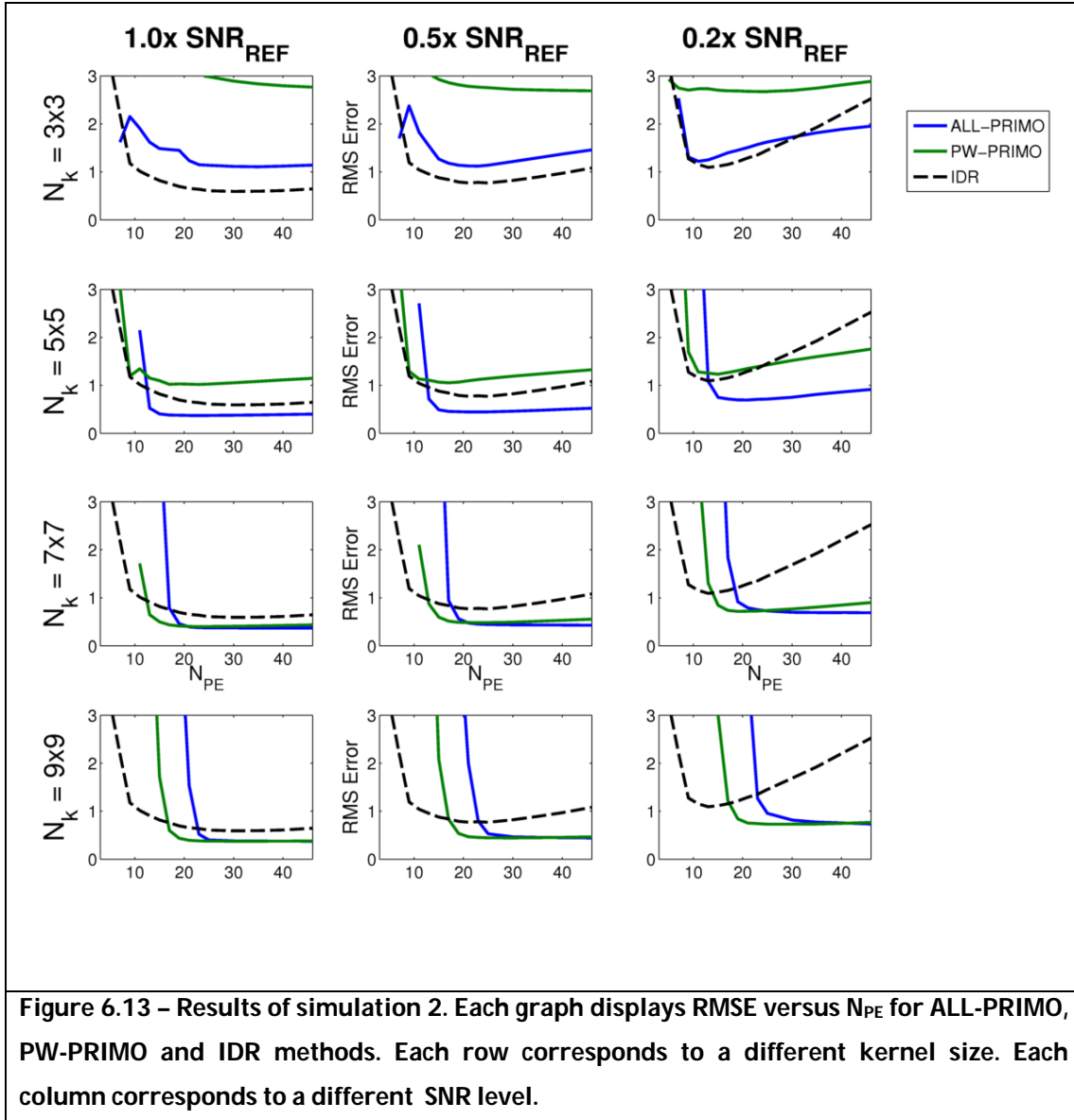


Figure 6.13 – Results of simulation 2. Each graph displays RMSE versus N_{PE} for ALL-PRIMO, PW-PRIMO and IDR methods. Each row corresponds to a different kernel size. Each column corresponds to a different SNR level.

6.4.3 In-Vivo Experiments

Figure 6.14 display the results from PRIMO and IDR applied to magnitude transmit field mapping in a transverse slice in the brain. The IDR reconstructions display the same behaviour as seen in the simulations. At high N_{PE} there is noise visible in the field maps, in addition to some residual tissue dependent modulations. Reducing N_{PE} produces a smoother field map. For very low N_{PE} the shape of the reconstructed field map becomes distorted as compared to the fully sampled case.

The PRIMO reconstructions always produce smooth fields that display spatial variations consistent with the IDR reconstructions. The $N_k=3$ PRIMO faithfully reconstructs the gross structure of the transmit field. Increasing N_k further refines the field to match the IDR case. Reducing N_{PE} eventually results in corrupted reconstructions. This occurs sooner for larger kernels, since more data is needed to estimate the larger number of weights.

Figure 6.15 shows sagittal slices through the reconstructed IDR and PRIMO maps. The reconstructions follow the similar trends as in the transverse case. The IDR reconstructions demonstrate more significant errors, especially in the sinuses (white arrow).

The effect of using an inappropriately small kernel are well demonstrated by the $N_k=3$ reconstructions. There are several slices in which the reconstructed fields do not follow the IDR fields. The white arrow gives an example of this. The failure of PRIMO is easily identifiable by strong field discontinuities between slices. This behaviour is seen for $N_k=3$ reconstructions at all N_{PE} .

Increasing N_k above 5 results in much improved reconstructed fields. They are consistent between slices when there is sufficient data ($N_k=5$, $N_{PE} \geq 23$; $N_k=7$, $N_{PE} \geq 30$; $N_k=9$, $N_{PE} \geq 30$). Reducing N_{PE} below these levels introduces artifacts. Furthermore, using PRIMO results in significantly improved field estimates in the sinus area.

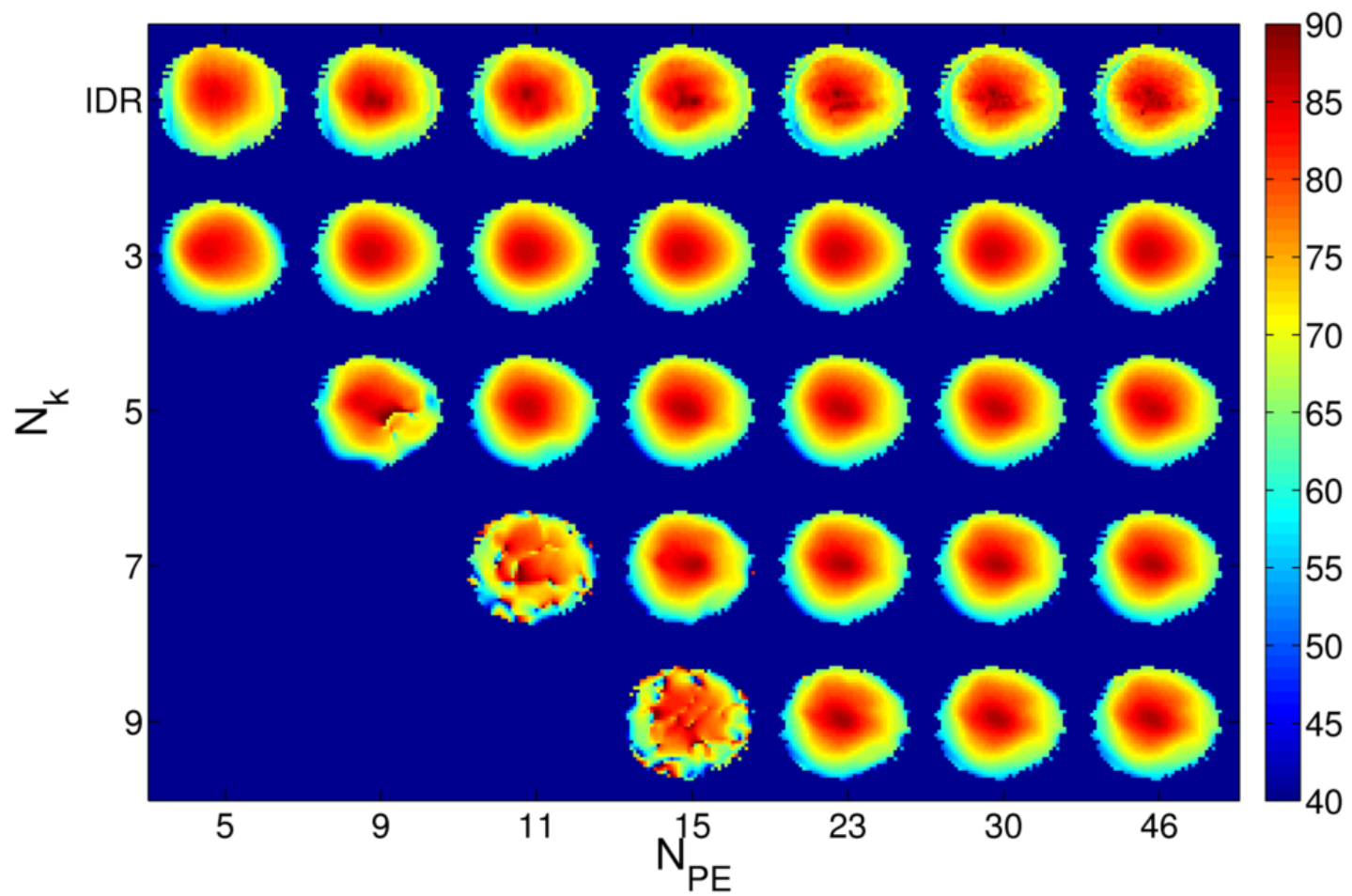


Figure 6.14 – Reconstructed magnitude transmit field maps for a transverse slice through the brain. The first row gives the IDR reconstruction. The remaining rows display PRIMO reconstruction for different N_k . Each column corresponds to a different N_{PE} .

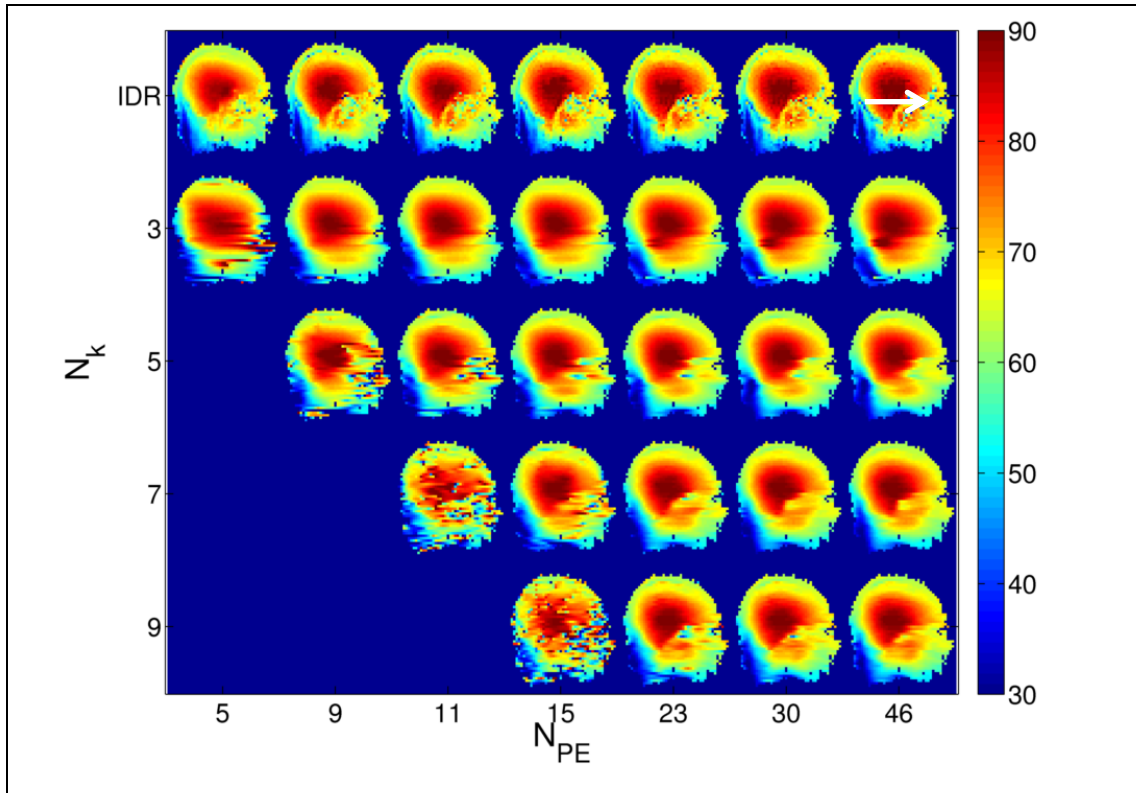


Figure 6.15 – Reconstructed magnitude transmit field maps for a sagittal slice through the brain. The left-right direction in the image corresponds to the posterior-anterior anatomical direction. The first row gives the IDR reconstruction. The remaining rows display PRIMO reconstruction for different N_k . Each column corresponds to a different N_{PE} .

Figure 6.16 displays results of using IDR, PW-PRIMO and ALL-PRIMO for relative transmit field mapping in a transverse slice through the thighs. Both IDR fields contain low-level noise.

The $N_k=3$ images show how using ALL-PRIMO is superior to PW-PRIMO when using small kernels. The PW fields do not accurately reproduce the field pattern shown in the IDR case (for example, see white arrows). Using ALL-PRIMO produces fields that are more consistent with IDR, but are still not faithful reconstructions of the fields (see red arrows – fields are more like IDR, but still not accurate). This is true at both levels of data sampling. Increasing the kernel size to $N_k=7$ significantly improves the PRIMO reconstructions for both PW and ALL-PRIMO. This is true for both data levels.

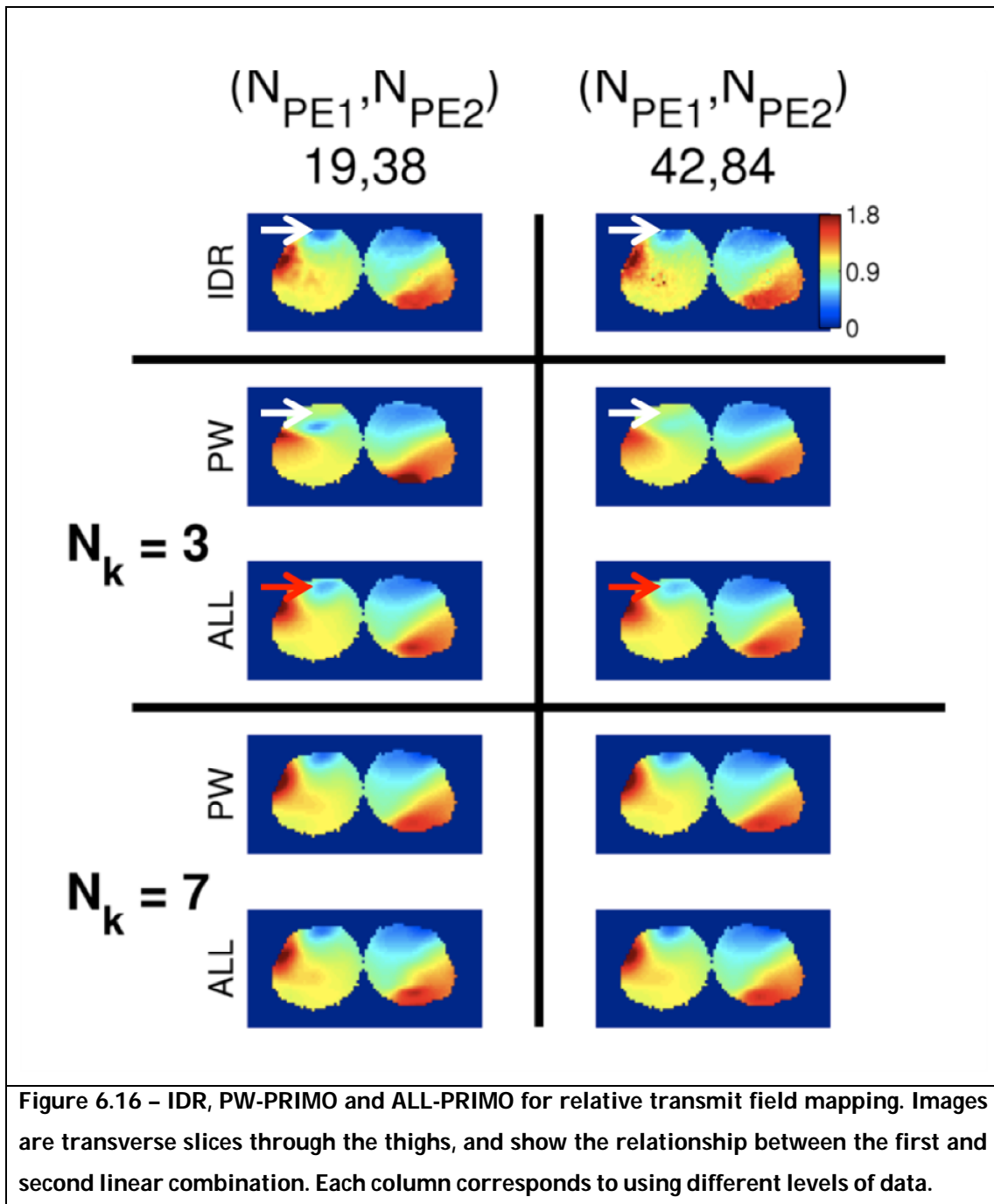


Figure 6.17 and Figure 6.18 display the IDR and ALL-PRIMO reconstructions for relative transmit field mapping in the thigh, using $N_k=5$ and all of the measured data. The greater susceptibility to noise of the IDR method is clearly demonstrated. Furthermore, localised errors are again present in areas of low spin density, here being the bone marrow (white arrows). PRIMO handles these areas in a superior manner, as the estimated field interpolates through the region in a realistic manner.

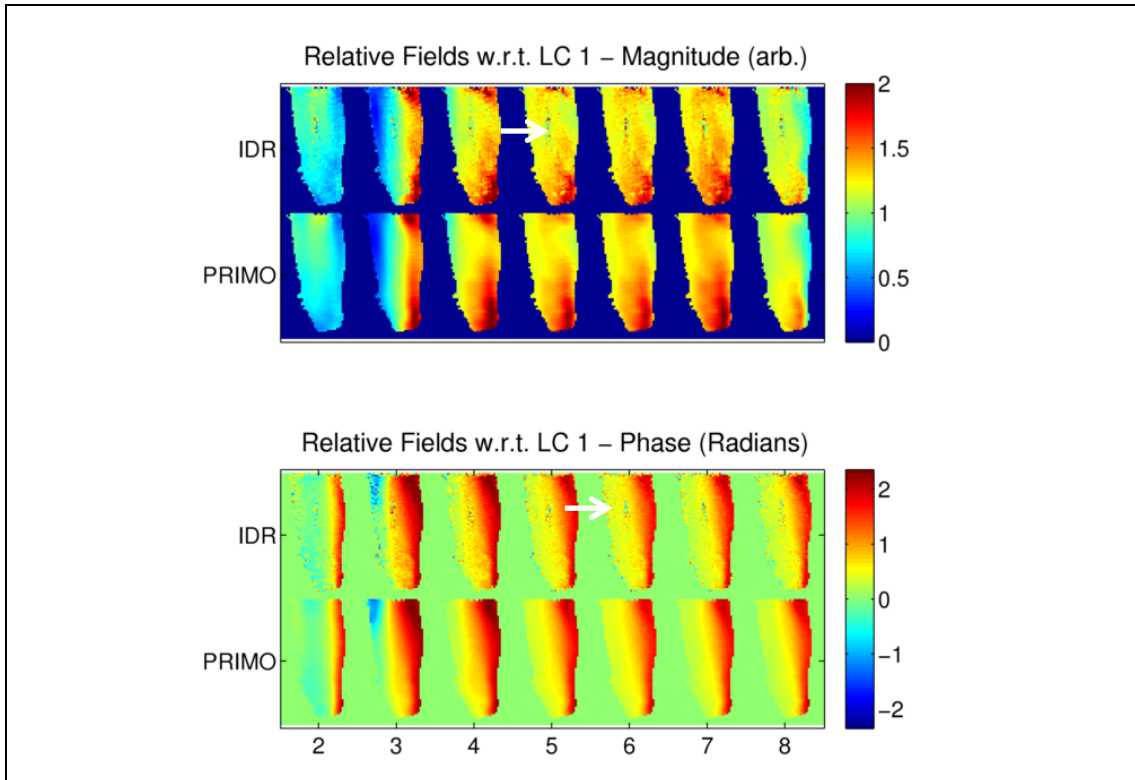


Figure 6.17 – IDR and ALL-PRIMO reconstructions for relative transmit field mapping for all LCs with respect to the first LC. The images correspond to a sagittal slice through the thigh. The IDR phase images are formed by averaging the relative phase from each receiver.

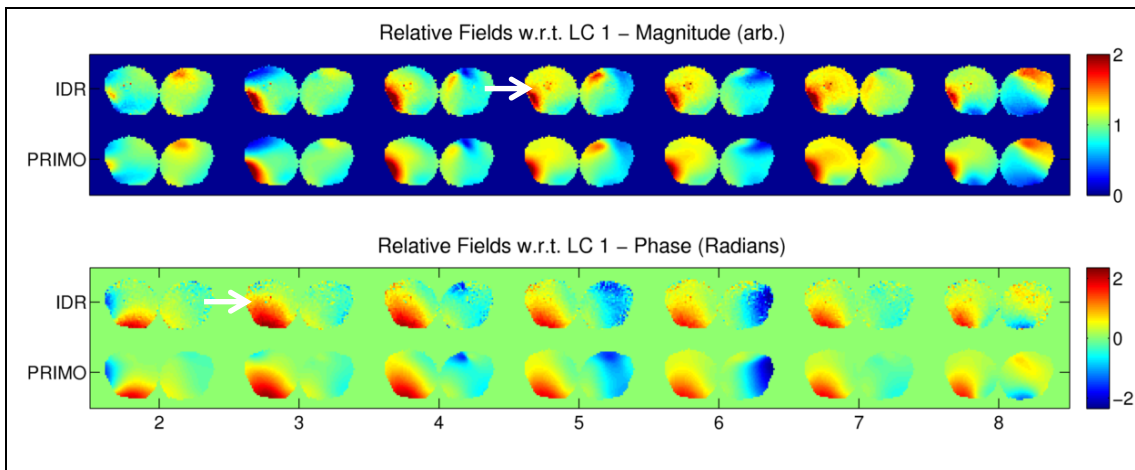
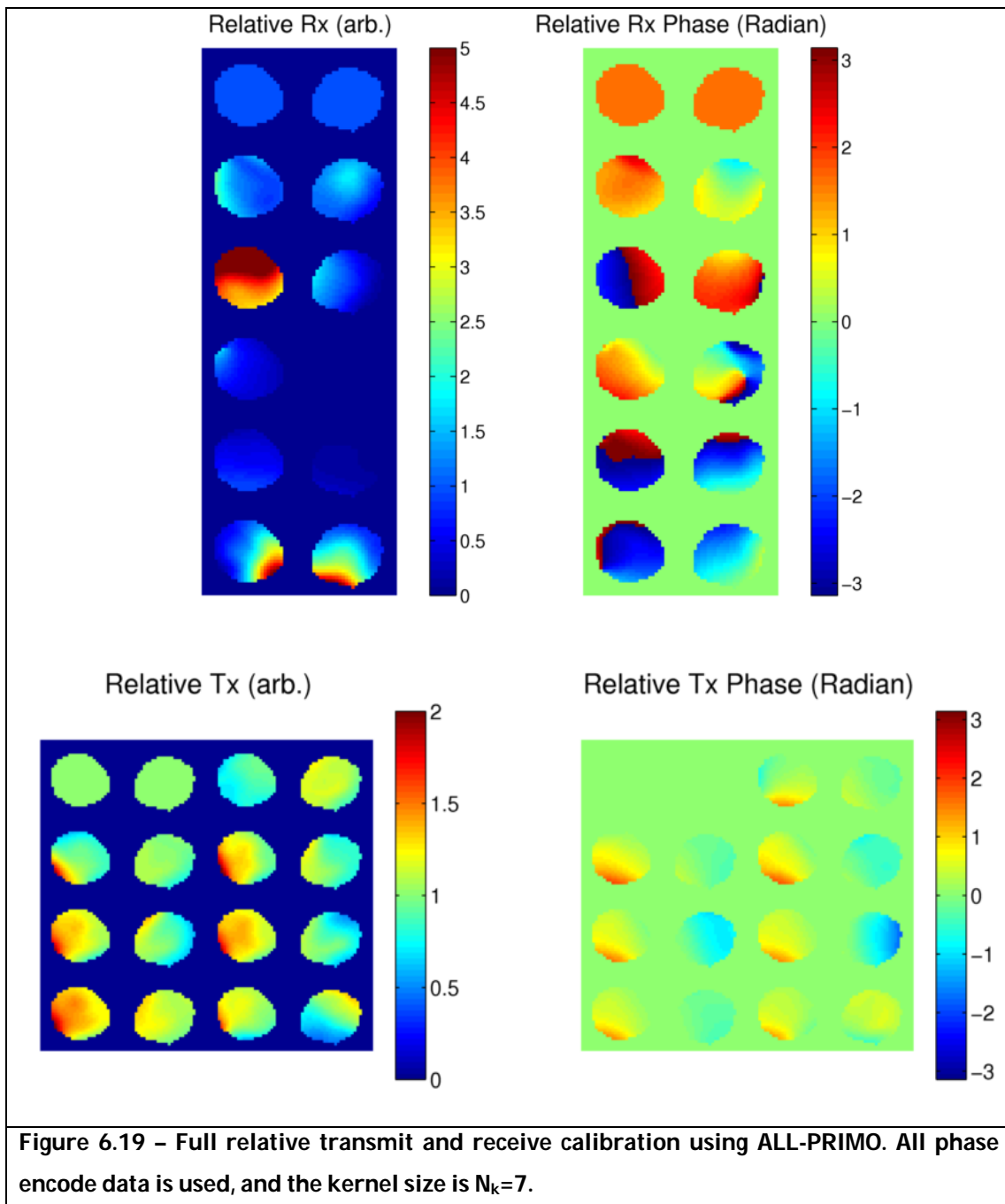


Figure 6.18 – IDR and ALL-PRIMO reconstructions for relative transmit field mapping for all LCs with respect to the first LC. The images correspond to a transverse slice through the thigh. The IDR phase images are formed by averaging the relative phase from each receiver.

Finally, Figure 6.19 presents full relative calibration results using ALL-PRIMO for relative transmit and receive. All relative receive fields are with respect to the first receiver, and all transmit fields are relative to the first linear combination. The relative receive fields show steeper spatial variations as compared to the transmit fields. This is because the receive array is constructed from smaller elements, as compared to the transmitters, which are designed to have spatial variation across the size of the magnet bore.



6.5 Discussion

This chapter has presented a novel reconstruction algorithm, PRIMO, which has been shown to produce superior RF field maps than standard image-domain methods. PRIMO builds upon previous work that demonstrated that receive fields could be extracted from k-space data. The method is resistant to the corrupting influence of noise, and produces field maps that are inherently smooth. It is sufficiently general to be applicable to any ratiometric RF field mapping sequence.

The generalisation of the Lustig approach to unified RF field mapping in a single step is natural. This is as in a real imaging scenario with a parallel reception and transmission system, all RF fields would have to be measured, and performing separate receive calibration and transmit calibration is not an optimal use of time.

PRIMO also circumvents the bootstrapping problem inherent to field mapping. As previously discussed (Brunner and Pruessmann, 2010), good transmit field estimation requires individual receive images to be suitably combined. However, in order to determine the phased combination of receivers to allow this, the receive fields must have been previously measured. This requires homogenous excitation, for which knowledge of transmit field maps is a prerequisite. This is a circular problem, for which Brunner proposed an SVD decomposition of low flip-angle images method as a possible solution (Brunner and Pruessmann, 2010). We tested this approach alongside PRIMO in our simulated experiments, and found that the Brunner method displayed the same behaviour as the IDR method. This demonstrates that a key component of PRIMO is the direct estimation of the convolution kernels relating each k-space measurement to every other.

There is an inherent trade-off between kernel size and the amount and quality of measured data. Selection of a large kernel for all PRIMO reconstructions would allow all spatial frequencies present in the field maps to be captured, enabling

accurate reconstructions. However, large kernel sizes increase the number of weights that need to be estimated making the matrix inversion more ill-posed. This can make the value of the weights be very sensitive to noise present in the data.

This trade-off between kernel size and quantity of data is seen in PRIMO reconstructions of simulated AFI data in Figure 6.11. A 7x7 kernel outperforms the 9x9 kernel when the SNR is low, since the incremental benefit of including more spatial harmonics does not outweigh the fact that more weights need to be estimated.

This trade-off is also seen when comparing PW-PRIMO and ALL-PRIMO. PW-PRIMO requires fewer coefficients to be estimated. This allows high-quality reconstructions to be performed with less data than ALL-PRIMO, as shown in Figure 6.13. Conversely, when the size of the kernel is too small, PW-PRIMO performs worse than ALL-PRIMO. This is because the benefit of allowing more coils to contribute to the synthesis of a k-space measurement outweighs the cost of having to estimate more coefficients.

This trade-off also informed selection of a slice-by-slice reconstruction strategy, despite PRIMO being sufficiently general to allow 3D kernels. Preliminary experiments showed that although 3D kernels have the attractive property of constraining field smoothness in all spatial directions, this came at the expense of requiring too much data for accurate determination of the weights. Figure 6.20 demonstrates this effect by comparing 2D and 3D PRIMO. $N_k=3$ 3D PRIMO does not contain enough spatial harmonics to produce an accurate field (black arrow indicates an example region of error). However, increasing the kernel size does not help, since the weights cannot be accurately synthesised. This violates the PRIMO eigenvalue equation, yielding eigenvectors with non-unity eigenvalues, resulting in localised errors, as indicated by blue arrows.

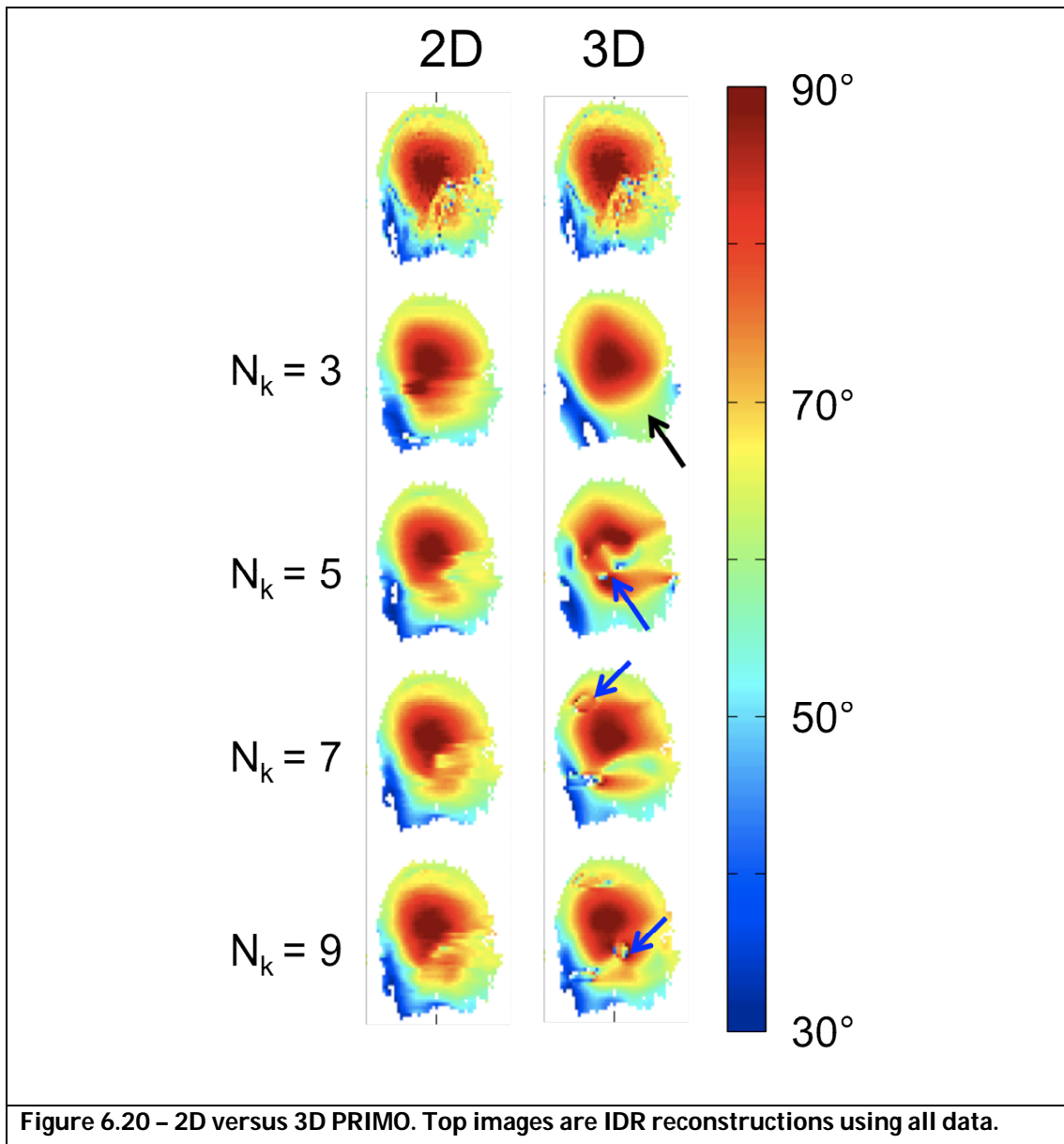


Figure 6.20 – 2D versus 3D PRIMO. Top images are IDR reconstructions using all data.

The relationship between kernel size and the quality of the reconstructed weights has recently been observed in the context of GRAPPA reconstructions (Bauer et al., 2011). The authors observed that when using a 32-channel receive coil, a 1x2 kernel produced reconstructions of lowest error, independent of the size of the calibration matrix. This mirrors the behaviour seen in Figure 6.11, where PW-PRIMO produces fields of higher RMSE than ALL-PRIMO when a kernel size is used which is smaller than the field variation of the coil.

Regularisation was shown to provide only a small improvement to reconstruction quality at high levels of data truncation. However, operating in

this regime is not recommended, as the level of stabilisation provided by regularisation cannot be reliably predicted.

The PRIMO also offers the potential to accelerate the RF field mapping process in several ways. Firstly, receive and transmit calibration no longer needs to be performed sequentially. Dedicated receive calibration scans are now redundant. Secondly, PRIMO is robust to noise. The relative transmit mapping method proposed by Van De Moortele (Van de Moortele and Ugurbil, 2009) is fast as it uses a short TR SPGR acquisition. However it is an inherently low SNR method, as a small flip angle is required to ensure the image signal is proportional to the transmit field amplitude. PRIMO allows the use of this technique with less sensitivity to noise. The use of the Van De Moortele method allows for only a single magnitude transmit field mapping scan to be performed. Until recently (Nehrke and Börnert, 2012), these methods have been the slowest part of RF field calibration.

The PRIMO framework is amenable to the incorporation of multi-echo data. This would allow B_0 field mapping, combined with the associated benefit of having more data with which to estimate all of the relationships. A kernel approach to B_0 field mapping and inhomogeneity correction has previously been demonstrated in ORACLE (Lin et al.).

The experiments performed here did not use both the absolute transmit field mapping data and relative field mapping data for receive estimation. The PRIMO framework can accommodate this if it is guaranteed that the k-space sampling scheme is the same for all acquisitions.

PRIMO utilises standard least-square fitting for calculation for kernel weights. More advanced methods have recently been proposed (Chang et al.; Huo and Wilson, 2008). Future work could explore if these allow further reduction in reconstructed field map error, and could enable 3D kernels to be used.

In summary, a novel calibration reconstruction method, PRIMO, has been presented. It provides an elegant framework with which to perform full RF field calibration in an SNR and data efficient way. The resulting field maps are superior to those generated by standard image domain division.

6.6 References

- Bauer, S., Markl, M., Honal, M., and Jung, B.A. (2011). The effect of reconstruction and acquisition parameters for GRAPPA-based parallel imaging on the image quality. *Magnetic Resonance in Medicine* 66, 402–409.
- Bernstein, M.A., King, K.F., and Zhou, X.J. (2004). *Handbook of MRI pulse sequences* (Elsevier).
- Brunner, D.O., and Pruessmann, K.P. (2008). A matrix approach for mapping array transmit fields in under a minute. *Quadrature* 60, 100.
- Brunner, D.O., and Pruessmann, K.P. (2010). SVD based calibration of transmit arrays. In *Proceedings 18th Scientific Meeting, International Society for Magnetic Resonance in Medicine, Stockholm*, p. 272.
- Chang, Y., Liang, D., and Ying, L. Nonlinear GRAPPA: A kernel approach to parallel MRI reconstruction. *Magnetic Resonance in Medicine*.
- Griswold, M.A., Jakob, P.M., Heidemann, R.M., Nittka, M., Jellus, V., Wang, J., Kiefer, B., and Haase, A. (2002). Generalized autocalibrating partially parallel acquisitions (GRAPPA). *Magnetic Resonance in Medicine* 47, 1202–1210.
- Huo, D., and Wilson, D.L. (2008). Robust GRAPPA reconstruction and its evaluation with the perceptual difference model. *Journal of Magnetic Resonance Imaging* 27, 1412–1420.
- Lai, P., Lustig, M., Brau, A.C., Vasanawala, S., Beatty, P.J., and Alley, M. (2010). Efficient L1SPIRiT reconstruction (ESPIRiT) for highly accelerated 3D volumetric MRI with parallel imaging and compressed sensing. *Stockholm, Sweden* 345.
- Larkman, D.J., and Nunes, R.G. (2007). Parallel magnetic resonance imaging. *Physics in Medicine and Biology* 52, R15–R55.
- Lin, C., Bernstein, M.A., Huston, J., and Fain, S. (2001). Measurements of T1 relaxation times at 3.0 T: implications for clinical MRA. In *Proceedings of the 9th Annual Meeting of ISMRM, Glasgow*, p. 1391.

Lin, W., Huang, F., Li, Y., and Reykowski, A. (2010). Optimally regularized GRAPPA/GROWL with experimental verifications. In Proceedings of the 18th Annual Meeting of ISMRM, Stockholm, Sweden, p. 2874.

Lin, W., Huang, F., Simonotto, E., Duensing, G.R., and Reykowski, A. (2012). Off-resonance artifacts correction with convolution in k-space (ORACLE). *Magnetic Resonance in Medicine* 67, 1547–1555.

Lustig, M., Lai, P., Murphy, M., Vasanawala, S., Elad, M., Zhang, J., and Pauly, J. (2011). An Eigen-Vector Approach to AutoCalibrating Parallel MRI, Where SENSE Meets GRAPPA. p. 479.

Lustig, M., and Pauly, J.M. (2010). SPIRiT: Iterative self-consistent parallel imaging reconstruction from arbitrary k-space. *Magnetic Resonance in Medicine* 64, 457–471.

Van de Moortele, P., and Ugurbil, K. (2009). Very fast multi channel B1 calibration at high field in the small flip angle regime. In Proceedings of the 17th Annual Meeting of ISMRM, Honolulu, Hawaii, USA, p. 367.

Nehrke, K., and Börnert, P. DREAM—a novel approach for robust, ultrafast, multislice B1 mapping. *Magnetic Resonance in Medicine*.

Pruessmann, K.P. (2006). Encoding and reconstruction in parallel MRI. *NMR in Biomedicine* 19, 288–299.

Pruessmann, K.P., Weiger, M., Scheidegger, M.B., and Boesiger, P. (1999). SENSE: Sensitivity encoding for fast MRI. *Magnetic Resonance in Medicine* 42, 952–962.

Sodickson, D.K., and Manning, W.J. (1997). Simultaneous acquisition of spatial harmonics (SMASH): Fast imaging with radiofrequency coil arrays. *Magnetic Resonance in Medicine* 38, 591–603.

Stanisz, G.J., Odobina, E.E., Pun, J., Escaravage, M., Graham, S.J., Bronskill, M.J., and Henkelman, R.M. (2005). T1, T2 relaxation and magnetization transfer in tissue at 3T. *Magnetic Resonance in Medicine* 54, 507–512.

Tieng, Q.M., Ullmann, P., Galloway, G.J., Hennig, J., Cowin, G.J., and Vegh, V. (2008). An Approach of Deriving Relative Sensitivity Profiles for Image Reconstruction in MRI. *IEEE Journal of Selected Topics in Signal Processing* 2, 817–827.

Vernickel, P., Röschmann, P., Findeklee, C., Lüdeke, K. -m, Leussler, C., Overweg, J., Katscher, U., Grässlin, I., and Schünemann, K. (2007). Eight-channel transmit/receive body MRI coil at 3T. *Magnetic Resonance in Medicine* 58, 381–389.

Yarnykh, V.L. (2007). Actual flip-angle imaging in the pulsed steady state: A method for rapid three-dimensional mapping of the transmitted radiofrequency field. *Magnetic Resonance in Medicine* 57, 192–200.

Chapter 7 Conclusions

Chapter 4 presented the first component of the thesis. This work was motivated by two active research areas in MRI. The first is the current push towards higher B_0 field strengths. Higher B_0 results in stronger inhomogeneity in the RF field, an effect that originates from the electromagnetic interaction between the patient and the field itself (Ibrahim et al., 2009). The work was also driven by recent developments in the field of image reconstruction, in which methods are being developed to reconstruct images in spite of subject motion (Melbourne et al., 2007; Prieto et al., 2010).

Given the interaction between the RF field and the subject, it was hypothesised that the field might change in the presence of subject motion. Changes in the RF field due to motion would impact the temporal evolution of the MR signal, an effect which could impact upon novel motion-robust reconstruction techniques.

The link between subject respiration and the RF field was therefore investigated in the liver at 3T. This study demonstrated that the RF field did change between maximum inhale and exhale respiratory states across a cohort of volunteers. The field changed both in terms of average amplitude in a ROI placed in the liver, and also spatially across the ROI. It was also shown that a multi-transmit array could be used to reduce the difference between the inhale and exhale RF fields.

A difference in transmit field between inhale and exhale states implied that a transition must occur between them at intermediate respiratory positions. No field mapping technique was capable of real-time transmit field measurement at the time this research was performed, and so a retrospective reconstruction method was developed. This method was hampered by the lengthy scan durations required and was therefore abandoned in favour of directly addressing the more general question of how to shorten calibration times.

Chapter 5 presented research into a novel method for accelerating magnitude transmit field mapping. This was initially motivated by the clear difficulties associated with time resolved mapping of the transmit field throughout the respiratory cycle. However,

faster transmit field mapping in itself is a desirable technology. This is particularly important for multi-transmit system architectures, which have recently been introduced – despite the many benefits offered by parallel transmission (Grissom et al., 2006; Setsompop et al., 2008; Malik et al., 2010), its wide clinical adoption is hindered by the significant time penalty required to calibrate all of the transmit channels.

The proposed approach utilised a model-based reconstruction that promoted a transmit field which is a smooth function of space, as widely observed experimentally (Wiesinger et al., 2006; Funai et al., 2007). The first two studies in Chapter 5 revealed that sampling the centre of k-space was a key contributor to reconstruction accuracy. This conclusion was reinforced in the third study, where it was also shown that the reconstruction performed best when the field map was reconstructed to a high-resolution spatial grid. If both of these criteria are met, the proposed reconstruction scheme outperforms standard image domain methods.

Chapter 6 presented an approach to full RF system calibration. This method was developed to unify two seemingly separate processes: receive field mapping and transmit field mapping. These two steps are currently performed serially, which extends the duration of the calibration portion of a scan session. However, there is a certain level of data redundancy by using the conventional approach. The proposed reconstruction scheme, named PRIMO, provided an elegant means of estimating all RF fields solely from transmit field mapping data. It was tested in simulations and in-vivo, and was shown to produce field maps superior to those produced by standard image domain methods.

7.1 Summary of Achievements

- RF field mapping and subject motion
 - Effects of changes in subject position on the sensitivity patterns of RF coils were investigated at 3T. It was demonstrated that changes in the subject's respiratory position could result in substantial changes in the transmit field in the liver.
 - Simulations demonstrated that parallel transmission can be utilised to correct for respiratory changes in the transmit field.

- A sequence and reconstruction method based on retrospective gating was developed to enable transmit field mapping throughout the respiratory cycle. The method was able to partially resolve inconsistencies in the data due to respiratory motion, but the resulting field maps contained residual artifacts, undermining the utility of the technique.
- Field maps from undersampled data
 - A novel reconstruction method was developed to allow accelerated transmit field mapping. This method exploited the observation that transmit fields are always a smooth function of space.
 - It was shown that this method could produce field maps of superior quality than standard image-domain approaches.
- Comprehensive RF field mapping
 - Finally, a whole-system calibration method, PRIMO, was developed. It allows estimation of all receive and transmit data from a typical calibration dataset.
 - PRIMO was shown to outperform current approaches, producing accurate, smooth and noise-robust field maps.

7.2 Future Work

There are several aspects of this work that are amenable to further investigation. It would be interesting to extend the work presented in Chapter 4 on the impact of subject motion on RF fields to investigations at higher B_0 field strengths. The RF field becomes more sensitive to the electromagnetic properties of tissue at higher fields, and therefore subject motion would likely induce a larger change in the measured fields. Further work might also investigate the effect of motion on more local transmit arrays. For example, many transmit arrays have been developed for cardiac and torso imaging at 7T which lie directly on the chest wall of the volunteer (Snyder et al., 2009; Vaughan et al., 2009). The proximity of the elements to the heart and liver could induce larger changes in the field due to respiratory and potentially cardiac motion.

The work in Chapter 5 on use of under-sampled acquisitions in field mapping would initially benefit from being validated on an in-vivo dataset. The results obtained are promising, so translation to a working implementation that could be generally used is an appealing goal. As part of this process, alternative minimisation methods (Clason and von Winckel, 2010), which might result in improved reconstructed field maps, should be tested. It might also be beneficial to express field maps in an alternative basis, such as with Fourier coefficients (Uecker et al., 2008) or polynomials (Ying and Sheng, 2007).

Finally, the PRIMO method developed in Chapter 6 would benefit from the inclusion of multi-echo data to allow B_0 field mapping as well as RF transmit and receive mapping in a single comprehensive calibration scheme. This would be likely to improve the estimation of all fields, since more data would be acquired, which would in turn improve the estimation of kernel weights. A similar approach to PRIMO for B_0 field mapping has already been proposed and demonstrated on in-vivo data (Lin et al). Further work could also test PRIMO at higher fields. This would test the impact of greater inhomogeneity on the necessary kernel size.

Our core preoccupation of effective and efficient calibration of RF fields, and the recognition that such fields may vary on a number of time scales during any single MR examination at higher field strength, is being taken up by an increasing number of research groups as they strive to develop higher field scanning methods in general and parallel transmit technology in particular. This is a fast moving area of study, which continues to offer exciting challenges and will surely lead to improved performance in both imaging and spectroscopy.

7.3 References

Clason, C., and von Winckel, G. (2010). On a bilinear optimization problem in parallel magnetic resonance imaging. *Applied Mathematics and Computation* 216, 1443–1452.

Funai, A., Fessler, J.A., Grissom, W., and Noll, D.C. (2007). Regularized B_1+ map estimation in MRI. In *Biomedical Imaging: From Nano to Macro, 2007. ISBI 2007. 4th IEEE International Symposium On*, pp. 616–619.

- Grissom, W., Yip, C., Zhang, Z., Stenger, V.A., Fessler, J.A., and Noll, D.C. (2006). Spatial domain method for the design of RF pulses in multicoil parallel excitation. *Magnetic Resonance in Medicine* 56, 620–629.
- Ibrahim, T.S., Hue, Y.-K., and Tang, L. (2009). Understanding and manipulating the RF fields at high field MRI. *NMR in Biomedicine* 22, 927–936.
- Lin, W., Huang, F., Simonotto, E., Duensing, G.R., and Reykowski, A. Off-resonance artifacts correction with convolution in k-space (ORACLE). *Magnetic Resonance in Medicine*.
- Lustig, M., Lai, P., Murphy, M., Vasanawala, S., Elad, M., Zhang, J., and Pauly, J. (2011). An Eigen-Vector Approach to AutoCalibrating Parallel MRI, Where SENSE Meets GRAPPA. p. 479.
- Malik, S.J., Keihaninejad, S., Hammers, A., and Hajnal, J.V. Tailored excitation in 3D with spiral nonselective (SPINS) RF pulses. *Magnetic Resonance in Medicine*.
- Malik, S.J., Larkman, D.J., O'Regan, D.P., and Hajnal, J.V. (2010). Subject-specific water-selective imaging using parallel transmission. *Magnetic Resonance in Medicine* 63, 988–997.
- Melbourne, A., Atkinson, D., White, M.J., Collins, D., Leach, M., and Hawkes, D. (2007). Registration of dynamic contrast-enhanced MRI using a progressive principal component registration (PPCR). *Physics in Medicine and Biology* 52, 5147–5156.
- Prieto, C., Uribe, S., Razavi, R., Atkinson, D., and Schaeffter, T. (2010). 3D undersampled golden-radial phase encoding for DCE-MRA using inherently regularized iterative SENSE. *Magnetic Resonance in Medicine* 64, 514–526.
- Setsompop, K., Wald, L.L., Alagappan, V., Gagoski, B.A., and Adalsteinsson, E. (2008). Magnitude least squares optimization for parallel radio frequency excitation design demonstrated at 7 Tesla with eight channels. *Magnetic Resonance in Medicine* 59, 908–915.
- Snyder, C. j., DelaBarre, L., Metzger, G. j., van de Moortele, P.-F., Akgun, C., Ugurbil, K., and Vaughan, J. t. (2009). Initial results of cardiac imaging at 7 tesla. *Magnetic Resonance in Medicine* 61, 517–524.
- Uecker, M., Hohage, T., Block, K.T., and Frahm, J. (2008). Image reconstruction by regularized nonlinear inversion—Joint estimation of coil sensitivities and image content. *Magnetic Resonance in Medicine* 60, 674–682.

Vaughan, J.T., Snyder, C.J., DelaBarre, L.J., Bolan, P.J., Tian, J., Bolinger, L., Adriany, G., Andersen, P., Strupp, J., and Ugurbil, K. (2009). Whole-body imaging at 7T: Preliminary results. *Magnetic Resonance in Medicine* 61, 244–248.

Wiesinger, F., Van de Moortele, P., Adriany, G., De Zanche, N., Ugurbil, K., and Pruessmann, K.P. (2006). Potential and feasibility of parallel MRI at high field. *NMR in Biomedicine* 19, 368–378.

Ying, L., and Sheng, J. (2007). Joint image reconstruction and sensitivity estimation in SENSE (JSENSE). *Magnetic Resonance in Medicine*, *Magnetic Resonance in Medicine* 57, 1196, 1196–1202, 1202.